

Theoretical Mechanistic Investigations of Carbene and Nitrene Transfer Reactions

Von der Fakultät für Mathematik, Informatik und Naturwissenschaften der RWTH Aachen
University zur Erlangung des akademischen Grades eines Doktors der
Naturwissenschaften genehmigte Dissertation

vorgelegt von

Chao Pei, M.Sc.

aus

Jiangsu, China

Berichter: *Professor Dr. Rene M. Koenigs*
Professor Dr. Frédéric W. Patureau

Tag der mündlichen Prüfung: *17th November 2022*

Diese Dissertation ist auf den Internetseiten der Universitätsbibliothek verfügbar.

The work reported in this thesis was performed at the Institute of Organic Chemistry at the RWTH Aachen University in Aachen from October 2019 until August 2022 under the supervision of Prof. Dr. Rene M. Koenigs.

Acknowledgement

Upon finishing thesis, I would like to express my great gratitude towards all those who have helped me a lot during the past three years. First and foremost, I would like to thank my supervisor, Prof. Dr. Rene M. Koenigs, who offered me the opportunity to apply CSC scholarship and start my study in RWTH University. During my research, he has provided expensive and high-performance computers for more complex computational studies, and given me insightful suggestions and constant encouragement for my research. In the life, he has provided accommodation to me in the first half a year, and taught me the positive life attitude, which will encourage me forever.

Furthermore, I want to thank all the group members in the Koenigs group. They create a pleasant working atmosphere. In particular, I am grateful to Yang Zhen for his kind assistance when I just started in our lab. Empel Claire, who is the lab manager, provides us with an orderly and good lab environment, and thus makes us focus on our research. I also appreciate all other nice group members, Yujing, Sripati, Feifei, Fang, Hao and Yun.

Finally, I would like to extend my deep gratefulness to my parents and friends, especially my girlfriend, whose encouragement and support make my accomplishments possible.

The following parts of this work have already been published:

Photochemical Ring Expansion Reactions: Synthesis of Tetrahydrofuran Derivatives and Mechanism Studies

S. Jana, Z. Yang, C. Pei, X. Xu, R. M. Koenigs, *Chem. Sci.* **2019**, *10*, 10129–10134.

Photochemical Fluoro-amino Etherification Reactions of Aryldiazoacetates with NFSI under Stoichiometric Conditions

F. He, C. Pei, R. M. Koenigs, *Chem. Commun.* **2020**, *56*, 599–602.

Substrate-Controlled Cyclopropanation Reactions of Glycals with Aryl Diazoacetates

Y. Guo, C. Pei, R. M. Koenigs, *ChemCatChem* **2020**, *12*, 4014–4018.

Photochemical Cyclopropanation of Cyclooctatetraene and (Poly-)unsaturated Carbocycles

Y. Guo,⁺ C. Empel,⁺ C. Pei, I. Atodiresei, T. Fallon, R. M. Koenigs, *Org. Lett.* **2020**, *22*, 5126–5130.

⁺equal contribution

Rhodium-Catalyzed Enamine Homologation of Sulfides with Triazoles as Carbene Precursor

F. Li, C. Pei, R. M. Koenigs, *Org. Lett.* **2020**, *22*, 6816–6821.

Access to *Gem*-Difluoro Olefines via C-H Functionalization and Dual Role of Anilines

Z. Yang, C. Pei, R. M. Koenigs, *Org. Lett.* **2020**, *22*, 7234–7238.

Photochemical OH Functionalization of Aryldiazoacetates with Phenols via Proton Transfer

C. Empel, S. Jana, C. Pei, T. V. Nguyen, R. M. Koenigs, *Org. Lett.* **2020**, *22*, 7225–7229.

Synthesis of Trifluoromethylated Tetrasubstituted Allenes via Palladium-Catalyzed Carbene Transfer Reaction

C. Pei, Z. Yang, R. M. Koenigs, *Org. Lett.* **2020**, *22*, 7300–7304.

C–H Functionalization Reactions of Unprotected *N*-Heterocycles by Gold-Catalyzed Carbene Transfer

S. Jana, C. Empel, C. Pei, P. Aseeva, T. V. Nguyen, R. M. Koenigs, *ACS Catal.* **2020**, *10*, 9925–9931.

Gold-catalyzed C–H Functionalization of Phenothiazines with Aryldiazoacetates

S. Jana, C. Empel, C. Pei, T. V. Nguyen, R. M. Koenigs, *Adv. Synth. Catal.* **2020**, *362*, 5721–5727.

Synthesis of Trifluoromethylated Aziridines via Photocatalytic Amination Reaction

Y. Guo, C. Pei, S. Jana, R. M. Koenigs, *ACS Catal.* **2021**, *11*, 337–342.

Photochemical Carbene Transfer Reactions of Aryl/Aryl Diazoalkanes - Experiment and Theory

S. Jana,[†] C. Pei,[†] C. Empel, R. M. Koenigs, *Angew. Chem. Int. Ed.* **2021**, *60*, 13271–13279.

[†]equal contribution

Rhodium-catalyzed Cascade Reactions of Triazoles with Organoselenium Compounds - A Combined Experimental and Mechanistic Study

F. Li, C. Pei, R. M. Koenigs, *Chem. Sci.* **2021**, *12*, 6362–6369.

Photoinduced Ruthenium-catalyzed Alkyl-alkyl Cross-coupling Reactions

S. Jana, C. Pei, S. B. Bahukhandi, R. M. Koenigs, *Chem Catal.* **2021**, *1*, 467–479.

1,3-Difunctionalization of Imino-Carbenes via Rhodium-Catalyzed Reactions of Triazoles with Acyl Selenides

F. Li, C. Pei, C. Quaranta, R. M. Koenigs, *Adv. Synth. Catal.* **2021**, *363*, 4365–4370.

Proton or Carbene Transfer? On the Dark and Light Reaction of Diazoalkanes with Alcohols

C. Empel,⁺ C. Pei,⁺ F. He, S. Jana, R. M. Koenigs, *Chem. Eur. J.* **2022**, DOI: 10.1002/chem.202104397.

⁺equal contribution

Unlocking Novel Reaction Pathways of Diazoalkanes with Visible Light

C. Empel, C. Pei, R. M. Koenigs, *Chem. Commun.* **2022**, *58*, 2788–2798.

Photochemical Nitrene Transfer Reactions of Iminoiodinanes with Sulfides

Y. Guo, C. Pei, C. Empel, S. Jana, R. M. Koenigs, *ChemPhotoChem* **2022**, DOI: 10.1002/cptc.202100293.

Photocatalytic *gem*-Difluoroolefination Reactions by a Formal C–C Coupling/Defluorination Reaction with Diazoacetates

F. Li, C. Pei, R. M. Koenigs, *Angew. Chem. Int. Ed.* **2022**, DOI: 10.1002/anie.202111892.

Hydrogen Bonding Networks Enable Bronsted Acid-Catalyzed Carbonyl-Olefin Metathesis

T. A. To, C. Pei, R. M. Koenigs, T. V. Nguyen, *Angew. Chem. Int. Ed.* **2022**, DOI: 10.1002/anie.202117366.

A Combined Experimental and Theoretical Study on the Reactivity of Nitrenes and Nitrene Radical Anions

Y. Guo, C. Pei, R. M. Koenigs, *Nature Commun.* **2022**, 13, 86.

Visible-Light-Induced, Sole-Metal-Catalyzed, Directed C–H Functionalization: Metal-Substrate Bound Complexes as Light-Harvesting Agents

C. Pei, C. Empel, R. M. Koenigs, *Angew. Chem. Int. Ed.* **2022**, DOI: 10.1002/anie.202201743.

A Computational Study on the Photochemical O–H Functionalization of Alcohols with Diazoacetates

C. Pei, R. M. Koenigs, *J. Org. Chem.* **2022**, 87, 6832–6837.

Intermolecular Amination of Allenes via 2-Fold Photocatalytic Nitrene Transfer Reactions

Y. Guo,[†] C. Empel,[†] C. Pei,[†] H. Fang, S. Jana, R. M. Koenigs. *Chem Catal.* **2022**, DOI: 10.1016/j.checat.2022.05.014.

[†]equal contribution

The following parts have been either submitted for publication or are currently in preparation:

C–H Functionalization of Heterocycles with Triplet Carbenes *via* An Unexpected 1,2-Alkyl Radical Migration

C. Empel, S. Jana, Ł. Ciszewski, K. Zawada, C. Pei, D. Gryko, R. M. Koenigs, *manuscript submitted*.

Photochemical Palladium-catalyzed Methylation and Alkylation Reactions in Cascade Reactions of Isonitriles

C. Pei, Z. Yang, R. M. Koenigs. *manuscript submitted*.

The following parts of this work have been presented in poster presentations on international conferences:

Carbene transfer reaction for sigmatropic rearrangement reactions

S. Jana, Z. Yang, C. Pei, R. M. Koenigs, GDCh-Wissenschaftsforum Chemie, Aachen/D., 19th September 2019.

Blue light induced Fluoro-aminoPEG-ylation of Diazoacetates

F. He, C. Pei, R. M. Koenigs, 12th New Years' Symposium, Aachen/D., 10. January 2020

Contents

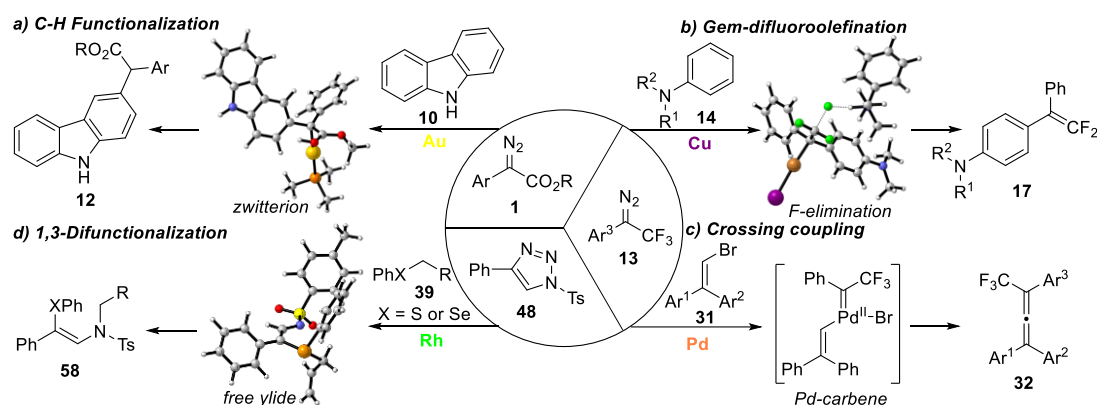
SUMMARY.....	I
1. CARBENE AND NITRENE.....	1
1.1 Introduction of Carbene and Nitrene	1
1.2 Carbene Transfer Reactions.....	1
1.3 Nitrene Transfer Reactions	9
1.4 Research Objective.....	12
2. MECHANISM STUDY OF METAL CARBENE REACTIONS	13
2.1 Mechanism Study of Au-Catalyzed Selective C–H Functionalization	13
2.2 Mechanism Study of Cu-catalyzed <i>gem</i> -Difluoro Olefination Reaction of Anilines	23
2.3 Pd-catalyzed Cross Coupling with Vinyl Bromides and α -CF ₃ Diazoalkanes	28
2.4 Mechanism Study of Rh-catalyzed Sigmatropic Rearrangement with Triazoles	39
2.5 Conclusion	51
3. MECHANISM STUDY OF PHOTOCHEMICAL CARBENE REACTIONS.....	53
3.1 Mechanism Study of Multi-reactivity of Diaryl Carbene with Alkynes	53
3.2 Mechanism study of Photoinduced O–H Insertion Reactions	63
3.3 Mechanism Study of Photoinduced Fluoro-amino Etherification Reactions	77
3.4 Mechanism Study of Photocatalytic Gem-Difluoroolefination Reactions	82
3.5 Conclusion	91
4. MECHANISM STUDY OF PHOTOINDUCED NITRENE REACTIONS	93
4.1 Brief Introduction: Photochemical Nitrene Transfer Reactions	93
4.2 Mechanism study of Photoinduced C–H functionalization and aziridination Reactions	96
4.3 Conclusion	105

5. MECHANISM STUDY OF PHOTOINDUCED RUTHENIUM AND PALLADIUM CATALYSIS	107
5.1 Brief Introduction: Visible Light-Induced Transition Metal Catalysis	107
5.2 Mechanism Study of Photoinduced Ruthenium-Catalyzed C(sp ³)-H Alkylation Reactions	111
5.3 Photoinduced Palladium-Catalyzed Cascade Cyclization with Isonitriles.....	118
5.4 Conclusion.....	131
6. OUTLOOK	132
7. GENERAL INFORMATION	134
8. ABBREVIATIONS.....	135
9. REFERENCES.....	137

Summary

This PhD thesis focuses on the mechanistic understanding of transition-metal catalyzed or photochemical carbene and nitrene transfer reactions, as well as new applications of these using photoredox catalysis. Furthermore, two types of palladium catalyzed transformations have been applied in the construction of relevant trifluoromethylated allenes and phenanthridine derivatives.

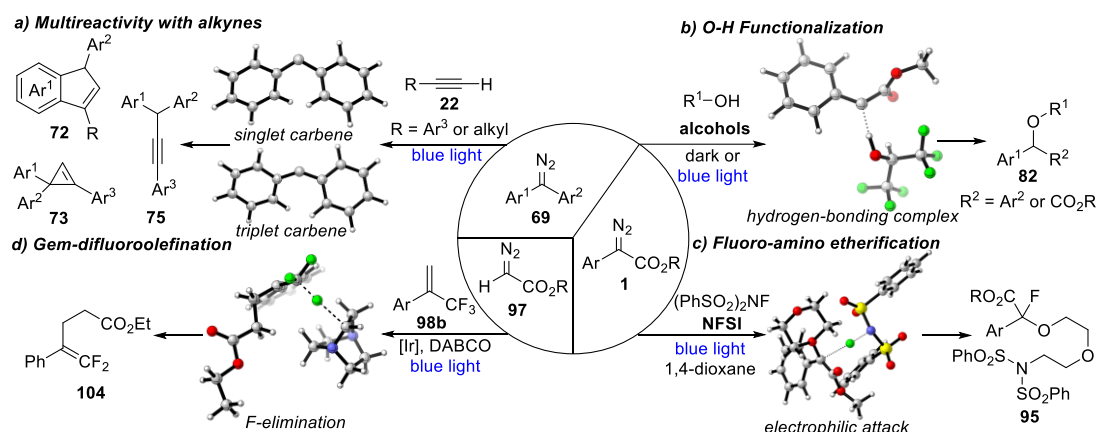
Specifically, chapter 2 describes the theoretical and experimental studies on different transition-metal-catalyzed carbene transfer reactions. Firstly, a detailed mechanistic investigation reveals that electrophilic gold(I)-carbene prefers a site-selective C–H functionalization of carbazole. Trace amounts of water play a crucial role in a key proton transfer step and rationalize the selectivity (Scheme 1a). Furthermore, replacement by trifluoromethyl diazoalkanes, *gem*-difluoro olefinations of anilines are realized via copper(I) catalysis. Calculations indicate that anilines play a dual role in this reaction, which not only form and stabilize the zwitterion intermediate but also promote the subsequent deprotonation step (Scheme 1b). In addition to C–H functionalization, trifluoromethyl diazoalkanes can also participate in Pd-catalyzed cross couplings with vinyl bromides, leading to synthetically challenging trifluoromethylated tetrasubstituted allenes (Scheme 1c). Moreover, several Rh(II)-catalyzed 1,3-difunctionalization reactions of triazoles with selenides or sulfides have been investigated by computational studies, which are identified to undergo rearrangements via free ylide intermediates (Scheme 1d).



Scheme 1: Transition-metal catalyzed carbene transfer reactions

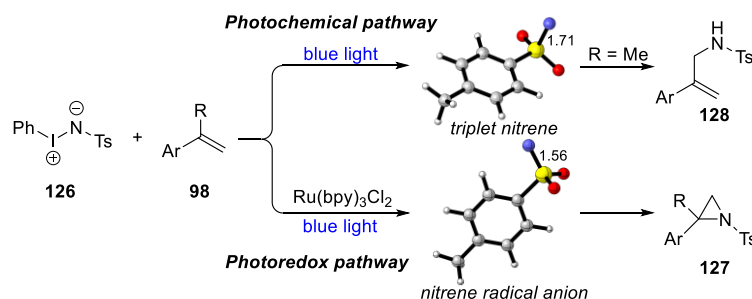
After investigating metal catalysis, we turned our attention to the emerging photochemical carbene transfer reactions in chapter 3. Firstly, under blue light irradiation, the spin states of photochemically generated diaryl carbenes are controlled by substituents on the aryl rings, which results in divergent reactivity such as cyclopropanations, C(sp)–H insertion, or cascade cyclization reactions with alkynes (Scheme 2a). Moreover, calculations indicate that photoinduced O–H insertion reactions of diaryl diazomethanes or aryl diazoacetates involve hydrogen-bond-assisted intersystem crossing processes. The reaction conditions and the possible reaction pathways strongly depend on the acidity of alcohols (Scheme 2b). In

addition, singlet carbenes generated from aryldiazoacetates, can also participate in three-component reaction with *N*-fluoro-benzenesulfonimide (NFSI) and 1,4-dioxane. Calculations support an oxonium ylide formation with 1,4-dioxane solvent, which is followed by the electrophilic addition of NFSI and to realize the fluoro-amino etherification of aryldiazoacetate (Scheme 2c). In the last section, the photosensitizer-promoted decomposition of ethyl diazoacetate (EDA) opens up its radical or triplet reactivity (Scheme 2d). Our calculations suggest *gem*-difluoroolefinations with α -CF₃ styrene involve triplet carbene intermediates, and 1,4-diazabicyclo[2.2.2]octane (DABCO) serves as a reductant to facilitate the photoredox catalysis and further fluoride elimination.



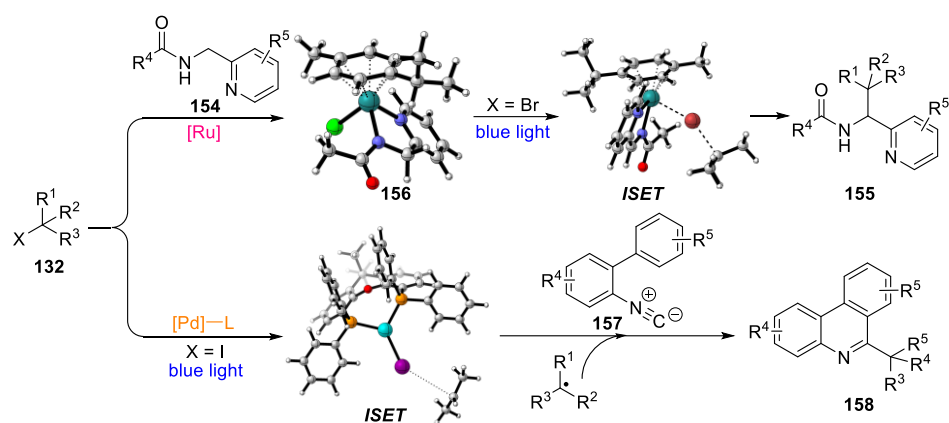
Scheme 2: Photoinduced carbene transfer reactions

Chapter 4 briefly describes the photocatalyst-controlled nitrene transfer reactions (Scheme 3). Theoretical studies explain that photochemical stepwise C–H aminations of α -methyl styrene with iminoiodinane are realized via triplet nitrene intermediates, while a photoredox catalyst serves as a reductant and unfolds nitrene radical anion reactivity to furnish aziridinations with styrenes.



Scheme 3: Catalyst-dependent photoinduced nitrene transfer reactions

In the last chapter, we conduct a detailed investigation on two recently novel photoredox reactions by experiment and computation (Scheme 4). In the first part, we identify that cyclometalated metal-substrate-bound complexes can be regarded as a photosensitizer, which promote further intramolecular single electron transfer (ISET) processes and C(sp³)–C(sp³) diradical coupling reactions. In addition, photoinduced palladium catalysis has also been applied in the formation of radical intermediates. This protocol realizes further cascade radical cyclization of isonitriles, affording phenanthridines in high efficiency.



Scheme 4: Ru- and Pd-based photoredox catalysis for radical transformations

1.

Carbene and Nitrene

1.1 Introduction of Carbene and Nitrene

Among the highly reactive species, carbenes and nitrenes represent neutral intermediates bearing six electrons with a divalent carbon or monovalent nitrogen atom, respectively, which can be present in singlet or triplet state. Various structural and chemical properties of their singlet and triplet states have been extensively characterized by experiment and computation. The singlet-triplet energy splitting ($\Delta E_{S/T}$) of carbenes and nitrenes is strongly dependent on sterically demanding and conjugating substituents, which reflects their divergent reactivity (Figure 1).¹⁻⁵ For example, :CCl_2 or :CBr_2 bearing two electron-donating groups have a singlet ground state. *N*-Heterocyclic carbenes (NHC) are kinetically stable in solution or in their solid state at ambient temperature. Similar to the carbene species, nitrenes have the tendency that alkyl or σ -electron-withdrawing groups support a triplet ground state. Significantly, halogen bonding, hydrogen bonding or solvent effects can switch the spin state of carbenes, which prefers to stabilize the singlet state. The variousness of carbenes and nitrenes exhibit their diverse reactivity and selectivity in organic chemistry.

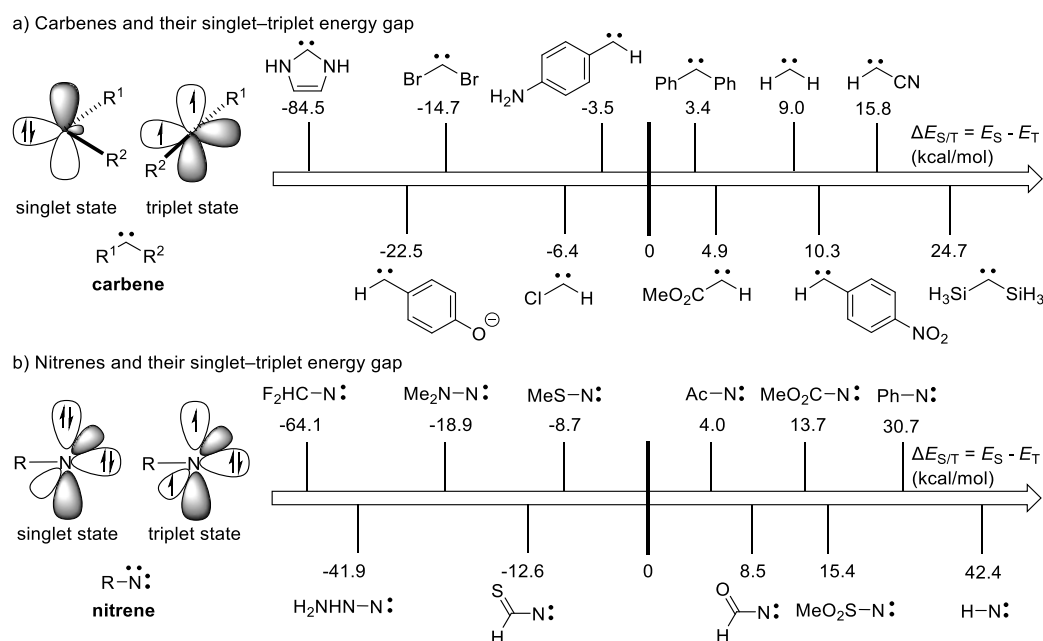


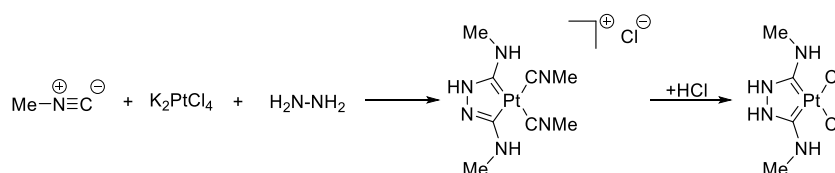
Figure 1: Carbenes, nitrenes and their spin states

1.2 Carbene Transfer Reactions

Carbenes have witnessed a long and fruitful history for more than a century due to their unique reactivities, which can participate in various organic transformations and construct molecular complexity.^{6,7} An early and important contribution is that Doering and his collaborators identified the :CCl_2 intermediate and applied it to the cyclopropanation

reaction of chloroform and alkenes.⁸ In addition, a persistent free carbene – NHC carbene has served as a key motif for versatile ligands in transition metal catalysis or as organocatalysts in the umpolung of aldehydes.^{9,10}

Besides free carbene species, a neutral divalent carbon ligand bound to a transition metal constitutes metal carbene complexes.¹¹ As far back as 1915, Chugaev reported the reaction of hydrazine, isocyanide, and Pt(II) salt to obtain a hydrazine-bridged platinum complex **34** (Scheme 5).¹² Around fifty years later, NMR and X-ray single crystal diffraction helped to prove a carbene-containing structure.¹³⁻¹⁵



Scheme 5: Synthesis of the Chugaev's salt

Due to the further emerging development of metal carbene chemistry, they are commonly classified as Fischer- and Schrock-type carbene complexes, which were firstly reported by Fischer in 1964 and Schrock in 1974, respectively (Figure 2).^{16,17} For the Fischer-type metal carbene complex, metal–carbon double bond constituted by carbene–metal σ -donation and simultaneous metal–carbene π -back donation. This type of carbenes are usually electrophilic and associated with low oxidation state metals.^{18,19} Conversely, a Schrock-type metal carbene has a covalent metal–carbon double bond that is constructed by the formal coupling of a triplet carbene and triplet state metal, which is nucleophilic and more like an ylide rather than a carbene.²⁰ Furthermore, one of the most important applications is to serve as a homogeneous catalyst for olefin-metathesis reaction.²¹⁻²³

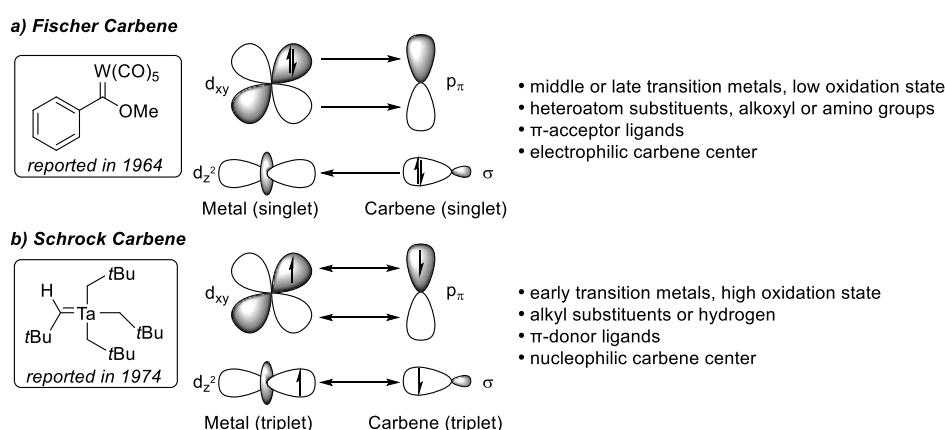
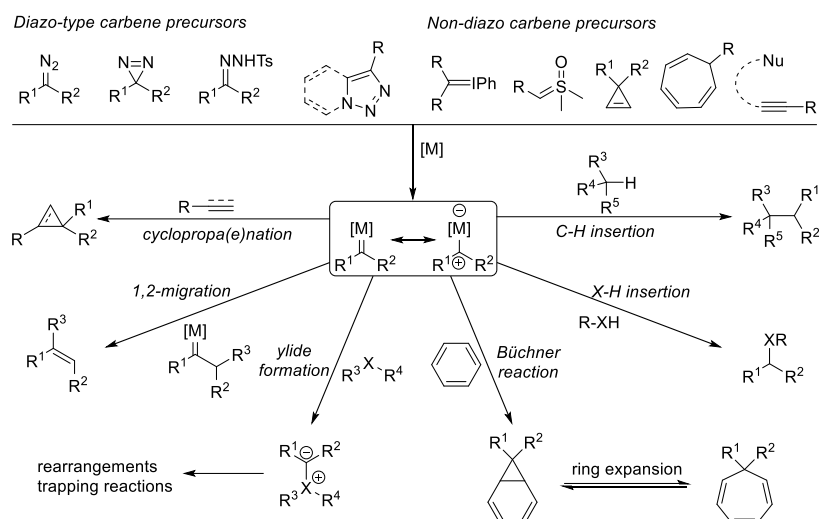


Figure 2: Metal-carbon bonding of Fischer and Schrock type carbene complexes

Actually, catalytic reactions with carbene precursors represent economical and efficient methods in carbene chemistry, in which transient transition metal carbene complexes are regarded as the key intermediates.^{6,24,25} Diazo compounds are the most widely-used carbene precursor, and diversified diazo compounds have been uncovered and applied in carbene transfer reactions.²⁶⁻²⁸ Besides, hydrazones,²⁹⁻³² triazoles,^{33,34} sulfoxonium and iodonium

ylides,^{35,36} cyclopropenes,³⁷ cycloheptatrienes,³⁸ and functionalized alkynes are also utilized as carbene precursors that broaden the carbene chemistry (Scheme 6).³⁹⁻⁴¹ Subsequently, these *in situ* generated metal carbene intermediates serve as efficient building blocks in organic synthesis, such as cyclopropa(e)nations, C–H functionalizations, heteroatom–H insertions, Büchner ring expansions, 1,2-migrations, ylide formations and further rearrangements or trapping reactions.^{26,28}



Scheme 6: Different carbene precursors and metal carbene transformations

Along with the fast-growing carbene field, a series of transition metal catalysts have been developed and applied in carbene transfer reactions, especially the chiral Rh(II) catalysts (Figure 3).^{42,43} For example, McKervy and co-workers explored a variety of proline-derived Rh(II) catalysts.⁴⁴ The famous one is Rh₂(*R*-DOSP)₄, which has been further developed by the Davies group and applied in enantioselective carbene transfer reactions, such as cyclopropanation reactions (Scheme 7a).⁴⁵ Interestingly, the Davies group applied the cyclopropanation products in the further development of cyclopropane carboxylate Rh(II) catalysts, which exhibit an effective, distinct selectivity and reactivity.⁴⁶ Furthermore, carboxamidate Rh₂(5S-MEPY)₄ and *N*-phthaloylamino acid-derived Rh₂(S-PTTL)₄ have been opened up in carbene area by the Doyle group and Hashimoto group, respectively.⁴⁷⁻⁴⁹

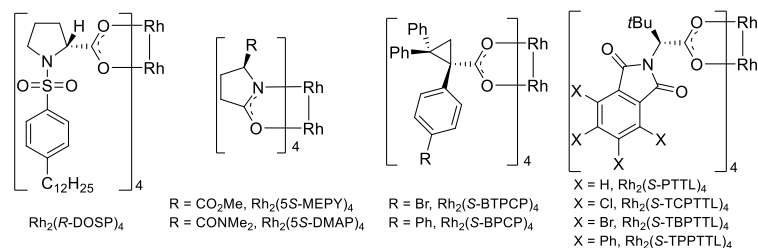
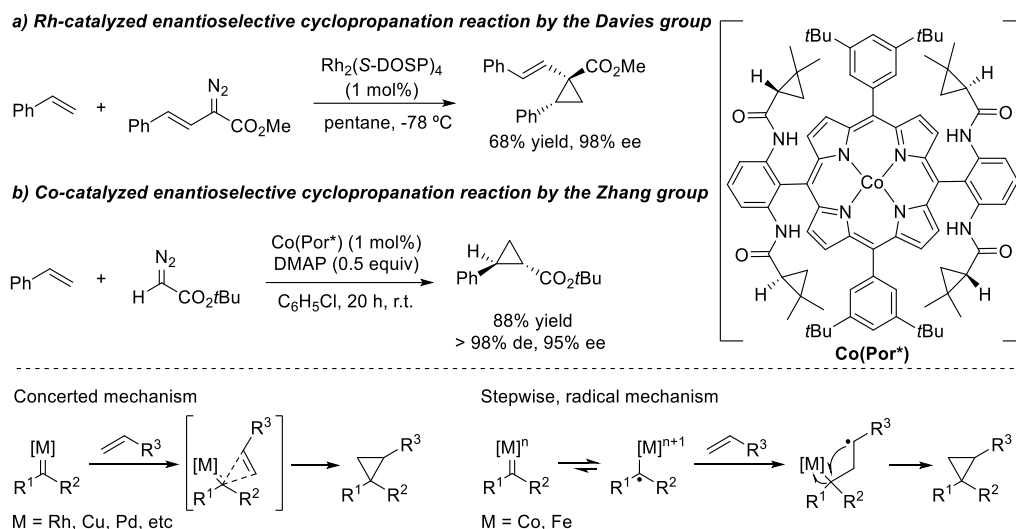


Figure 3: Dirhodium(II) tetracarboxylates and tetracarboxamidates catalysts

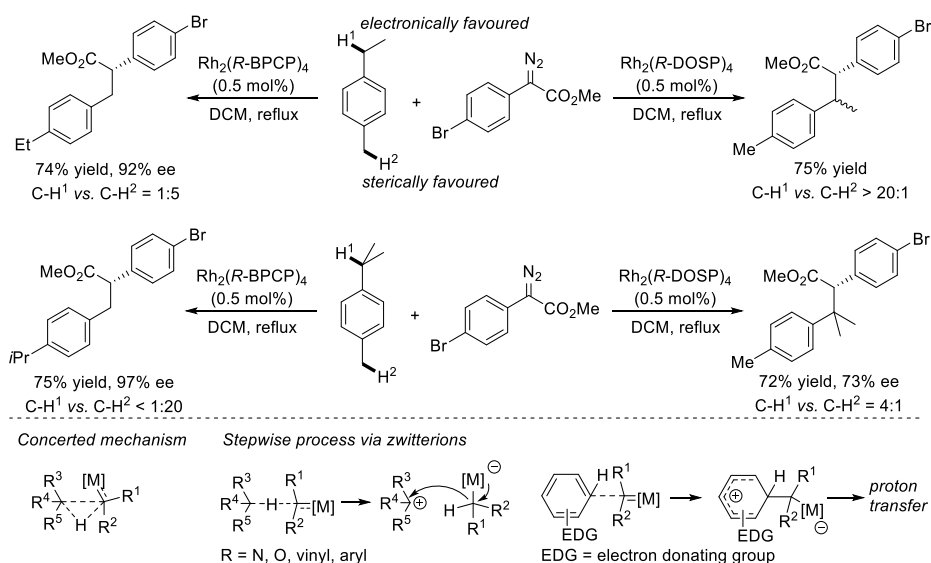
Instead of a Rh(II) catalyst, various ligands and transition metal complexes have also been exploited in asymmetric carbene transfer reaction.^{50,51} For instance, the Zhang group have realized highly enantioselective and diastereoselective cyclopropanation reaction with styrenes and diazoacetates by using cobalt(II) complexes of chiral porphyrins (Scheme 7b).⁵²

Actually, the mechanism of cyclopropanation via carbene intermediates strongly depends on the transition metal center. Experimental and computational studies reveal that Rh, Cu, Pd, etc complexes prefer a concerted addition step of metal carbene with double bonds.⁵³ Instead, Co,^{54,55} Fe,^{56,57} and recent heme catalysis^{58,59} involve a potential metalloradical intermediate through a stepwise process.



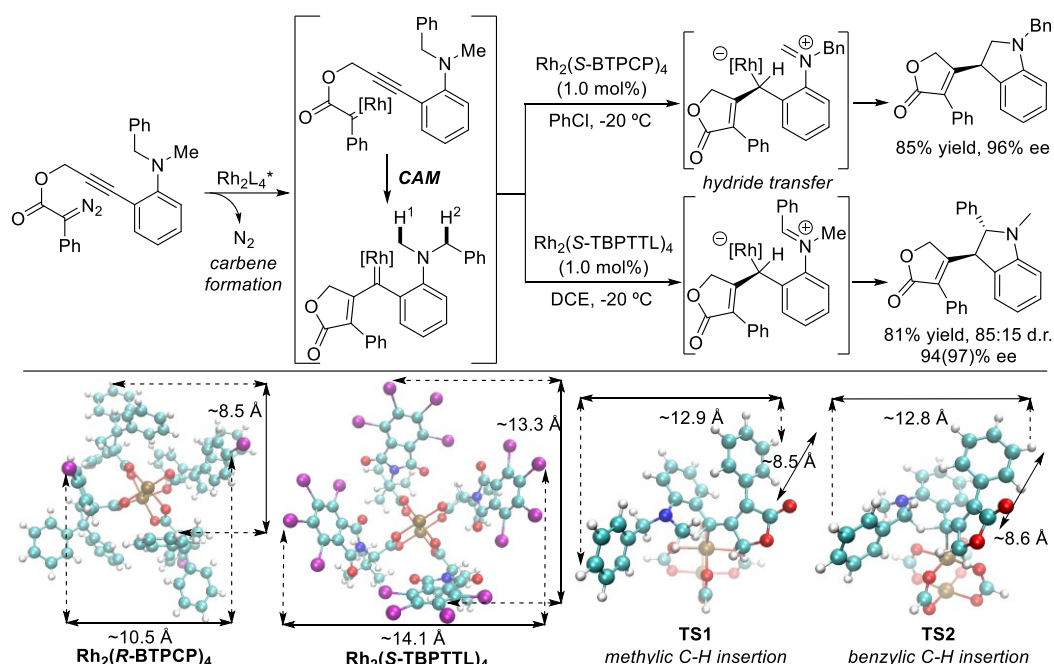
Scheme 7: Transition-metal-catalyzed enantioselective cyclopropanation reactions

The metal carbene-mediated insertion into C–H bonds is recognized as one of the typical carbene transfer reactions, which can selectively furnish direct functionalization of inactivated C–H bonds, especially C(sp³)–H bonds.^{60–62} In 2014, the Davies group found that a site-selectivity of benzylic C–H insertion is controlled by the choice of ligand (Scheme 8).⁶³ When cyclopropane carboxylate Rh₂(R-BPCP)₄ catalyst is employed in the reaction, a selective primary C–H insertion product can be obtained with excellent enantioselectivity. However, Rh₂(R-DOSP)₄ catalyst prefers an electronically favored, secondary C–H bond insertion.



Scheme 8: Ligand-controlled Rh(II)-catalyzed selective benzylic C–H insertion

Mechanistically, such inert C(sp³)-H bond insertion is regarded to undergo a concerted pathway via a three-center two-electron transition state.⁶⁴⁻⁶⁶ However, activated C-H bonds with α -amino or α -alkoxyl group proceed through hydride transfer and generate a zwitterionic intermediate (Scheme 8).^{67,68} Combining activated C-H bond insertion with carbene/alkyne metathesis strategy (CAM),⁶⁹⁻⁷¹ the Xu group reported a ligand-controlled, site-selective cascade C(sp³)-H insertion, leading to enantioselective construction of Dihydroindoles (Scheme 9).⁷² Theoretical analysis reveals that non-bulky catalyst such as Rh₂(S-TBPTTL)₄ supports an insertion into electronically favored secondary or tertiary C-H bonds, while bulky Rh₂(S-BTPCP)₄ catalyst favors less hindering, primary C-H bond insertions.

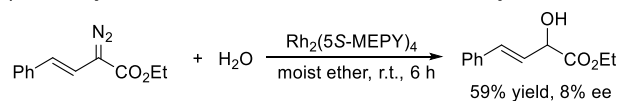


Scheme 9: Ligand-controlled Rh(II)-catalyzed selective C(sp³)-H insertion via CAM process

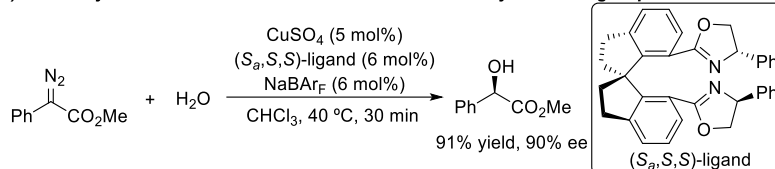
As most organic compounds contain carbon-heteroatom (C-X) bonds, the carbene-involved heteroatom-H (X-H, X = N, O, S, Si, etc.) insertion reactions are one of the most efficient tools for the construction of C-X bonds in a chemoselective and enantioselective way.^{73,74} In 1997, Landais and co-workers attempted the asymmetric O-H insertion reaction of vinyl diazoacetate and water with Rh₂(5S-MEPY)₄ catalyst, and unfortunately obtained poor enantiomeric excess (ee value) of 8% (Scheme 10a).⁷⁵ Recently, through the use of copper catalysts carrying chiral ligands, the Fu and Zhou group independently realized a highly enantioselective O-H insertions with diazoacetates as carbene precursor.^{76,77} For example, using a spiro bisoxazoline ligand, copper-catalyzed insertions into water have been applied to synthesize chiral α -hydroxyesters with high yield and excellent enantioselectivity (Scheme 10b). There remained a key question: why is Cu-catalysis more effective than Rh-catalysis in asymmetric O-H insertions? Further detailed theoretical study was conducted by the Yu group, which indicated the [1,2]-proton shift process favors the copper-associated ylide process and chiral environment was formed to induce high selectivity.⁷⁸ Contrarily, Rh(II)-

catalyzed carbene-mediated O–H insertion prefers to undergo a free ylide pathway, and a possible free enol intermediate is involved.

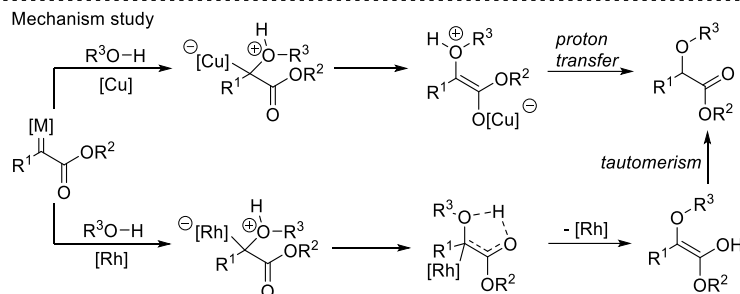
a) Rh-catalyzed enantioselective O–H insertion reaction by the Landais group



b) Cu-catalyzed enantioselective O–H insertion reaction by the Zhou group

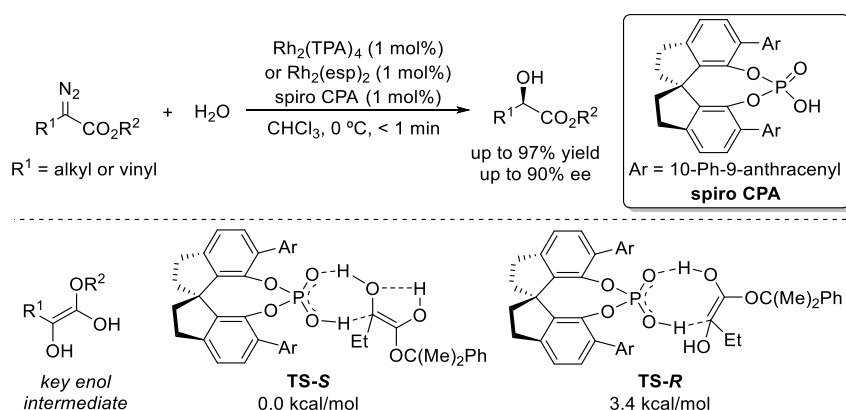


Mechanism study



Scheme 10: Catalyst-dependent enantioselective O–H insertion reactions

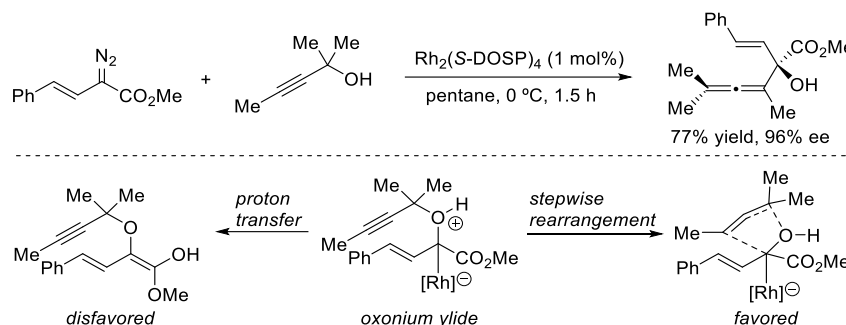
Based on the proposed enol intermediate in O–H insertion reactions, the Zhou group identified highly enantioselective O–H bond insertion between α -alkyl- or α -alkenyl diazoacetates with water.⁷⁹ In this case, the achiral $\text{Rh}(\text{II})$ catalyst would furnish the formation of carbenes and enol intermediates, while chiral spiro phosphoric catalyst (spiro CPA) served as a proton shuttle and realized the chiral control of enolic tautomerism (Scheme 11). Moreover, this co-catalyzed methodology has been successfully applied in either asymmetric trapping reaction of enol intermediates by external electrophiles⁸⁰ or $\text{C}(\text{sp}^2)\text{-H}$ functionalizations of electron-rich aromatic system.⁸¹



Scheme 11: $\text{Rh}(\text{II})$ and chiral phosphoric acid co-catalyzed enantioselective O–H insertion reaction

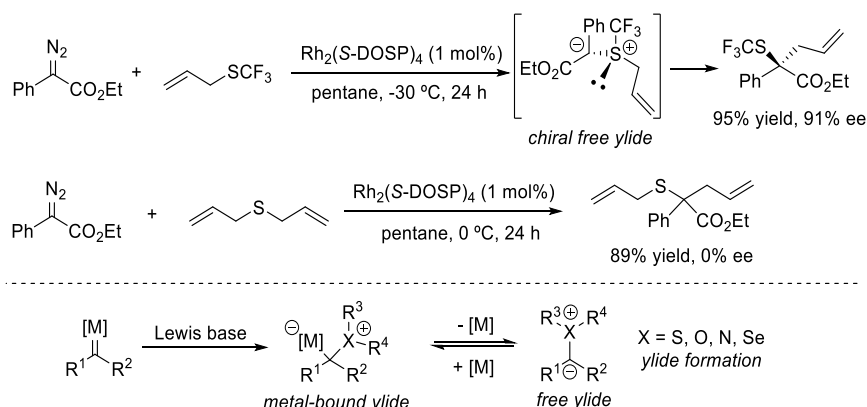
Besides the insertion reaction of alcohols with diazo compounds, a competitive rearrangement can also occur with the proposed oxonium ylide intermediates.^{82–84} The Davies group reported that propargylic or allylic alcohols undergo a $\text{Rh}(\text{II})$ -catalyzed domino ylide formation/[2,3]-sigmatropic rearrangement with diazoacetates (Scheme 12). Detailed

computational studies revealed the proton transfer process from oxonium ylide was interrupted by a more favored stepwise [2,3]-sigmatropic rearrangement. Instead of metal-free enol intermediate, a chiral Rh(II)-bound rearrangement process affords a high asymmetric induction.



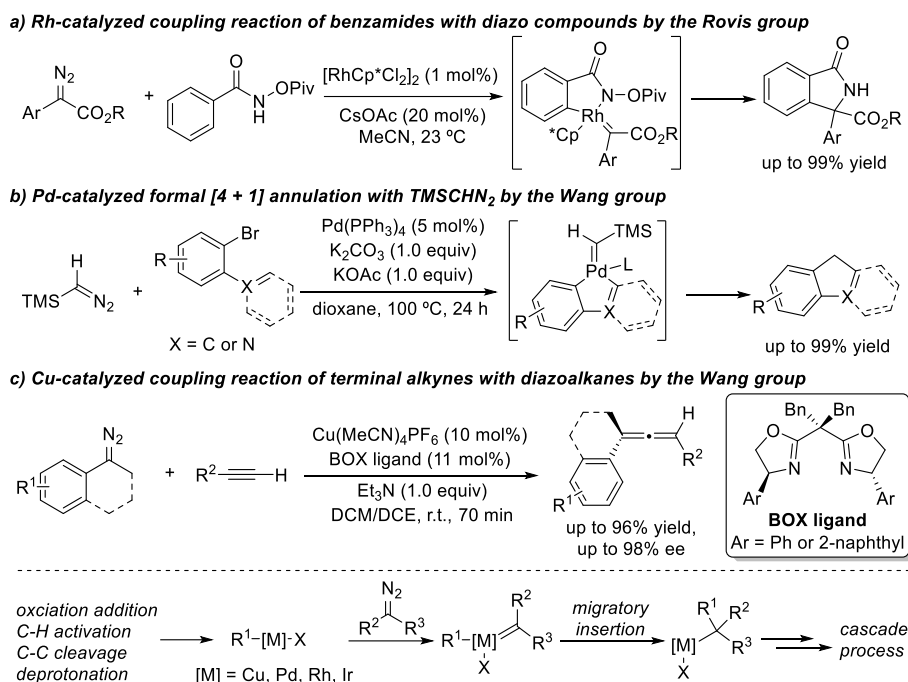
Scheme 12: Rh(II)-catalyzed asymmetric [2,3]-sigmatropic rearrangements of propargyl alcohols

In addition to oxonium ylides, the electrophilic metal-carbene reacts with diverse Lewis-basic system, which forms ammonium, sulfonium, selenonium, bromonium, and iodonium ylides, respectively. These highly reactive ylide species undergo subsequent [1,2]- or [2,3]-sigmatropic rearrangement and furnish new C-C/C-heteroatom bonds in one step.⁸⁵⁻⁸⁸ Despite strides in various sigmatropic rearrangement reactions (such as Doyle-Kirmse, Stevens, or Sommelet-Hauser rearrangement), the control of stereo-, chemo- and regioselectivities is still a key question. A series of chiral copper, rhodium catalysts have been applied in the carbene-mediated rearrangements. In 2017, the Wang group identified the first catalytic asymmetric Doyle-Kirmse reaction with high yields and enantioselectivities (Scheme 13).⁸⁹ In this case, the chiral free ylide is proposed to be a key intermediate under the catalysis of chiral Rh(II) or Cu(I) complex, which then transfers chirality from sulfur of ylide to the carbon of the allene product. Recent DFT calculations studies by the Tantillo group and Dang group answered the question of metal-bound or free ylides in Doyle-Kirmse rearrangement.^{90,91} It strongly depends on the use of catalyst, heteroatom center and adjacent substituents of carbene center, which provides profound enlightenment for the further design of reactions or chiral metal catalysts.



Scheme 13: Rh(II)-catalyzed enantioselective [2,3]-sigmatropic rearrangements of sulfides

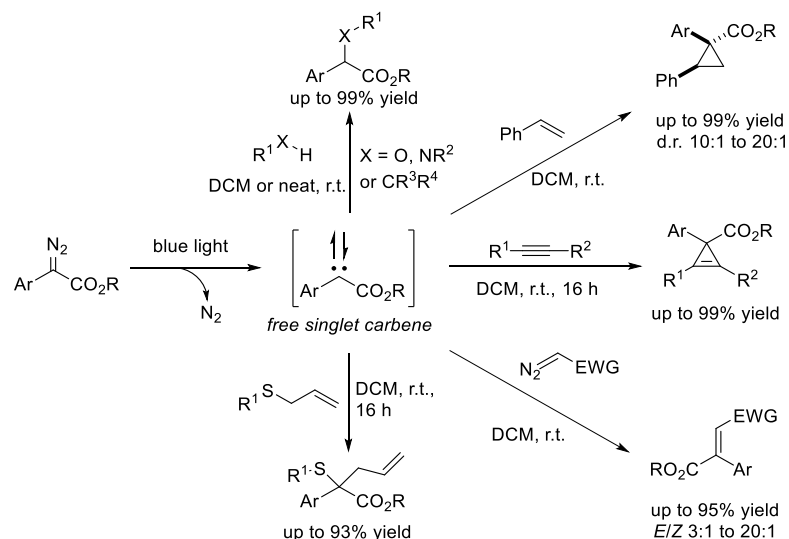
Apart from the metal carbene transfer reactivities, when introducing a suitable R ligand to metal center, a possible migration can occur from R ligand to the unsaturated carbenic carbon and form a new metal complex.^{92,93} In this case, the carbene precursors serve as a coupling partner and mediate new C–C or C–heteroatom bond formation. For example, using a C–H activation strategy via concerted-metalation deprotonation (CMD), the Rovis group reported a Rh(III)-catalyzed formal [4 + 1]-annulation of benzamides with diazo compounds (Scheme 14a).⁹⁴ Furthermore, the oxidative addition of aryl and allyl halides or pseudohalides with palladium catalyst is the key step in cross-coupling reactions, which generates the alkyl palladium species.^{95–97} In 2017, the Wang group utilized this methodology into the coupling reaction of TMSCHN₂ with 2-bromo-1,1'-biphenyl or 1-(2-bromophenyl)-1H-pyrrole derivatives (Scheme 14b).⁹⁸ This reaction was proposed to proceed via palladacyclic carbenoid intermediate, which underwent further migratory insertion and reductive elimination to give (hetero)polycyclic aromatic hydrocarbons. In addition, through an alkynyl migratory insertion of Cu(I) carbene species, the Wang group realized a synthetically useful, enantioselective synthesis of trisubstituted allenes (Scheme 14c).⁹⁹



Scheme 14: Transition-metal-catalyzed coupling reactions with diazo compounds

Despite the exquisite control on the reactivity and selectivity of catalytic carbene transfer reactions, photolysis of diazoalkanes could trace back to a century ago.^{100–104} However, the synthetic utility of this approach was limited due to the low selectivity of free carbene and highly energetic UV light. One of the most important applications is Wolff rearrangement from the decomposition of α -diazo carbonyl compounds, in which ketenes can be obtained and trapped by nucleophiles or further [2+2] additions.^{105,106} More recently, colored donor/acceptor diazoalkanes were found to present an absorbance in the visible region (400 to 500 nm). The Davies,¹⁰⁷ Koenigs¹⁰⁸ and Zhou groups¹⁰⁹ independently uncovered the singlet carbene reactivity of aryl diazoacetates under blue light irradiation (Scheme 15). In

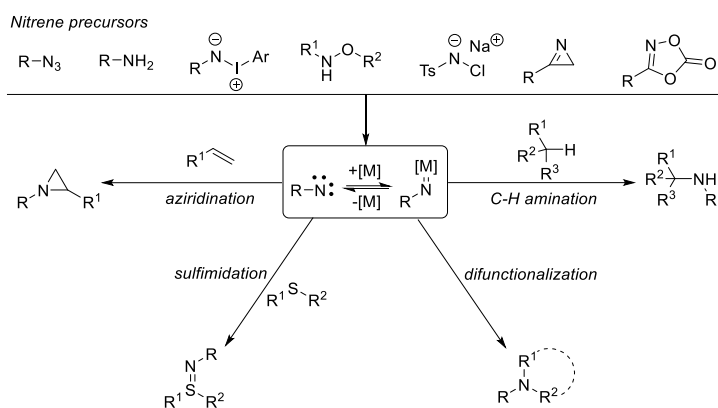
their seminal reports, weak irradiation of blue light reduces the undesired side reactions of substrates and leads to high efficiency of free carbene transfer reactions, such as rearrangements,¹¹⁰⁻¹¹² X-H insertions,¹¹³⁻¹¹⁷ cyclopropa(e)nations^{108,118-122} and coupling reactions.¹⁰⁹



Scheme 15: Photoinduced carbene transfer reactions with aryl diazoacetates

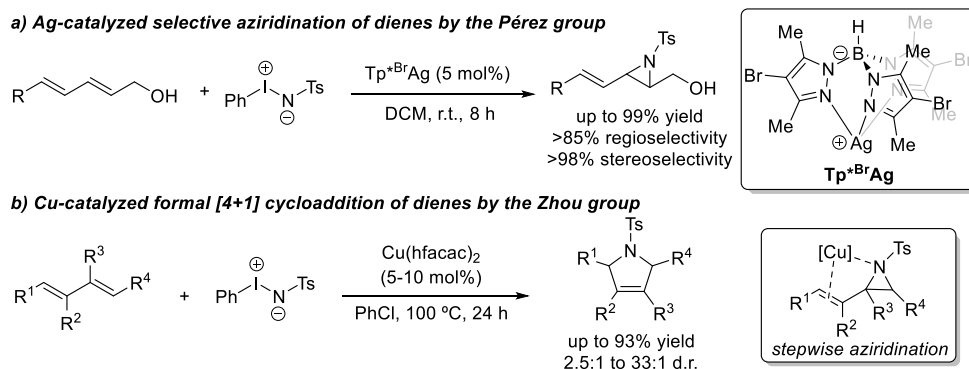
1.3 Nitrene Transfer Reactions

Similar to carbene species, nitrene intermediates with six valence electrons are generally used as nitrogen-containing building blocks, and have attracted continuous interest from synthetic chemists. As we know, in Hofmann degradation and Curtius rearrangement, free nitrenes are proposed to be the possible intermediates.¹²³ Recently, and to avoid these challenging rearrangement side-reactions, various nitrene precursors and catalytic systems have been developed into selective nitrene-based transformations.^{124,125} The Ochiai group found hypervalent sulfonylimino- λ^3 -bromane could mediate a metal-free C–C amination reaction of unactivated alkanes, and furthermore the functionalization of tertiary or secondary C–H bonds.¹²⁶ Furthermore, new reagents such as *N*-pivaloyloxy-*N*-alkoxyamides and $N_3SO_2N_3$ were applied in the activation of secondary aliphatic amines to yield carbon–carbon coupling products via an isodiazene – amino-stabilized nitrene intermediate, which reported by the Levin group and Lu group, respectively.^{127,128} During recent decades, multifarious nitrene sources has been applied in catalytic nitrene transformations, such as azides,^{129,130} iminoiodinanes,¹³¹ dioxazoles,^{125,132} amide *N*-ethers/esters,¹³³⁻¹³⁶ chloramine-T¹³⁷ and in situ oxidation of amides (Scheme 16).¹³⁸ Accordingly, wide range of catalyst systems were developed for catalytic C–H aminations,^{139,140} aziridinations,¹⁴¹ sulfimidations¹⁴² or difunctionalizations reaction with applications in complex molecule synthesis.¹⁴³



Scheme 16: Transition-metal catalyzed nitrene precursors and their transformations

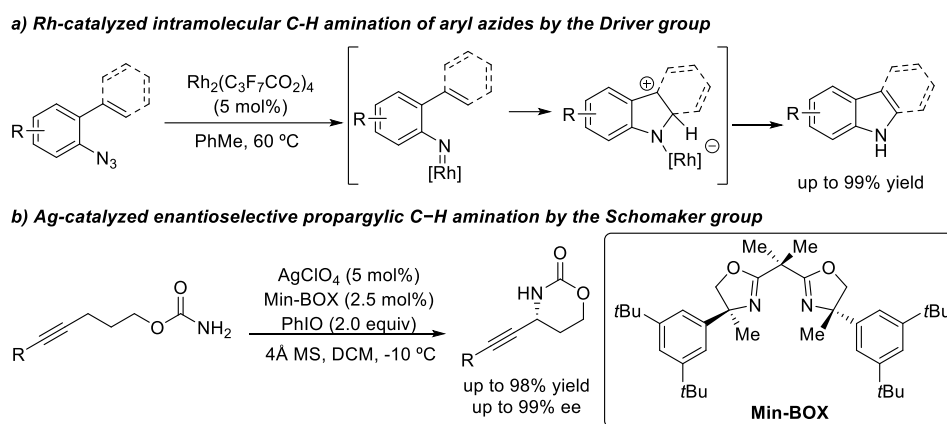
The aziridination of olefins is a typical nitrene transfer reaction, which gives important building blocks for medicinal chemistry and organic synthesis. A wide variety of organocatalytic or transition-metal catalyzed enantioselective aziridination reactions have been developed in the past decades. Recently, Pérez and co-workers employed trispyrazolylborate ligands in silver-catalyzed aziridination reactions of conjugated 2,4-diene-1-ols, in which iminoiodinane served as the nitrene precursors (Scheme 17a).¹⁴⁴ Mechanistic learnings revealed that a triplet silver-nitrene complex is involved, and hydrogen bond of OH group is critical to proceed this reaction in a chemo-, regio-, and stereoselective manner. Distinctively, the Zhou group found that copper catalysis of conjugated dienes with iminoiodinane led to a formal [4 + 1] cyclization and formed 3-pyrroline derivatives (Scheme 17b).¹⁴⁵ According to detailed control experiments, a stepwise process including diene aziridination and ring expansion was unlocked.



Scheme 17: Transition-metal-catalyzed nitrene transfer reactions of dienes and iminoiodinane

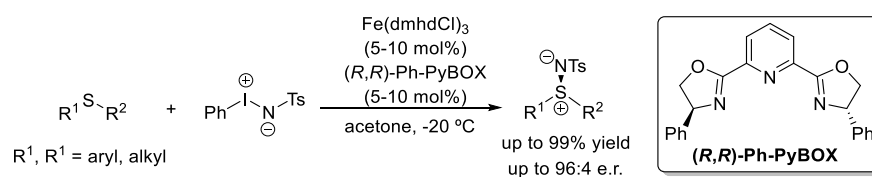
Aside from aziridinations, direct C–H amination is one of the most powerful strategies for the synthesis of aza-compounds. In 2008, with the built-in azide group, the Driver group realized a Rh(II)-catalyzed intramolecular amination of vinyl or aryl C–H bonds from aryl azides, which provides a new access for indoles and carbazoles synthesis (Scheme 18a).^{146,147} Moreover, asymmetric C–H amination via nitrene transfer leads to enantioenriched amine precursors from abundant C–H bonds, which can be promoted by chiral catalyst systems. For instance, the Schomaker group reported a Ag(I)-catalyzed regio- and enantioselective propargylic C–H amination with new chiral bis(oxazoline) (BOX) ligand (Scheme 18b).¹⁴⁸ Through the

oxidation of carbamate ester with PhIO, in situ generated iminoiodinanes afford a silver–nitrene intermediate, which is more precisely described as a Ag(II)–nitrene radical anion based on theoretical studies.



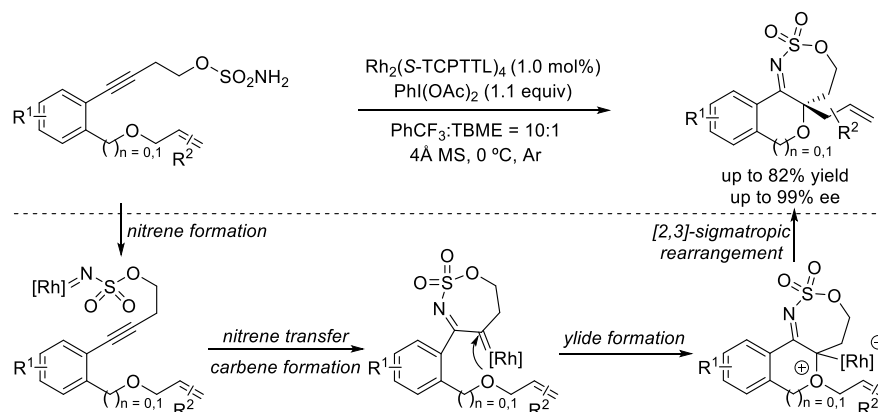
Scheme 18: Transition-metal catalyzed intramolecular C–H amination reactions

Due to the unique biological properties of sulfimides, sulfimidation using nitrenoids has gained considerable attention among chemists, which are also important in agricultural science and medicinal chemistry. Recently, the Bolm group firstly developed an iron-catalyzed asymmetric imidation of sulfides, in which available Fe(III) catalyst and PyBOX ligand were utilized to obtain high yields and excellent enantioselectivities (Scheme 19).¹⁴⁹



Scheme 19: Fe-catalyzed enantioselective sulfimidation with iminoiodinane

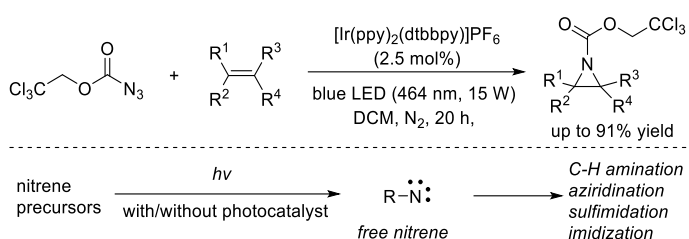
Unlike the cyclopropanations of carbene with alkynes, distinctive reactivities of nitrene with alkynes were found to undergo difunctionalizations or cascade processes.^{150–152} As shown in Scheme 20, the Blakey group firstly proved a novel nitrene/alkyne reactivity that allows rhodium transfer from nitrene center to carbene center using alkyne-tethered sulfamates as



Scheme 20: Rh(II)-catalyzed asymmetric nitrene/alkyne metathesis (NAM) cascade reaction

nitrene precursors. Importantly, in the recent reports by the Xu group, a chiral dirhodium catalyst was explored in such transformation, which is responsible for an asymmetric induction of terminal [2,3]-sigmatropic rearrangement.¹⁵³

More recently, significant advances have been made in photochemical nitrene transfer reactions, which expand concepts in classic metal-catalyzed nitrene transfer reactions to photochemistry. In this case, pivotal and reactive nitrene intermediates would be provided via photoexcitation of nitrene sources with or without catalysts, which are further applied in C–H aminations,¹⁵⁴⁻¹⁵⁷ aziridinations,^{158,159} sulfimidations^{160,161} and others.^{162,163} For example, the Yoon group demonstrated that the photosensitizer could facilitate the spin-selective generation of triplet nitrenes under blue light irradiation (Scheme 21).¹⁵⁹ This mild strategy has been applied in selective aziridination reactions of alkenes, which avoids direct photolysis and competitive allylic amination with strong UV-light strategy aziridination.



Scheme 21: Photocatalytic nitrene transfer reactions

1.4 Research Objective

Besides the above carbene and nitrene transfer reactions, there are still many open questions on their reactions and mechanisms. This thesis mainly aims at detailed computational studies of novel carbene and nitrene transformations, and at the development of new approaches for the construction of synthetically useful molecules. More specifically, several transition-metal catalyzed C–H functionalization, rearrangements and cross coupling have been investigated theoretically and experimentally. Furthermore, fundamental studies have also been performed for the understanding of photochemical carbene and nitrene generations and further transformations. Additionally, two emerging photochemical methodologies involving photo-palladium catalysis and a metal-substrate-bound photoredox strategy, have been described in the last chapter as well.

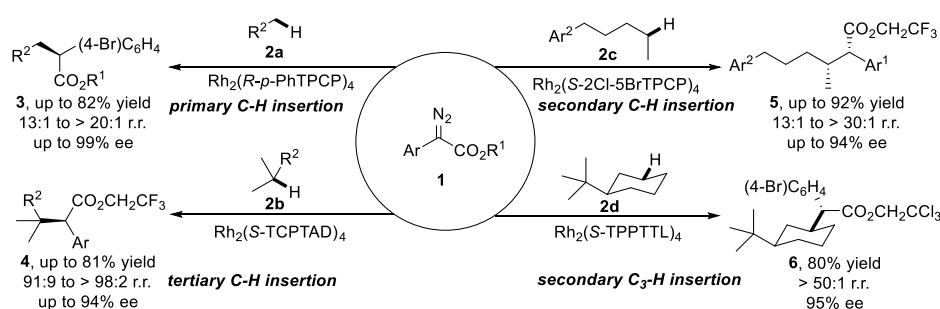
2. Mechanism Study of Metal Carbene Reactions

2.1 Mechanism Study of Au-Catalyzed Selective C-H Functionalization

2.1.1 Brief Introduction: Selective C-H Functionalization

The site-selective direct C-H functionalization reaction represents a straightforward and atom-economic strategy to rapidly build up molecular complexity. Traditional sites for modification of organic molecules rely on reactive or polarizable functional groups, which introduce new functional groups onto the molecules. In the past decades, organometallic chemists have focused much attention on developing direct C-H activation strategies,¹⁶⁴⁻¹⁶⁶ in which a very promising “carbon-hydrogen functionalization” method involves the insertion of metal carbenes into C-H bonds.⁶⁰⁻⁶²

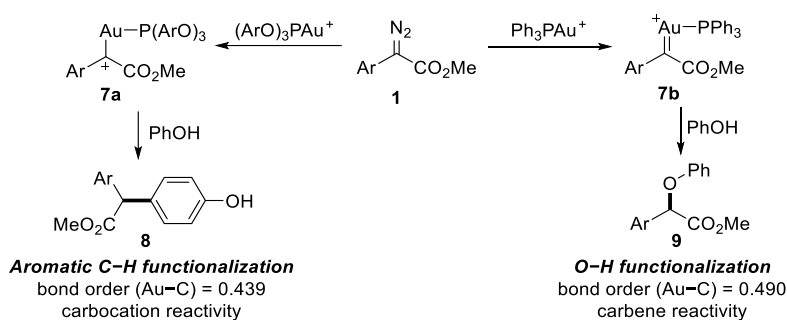
Recently, Davies and coworkers developed a series of rhodium(II) catalysts, such as modified phthalimido amino acid catalysts and triphenylcyclopropane carboxylate (TPCP) catalysts, which are capable to furnish site-selective reactions to occur at either unactivated primary, secondary or tertiary C-H bonds.¹⁶⁷⁻¹⁷⁰ The modified phthalimido amino acid catalysts like $\text{Rh}_2(\text{TCPTAD})_4$ have sufficiently small steric demand that could access the electronically preferred tertiary or secondary C-H functionalization via donor-acceptor $\text{Rh}(\text{II})$ -carbene intermediates. Instead, the $\text{Rh}_2(\text{TPCP})_4$ catalyst classes are far more sterically demanding that the reaction occurs preferentially at the most accessible primary C-H bond (Scheme 22). Further detailed theoretical calculation studies on the catalyst and rhodium-carbene complex were performed in order to explain the site-selectivity.



Scheme 22: Catalyst-controlled site-selective C-H insertion through Rh-carbene intermediate

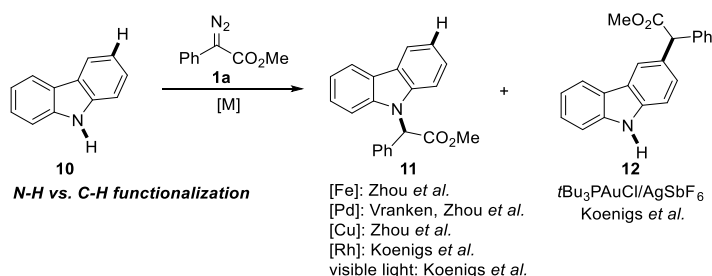
In fact, the site-selectivity is not only controlled by steric effects of ligands on the metal center, but is also influenced by electronic effect of ligands. In recent years, gold catalysis has attracted a lot of attention to conduct C-H functionalization.^{171,172} Compared to other transition metals (e.g., Rh, Pd, Cu), gold complexes display their unique catalytic activity in carbene transformations. Most notably, the chemoselectivity of gold-carbene is heavily

dependent on the nature of the ligand.¹⁷³⁻¹⁷⁵ DFT calculations show that the bond order of Au–C is 0.490 with the phosphine ligand PPh₃, which reveals the reactivity of carbenes compares to commonly used copper and rhodium catalysts to generate O–H insertion product with phenol. The electron-deficient phosphite ligand (2,4-*t*Bu₂C₆H₃O)₃P has a Au–C bond order of 0.439, and the carbene therefore acts as a “carbophilic carbocation” to prefer aromatic C–H functionalization of phenol (Scheme 23).



Scheme 23: Catalyst-controlled site-selective C–H insertion through Rh-carbene intermediate

Inspired by the unique reactivity of gold-carbene species, our group found that a selective C–H functionalization reactions of unprotected carbazoles can be realized by this concept.¹⁷⁶⁻¹⁷⁸ Interestingly, Fe(III), Cu(I), Pd(II) and Rh(II) catalyst or photochemical procedures all led to a selective N–H insertion product, which have already been reported by the Zhou,^{179,180} Vranken¹⁸¹ and our group,¹¹³ respectively (Scheme 24). Thus, it is of high demand to obtain insight into this unusual Au-catalyzed selective C–H functionalization and inherent difference from other metal catalysts.



Scheme 24: Catalyst-controlled site-selective N–H or C–H insertion of carbazole

2.1.2 Computational Study

To further rationalize for the regioselectivity of the gold catalysis, we conducted detailed density functional theory (DFT) studies at M06/6-31G(d)/LANL2DZ level of theory using Gaussian 09 program. For simplification of the calculations, carbazole **10** and diazo acetate **1a** were chosen as the model substrate and Me_3PAu^+ was used to model the giant cationic catalyst $t\text{Bu}_3\text{PAu}^+$. Firstly, the electrophilic gold catalyst coordinates to diazo compound **1a** to form **INT1**, which underwent a facile denitrogenation process to afford gold carbene **INT2** *via* transition state **TS1** with an activation free energy of 6.8 and 8.6 kcal/mol for Me_3PAu^+ and $t\text{Bu}_3\text{PAu}^+$, respectively (Figure 4).

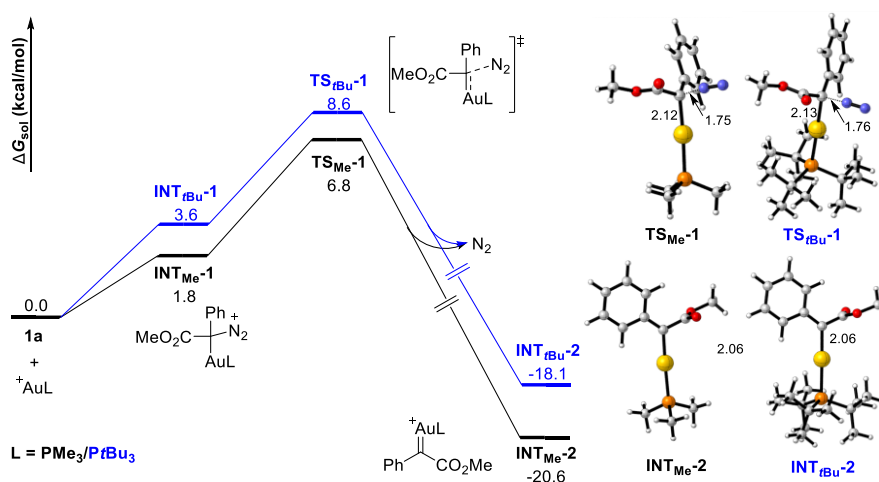
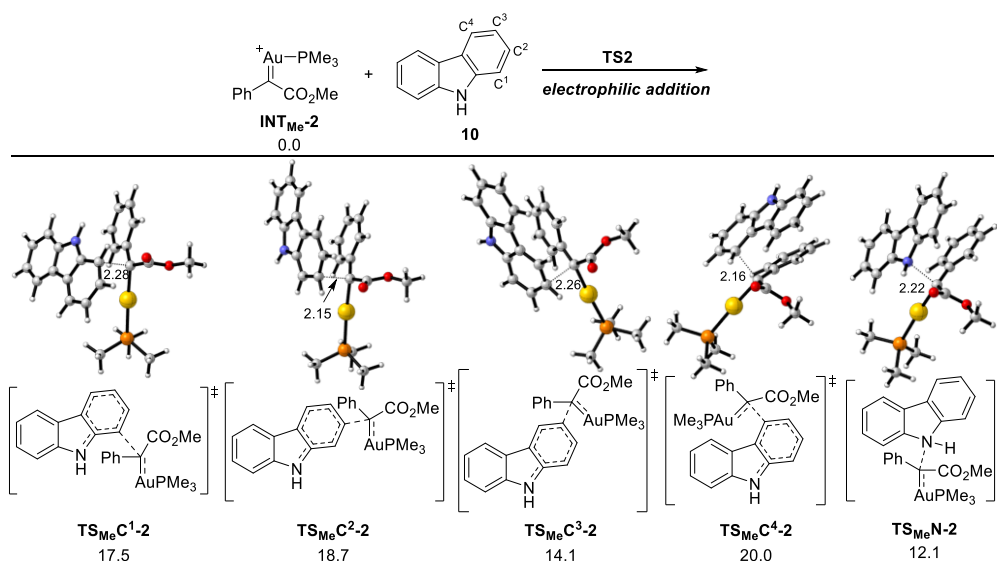


Figure 4: Potential energy surface of Au carbene formation

In the next step, we considered all possible C–H or N–H functionalization pathways through the nucleophilic addition of carbazole to the electrophilic gold carbene complex (Scheme 25). According to these computational results, there were two favorable pathways involving addition from N or C3 position of carbazole via **TS_{Me}N-2** or **TS_{Me}C³-2** with similar activation free energies of 12.1 and 14.1 kcal/mol, respectively.



Scheme 25: Site-selective electrophilic addition of gold carbene onto carbazole

Following the formation of the addition intermediate $\text{INT}_{\text{Me}}\text{N-3}$ or $\text{INT}_{\text{Me}}\text{C}^3\text{-3}$, a 1,4-proton transfer step occurred via low-lying transition states $\text{TS}_{\text{Me}}\text{N-3}$ and $\text{TS}_{\text{Me}}\text{C}^3\text{-3}$ gave $\text{INT}_{\text{Me}}\text{N-4}$ or $\text{INT}_{\text{Me}}\text{C}^3\text{-4}$, respectively. It was notable that the process through $\text{TS}_{\text{Me}}\text{N-3}$ that converted $\text{INT}_{\text{Me}}\text{N-3}$ to $\text{INT}_{\text{Me}}\text{N-4}$ was reversible (Figure 5). While further deauration and water-mediated proton shuttle led to the final product and were irreversible due to their higher lying transition states and extremely exergonic process, which were the rate-determining step in the whole energy surface. Moreover, in the case of C–H functionalization, the proton shuttle step proceeded from the low-energy $\text{INT}_{\text{C}}\text{5}$ via $\text{TS}_{\text{C-4-2w}}$ with an activation free energy of only 15.4 kcal/mol, which accounted for the formation of reaction product **12**. Instead, the N–H functionalization product was formed via the intermediate $\text{INT}_{\text{N}}\text{5}$, which reacted via a high-lying $\text{TS}_{\text{N-4-2w}}$ with an activation free energy of 18.3 kcal/mol to give reaction product **11**. In addition, proton transfer transition states $\text{TS}_{\text{N-4-1w}}$ and $\text{TS}_{\text{C-4-1w}}$ involving one water molecule was also considered, which has higher energy barriers than two-water assisted $\text{TS}_{\text{N-4-2w}}$ and $\text{TS}_{\text{C-4-2w}}$ transition states. Actually, direct 1,2-proton migration of the $\text{INT}_{\text{Me}}\text{N-3}$ or $\text{INT}_{\text{Me}}\text{C}^3\text{-3}$ could also account for the product formation. However, the corresponding energy barriers via $\text{TS}_{\text{Me}}\text{N-3'}$ and $\text{TS}_{\text{Me}}\text{C}^3\text{-3'}$ was 47.1 kcal/mol and 31.0 kcal/mol, respectively, which is definitely ruled out for the considerable energy barriers.

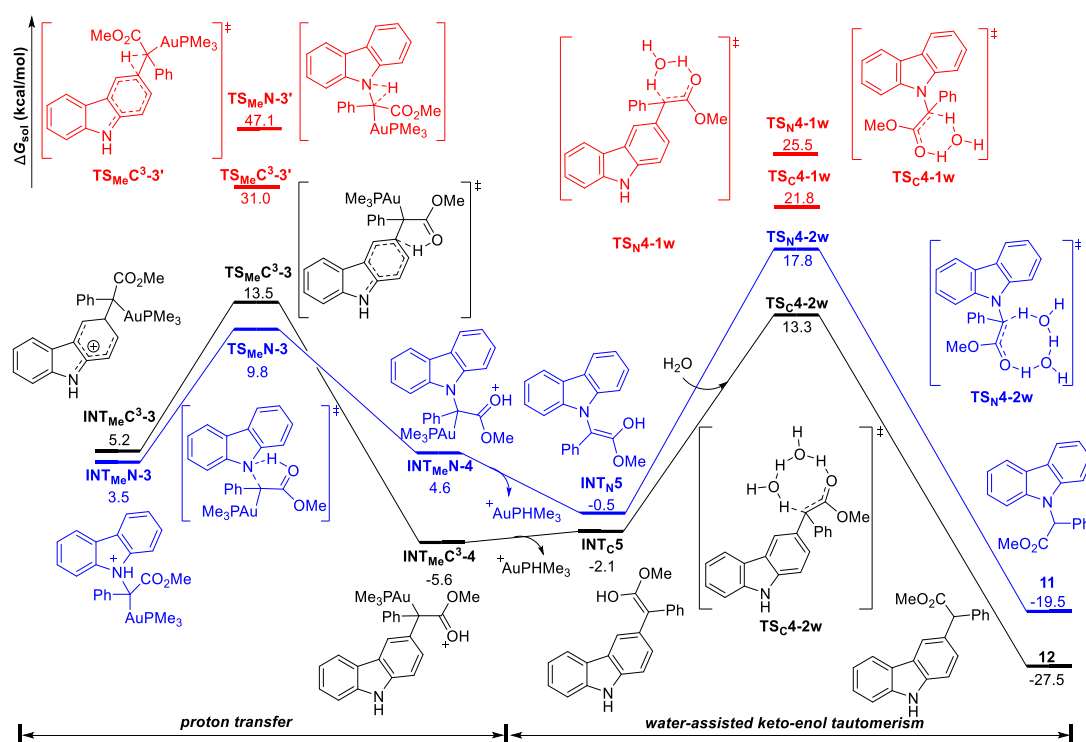
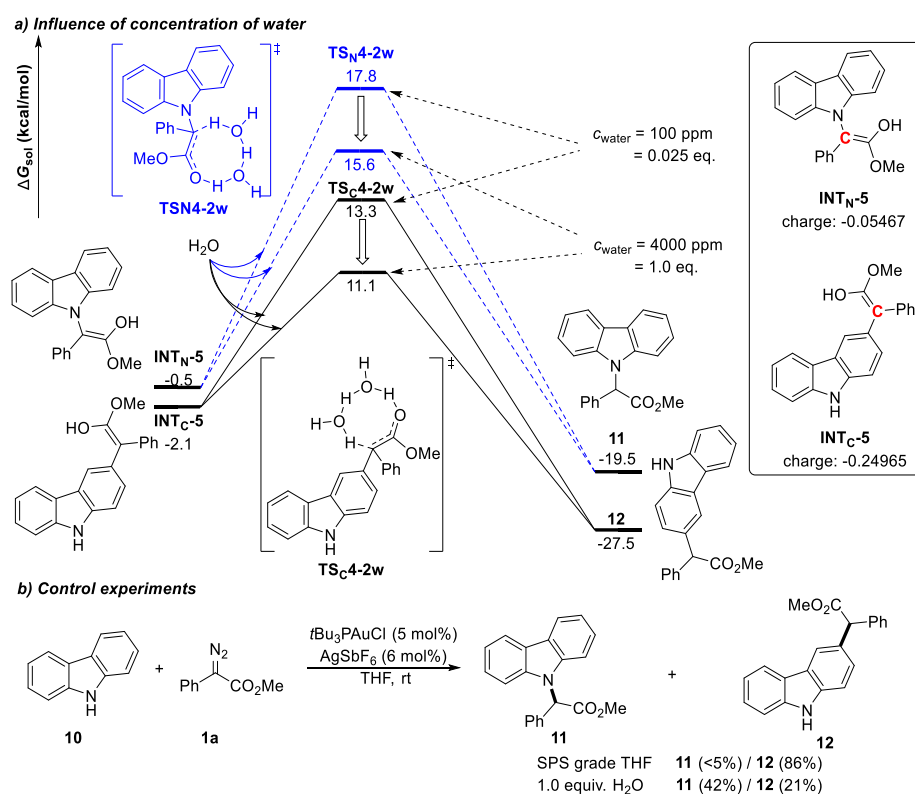


Figure 5: Potential energy surfaces of proton transfer and water-assisted tautomerism pathways

Furthermore, the activation free energy of proton shuttle step was strongly dependent on residual amounts of water in the reaction mixture, which could switch the selectivity of this reaction. We considered the concentration of trace water of 0.00125 mol/L in the solvent from SPS system (SPS-grade THF, typical amount of remaining water: <100 ppm or <0.0013 mol/L or 0.02 equivalent). While a large amount of water (4000 ppm, 1.0 equivalent with

respect to the diazoalkane **1a**) promoted both proton shuttle pathways and resulted in a smaller activation free energy (15.6 kcal/mol for N–H vs 11.1 kcal/mol for C–H functionalization), which was even lower than that of nucleophilic addition **TS_{MeN-2}** or **TS_{MeC³-2}** and resulted in a poor selectivity of the N–H or C–H functionalization (Scheme 26). Moreover, the differences in activation free energy of two proton shuttle pathways could be rationalized by NBO charge analysis of intermediates **INT_{N-5}** and **INT_{C-5}**, which suggested significantly higher nucleophilicity of **INT_{C-5}** and consequently a lower activation free energy for the proton shuttle step. Indeed, further control experiment in the presence of 1.0 equiv of water produced a 2:1 ratio of N–H vs C–H functionalization product mixture, which was consistent with our calculation results.¹⁷⁷

**Experimental work was done by Sripati Jana.*



Scheme 26: Influence of concentration of water on the Gibbs free energy of **TS_{N-4-2w} and **TS_{C-4-2w}****

We then refreshed the whole energy surface with $t\text{Bu}_3\text{PAu}^+$ catalyst by using Gaussian 16 program when we had more computational capacity. As expected, we obtained similar computational results, which led to the same selectivity (Figure 6).

Next, we investigated the different selectivity of rhodium-catalyzed reaction of carbazole **10** with methyl phenyldiazoacetate **1a** by theoretical calculations at same level of theory (M06/6-31G(d)/LANL2DZ), which gave selective N–H functionalization in our experiments. Beginning with the Rh-carbene intermediate **INT_{Rh-1}**, a similar energy surface was been calculated, in which both nucleophilic addition of carbazole and proton shuttle step had the similar energy barriers (Figure 7). However, a weak interaction of enol double bond with rhodium catalyst was found in the **INT_{RhN-3}** and **INT_{RhC-3}**, which were quite different from

the Au-bound complexes and led to an exergonic and irreversible dissociation process. These irreversible nucleophilic addition and 1,4-proton transfer steps were selectivity-determining step and led to dynamically favored N-H functionalization product.

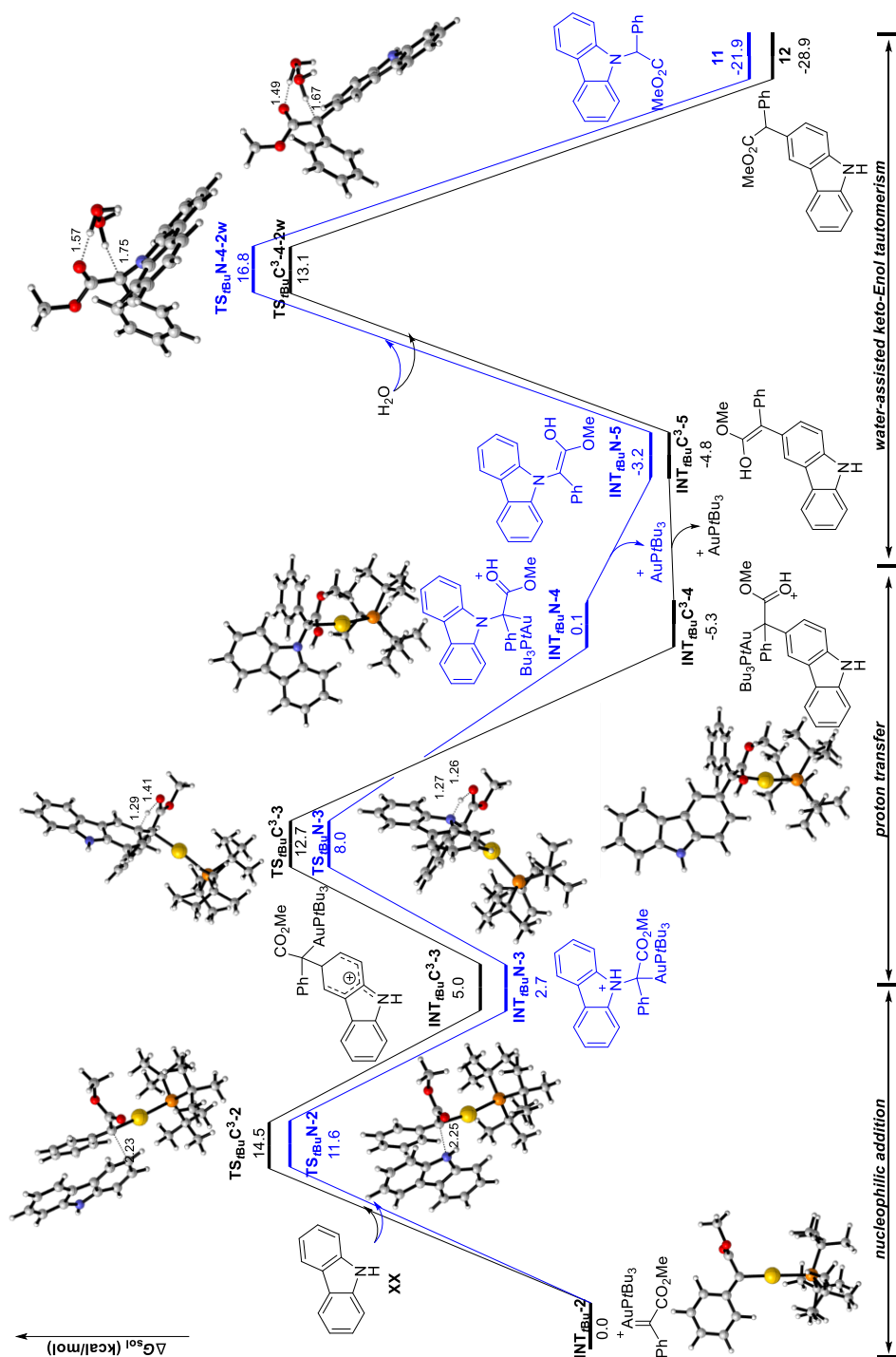


Figure 6: Potential energy surface of $t\text{Bu}_3\text{PAu}^+$ -catalyzed selective C-H functionalization of carbazole

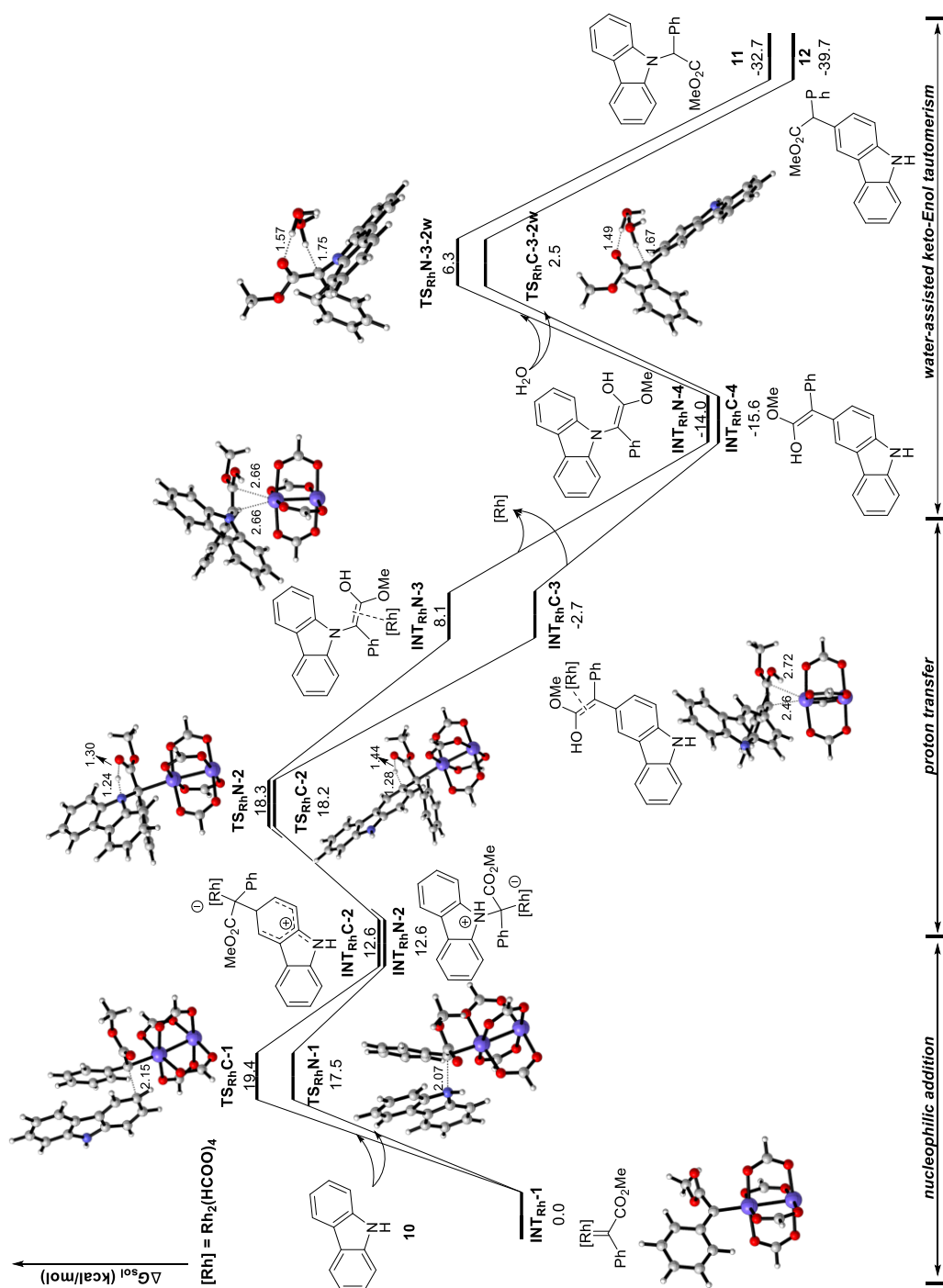


Figure 7: Potential energy surface of Rh-catalyzed selective N-H functionalization of carbazole

2.1.3 Computational Data

All calculations were performed with the Gaussian 09 program.¹⁸² Additionally, we have also studied the $t\text{Bu}^3\text{PAu}^+$ and Rh-catalyzed process with Gaussian 16 program.¹⁸³ Geometry optimizations of all the minima and transition states involved were carried out at the M06 level of theory^{184,185} in the gas phase. The LANL2DZ basis set¹⁸⁶ and pseudopotential were used for Au, Rh and P and the 6-31G(d) basis set¹⁸⁷⁻¹⁸⁹ for the other atoms. Harmonic vibrational frequency calculations at the same level were performed for all of the stationary points to confirm them as a local minima or transition structures. The combination of the functional and the basis sets has been demonstrated to generate accurate results for organometallics especially in the Au(I)-catalyzed systems.^{190,191} Key transition-state structures were confirmed to connect corresponding reactants and products by intrinsic reaction coordinate (IRC) calculations.^{192,193} Furthermore, the solvent effect of corresponding solvent (THF and DCM) was evaluated using the PCM model¹⁹⁴ based on the gas-phase optimized structures. Standard state concentrations of 1.0 mol/L were used for all species in calculations ($G_{\text{sol}} = TCG + E_{\text{sol}} + 1.89 \text{ kcal/mol}$). The computed structures are plotted using CYLView.¹⁹⁵

Thermal correction to Gibbs free energies (**TCG**, in Hartree), thermal correction to enthalpies (**TCH**, in Hartree), sum of electronic and thermal free energies (**G**, in Hartree), sum of electronic and thermal enthalpies (**H**, in Hartree), and single point energies in THF or DCM computed at the M06/6-31G(d)/LANL2DZ level (E_{sol} , in Hartree) are shown in Table 1.

Table 1: Computed Energies of all Stationary Points

Name	TCG/a.u.	TCH/a.u.	G/a.u.	H/a.u.	E_{sol} /a.u.
Me ₃ PAu ⁺ -catalyzed process in tetrahydrofuran based on Gaussian 09					
1a	0.120001	0.171258	-607.171381	-607.120124	-607.296302
Me₃PAu⁺	0.080017	0.124446	-261.252752	-261.208323	-261.411574
INT_{Me}-1	0.217506	0.296553	-868.444617	-868.365571	-868.719507
TS_{Me}-1	0.215551	0.294861	-868.439155	-868.359845	-868.709622
N₂	-0.012828	0.008926	-109.471777	-109.450023	-109.459265
INT_{Me}-2	0.210807	0.285551	-759.013732	-758.938988	-759.279446
10	0.142361	0.186216	-516.933657	-516.889802	-517.082229
TS_{Me}N-2	0.381137	0.473150	-1275.936085	-1275.844071	-1276.367405
TS_{Me}C¹-2	0.379849	0.473440	-1275.926332	-1275.832741	-1276.357418
TS_{Me}C²-2	0.378516	0.472559	-1275.923604	-1275.829560	-1276.354205
TS_{Me}C³-2	0.377511	0.472942	-1275.931256	-1275.835825	-1276.360577
TS_{Me}C⁴-2	0.378990	0.472744	-1275.922884	-1275.829130	-1276.352677
INT_{Me}N-3	0.382121	0.475510	-1275.948950	-1275.855561	-1276.381961
INT_{Me}C¹-3	0.381672	0.475165	-1275.941984	-1275.848491	-1276.375365
INT_{Me}C²-3	0.377383	0.473733	-1275.935027	-1275.838677	-1276.366379
INT_{Me}C³-3	0.379674	0.474577	-1275.942884	-1275.847980	-1276.376897
INT_{Me}C⁴-3	0.382052	0.474628	-1275.931373	-1275.838798	-1276.366277

TS_{Me}N-3	0.378000	0.470745	-1275.939745	-1275.847000	-1276.367889
INT_{Me}N-4	0.382992	0.475015	-1275.944776	-1275.852753	-1276.381122
TS_{Me}N-3'	0.373215	0.468287	-1275.876504	-1275.781432	-1276.303702
TS_{Me}C³-3	0.376476	0.470025	-1275.933135	-1275.839586	-1276.360447
INT_{Me}C³-4	0.378810	0.474943	-1275.961610	-1275.865476	-1276.393189
TS_{Me}C³-3'	0.374239	0.469429	-1275.902668	-1275.807478	-1276.330378
H₂O	0.003290	0.025375	-76.372609	-76.350524	-76.382216
INT_N-5	0.279986	0.348643	-1014.669978	-1014.601321	-1014.957718
TS_N-4-2w	0.323485	0.398515	-1167.396145	-1167.321115	-1167.730341
TS_N-4-1w	0.297635	0.369240	-1091.005132	-1090.933528	-1091.316184
11	0.280039	0.348959	-1014.698353	-1014.629433	-1014.988007
INT_C-5	0.279047	0.348693	-1014.670131	-1014.600486	-1014.959286
TS_C-4-2w	0.320185	0.397091	-1167.399536	-1167.322631	-1167.734209
TS_C-4-1w	0.296430	0.369449	-1091.010077	-1090.937058	-1091.320898
12	0.276799	0.348846	-1014.709587	-1014.637540	-1014.997588
<i>t</i>Bu₃PAu⁺-catalyzed process in tetrahydrofuran based on Gaussian 16					
1a	0.119102	0.170998	-607.172211	-607.120314	-607.296237
<i>t</i>Bu₃PAu⁺	0.323757	0.390631	-614.542944	-614.476070	-614.930508
INT_{<i>t</i>Bu}-1	0.464370	0.563154	-1221.724155	-1221.625371	-1222.239442
TS_{<i>t</i>Bu}-1	0.460641	0.561206	-1221.717862	-1221.617297	-1222.227817
N₂	-0.012843	0.008911	-109.471783	-109.450029	-109.459256
INT_{<i>t</i>Bu}-2	0.455862	0.551923	-1112.291099	-1112.195039	-1112.796538
10	0.142281	0.186212	-516.933792	-516.889861	-517.082284
TS_{<i>t</i>Bu}N-2	0.626136	0.739376	-1629.213595	-1629.100355	-1629.885389
TS_{<i>t</i>Bu}C³-2	0.623492	0.739047	-1629.206751	-1629.091195	-1629.878122
INT_{<i>t</i>Bu}N-3	0.627698	0.741617	-1629.226697	-1629.112777	-1629.901047
INT_{<i>t</i>Bu}C³-3	0.624554	0.740923	-1629.218654	-1629.102285	-1629.894328
TS_{<i>t</i>Bu}N-3	0.622996	0.73672	-1629.219638	-1629.105914	-1629.887864
INT_{<i>t</i>Bu}N-4	0.625627	0.741019	-1629.229286	-1629.113894	-1629.903073
TS_{<i>t</i>Bu}C³-3	0.621967	0.736226	-1629.210614	-1629.096355	-1629.879403
INT_{<i>t</i>Bu}C³-4	0.626701	0.741530	-1629.238585	-1629.123756	-1629.912822
H₂O	0.003294	0.025379	-76.372600	-76.350515	-76.382211
INT_{<i>t</i>Bu}N-5	0.278655	0.348440	-1014.671269	-1014.601484	-1014.957689
TS_{<i>t</i>Bu}N-4-2w	0.322046	0.398133	-1167.397601	-1167.321514	-1167.730368
11	0.279303	0.348685	-1014.699146	-1014.629764	-1014.988067
INT_{<i>t</i>Bu}C³-5	0.277747	0.34848	-1014.671531	-1014.600798	-1014.959356
TS_{<i>t</i>Bu}C³-4-2w	0.320115	0.397125	-1167.399722	-1167.322712	-1167.734314
12	0.277648	0.34893	-1014.708826	-1014.637544	-1014.997626
Rh₂(HCOO)₄-catalyzed process in dichloromethane based on Gaussian 16					
INT_{Rh}-1	0.193962	0.277052	-1473.051554	-1472.968463	-1473.265986
10	0.142281	0.186212	-516.933792	-516.889861	-517.082570

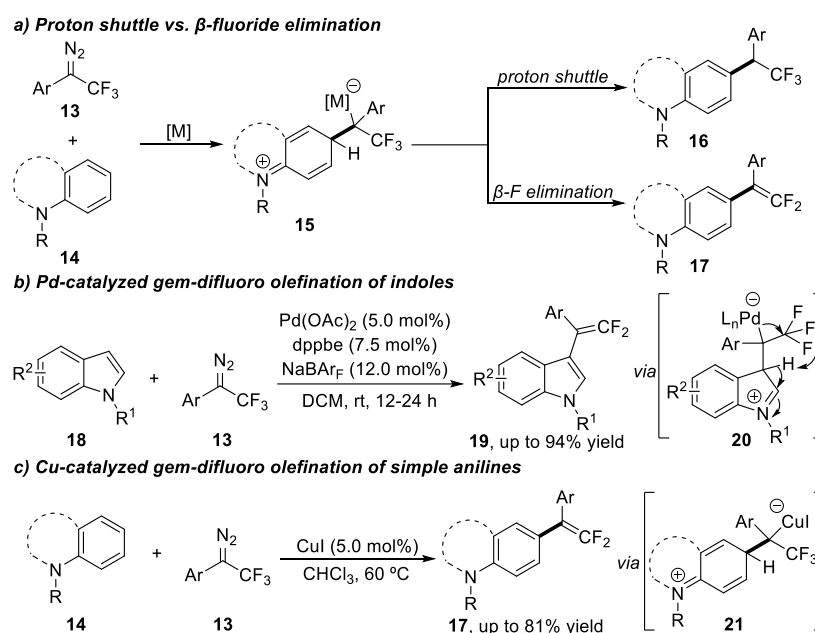
TS_{Rh}N-1	0.364626	0.465184	-1989.960948	-1989.860391	-1990.346012
TS_{Rh}C-1	0.363292	0.464541	-1989.953163	-1989.851914	-1990.341697
INT_{Rh}N-2	0.366792	0.467202	-1989.966264	-1989.865853	-1990.356031
INT_{Rh}C-2	0.364638	0.466121	-1989.958843	-1989.857360	-1990.353800
TS_{Rh}N-2	0.360978	0.462198	-1989.959304	-1989.858084	-1990.341191
INT_{Rh}N-3	0.366689	0.467312	-1989.977746	-1989.877124	-1990.363060
TS_{Rh}C-2	0.360665	0.461643	-1989.952021	-1989.851043	-1990.340889
INT_{Rh}C-3	0.362357	0.467201	-1989.99145	-1989.886606	-1990.375910
H₂O	0.003294	0.025379	-76.372600	-76.350515	-76.382455
INT_{Rh}N-4	0.278655	0.348440	-1014.671269	-1014.601484	-1014.958036
TS_{Rh}N-3-2w	0.322046	0.398133	-1167.397601	-1167.321514	-1167.730866
11	0.279303	0.348685	-1014.699146	-1014.629764	-1014.988512
INT_{Rh}C-4	0.277747	0.34848	-1014.671531	-1014.600798	-1014.959805
TS_{Rh}C-3-2w	0.320115	0.397125	-1167.399722	-1167.322712	-1167.734974
12	0.277648	0.348930	-1014.708826	-1014.637544	-1014.998119

2.2 Mechanism Study of Cu-catalyzed *gem*-Difluoro Olefination Reaction of Anilines

2.2.1 Brief Introduction: *gem*-Difluoro Olefination

After understanding stepwise C–H functionalization with α -ester metal carbene, we consider whether the α -CF₃ metal carbene can be capable of similar C–H functionalization that introduces a CF₃ group to molecules, or an unprecedented β -fluoride elimination occurs to realize *gem*-difluoro olefination reactions (Scheme 27a)? Actually, such *gem*-difluoro olefins are a unique structural motif with important applications in drug discovery.¹⁹⁶⁻¹⁹⁸

During the past decades, the synthesis of *gem*-difluoro olefines has received broad attention, such as Wittig reaction of carbonyl compounds or the application of difluorocarbene.¹⁹⁹⁻²⁰¹ Recently, our group firstly uncovered a Pd-catalyzed *gem*-difluoro olefination reaction of indoles with fluorinated diazo compounds **13**, which underwent a C–H functionalization and β -fluoride elimination strategy under mild reaction conditions (Scheme 27b).²⁰² Importantly, according to control experiments, a potential cyclopropane intermediate was ruled out in the reaction, which underlined the significance of bidentate phosphine ligands and weakly coordinating counteranion NaBAr_F. Shortly after this discovery, our group extended this β -fluoride elimination strategy to anilines with more concise CuI-catalysis system (Scheme 27c).²⁰³ To our delight, neither base nor additives were necessary to facilitate this transformation, which aroused our interest to understand this underlying reaction mechanism.



Scheme 27: α -CF₃-Metal carbene mediated *gem*-difluoro olefination reactions

2.2.2 Computational Study

We then studied the detailed mechanism of this Cu-catalyzed *gem*-difluoro olefination reaction by DFT calculations at B3LYP-D3/6-311+G(d,p)(SDD)//B3LYP/6-31G(d)(SDD) (solvent = chloroform) level of theory. In this case, *N,N*-dimethyl aniline **14a**, 1-phenyl-2,2,2-trifluorodiazooethane **13a** and CuI catalyst were chosen as the model substrate. As shown in Figure 8, our calculations indicated that the initial step of the coordination of CuI with diazo compound **13a** to form complex **INT1** was a facile process and exergonic by 4.6 kcal/mol. Then, intermediate **INT1** underwent another facile denitrogenation process via **TS1** with an activation free energy of 6.4 kcal/mol, which led to the Cu-carbene **INT2** ($\Delta G = -20.2$ kcal/mol). For the following transformation, we considered the nucleophilic attack of *N,N*-dimethyl aniline **14a** onto electron-deficient carbene carbon, which was nearly a barrierless process to afford the trifluoromethylated zwitterion **INT3**. Unexpectedly, another molecule **14a** could be regarded as a suitable base to promote a deprotonation process via **TS3** with an energy barrier of 10.6 kcal/mol, which gave the rearomatized intermediate **INT4**. In the last step, fluoride elimination converted intermediate **INT4** to the final product via a low-lying transition state **TS4** with a low activation free energy of 2.6 kcal/mol, simultaneously regenerating CuI catalyst to continue the next catalytic cycle. Actually, the HF-**14a** adduct had not been detected in the experiment, which was likely to be reasoned by the glass reaction tube or the silica gel column.

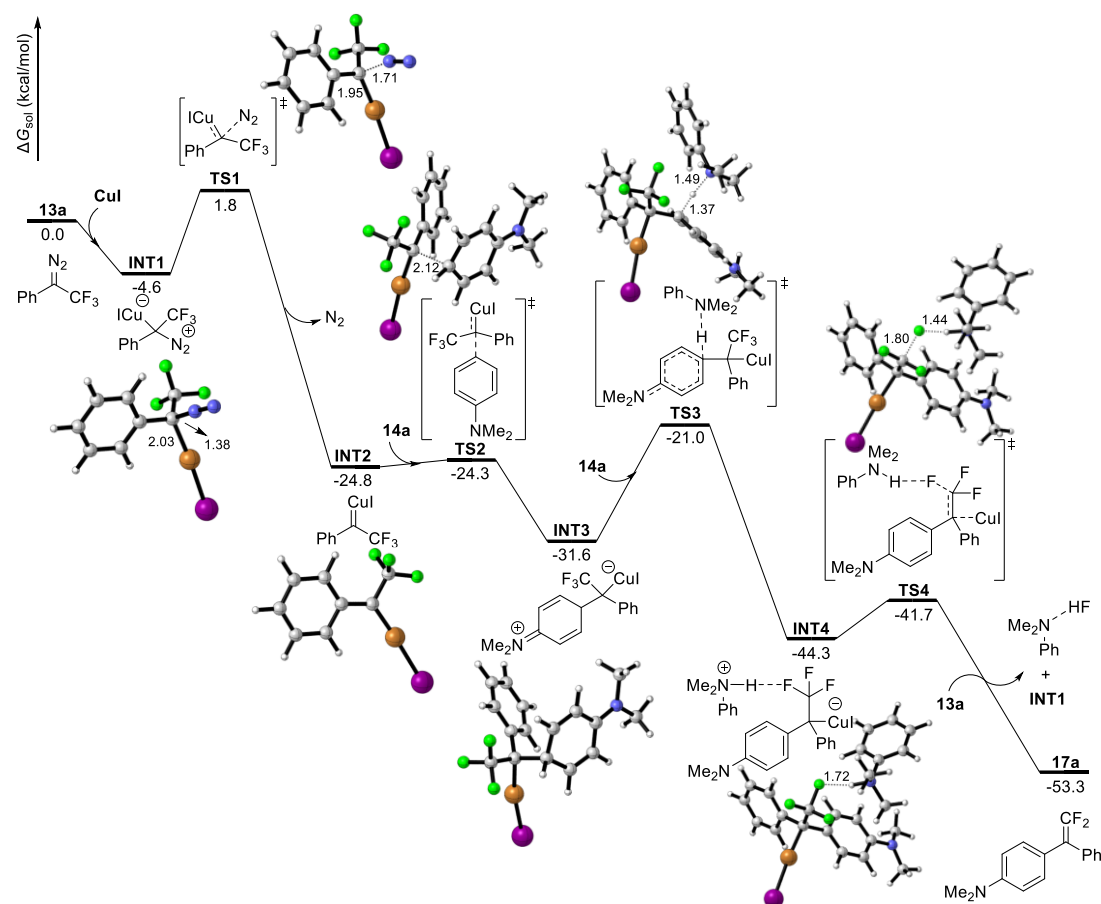


Figure 8: Potential energy surface of Cu-catalyzed *gem*-difluoro olefination reaction

Besides aniline-promoted HF elimination mechanism, we hypothesized that electron-rich *N,N*-dimethyl aniline **14a** was able to undergo a nucleophilic substitution of possible (1,2,2-trifluorovinyl)benzene intermediate **INT5** to form final product. However, all efforts to locate such transition states from Cu-carbene led to 1,2-F migration transition state **TS5** and β -F elimination transition state **TS6**. Both processes had high energy barriers (> 40 kcal/mol) and were energetically unfavorable to form (1,2,2-trifluorovinyl)benzene **INT5** (Figure 9).

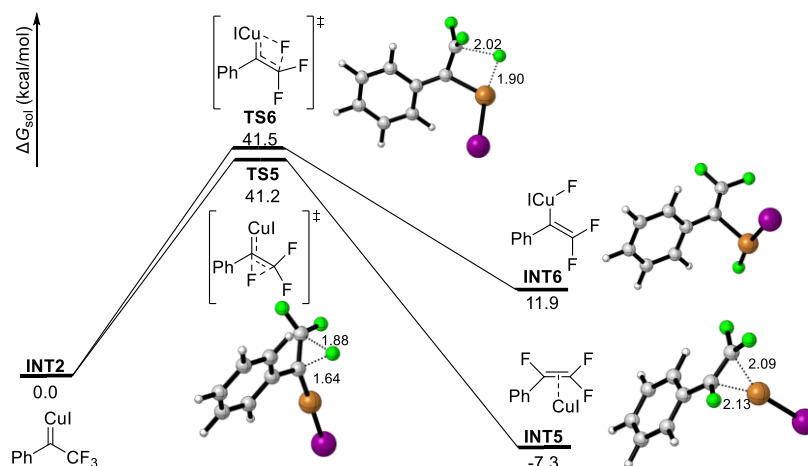


Figure 9: Potential energy surface of 1,2-F migration and β -F elimination of Cu-carbene **INT2**

Apart from the base-promoted deprotonation step of **INT3**, we also considered the direct 1,2-proton migration (via **TS7**) and 1,3-HF elimination (via **TS8**) process, which both had higher energy barrier of 21.7 and 29.5 kcal/mol, respectively (Figure 10). Furthermore, direct β -fluoride elimination from **INT3** or stepwise fluoride elimination through cyclopropane intermediate **INT7** were also identified via transition states **TS9** and **TS10**, respectively. Unfortunately, both pathways were less favorable than base-promoted deprotonation via **TS3**, which could not account for the *gem*-difluoro olefin formation.

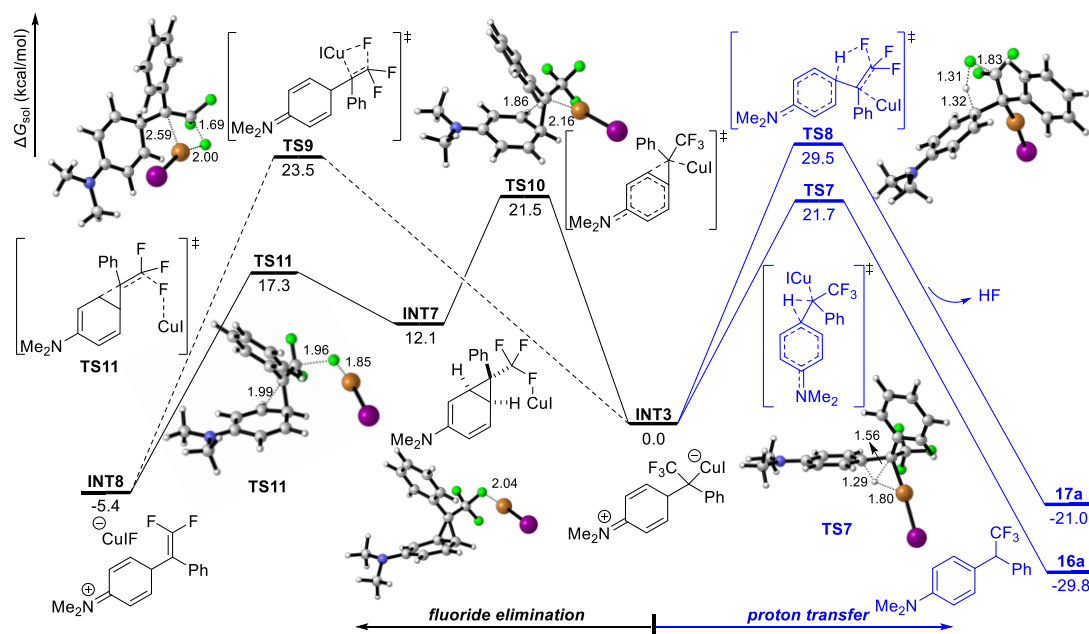


Figure 10: Potential energy surface of competitive fluoride elimination and proton transfer pathways

2.2.3 Computational Data

All the calculations were performed with the Gaussian 09 program.¹⁸² Geometry optimizations of all the minima and transition states involved were carried out at the B3LYP level of theory^{204,205} in the gas phase. The SDD basis set^{206,207} and pseudopotential were used for Cu and I, and the 6-31G(d) basis set¹⁸⁷⁻¹⁸⁹ for the other atoms. Harmonic vibrational frequency calculations at the same level were performed for all the stationary points to confirm them as a local minima or transition structures. Key transition-state structures were confirmed to connect corresponding reactants and products by intrinsic reaction coordinate (IRC) calculations.^{192,193} Solvation energies in chloroform ($\epsilon = 4.7113$) were evaluated by IEFPCM calculations with radii and non-electrostatic terms for SMD solvation model²⁰⁸ using the gas-phase optimized structures. Standard state concentrations of 1.0 mol/L were used for all species in calculations. Furthermore, to improve the calculation accuracy, single-point energies calculations were computed at the B3LYP-D3 level of theory²⁰⁹ with the SDD basis set and pseudopotential for Cu and I, and the 6-311+G(d,p) basis set^{210,211} for the other atoms. The given Gibbs free energies in chloroform were calculated according to the formula: $G_{\text{sol}} = \text{TCG} + \Delta G_{\text{sol}} + \text{SPE} + 1.89 \text{ kcal/mol}$. The CYL View software was employed to show the 3D structures of the studied species.¹⁹⁵

Thermal correction to Gibbs free energies (**TCG**, in Hartree), sum of electronic and thermal free energies (**G**, in Hartree), sum of electronic and thermal enthalpies (**H**, in Hartree), solvation Gibbs free energies in chloroform (ΔG_{sol} , in Hartree), and single point energies computed at the B3LYP-D3/6-311+G(d,p)/SDD level (**SPE**, in Hartree) are shown in Table 2.

Table 2: Computed Energies of all Stationary Points

Name	TCG/a.u.	G/a.u.	H/a.u.	ΔG_{sol} /a.u.	SPE/a.u.
13a	0.081389	-716.752105	-716.701549	-0.005783	-717.059183
CuI	-0.024732	-208.840060	-208.810966	-0.029090	-208.815385
INT1	0.073629	-925.597229	-925.533707	-0.022700	-925.908089
TS1	0.072045	-925.588746	-925.525519	-0.021048	-925.897875
INT2	0.068376	-816.103538	-816.045907	-0.023778	-816.369866
N₂	-0.012851	-109.536980	-109.515225	0.005172	-109.559422
14a	0.140815	-366.074378	-366.031334	-0.011914	-366.327458
TS2	0.231100	-1182.149648	-1182.069382	-0.036256	-1182.714765
INT3	0.232914	-1182.154225	-1182.074399	-0.045091	-1182.719423
TS3	0.392730	-1548.193184	-1548.092350	-0.050262	-1549.052697
INT4	0.396090	-1548.228802	-1548.124403	-0.057018	-1549.086365
TS4	0.394149	-1548.227729	-1548.123706	-0.050643	-1549.086655
HF-14a	0.151511	-466.505528	-466.458050	-0.014835	-466.829120
17a	0.226548	-872.909833	-872.845148	-0.017528	-873.407755
TS5	0.066475	-816.036869	-815.979471	-0.025495	-816.300587
INT5	0.067879	-816.112050	-816.053895	-0.025039	-816.379690
TS6	0.065897	-816.030144	-815.972776	-0.027229	-816.297752

INT6	0.066298	-816.074392	-816.015429	-0.025967	-816.346645
TS7	0.226746	-1182.130810	-1182.051175	-0.036726	-1182.687048
16a	0.240617	-973.376567	-973.309118	-0.018741	-973.927356
TS8	0.228831	-1182.115190	-1182.036571	-0.036529	-1182.676849
HF	-0.007377	-100.427548	-100.407814	-0.006155	-100.482212
TS9	0.231587	-1182.118283	-1182.039026	-0.038183	-1182.687536
TS10	0.232295	-1182.132008	-1182.053051	-0.034569	-1182.695118
INT7	0.231820	-1182.153348	-1182.072740	-0.032406	-1182.711714
TS11	0.230376	-1182.132434	-1182.051361	-0.038514	-1182.695950
INT8	0.229012	-1182.159749	-1182.075243	-0.044806	-1182.724383

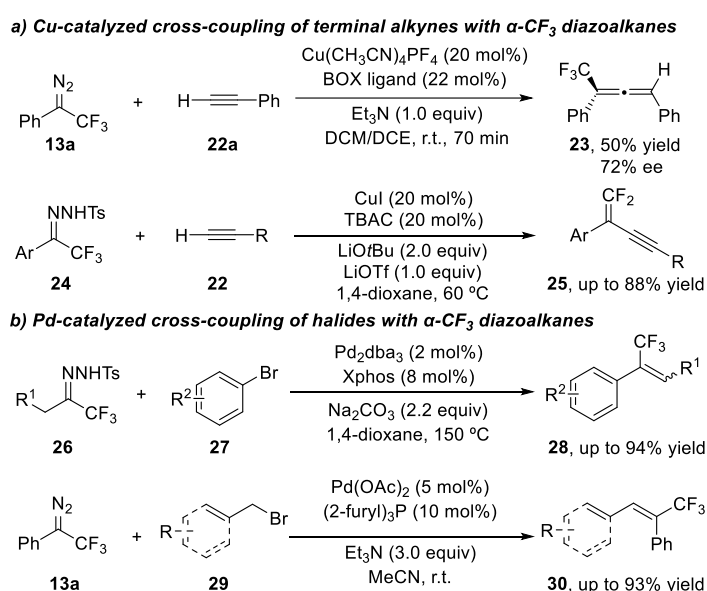
2.3 Pd-catalyzed Cross Coupling with Vinyl Bromides and α -CF₃ Diazoalkanes

2.3.1 Brief Introduction: Cross-coupling of α -CF₃ Diazoalkanes

Trifluoromethylated diazoalkanes are fluorinated building blocks to introduce trifluoromethyl group into organic molecules.²¹²⁻²¹⁷ In addition to the classic carbene transfer reactions with α -CF₃ diazoalkanes such as cyclopropa(e)nations, C–H or X–H functionalization, they can also participate in various metal-catalyzed cross-couplings.

As we mentioned in preceding chapter, the Wang group applied 1-phenyl-2,2,2-trifluorodiazoethane **13a** in the enantioselective synthesis of trisubstituted allenes. However, only one example was presented in moderate yield and enantioselectivity.⁹⁹ Furthermore, when using trifluoromethylated *N*-tosylhydrazones **24** as carbene precursor, the additive LiOTf was employed in CuI-catalytic system to promote C–F bond cleavage, which yielded 1,1-difluoro-1,3-enynes **25** in high efficiency (Scheme 28a).²¹⁸ Importantly, trifluoromethylated diazoalkanes are presented as a very convenient substrate for the palladium-catalysis with halides as well. For example, trifluoromethylated alkenes or dienes could be accessed through Pd-catalyzed cross-couplings with aryl bromides, benzyl bromides or allyl bromides, which were reported by the Valdés group and Wang group, respectively.^{219,220}

Inspired by carbene-mediated cross coupling reactions with α -CF₃ diazoalkanes, we propose a similar approach via Pd-catalyzed coupling reaction with vinyl bromides as coupling partner.²²¹ In this case, tetrasubstituted trifluoromethyl allenes can be obtained, which still remain a synthetic challenge.²²²⁻²²⁴



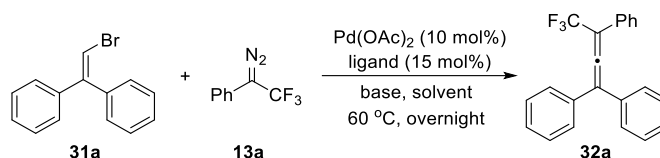
Scheme 28: Carbene-mediated crossing-coupling reactions with trifluoromethylated diazoalkanes

2.3.2 Results and Discussion

At the outset of the investigation, we studied the reaction of trifluoromethylated diazoalkane **13a** and vinyl bromide **31a** with a stoichiometry of 1.5 : 1. Based on the previous study of this coupling reaction,²²⁵ we isolated tetrasubstituted trifluoromethyl allene **32a** in

**This optimization part was performed by Zhen Yang and Chao Pei.*

Table 3: Optimization of crossing-coupling with vinyl bromide and α -CF₃ diazoalkane

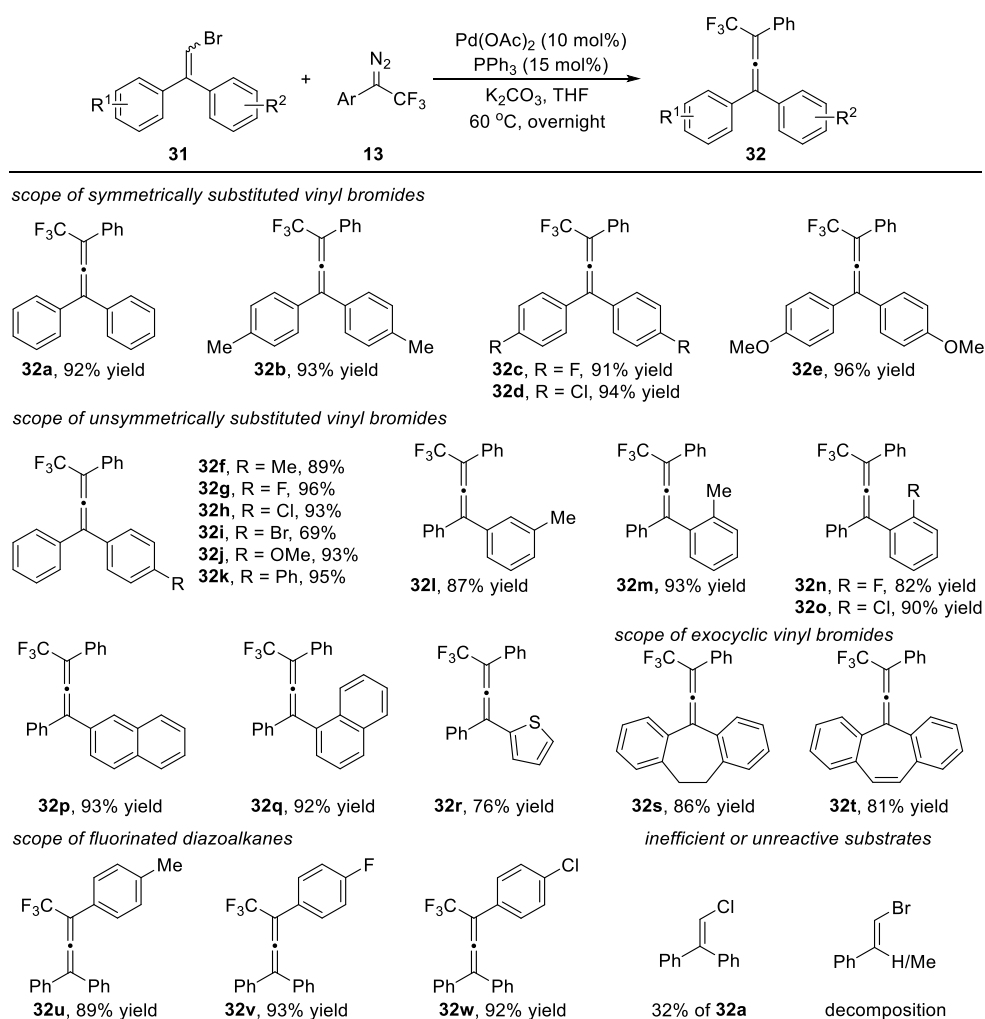


Entry ^[a]	Ligand	Solvent	Base	Yield (%)
1	dpph	THF	CsOAc	15
2	dpph	THF	KOH	9
3	dpph	THF	K ₂ CO ₃	72
4	dpph	THF	Li ₂ CO ₃	8
5	dpph	THF	LiOH	3
6	dpph	THF	NaOAc	5
7	dpph	THF	NEt ₃	8
8	dppb	THF	K ₂ CO ₃	74
9	dppe	THF	K ₂ CO ₃	76
10	dppf	THF	K ₂ CO ₃	71
11	<i>rac</i> -BINAP	THF	K ₂ CO ₃	5
12	PAd ₂ nBu	THF	K ₂ CO ₃	72
13	DavePhos	THF	K ₂ CO ₃	4
14	SPhos	THF	K ₂ CO ₃	<i>trace</i>
15	XPhos	THF	K ₂ CO ₃	<i>trace</i>
16	RuPhos	THF	K ₂ CO ₃	<i>trace</i>
17	P(2-furyl) ₃	THF	K ₂ CO ₃	67
18	PoTol ₃	THF	K ₂ CO ₃	6
19	PPh ₃	THF	K ₂ CO ₃	95 (92) ^[b]
20	PPh ₃	1,2-DCE	K ₂ CO ₃	42
21	PPh ₃	toluene	K ₂ CO ₃	56
22	PPh ₃	1,4-dioxane	K ₂ CO ₃	92
23	PPh ₃	DMF	K ₂ CO ₃	19
24 ^[c]	-	THF	K ₂ CO ₃	<i>trace</i>
25 ^[d]	PPh ₃	THF	K ₂ CO ₃	8

^[a] Reaction condition: 0.2 mmol **31a**, 0.3 mmol **13a**, 10 mol% Pd(OAc)₂, 15 mol% ligand and 0.3 mmol base were dissolved in 2.5 mL solvent and stirred at 60 °C overnight under argon atmosphere. The yield was determined by ¹⁹F-NMR of the crude reaction with PhCF₃ as internal standard. ^[b] Isolated yield. ^[c] Without ligand. ^[d] 5 mol% Pd₂(dba)₃ was used.

15% yield when choosing Pd(OAc)₂/dpph as the catalytic system, CsOAc as the base and THF as the solvent (Table 3, entry 1). We then proceeded to optimize the reaction by first screening the bases, which had a significant influence on efficiency of the reaction, and found that K₂CO₃ gave the best results (Table 3, entry 1-7). To further improve the reaction yield, we next screened different bidentate phosphine and monodentate phosphine ligands (Table 3, entry 8-19). To our surprise, the simple triphenyl phosphine gave the best isolated yield of 92% (Table 3, entry 19). Subsequent test of various solvents indicated that the ether solvent was beneficial to the reaction yield (Table 3, entry 20-23). Indeed, the PPh₃ ligand was crucial to promote this transformation as well as using the Pd(OAc)₂ as palladium source (Table 3, entry 24 and 25).

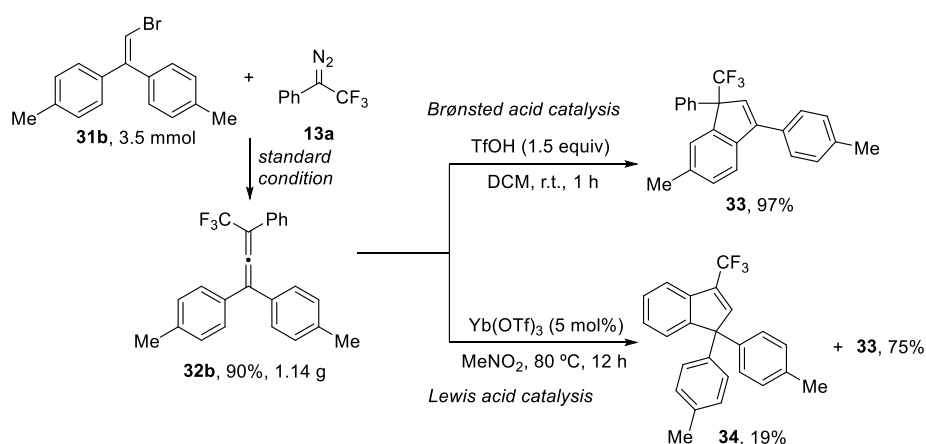
With the optimized reaction conditions in hand, we next embarked on the substrate scope with a series of 2,2-diaryl vinyl bromide (**31**) reaction partner. As illustrated in Scheme 29, various symmetrically substituted vinyl bromides could react smoothly with trifluoromethylated diazoalkane **12a** to afford the trifluoromethyl-substituted allene product **32a-e** in excellent yield. Similarly, different unsymmetrically substituted vinyl bromides were well tolerated under the reaction condition and the corresponding tetrasubstituted allenes were obtained in very good yield. Furthermore, either *ortho*- or *meta*- substituents would



Scheme 29: Substrate scopes of different vinyl bromides and α -CF₃ diazoalkanes

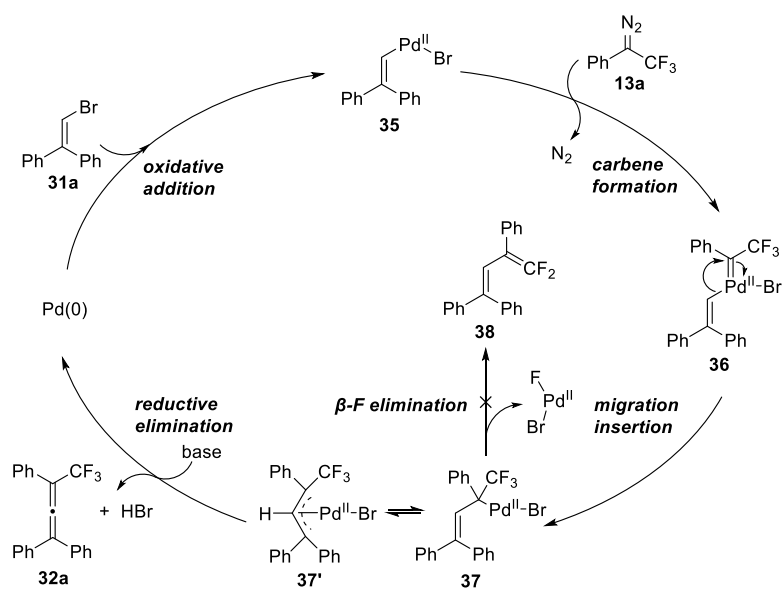
not influence the reaction efficiency (**32l-o**). However, in the case of a bromo-substituent substrate, a slightly reduced yield of 69% was found, which could be rationalized by the competitive oxidative insertion of palladium catalyst into C(aryl)-Br bond. Actually, naphthyl or thienyl substituted vinyl bromides were compatible to this reaction and converted to corresponding tetrasubstituted allene products in high yield (**32p-r**). Importantly, dibenzosuberone-derived exocyclic vinyl bromides could also lead to allenes **32s** and **32t** in good yield. Moreover, different substitution patterns of the trifluoromethyl-substituted diazoalkane were also applied in the Pd-catalyzed cross-coupling reaction and could give the coupling products in 89-93% yield (**32u-w**). Next, inert vinyl chloride was also studied in the coupling reaction, however, only 32% of the allene product **32a** was obtained. *Trans*- β -bromo-styrene and alkyl-aryl vinyl bromide both resulted in the decomposition of diazoalkane and inseparable mixture.

To demonstrate the practical usefulness of this reaction, a gram-scale experiment was carried out, which gave 1.14 g **32b** in comparable 90% yield (Scheme 30). Last, intramolecular Friedel-Crafts reaction of **32b** could be realized via catalysis of Brønsted acid - triflic acid or Lewis acid - Yb(OTf)₃, in which trifluoromethylated indene product **33** and **34** were obtained in high yield.



Scheme 30: Scale-up reaction and derivatizations

Based on the investigations in literature precedents,^{219,220,225} a plausible mechanism was proposed to account for this Pd-catalyzed crossing-coupling reaction (Scheme 31). Firstly, vinyl bromide **31a** underwent an initial oxidative insertion with Pd(0) catalyst to yield an intermediate Pd(II) complex **35**. Subsequently, Pd-carbene **36** was generated through denitrogenation of trifluoromethylated diazoalkane **13a**. Following migration insertion process gave the η^1 -coordinated Pd(II) complex **37** or η^3 -coordinated Pd(II)-allyl complex **37'**. Final reductive elimination under basic condition led to tetrasubstituted allene product **32a** and regenerated the Pd(0) catalyst for next catalytic cycle. In addition, a potential β -fluoride elimination of Pd(II) complex **37** would lead to the formation *gem*-difluoro olefin **38**. However, high oxidation state Pd(II)BrF complex would be generated simultaneously in this step, which was difficult to regenerate Pd(0) catalyst and thus ruled out this pathway.



Scheme 31: Proposed mechanism

2.3.2 Experimental Data

General procedure of Pd-catalyzed crossing-coupling reaction

In a test tube, the Pd(OAc)₂ (4.5 mg, 10 mol%), PPh₃ (7.9 mg, 15 mol%) and K₂CO₃ (41.4 mg, 1.5 equiv.) were dissolved in 1.0 mL THF under argon and stirred in a pre-heated oil bath at 60 °C for 15 min. 2,2-Diarylvinyli halides (0.2 mmol, 1.0 equiv.) and trifluorodiazalkanes (1.5 equiv.) in THF (1.5 mL) was added and stirred at 60 °C overnight. The product was purified by column chromatography using *n*-hexane : ethyl acetate as eluent.

(4,4,4-Trifluorobuta-1,2-diene-1,1,3-triyl)tribenzene (32a)

Colorless oil; ¹H NMR (600 MHz, Chloroform-*d*): δ = 7.56 (d, *J* = 7.8 Hz, 2H), 7.44 – 7.37 (m, 12H), 7.34 (t, *J* = 7.4 Hz, 1H) ppm. ¹³C NMR (151 MHz, Chloroform-*d*): δ = 207.0 (q, *J* = 3.9 Hz), 134.3, 129.8, 129.0, 128.9, 128.8, 128.6, 127.2, 123.5 (q, *J* = 275.2 Hz), 118.3, 104.6 (q, *J* = 34.3 Hz) ppm. Due to the overlap of aromatic carbon peaks, one carbon signal is missing. ¹⁹F NMR (565 MHz, Chloroform-*d*): δ = -59.91 ppm. HRMS (ESI) *m/z*: [M]⁺ mass found: 336.1119, mass calculated for C₂₂H₁₅F₃⁺: 336.1120. IR (KBr): 3061, 3032, 2926, 2855, 2321, 2162, 2049, 1947, 1888, 1805, 1763, 1598, 1493, 1447, 1375, 1296, 1167, 1118, 1031, 999, 928, 841, 763, 691, 663 cm⁻¹.

4,4'-(4,4,4-Trifluoro-3-phenylbuta-1,2-diene-1,1-diyl)bis(methylbenzene) (32b)

White solid; ¹H NMR (600 MHz, Chloroform-*d*): δ = 7.54 (d, *J* = 7.7 Hz, 2H), 7.39 (t, *J* = 7.6 Hz, 2H), 7.33 (d, *J* = 7.2 Hz, 1H), 7.30 (d, *J* = 8.0 Hz, 4H), 7.21 (d, *J* = 7.9 Hz, 4H), 2.40 (s, 6H) ppm. ¹³C NMR (151 MHz, Chloroform-*d*): δ = 206.9 (q, *J* = 3.9 Hz), 138.7, 131.4, 130.0, 129.6, 128.9, 128.6, 128.4, 127.1, 123.5 (q, *J* = 275.1 Hz), 118.1, 104.1 (q, *J* = 34.3 Hz), 21.4 ppm. ¹⁹F NMR (565 MHz, Chloroform-*d*): δ = -59.91 ppm. HRMS (ESI) *m/z*: [M]⁺ mass found: 364.1435, mass calculated for C₂₄H₁₉F₃⁺: 364.1433. IR (KBr): 3352, 3027, 2924, 2857, 2159, 2042, 1913, 1732, 1661, 1606, 1505, 1450, 1414, 1373, 1290, 1187, 1156, 1119, 1031, 968, 928, 821, 761, 718, 696, 658 cm⁻¹.

4,4'-(4,4,4-Trifluoro-3-phenylbuta-1,2-diene-1,1-diyl)bis(fluorobenzene) (32c)

Colorless oil; ¹H NMR (600 MHz, Chloroform-*d*): δ = 7.53 (d, *J* = 7.7 Hz, 2H), 7.41 (t, *J* = 7.7 Hz, 2H), 7.38 – 7.34 (m, 5H), 7.11 (t, *J* = 8.5 Hz, 4H) ppm. ¹³C NMR (151 MHz, Chloroform-*d*): δ = 206.6 (q, *J* = 4.2 Hz), 163.1 (d, *J* = 249.2 Hz), 130.4 (d, *J* = 8.3 Hz), 130.1 (d, *J* = 3.5 Hz), 129.5, 129.1, 128.8, 127.1, 123.3 (q, *J* = 275.1 Hz), 116.6, 116.1 (d, *J* = 21.8 Hz), 104.8 (q, *J* = 34.3 Hz) ppm. ¹⁹F NMR (565 MHz, Chloroform-*d*): δ = -60.00 (s, 3F), -112.33 – -112.38 (m, 2F) ppm. HRMS (ESI) *m/z*: [M]⁺ mass found: 372.0932, mass calculated for C₂₂H₁₃F₅⁺: 372.0931. IR (KBr): 3340, 3063, 2926, 2157, 2029, 1895, 1767, 1653, 1601, 1504, 1418, 1370, 1296, 1230, 1162, 1120, 1014, 929, 836, 763, 721, 690, 659 cm⁻¹.

4,4'-(4,4,4-Trifluoro-3-phenylbuta-1,2-diene-1,1-diyl)bis(chlorobenzene) (32d)

Colorless oil; ¹H NMR (600 MHz, Chloroform-*d*): δ = 7.51 (d, *J* = 7.7 Hz, 2H), 7.42 – 7.35 (m, 7H), 7.31 (d, *J* = 8.5 Hz, 4H) ppm. ¹³C NMR (151 MHz, Chloroform-*d*): δ = 206.7 (q, *J* = 3.9 Hz), 135.0, 132.4, 129.9, 129.3, 129.2, 129.1, 128.9, 127.1, 123.2 (q, *J* = 275.4 Hz), 116.6, 105.3 (q, *J* = 34.3 Hz) ppm. ¹⁹F NMR (565 MHz, Chloroform-*d*): δ = -59.96 ppm. HRMS (ESI) *m/z*: [M]⁺ mass found: 404.0344, mass calculated for C₂₂H₁₃Cl₂F₃⁺: 404.0340. IR (KBr): 3333, 3064, 2926, 2856, 2163, 2033, 1902, 1771, 1653, 1592, 1489, 1409, 1369, 1296, 1168, 1123, 1091, 1013, 928, 909, 829, 765, 719, 692, 662 cm⁻¹.

4,4'-(4,4,4-Trifluoro-3-phenylbuta-1,2-diene-1,1-diyl)bis(methoxybenzene) (32e)

Colorless oil; ^1H NMR (600 MHz, Chloroform-*d*): δ = 7.53 (d, J = 7.8 Hz, 2H), 7.38 (t, J = 7.6 Hz, 2H), 7.36 – 7.30 (m, 5H), 6.93 (d, J = 8.7 Hz, 4H), 3.84 (s, 6H) ppm. ^{13}C NMR (151 MHz, Chloroform-*d*): δ = 206.8 (q, J = 3.9 Hz), 160.1, 130.2, 130.0, 128.9, 128.3, 127.0, 126.6, 123.5 (q, J = 275.1 Hz), 117.6, 114.3, 103.9 (q, J = 34.1 Hz), 55.5 ppm. ^{19}F NMR (565 MHz, Chloroform-*d*): δ = -59.93 ppm. HRMS (ESI) m/z : $[\text{M}]^+$ mass found: 396.1329, mass calculated for $\text{C}_{24}\text{H}_{19}\text{F}_3\text{O}_2^+$: 396.1331. IR (KBr): 3005, 2932, 2841, 2547, 2195, 2043, 1893, 1730, 1605, 1507, 1461, 1371, 1294, 1247, 1168, 1117, 1031, 928, 834, 762, 729, 693, 658 cm^{-1} .

(4,4,4-Trifluoro-1-(*p*-tolyl)buta-1,2-diene-1,3-diyl)dibenzene (32f)

Colorless oil; ^1H NMR (600 MHz, Chloroform-*d*): δ = 7.55 (d, J = 7.7 Hz, 2H), 7.43 – 7.37 (m, 7H), 7.34 (d, J = 7.3 Hz, 1H), 7.31 (d, J = 7.5 Hz, 2H), 7.22 (d, J = 7.8 Hz, 2H), 2.40 (s, 3H) ppm. ^{13}C NMR (151 MHz, Chloroform-*d*): δ = 206.9 (q, J = 3.7 Hz), 138.8, 134.5, 131.3, 123.0, 129.7, 129.0, 128.9, 128.8, 128.7, 128.6, 128.5, 127.2, 123.5 (q, J = 275.1 Hz), 118.2, 104.4 (q, J = 34.0 Hz), 21.4 ppm. ^{19}F NMR (565 MHz, Chloroform-*d*): δ = -59.91 ppm. HRMS (ESI) m/z : $[\text{M}]^+$ mass found: 350.1274, mass calculated for $\text{C}_{23}\text{H}_{17}\text{F}_3^+$: 350.1276. IR (KBr): 3030, 2924, 2859, 2166, 1944, 1802, 1763, 1601, 1495, 1448, 1413, 1372, 1297, 1166, 1118, 1031, 968, 928, 820, 762, 694, 660 cm^{-1} .

(4,4,4-Trifluoro-1-(4-fluorophenyl)buta-1,2-diene-1,3-diyl)dibenzene (32g)

Colorless oil; ^1H NMR (600 MHz, Chloroform-*d*): δ = 7.55 (d, J = 7.8 Hz, 2H), 7.46 – 7.33 (m, 10H), 7.11 (t, J = 8.5 Hz, 2H) ppm. ^{13}C NMR (151 MHz, Chloroform-*d*): δ = 206.7 (q, J = 4.0 Hz), 163.0 (d, J = 248.6 Hz), 134.1, 130.4 (d, J = 8.1 Hz), 130.2 (d, J = 3.4 Hz), 129.5, 129.0, 128.9, 128.8, 128.6, 127.0, 123.3 (q, J = 275.1 Hz), 117.4, 115.9 (d, J = 21.9 Hz), 104.6 (q, J = 34.4 Hz) ppm. Due to the overlap of aromatic carbon peaks, one carbon signal is missing. ^{19}F NMR (565 MHz, Chloroform-*d*): δ = -59.95 (s, 3F), -112.64 – -112.68 (m, 1F) ppm. HRMS (ESI) m/z : $[\text{M}]^+$ mass found: 354.1027, mass calculated for $\text{C}_{22}\text{H}_{14}\text{F}_4^+$: 354.1026. IR (KBr): 3062, 2926, 2168, 1947, 1893, 1766, 1600, 1503, 1448, 1413, 1372, 1296, 1231, 1165, 1120, 1031, 967, 929, 838, 761, 694, 661 cm^{-1} .

(1-(4-Chlorophenyl)-4,4,4-trifluorobuta-1,2-diene-1,3-diyl)dibenzene (32h)

Colorless oil; ^1H NMR (600 MHz, Chloroform-*d*): δ = 7.55 (d, J = 7.3 Hz, 2H), 7.44 – 7.38 (m, 9H), 7.38 – 7.33 (m, 3H) ppm. ^{13}C NMR (151 MHz, Chloroform-*d*): δ = 206.9 (q, J = 4.1 Hz), 134.8, 133.9, 132.8, 130.0, 129.4, 129.2, 129.1, 129.06, 129.02, 128.8, 128.7, 127.2, 123.4 (q, J = 275.2 Hz), 117.5, 104.9 (q, J = 34.4 Hz) ppm. ^{19}F NMR (565 MHz, Chloroform-*d*): δ = -59.91 ppm. HRMS (ESI) m/z : $[\text{M}]^+$ mass found: 370.0729, mass calculated for $\text{C}_{22}\text{H}_{14}\text{ClF}_3^+$: 370.0730. IR (KBr): 3062, 2926, 2856, 2168, 2025, 1944, 1900, 1768, 1702, 1596, 1489, 1448, 1405, 1371, 1296, 1168, 1211, 1013, 966, 928, 830, 760, 730, 693, 661 cm^{-1} .

(1-(4-Bromophenyl)-4,4,4-trifluorobuta-1,2-diene-1,3-diyl)dibenzene (32i)

Colorless oil; ^1H NMR (600 MHz, Chloroform-*d*): δ = 7.55 – 7.50 (m, 4H), 7.45 – 7.33 (m, 8H), 7.28 (d, J = 8.5 Hz, 2H) ppm. ^{13}C NMR (151 MHz, Chloroform-*d*): δ = 206.8 (q, J = 3.8 Hz), 133.8, 133.3, 132.2, 130.3, 129.4, 129.1, 129.07, 129.03, 128.8, 128.7, 127.2, 123.3 (q, J = 275.3 Hz), 123.0, 117.5, 105.0 (q, J = 34.4 Hz) ppm. ^{19}F NMR (565 MHz, Chloroform-*d*): δ = -59.94 ppm. HRMS (ESI) m/z : $[\text{M}]^+$ mass found: 414.0227, mass calculated for $\text{C}_{22}\text{H}_{14}\text{BrF}_3^+$: 414.0225. IR (KBr): 3061, 3032, 2925, 2856, 2324, 2077, 1946, 1901, 1767, 1594, 1488, 1448, 1400, 1370, 1296, 1167, 1120, 1071, 1009, 965, 928, 827, 760, 692, 664 cm^{-1} .

(4,4,4-Trifluoro-1-(4-methoxyphenyl)buta-1,2-diene-1,3-diyl)dibenzene (32j)

Colorless oil; ^1H NMR (600 MHz, Chloroform-*d*): δ = 7.38 (d, J = 7.8 Hz, 2H), 7.28 – 7.19 (m, 7H), 7.17 (d, J = 8.7 Hz, 3H), 6.77 (d, J = 8.5 Hz, 2H), 3.67 (s, 3H) ppm. ^{13}C NMR (151 MHz, Chloroform-*d*): δ = 206.9 (q, J = 4.0 Hz), 160.2, 134.6, 130.0, 129.0, 128.9, 128.8, 128.7, 128.5, 127.1, 126.3, 123.5 (q, J = 275.2 Hz), 118.0, 114.4, 104.3 (q, J = 34.2 Hz), 55.5 ppm. Due to the overlap of aromatic carbon peaks, one carbon signal is missing. ^{19}F NMR (565 MHz, Chloroform-*d*): δ = -59.89 ppm. HRMS (ESI) m/z : $[\text{M} + \text{H}]^+$ mass found: 367.1293, mass calculated for $\text{C}_{23}\text{H}_{18}\text{F}_3\text{O}^+$: 367.1304. IR (KBr): 3033, 2933, 2840, 2208, 2157, 2056, 1944, 1888, 1734, 1604, 1508, 1449, 1372, 1295, 1249, 1168, 1117, 1032, 966, 928, 833, 801, 764, 726, 695, 660 cm^{-1} .

4-(4,4,4-Trifluoro-1,3-diphenylbuta-1,2-dien-1-yl)-1,1'-biphenyl (32k)

Colorless oil; ^1H NMR (600 MHz, Chloroform-*d*): δ = 7.63 (t, J = 7.6 Hz, 4H), 7.58 (d, J = 7.8 Hz, 2H), 7.53 – 7.31 (m, 13H) ppm. ^{13}C NMR (151 MHz, Chloroform-*d*): δ = 207.1 (q, J = 3.9 Hz), 141.7, 140.6, 134.3, 133.2, 129.8, 129.2, 129.07, 129.02, 128.9, 128.8, 128.6, 127.8, 127.7, 127.2, 127.19, 127.18, 123.5 (q, J = 275.3 Hz), 118.1, 104.7 (q, J = 34.2 Hz) ppm. ^{19}F NMR (565 MHz, Chloroform-*d*): δ = -59.85 ppm. HRMS (ESI) m/z : $[\text{M}]^+$ mass found: 412.1431, mass calculated for $\text{C}_{28}\text{H}_{19}\text{F}_3^+$: 412.1433. IR (KBr): 3060, 3032, 2925, 2856, 2236, 2156, 2020, 1945, 1803, 1752, 1679, 1599, 1489, 1448, 1407, 1373, 1296, 1166, 1119, 1032, 1004, 967, 927, 841, 762, 731, 693, 662 cm^{-1} .

(4,4,4-Trifluoro-1-(*m*-tolyl)buta-1,2-diene-1,3-diyl)dibenzene (32l)

Colorless oil; ^1H NMR (600 MHz, Chloroform-*d*): δ = 7.56 (d, J = 7.9 Hz, 2H), 7.44 – 7.37 (m, 7H), 7.34 (t, J = 7.4 Hz, 1H), 7.31 (t, J = 7.8 Hz, 1H), 7.25 – 7.19 (m, 3H), 2.38 (s, 3H) ppm. ^{13}C NMR (151 MHz, Chloroform-*d*): δ = 206.9 (q, J = 3.6 Hz), 138.7, 134.4, 134.2, 129.8, 129.6, 129.3, 129.0, 128.9, 128.8, 128.79, 128.74, 128.5, 127.1, 126.0, 123.5 (q, J = 275.2 Hz), 118.4, 104.4 (q, J = 34.3 Hz), 21.6 ppm. ^{19}F NMR (565 MHz, Chloroform-*d*): δ = -59.89 ppm. HRMS (ESI) m/z : $[\text{M}]^+$ mass found: 350.1275, mass calculated for $\text{C}_{23}\text{H}_{17}\text{F}_3^+$: 350.1276. IR (KBr): 3032, 2925, 2859, 2161, 2039, 1947, 1882, 1764, 1701, 1600, 1492, 1448, 1372, 1296, 1209, 1165, 1119, 1032, 999, 928, 838, 763, 694, 663 cm^{-1} .

(4,4,4-Trifluoro-1-(*o*-tolyl)buta-1,2-diene-1,3-diyl)dibenzene (32m)

White solid; ^1H NMR (600 MHz, Chloroform-*d*): δ = 7.58 (d, J = 7.8 Hz, 2H), 7.43 (t, J = 7.7 Hz, 2H), 7.40 – 7.26 (m, 10H), 2.26 (s, 3H) ppm. ^{13}C NMR (151 MHz, Chloroform-*d*): δ = 205.5 (q, J = 4.0 Hz), 137.1, 134.0, 133.7, 130.8, 130.2, 130.0, 129.1, 129.0, 128.8, 128.6, 128.5, 127.3, 126.4, 123.6 (q, J = 275.1 Hz), 116.5, 104.1 (q, J = 34.3 Hz), 20.2 ppm. Due to the overlap of aromatic carbon peaks, one carbon signal is missing. ^{19}F NMR (565 MHz, Chloroform-*d*): δ = -59.68 ppm. HRMS (ESI) m/z : $[\text{M}]^+$ mass found: 350.1276, mass calculated for $\text{C}_{23}\text{H}_{17}\text{F}_3^+$: 350.1276. IR (KBr): 3062, 3022, 2924, 2856, 2319, 2076, 1944, 1891, 1808, 1736, 1598, 1491, 1451, 1375, 1296, 1123, 1031, 999, 928, 868, 839, 804, 763, 725, 692, 661 cm^{-1} .

(4,4,4-Trifluoro-1-(2-fluorophenyl)buta-1,2-diene-1,3-diyl)dibenzene (32n)

Colorless oil; ^1H NMR (600 MHz, Chloroform-*d*): δ = 7.57 (d, J = 7.9 Hz, 2H), 7.47 – 7.33 (m, 10H), 7.21 (t, J = 7.5 Hz, 1H), 7.17 (t, J = 9.1 Hz, 1H) ppm. ^{13}C NMR (151 MHz, Chloroform-*d*): δ = 206.9 (q, J = 3.9 Hz), 160.4 (d, J = 250.4 Hz), 133.7, 131.5 (d, J = 2.6 Hz), 130.6 (d, J = 8.0 Hz), 129.4, 129.02, 129.00, 128.8, 128.7, 127.7, 127.3, 124.6 (d, J = 3.7 Hz), 123.4 (q, J = 275.0 Hz), 122.0 (d, J = 14.6 Hz), 116.4 (d, J = 21.5 Hz), 112.2, 104.4 (q, J = 34.0 Hz) ppm. ^{19}F NMR (565 MHz, Chloroform-*d*): δ = -59.95 (s, 3F), -111.58 – -111.62 (m, 1F) ppm. HRMS (ESI) m/z : $[\text{M}]^+$ mass found: 354.1026, mass calculated for

$C_{22}H_{14}F_4^+$: 354.1026. IR (KBr): 3063, 2926, 2856, 2157, 1949, 1803, 1765, 1582, 1491, 1450, 1376, 1297, 1259, 1221, 1168, 1120, 1032, 999, 929, 861, 815, 757, 662 cm^{-1} .

(1-(2-Chlorophenyl)-4,4,4-trifluorobuta-1,2-diene-1,3-diyl)dibenzene (32o)

Colorless oil; 1H NMR (600 MHz, Chloroform-*d*): δ = 7.60 (d, J = 7.8 Hz, 2H), 7.53 – 7.49 (m, 1H), 7.47 – 7.44 (m, 1H), 7.43 – 7.33 (m, 8H), 7.29 – 7.26 (m, 2H) ppm. ^{13}C NMR (151 MHz, Chloroform-*d*): δ = 206.0 (q, J = 3.7 Hz), 134.2, 133.3, 131.8, 130.3, 130.1, 129.3, 129.04, 129.01, 128.72, 128.71, 127.4, 127.3, 127.2, 123.4 (q, J = 275.1 Hz), 115.5, 105.0 (q, J = 34.3 Hz) ppm. Due to the overlap of aromatic carbon peaks, one carbon signal is missing. ^{19}F NMR (565 MHz, Chloroform-*d*): δ = -59.77 ppm. HRMS (ESI) m/z : $[M]^+$ mass found: 370.0730, mass calculated for $C_{22}H_{14}ClF_3^+$: 370.0730. IR (KBr): 3063, 2926, 2161, 2035, 1950, 1805, 1738, 1597, 1493, 1445, 1376, 1297, 1168, 1120, 1054, 1034, 929, 866, 838, 756, 728, 690, 662 cm^{-1} .

2-(4,4,4-Trifluoro-1,3-diphenylbuta-1,2-dien-1-yl)naphthalene (32p)

Colorless oil; 1H NMR (600 MHz, Chloroform-*d*): δ = 7.90 – 7.85 (m, 2H), 7.85 – 7.79 (m, 2H), 7.60 (d, J = 7.8 Hz, 2H), 7.55 (dd, J = 8.6, 1.8 Hz, 1H), 7.54 – 7.47 (m, 4H), 7.47 – 7.38 (m, 5H), 7.36 (t, J = 7.3 Hz, 1H) ppm. ^{13}C NMR (151 MHz, Chloroform-*d*): δ = 207.4 (q, J = 3.9 Hz), 134.4, 133.5, 133.4, 131.7, 129.8, 129.1, 129.0, 128.9, 128.8, 128.7, 128.6, 128.4, 128.1, 127.9, 127.2, 126.8, 126.7, 126.3, 123.5 (d, J = 275.2 Hz), 118.5, 104.7 (q, J = 34.3 Hz) ppm. ^{19}F NMR (565 MHz, Chloroform-*d*): δ = -59.83 ppm. HRMS (ESI) m/z : $[M]^+$ mass found: 386.1276, mass calculated for $C_{26}H_{17}F_3^+$: 386.1276. IR (KBr): 3059, 2924, 2854, 2318, 2074, 1944, 1760, 1598, 1495, 1447, 1378, 1296, 1237, 1167, 1120, 1030, 1000, 963, 928, 859, 816, 748, 694 cm^{-1} .

1-(4,4,4-Trifluoro-1,3-diphenylbuta-1,2-dien-1-yl)naphthalene (32q)

White solid; 1H NMR (600 MHz, Chloroform-*d*): δ = 7.95 – 7.87 (m, 3H), 7.60 (d, J = 7.0 Hz, 1H), 7.58 – 7.54 (m, 3H), 7.50 (t, J = 7.5 Hz, 1H), 7.44 – 7.35 (m, 3H), 7.35 – 7.25 (m, 6H) ppm. ^{13}C NMR (151 MHz, Chloroform-*d*): δ = 206.2 (q, J = 3.6 Hz), 134.4, 134.0, 131.9, 131.7, 129.8, 129.3, 129.04, 129.02, 128.65, 128.60, 128.5, 127.9, 127.4, 127.3, 126.6, 126.3, 126.1, 125.7, 123.5 (q, J = 275.2 Hz), 115.7, 104.2 (q, J = 34.2 Hz) ppm. ^{19}F NMR (565 MHz, Chloroform-*d*): δ = -59.72 ppm. HRMS (ESI) m/z : $[M]^+$ mass found: 386.1275, mass calculated for $C_{26}H_{17}F_3^+$: 386.1276. IR (KBr): 3347, 3058, 2923, 2854, 2667, 2318, 2079, 1937, 1815, 1732, 1592, 1493, 1446, 1394, 1369, 1338, 1292, 1252, 1206, 1163, 1123, 1028, 970, 926, 863, 797, 770, 694 cm^{-1} .

2-(4,4,4-Trifluoro-1,3-diphenylbuta-1,2-dien-1-yl)thiophene (32r)

White solid; 1H NMR (600 MHz, Chloroform-*d*): δ = 7.60 – 7.50 (m, 4H), 7.46 – 7.31 (m, 7H), 7.14 – 7.04 (m, 2H) ppm. ^{13}C NMR (151 MHz, Chloroform-*d*): δ = 206.9 (q, J = 3.9 Hz), 136.7, 134.1, 129.6, 129.1, 129.0, 128.9, 128.7, 128.6, 127.94, 127.92, 127.4, 127.0, 123.1 (q, J = 275.5 Hz), 113.1, 104.7 (q, J = 34.5 Hz) ppm. ^{19}F NMR (565 MHz, Chloroform-*d*): δ = -60.12 ppm. HRMS (ESI) m/z : $[M]^+$ mass found: 342.0680, mass calculated for $C_{20}H_{13}F_3S^+$: 342.0684. IR (KBr): 3064, 3032, 2926, 2674, 2325, 2089, 1884, 1803, 1702, 1598, 1530, 1493, 1446, 1379, 1295, 1260, 1228, 1166, 1121, 1033, 998, 927, 834, 761, 694, 663 cm^{-1} .

5-(3,3,3-Trifluoro-2-phenylprop-1-en-1-ylidene)-10,11-dihydro-5H-dibenzo[*a,d*][7]annulene (32s)

Colorless oil; ^1H NMR (600 MHz, Chloroform-*d*): δ = 7.49 (d, J = 7.8 Hz, 2H), 7.43 (d, J = 7.4 Hz, 2H), 7.37 (t, J = 7.6 Hz, 2H), 7.30 (t, J = 7.2 Hz, 1H), 7.26 (t, J = 7.1 Hz, 2H), 7.21 – 7.19 (m, 4H), 3.35 – 3.30 (m, 2H), 3.17 – 3.11 (m, 2H) ppm. ^{13}C NMR (151 MHz, Chloroform-*d*): δ = 207.5 (q, J = 4.1 Hz), 139.5, 133.9, 130.0, 129.8, 129.2, 128.9, 128.8, 128.4, 127.2, 126.7, 123.8 (q, J = 275.1 Hz), 119.1, 102.6 (q, J = 34.0 Hz), 33.5 ppm. ^{19}F NMR (565 MHz, Chloroform-*d*): δ = -59.87 ppm. HRMS (ESI) m/z : $[\text{M}]^+$ mass found: 362.1277, mass calculated for $\text{C}_{24}\text{H}_{17}\text{F}_3^+$: 362.1276. IR (KBr): 3069, 3022, 2922, 2855, 2325, 2086, 1945, 1807, 1732, 1599, 1488, 1447, 1369, 1300, 1185, 1159, 1116, 1035, 928, 892, 836, 806, 752, 717, 691, 663 cm^{-1} .

5-(3,3,3-Trifluoro-2-phenylprop-1-en-1-ylidene)-5H-dibenzo[*a,d*][7]annulene (32t)

White solid; ^1H NMR (600 MHz, Chloroform-*d*): δ = 7.49 (d, J = 7.0 Hz, 2H), 7.42 (d, J = 7.5 Hz, 2H), 7.40 – 7.31 (m, 8H), 7.28 (d, J = 7.2 Hz, 1H), 6.89 (s, 2H) ppm. ^{13}C NMR (151 MHz, Chloroform-*d*): δ = 207.3 (q, J = 4.2 Hz), 134.8, 133.6, 131.2, 129.7, 129.5, 129.3, 128.86, 128.85, 128.6, 128.3, 127.2, 124.0 (q, J = 275.0 Hz), 118.5, 102.1 (q, J = 33.9 Hz) ppm. ^{19}F NMR (565 MHz, Chloroform-*d*): δ = -59.89 ppm. HRMS (ESI) m/z : $[\text{M}]^+$ mass found: 360.1122, mass calculated for $\text{C}_{24}\text{H}_{15}\text{F}_3^+$: 360.1120. IR (KBr): 3063, 3026, 2926, 2859, 2162, 2037, 1949, 1720, 1597, 1490, 1435, 1374, 1297, 1227, 1163, 1121, 1039, 973, 929, 878, 849, 798, 765, 742, 691, 665 cm^{-1} .

(4,4,4-Trifluoro-3-(*p*-tolyl)buta-1,2-diene-1,1-diyl)dibenzene (32u)

Colorless oil; ^1H NMR (600 MHz, Chloroform-*d*): δ = 7.43 (d, J = 8.0 Hz, 2H), 7.41 – 7.36 (m, 10H), 7.20 (d, J = 8.1 Hz, 2H), 2.37 (s, 3H) ppm. ^{13}C NMR (151 MHz, Chloroform-*d*): δ = 206.7 (q, J = 4.0 Hz), 138.6, 134.4, 129.7, 128.9, 128.8, 128.7, 127.0, 126.7, 123.5 (q, J = 275.3 Hz), 118.1, 104.5 (q, J = 34.3 Hz), 21.3 ppm. ^{19}F NMR (565 MHz, Chloroform-*d*): δ = -60.02 ppm. HRMS (ESI) m/z : $[\text{M}]^+$ mass found: 350.1276, mass calculated for $\text{C}_{23}\text{H}_{17}\text{F}_3^+$: 350.1276. IR (KBr): 3335, 3059, 3031, 2923, 2855, 2221, 2038, 1948, 1901, 1805, 1736, 1656, 1599, 1513, 1492, 1449, 1373, 1296, 1166, 1118, 1029, 927, 818, 767, 743, 694 cm^{-1} .

(4,4,4-Trifluoro-3-(4-fluorophenyl)buta-1,2-diene-1,1-diyl)dibenzene (32v)

White solid; ^1H NMR (600 MHz, Chloroform-*d*): δ = 7.51 (dd, J = 8.0, 5.5 Hz, 2H), 7.43 – 7.38 (m, 10H), 7.09 (t, J = 8.7 Hz, 2H) ppm. ^{13}C NMR (151 MHz, Chloroform-*d*): δ = 206.7 (q, J = 3.7 Hz), 162.8 (d, J = 248.9 Hz), 134.2, 129.0 (d, J = 7.5 Hz), 128.99, 128.90, 128.7, 125.8 (d, J = 3.6 Hz), 118.5, 116.1 (d, J = 21.8 Hz), 103.7 (q, J = 34.7 Hz) ppm. Due to the overlap of aromatic carbon peaks, one carbon signal is missing. ^{19}F NMR (565 MHz, Chloroform-*d*): δ = -60.23 (s, 3F), -112.80 – -112.85 (m, 1F) ppm. HRMS (ESI) m/z : $[\text{M}]^+$ mass found: 354.1028, mass calculated for $\text{C}_{22}\text{H}_{14}\text{F}_4^+$: 354.1026. IR (KBr): 3065, 2925, 2856, 2325, 1892, 1764, 1734, 1649, 1601, 1508, 1449, 1368, 1292, 1236, 1171, 1123, 1025, 998, 967, 927, 835, 770, 744, 694, 663 cm^{-1} .

(3-(4-Chlorophenyl)-4,4,4-trifluorobuta-1,2-diene-1,1-diyl)dibenzene (32w)

Colorless oil; ^1H NMR (600 MHz, Chloroform-*d*): δ = 7.46 (d, J = 8.2 Hz, 2H), 7.43 – 7.34 (m, 12H) ppm. ^{13}C NMR (151 MHz, Chloroform-*d*): δ = 206.9 (q, J = 3.8 Hz), 134.6, 134.0, 129.2, 129.0, 128.9, 128.7, 128.4, 128.3, 123.2 (q, J = 275.1 Hz), 118.7, 103.7 (q, J = 34.7 Hz) ppm. ^{19}F NMR (565 MHz, Chloroform-*d*): δ = -60.10 ppm. HRMS (ESI) m/z : $[\text{M}]^+$ mass found: 370.0725, mass calculated for $\text{C}_{22}\text{H}_{14}\text{ClF}_3^+$:

370.0730. IR (KBr): 3061, 2926, 2857, 2185, 1948, 1897, 1765, 1710, 1596, 1492, 1450, 1369, 1296, 1170, 1120, 1015, 966, 927, 902, 828, 766, 695 cm⁻¹.

General procedure of TfOH-catalyzed Friedel-Crafts alkylation of allene

To a suspension of trifluoromethylated allene **32b** (72.8 mg, 0.2 mmol) in CH₂Cl₂ (2.0 mL) was added TfOH (18 μL, 0.15 mmol) at room temperature. The resulting mixture was stirred at room temperature for 2 h. Then the mixture was poured into ice water (20 mL) and extracted with CH₂Cl₂. The combined organic layers were washed with saturated NaHCO₃ (aq.), dried over MgSO₄ and concentrated in vacuo. The residue was purified by column chromatography using *n*-hexane as eluent to afford the 1*H*-indene **33** (71 mg, 97% yield).

6-Methyl-1-phenyl-3-(*p*-tolyl)-1-(trifluoromethyl)-1*H*-indene (33**)**

Colorless oil; ¹H NMR (400 MHz, Chloroform-*d*): δ = 7.57 (d, *J* = 8.1 Hz, 2H), 7.54 (d, *J* = 8.1 Hz, 2H), 7.47 (d, *J* = 7.8 Hz, 2H), 7.38 – 7.31 (m, 3H), 7.29 (d, *J* = 7.8 Hz, 2H), 7.24 (d, *J* = 7.9 Hz, 1H), 6.58 (s, 1H), 2.45 (s, 3H), 2.43 (s, 3H) ppm. ¹³C NMR (101 MHz, Chloroform-*d*): δ = 147.1, 144.3, 141.0, 138.5, 136.6, 135.0, 131.6, 130.7, 129.5, 129.3, 128.7, 128.0, 127.9, 127.7, 126.8 (q, *J* = 282.6 Hz), 126.6, 121.4, 64.0 (q, *J* = 26.7 Hz), 21.7, 21.4 ppm. ¹⁹F NMR (376 MHz, Chloroform-*d*): δ = -67.38 ppm. HRMS (ESI) *m/z*: [M]⁺ mass found: 364.1434, mass calculated for C₂₄H₁₉F₃⁺: 364.1433. IR (KBr): 3030, 2923, 2865, 1902, 1803, 1607, 1505, 1449, 1380, 1346, 1246, 1151, 1068, 1037, 975, 939, 889, 809, 758, 718, 695, 663 cm⁻¹.

General procedure of Yb(OTf)₃-catalyzed Friedel-Crafts alkylation of allene

To a test tube were successively added **32b** (72.8 mg, 0.2 mmol), Yb(OTf)₃ (6.2 mg, 5 mol%) and CH₃NO₂ (2.0 mL). The resulting mixture was stirred in a pre-heated oil bath at 80 °C for 12 h. On completion, the reaction mixture was concentrated in vacuo and the product was directly purified by column chromatography using *n*-hexane as eluent to afford the **33** (55 mg, 75% yield) and **34** (14 mg, 19% yield).

1,1-Di-*p*-tolyl-3-(trifluoromethyl)-1*H*-indene (34**)**

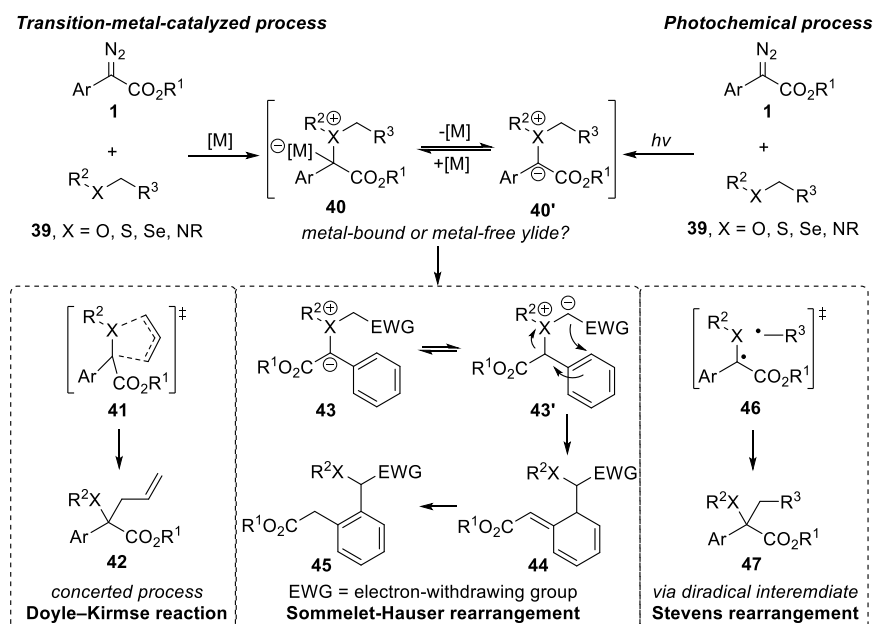
Colorless oil; ¹H NMR (600 MHz, Chloroform-*d*): δ = 7.49 (d, *J* = 7.5 Hz, 1H), 7.39 – 7.31 (m, 2H), 7.28 (t, *J* = 7.4 Hz, 1H), 7.18 (s, 1H), 7.07 (s, 8H), 2.31 (s, 6H) ppm. ¹³C NMR (151 MHz, Chloroform-*d*): δ = 150.6, 146.2 (q, *J* = 5.0 Hz), 138.7, 137.2, 137.1, 132.2 (q, *J* = 34.3 Hz), 129.4, 127.7, 127.6, 127.1, 125.7, 124.2 (q, *J* = 270.1 Hz), 121.6, 65.6, 21.1 ppm. ¹⁹F NMR (565 MHz, Chloroform-*d*): δ = -63.91 ppm. HRMS (APCI) *m/z*: [M + H]⁺ mass found: 365.1511, mass calculated for C₂₄H₂₀F₃⁺: 365.1508. IR (KBr): 3025, 2924, 2866, 2164, 2027, 1907, 1736, 1628, 1580, 1508, 1461, 1377, 1312, 1288, 1267, 1211, 1169, 1121, 1023, 979, 919, 851, 813, 767, 743, 663 cm⁻¹.

2.4 Mechanism Study of Rh-catalyzed Sigmatropic Rearrangement with Triazoles

2.4.1 Brief Introduction: Carbene-mediated Sigmatropic Rearrangement

Transition-metal-catalyzed ylide-formation/sigmatropic rearrangement reactions constitute an important methodology for the construction of C–heteroatom bonds or quaternary carbon centers.^{85–88} The key ylide intermediates are generated through the reaction of an electrophilic metal carbene complex with nucleophilic species, such as ethers, amines, thioethers, selenides and others (Scheme 32). Similarly, latest developments in photoinduced carbene transfer reactions have further extended this research area to realize sigmatropic rearrangement reactions in metal-free fashion, such as Doyle–Kirmse reaction,^{108,111} Stevens rearrangement²²⁶ and Sommelet–Hauser rearrangement.¹¹⁰

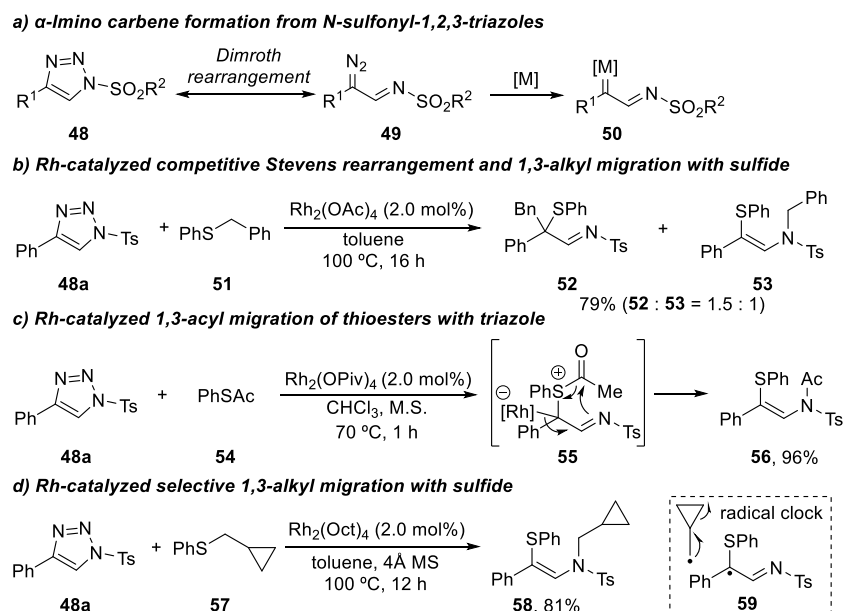
Despite these advances, two open questions of mechanism in the sigmatropic rearrangement still remained. One is if these reactions proceed via a metal-bound ylide intermediate or a free ylide intermediate; another one is if this rearrangement process is concerted process or a stepwise reaction involved diradical intermediate. Recently, the Tantillo group proposed that the metal-bound ylide or a free ylide in the [2,3]-sigmatropic rearrangement was strongly dependent on the metal catalyst used, the substituents attached to the carbene carbon and the type of onium ylide through computational investigations.⁹¹ Furthermore, a concerted electrocyclic mechanism for a [2,3]-sigmatropic rearrangement is stereoelectronically feasible, while orbital symmetry unfavored [1,2]-sigmatropic rearrangement proceed by means of diradical intermediates.



Scheme 32: Carbene-mediated sigmatropic rearrangements and possible mechanism

Besides diazo compounds, *N*-sulfonyl-1,2,3-triazoles **48** represent a safe precursor for the formation of metal-bound imino carbene intermediates, which can undergo a variety of synthetically useful carbene transformations (Scheme 33a).^{33,34} Interestingly, ylide formation

from α -imino carbene **50** with nucleophilic species **39** opens up different rearrangement modes. In 2013, Anbarasan and coworkers found that similar [2,3]-sigmatropic rearrangement (Doyle–Kirmse reaction) could be accessed with *N*-sulfonyl-1,2,3-triazoles and allylphenyl sulfides. However, when benzyl sulfide **51** was applied in such a reaction, an inseparable mixture of 1,3-alkyl migration product and [1,2]-sigmatropic rearrangement product could be observed (Scheme 33b).²²⁷ Recently, Murakami and coworkers reported on a 1,3-difunctionalization of α -imino carbene **50** with thioesters **54**, which produces β -sulfanyl enamides **56** through a 1,3-acyl migration of sulfur ylide intermediate **55** (Scheme 33c).²²⁸ Based on the previous results, our group tried to understand this 1,3-difunctionalization or competitive [1,2]-sigmatropic rearrangement by studying the reactivity of cyclopropylmethyl thioether **57** (Scheme 33d).²²⁹ Actually, a highly selective formation of enamine homologation product **58** was observed without any byproducts that arise from the [1,2]-sigmatropic rearrangement process via potential radical clock reaction of **59**.



Scheme 33: Stevens rearrangement vs. 1,3-acyl or alkyl migration with triazole as carbene precursor

2.4.2 Computational Study

To investigate the reaction mechanism of this 1,3-difunctionalization of α -imino carbene, we studied the reaction by DFT calculations at the B3LYP/6-311+G(d,p)/LANL2DZ//B3LYP/6-31G(d)/LANL2DZ level, in which triazole **48a**, cyclopropylmethyl sulfide **57**, and simple $\text{Rh}_2(\text{OAc})_4$ catalyst were used as computational model ($\text{Rh}_2(\text{OAc})_4$ leads to **58** in 76% yield).²²⁹ The calculations reveal that the formation of diazoimine intermediate **49a** was preceded by Dimroth rearrangement of *N*-sulfonyl-1,2,3-triazole **48a** with an activation free energy of 17.6 kcal/mol. Further trapping of **49a** with $\text{Rh}_2(\text{OAc})_4$ afforded the corresponding α -imino carbene **50a** via **TS2** with a totally high energy barrier of 25.3 kcal/mol, which rationalized the high reaction temperatures required in this transformation (Figure 11).

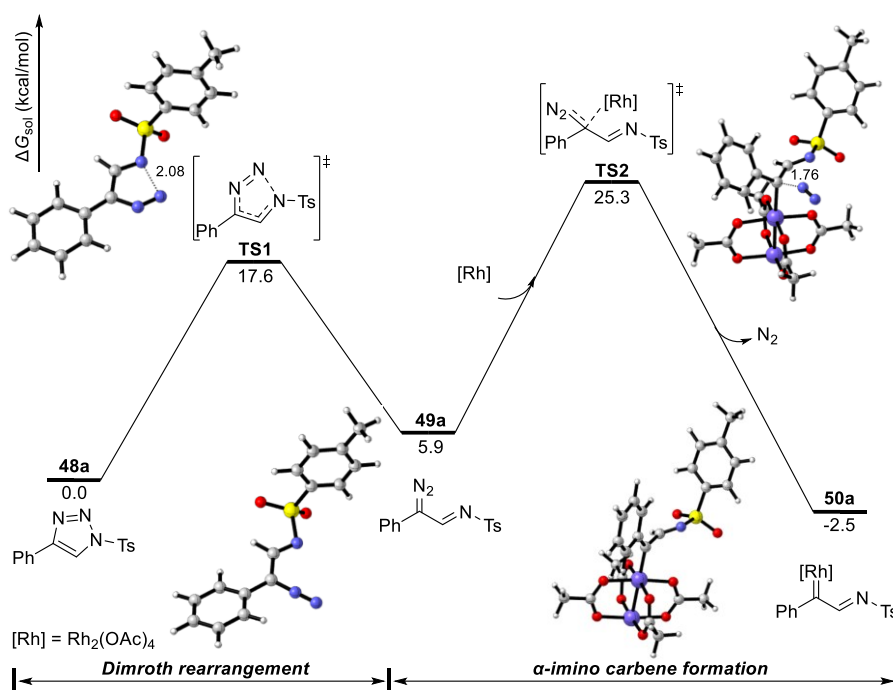


Figure 11: Potential energy surface of Rh-catalyzed α -imino carbene formation with triazole

Subsequent nucleophilic addition of cyclopropylmethyl sulfide **57** with **50a** led to a metal-bound ylide intermediate **INT1**, which was reversible and needs an activation free energy of 18.3 kcal/mol (Figure 12). This intermediate could directly undergo a 1,3-alkyl migration process via transition state **TS5**, which required a high activation free energy of in total 33.4 kcal/mol to give a side-on coordinated enamine complex **INT3**. Alternatively, an exergonic demetalation led to free ylide intermediate **INT2**, which underwent a low-energy-barrier 1,3-alkyl migration via **TS4** ($\Delta G^\ddagger = 13.0$ kcal/mol) and directly gave reaction product **58**. Current calculations indicated that this enamine homologation reaction presumably proceeded via a concerted pathway from metal-free ylide intermediate.

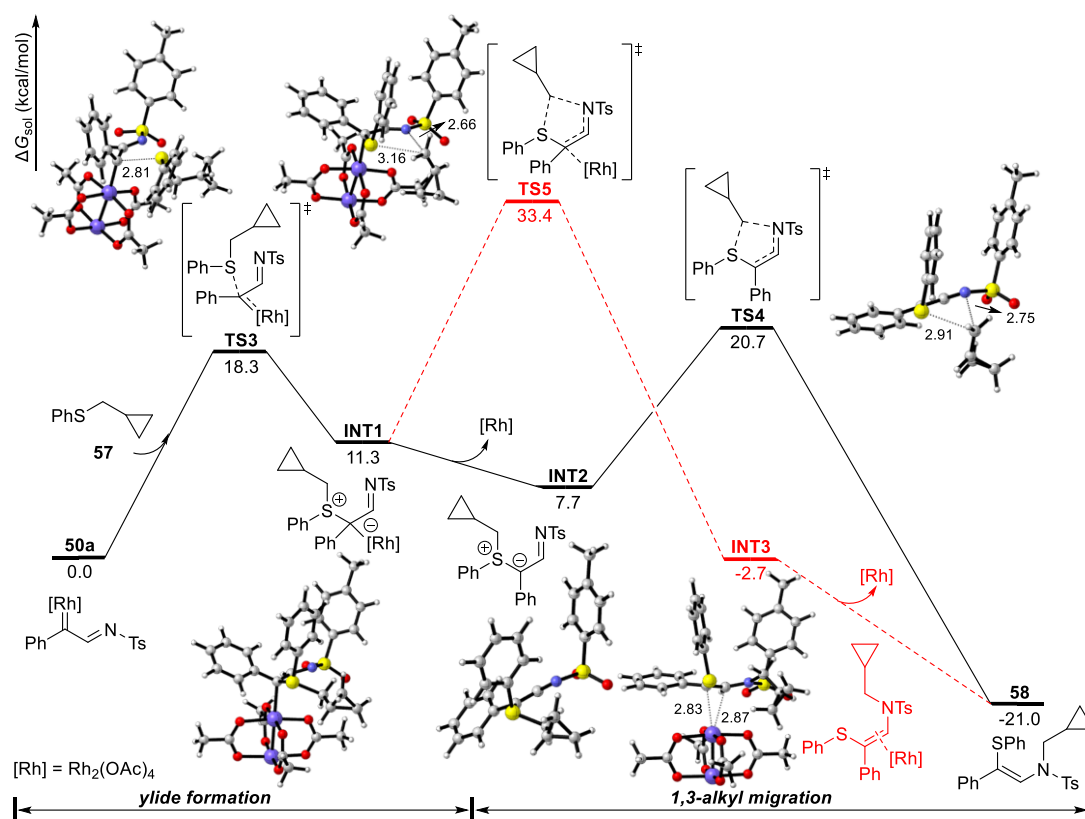
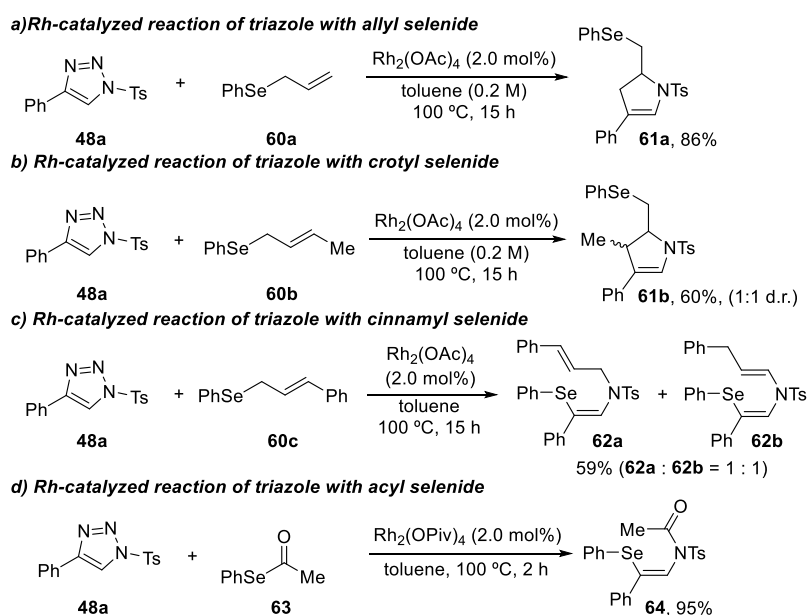


Figure 12: Potential energy surface of 1,3-alkyl migration of sulfur ylides

After the identification of this concerted 1,3-alkyl migration mechanism with sulfur ylides, our group became intrigued in studying the reaction of triazoles with organoselenium compounds.²³⁰⁻²³² To our delight, the increased nucleophilicity and basicity of selenides led to unexpected reactivities with triazoles in presence of Rh(II) catalysts (Scheme 34).²³³ When using the allyl selenide **60a** as the substrate, a formal [3 + 2] cycloaddition reaction occurred

*Experimental work was performed by Fang Li.



Scheme 34: Rh-catalyzed reactions of triazole with different selenides

and gave the dihydropyrrole product **61a** in 86% yield (Scheme 34a). However, further investigation of crotyl selenide **60b** with triazole resulted in the sole formation of dihydropyrrole **61b** with 1:1 diastereoselective ratio, which ruled out a concerted [3 + 2] cycloaddition mechanism (Scheme 34b). However, cinnamyl selenide **60c** exhibited a quite different reactivity, in which a formal 1,3-cinnamyl migration occurred and led to a mixture product of **62a** and **62b** in 1:1 ratio (Scheme 34c). Furthermore, similar 1,3-acyl migration reactions were realized in excellent yield when acyl selenide **63** was applied in the reaction with triazoles (Scheme 34d).²³⁴

To rationalize for the divergent reactivities of selenides with triazoles, we performed detailed computational studies at 373.15 K at B3LYP-D3/def2-tzvp/SMD(toluene)//B3LYP-D3/def2-SVP/SMD(toluene) level of theory, in which triazole **48a**, allyl selenide **60a**, and Rh₂(OAc)₄ catalyst were used as calculation model (Figure 13). Similarly, we first started our calculation with selenium ylide formation, which required an activation free energy of 9.1 kcal/mol via transition state **TS6**. Subsequent [2,3]-sigmatropic rearrangement from **INT4** through **TS7** led to **65a** with an energy barrier of 13.3 kcal/mol. However, dissociation of the rhodium complex and formation of the free ylide intermediate **INT5** was exergonic by 5.4 kcal/mol, which could undergo a more feasible metal-free [2,3]-sigmatropic rearrangement via **TS8** with an activation free energy of 11.5 kcal/mol. In this case, we took potential aza-Cope rearrangement of **65a** into account, which is an unlikely process due to the kinetic and thermodynamic reasons (**TS9**, $\Delta G^\ddagger = 33.3$ kcal/mol, $\Delta G_R = 3.2$ kcal/mol).

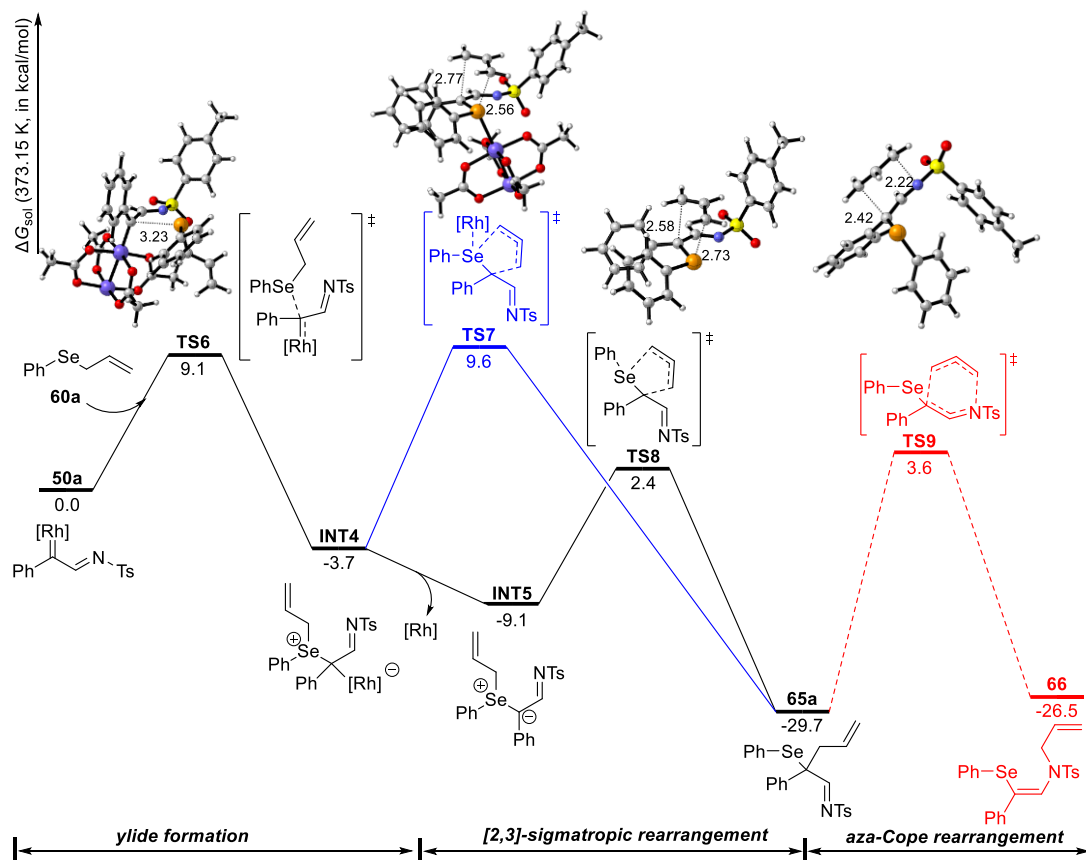
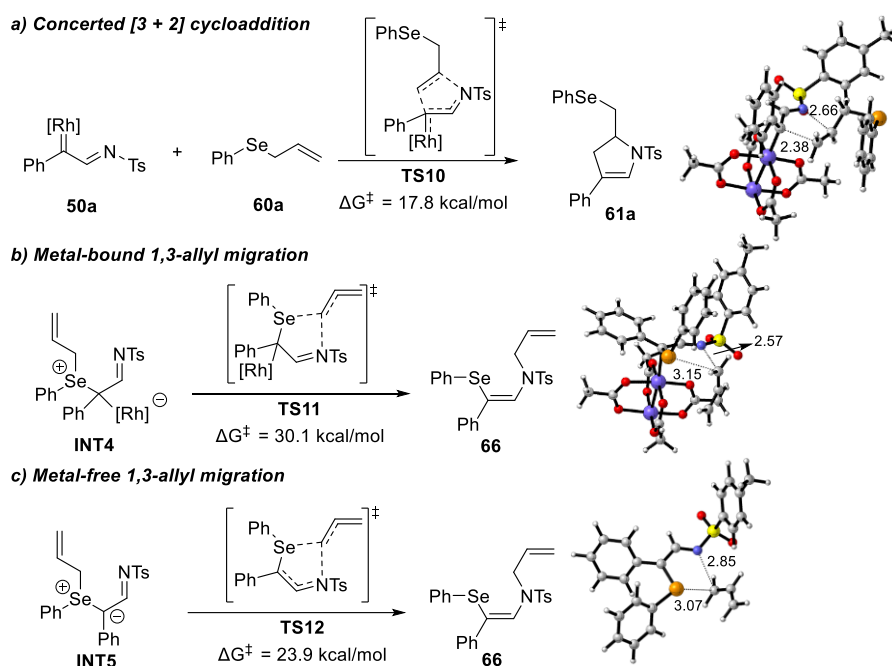


Figure 13: Potential energy surfaces of Rh-catalyzed reactions of triazole with allyl selenide

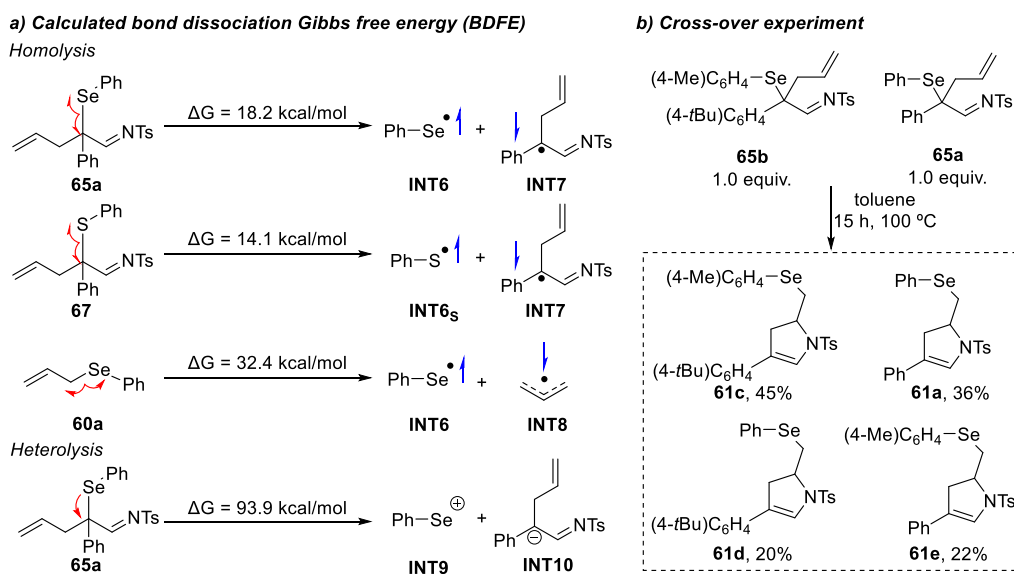
Furthermore, we also considered a concerted [3 + 2] cycloaddition mechanism to account for the formation of dihydropyrrole product **61a**. However, this cycloaddition step via **TS10** had a higher activation energy of 17.8 kcal/mol, which was unfavorable compared to irreversible rearrangement process (Scheme 35a). Indeed, metal-bound or metal-free 1,3-allyl migration of selenium ylides are energetically disfavored for the higher energy barrier of 30.1 and 23.9 kcal/mol via **TS11** or **TS12**, respectively (Scheme 35b, c).



Scheme 35: Calculations of possible competitive pathways

Until this point, we just identified the formation of [2,3]-sigmatropic rearrangement product **65a**, which could be isolated in a short reaction time. We thus turned to study the properties of intermediate **65a** experimentally and computationally, which might transfer to final

**Cross-over experiment was done by Fang Li.*

Scheme 36: Experimental and computational studies of **65**

dihydropyrrole product **61a** (Scheme 36).²³³ Actually, homolysis of **65a** was significantly favored than heterolysis under thermal condition according to the analysis of bond dissociation Gibbs free energy (BDFE, 18.2 kcal/mol vs. 93.9 kcal/mol). Further control experiments that were performed by my colleague have identified the existence of selenyl radical intermediates by trapping this radical with TEMPO. Meanwhile, four dihydropyrrole products (**61a**, **c**, **d** and **e**) could be obtained under thermal condition in the cross-over experiment involving two different rearrangement products **65a** and **65b** (Scheme 36b). This observation was supportive of the potential arylselenium radical transfer mechanism.

Based on the control experiments, we next studied the further radical-mediated cascade steps from **65a** (Figure 14). We could identify a radical addition of selenyl radical onto the terminal carbon of double bond, giving a secondary alkyl radical **INT11** via **TS13** with an activation energy of 7.6 kcal/mol. Subsequent radical cyclization via **TS14** furnished the dihydropyrrole product with a total energy barrier of 19.5 kcal/mol, and cleavage of C-Se simultaneously occurred to regenerated new selenyl radical for further reaction cycle. Instead, an alternative pathway suggested the direct cyclization of an enamine radical **INT7** via relatively high-lying **TS15** ($\Delta G^\ddagger = 25.6$ kcal/mol), which was thus not feasible. In contrast to selenide **65a**, we also considered the radical cyclization of sulfide **67** with sulfur radical. However, this sulfur radical-mediated cascade cyclization was energetically disfavored and required a total activation free energy of 26.6 kcal/mol, which was consistent with the previous experimental results.²²⁷

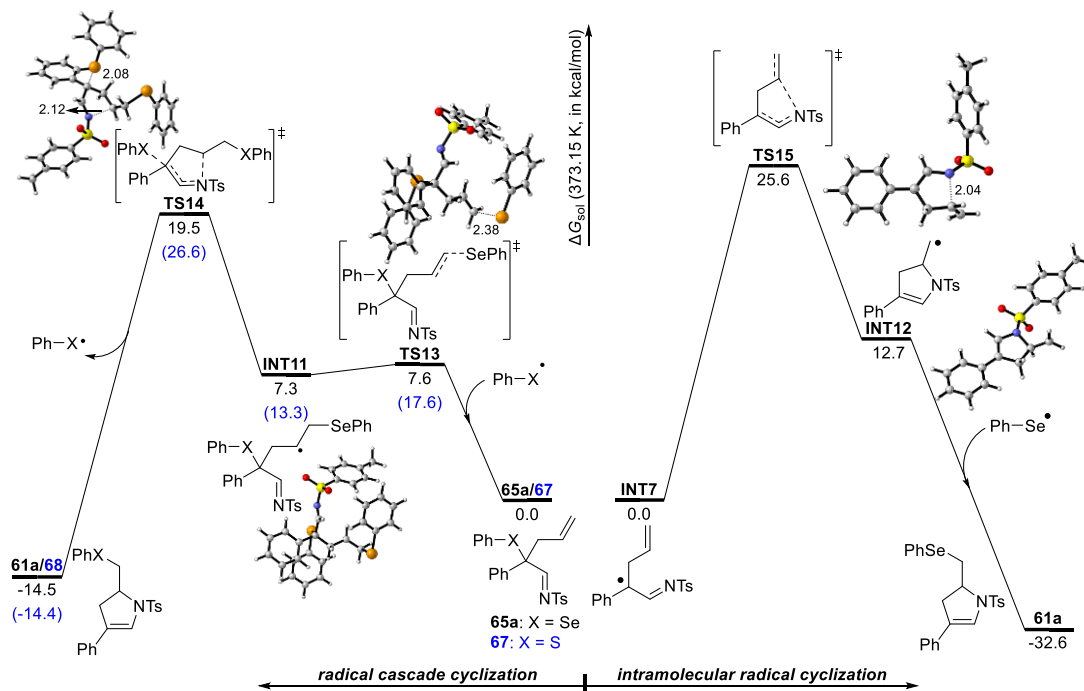


Figure 14: Potential energy surfaces of radical-mediated cyclization

Due to the observation of 1,3-difunctionalization product in the reaction with cinnamyl selenide in Scheme 34c, we revisited it with computational studies (Figure 15). Calculations indicated that the [2,3]-sigmatropic rearrangement process via **TS16** was favored by 9.7

kcal/mol compared to direct 1,3-cinnamyl migration via **TS18**. This rearrangement product **65c** could undergo a facile aza-Cope rearrangement via **TS17** to give the observed reaction product with an energy barrier of 18.5 kcal/mol, which was much lower than that of allyl selenide (**TS9**, Figure 13). This considerable energy difference could be reasoned by the stabilization of the transition state through π - π stacking interaction of the migrating cinnamyl group with the phenyl ring. In addition, the re-conjugation of phenyl ring with double bond in former cinnamyl group was another possible motivation to promote this aza-Cope rearrangement.

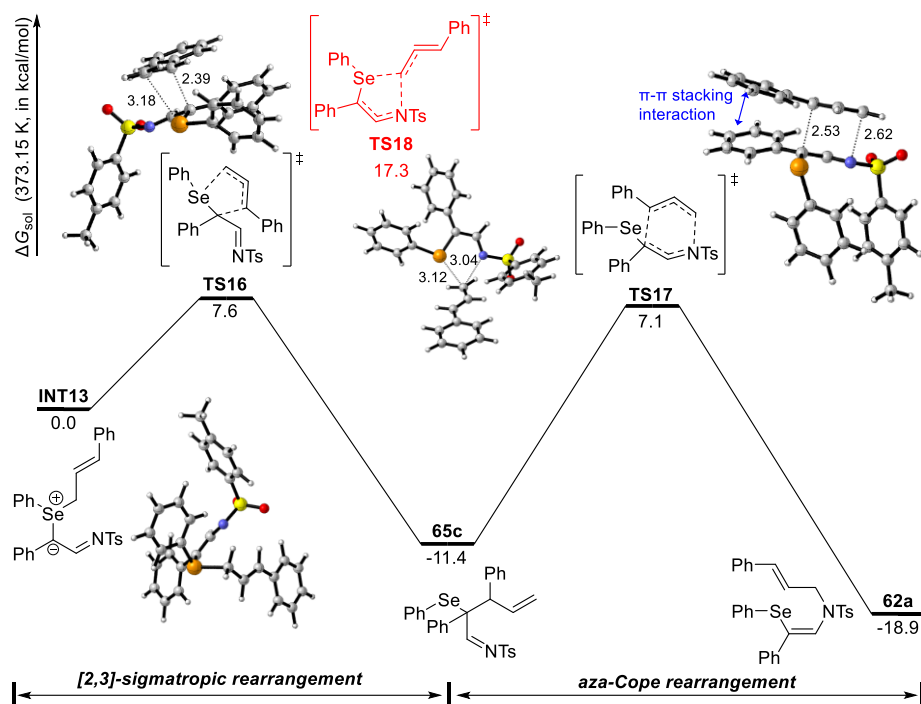


Figure 15: Potential energy surfaces of rearrangement of triazole with cinnamyl selenide

Besides the calculations of reaction with allyl selenide, we also performed detailed theoretical studies on the highly efficient 1,3-difunctionalization of α -imino carbene with acyl selenides at the same computational level of theory (Figure 16). The calculations revealed a facile nucleophilic addition of the acyl selenide with α -imino carbene **50a** via **TS19** with a low energy barrier of 9.6 kcal/mol, which directly gave the Rh-bound product **64**-[Rh] without formation of metal-bound ylide. Final dissociation step of **64**-[Rh] regenerated the catalyst for further catalytic cycle and releases the product **64**. When probing a hypothetical metal-free ylide intermediate **INT14**, calculations suggested a 1,3-acyl migration with an activation free energy of only 2.4 kcal/mol, which supported this facile concerted asynchronous acyl migration in metal-bound process.

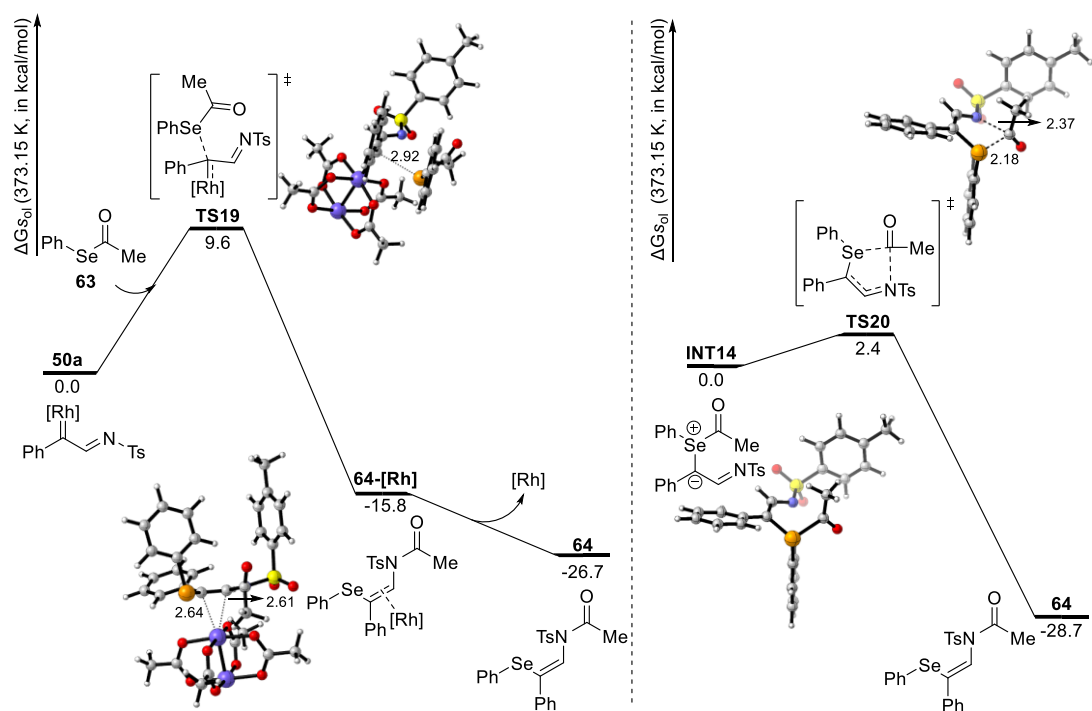


Figure 16: Potential energy surfaces of Rh-catalyzed reactions of triazole with acyl selenide

2.4.3 Computational Data

Computational Details of reaction of triazole with cyclopropylmethyl sulfide

All the calculations were performed with Gaussian 16 program.¹⁸³ DFT method Geometry optimizations of all the minima and transition states involved were carried out at the B3LYP level of theory^{204,205} in the gas phase. The LANL2DZ basis set¹⁸⁶ and pseudopotential were used for Rh and S, and the 6-31G(d) basis set¹⁸⁷⁻¹⁸⁹ for the other atoms. Harmonic vibrational frequency calculations at the same level were performed for all of the stationary points to confirm them as a local minima or transition structures. Key transition-state structures were confirmed to connect corresponding reactants and products by intrinsic reaction coordinate (IRC) calculations.^{192,193} Solvation energies in toluene ($\epsilon = 2.3741$) were evaluated by IEFPCM calculations with radii and non-electrostatic terms for SMD solvation model²⁰⁸ using the gas-phase optimized structures. Standard state concentrations of 1.0 mol/L were used for all species in calculations. Furthermore, to improve the calculation accuracy, single-point energies calculations were computed at the B3LYP level with the LANL2DZ basis set and pseudopotential for Rh and S, and the 6-311+G(d,p) basis set^{210,211} for the other atoms. The given Gibbs free energies in toluene were calculated according to the formula: $G_{sol} = TCG + \Delta G_{sol} + SPE + 1.89 \text{ kcal/mol}$. The CYL View software was employed to show the 3D structures of the studied species.¹⁹⁵

Thermal correction to Gibbs free energies (**TCG**, in Hartree), sum of electronic and thermal free energies (**G**, in Hartree), sum of electronic and thermal enthalpies (**H**, in Hartree), solvation Gibbs free energies in chloroform (ΔG_{sol} , in Hartree), and single point energies computed at the B3LYP/6-311+G(d,p)/LANL2DZ level (**SPE**, in Hartree) are shown in Table 4.

Table 4: Computed Energies of all Stationary Points

name	TCG/a.u.	G/a.u.	H/a.u.	ΔG_{sol} /a.u.	SPE/a.u.
48a	0.204524	-903.774700	-903.703856	-0.020692	-904.219270
TS1	0.202079	-903.747056	-903.676201	-0.018697	-904.190811
49a	0.201650	-903.762940	-903.690137	-0.018679	-904.208983
Rh₂(OAc)₄	0.157186	-1132.956085	-1132.87918	-0.017349	-1133.398155
TS2	0.381021	-2036.693589	-2036.567098	-0.027467	-2037.603955
50a	0.376550	-1927.204959	-1927.083314	-0.032534	-1928.075094
N₂	-0.012851	-109.536980	-109.515225	0.005594	-109.559421
57	0.153636	-398.193561	-398.142702	-0.014444	-398.459483
TS3	0.555486	-2325.373813	-2325.225714	-0.039707	-2326.534969
INT1	0.557412	-2325.379898	-2325.231942	-0.041346	-2326.546327
INT2	0.373675	-1192.421315	-1192.325536	-0.03464	-1193.119837
TS4	0.370585	-1192.401864	-1192.306012	-0.032104	-1193.098558
58	0.375183	-1192.474362	-1192.379169	-0.031039	-1193.170658
TS5	0.552247	-2325.340938	-2325.190897	-0.043992	-2326.503385
INT3	0.557078	-2325.408237	-2325.258518	-0.039589	-2326.570149

Computational Details of reaction of triazole with selenides

All the calculations were performed with the Gaussian 16 program.¹⁸³ The (U)B3LYP functional^{1204,205} together with Grimme's dispersion correction²⁰⁹ (denoted (U)B3LYP-D3) and the def2-SVP basis set²³⁵ were applied for the optimization of all stationary points at 373.15 K in the toluene, in which the solvent effects ($\epsilon = 2.3741$) were evaluated by SMD solvation model.²⁰⁸ Harmonic vibrational frequency calculations at the same level were performed for all of the stationary points to confirm them as a local minima or transition state structures. Key transition-state structures were confirmed to connect corresponding reactants and products by intrinsic reaction coordinate (IRC) calculations.^{192,193} To improve the calculation accuracy, single point energy calculations using larger def2-TZVP basis set²³⁵ at the (U)B3LYP-D3 level with SMD solvation model were performed based on the optimized geometries of all species at 373.15 K. The given Gibbs free energies in toluene were calculated according to the formula: $G_{\text{sol}} = TCG + E_{\text{sol}}$ (kcal/mol).

Thermal correction to Gibbs free energies (**TCG**, in Hartree), thermal correction to enthalpies (**TCH**, in Hartree), sum of electronic and thermal free energies (**G**, in Hartree), single point energies in toluene computed at the (U)B3LYP-D3/def2-TZVP level (E_{sol} , in Hartree), and total spin-squared operator of open-shell species S^2 are shown in Table 5.

Table 5: Computed Energies of all Stationary Points

Name	TCG/a.u.	TCH/a.u.	G/a.u.	E_{sol} /a.u.	S^2
50a	0.347188	0.516616	-2316.382776	-2318.894358	-
Rh₂(OAc)₄	0.138647	0.242039	-1134.523056	-1134.419664	-
TS6	0.489336	0.695597	-5066.285831	-5069.607110	-
INT4	0.490582	0.697389	-5066.308225	-5069.628738	-
TS7	0.497281	0.695789	-5066.285984	-5069.614194	-
65a	0.321344	0.453478	-3931.808233	-3933.858497	-
INT5	0.317662	0.452341	-3931.770943	-3933.822041	-
TS8	0.322314	0.450700	-3931.752890	-3933.808350	-
TS9	0.324347	0.451170	-3931.754860	-3933.808506	-
66	0.324833	0.453713	-3931.806229	-3933.856912	-
TS10	0.489316	0.695670	-5066.271037	-5069.593131	-
61a	0.327488	0.455639	-3931.837299	-3933.887688	-
TS11	0.492799	0.695390	-5066.261003	-5069.582956	-
TS12	0.316203	0.449912	-3931.734270	-3933.782535	-
INT6	0.048477	0.099968	-2632.706863	-2633.300165	0.7530
INT7	0.243417	0.350455	-1299.067723	-1300.499828	0.7729
INT8	0.032899	0.072479	-117.148486	-117.314607	0.7787
INT9	0.050734	0.099700	-2632.461811	-2633.055832	-
INT10	0.245251	0.349775	-1299.186344	-1300.627636	-
TS13	0.395845	0.554148	-6564.507266	-6567.172611	0.7712
INT11	0.396324	0.555057	-6564.508923	-6567.173563	0.7579

TS14	0.395727	0.553656	-6564.491101	-6567.153485	0.7697
TS15	0.243452	0.347626	-1299.030014	-1300.459054	0.7783
INT12	0.245442	0.349846	-1299.054913	-1300.481675	0.7541
67	0.325135	0.454379	-1928.597321	-1930.494450	-
INT6_s	0.050650	0.100262	-629.501752	-629.941078	0.7680
TS13_s	0.402112	0.555235	-2558.075376	-2560.433746	0.7742
INT11_s	0.401411	0.556209	-2558.083087	-2560.439901	0.7556
TS14_s	0.403257	0.555025	-2558.063441	-2560.420606	0.7704
68	0.329972	0.456331	-1928.625504	-1930.522313	-
INT13	0.392416	0.541289	-4162.617020	-4164.982982	-
TS16	0.394911	0.539753	-4162.606442	-4164.973358	-
65c	0.398452	0.542505	-4162.636734	-4165.007095	-
TS17	0.395778	0.539462	-4162.606191	-4164.974951	-
62a	0.395669	0.542525	-4162.650679	-4165.016237	-
TS18	0.391049	0.539010	-4162.586733	-4164.954069	-
63	0.086305	0.153266	-2785.844420	-2786.653283	-
TS19	0.467722	0.670986	-5102.221404	-5105.566643	-
64-[Rh]	0.469107	0.674097	-5102.270290	-5105.608409	-
64	0.300434	0.429489	-3967.752785	-3969.822926	-
INT14	0.297564	0.427992	-3967.699773	-3969.774255	-
TS20	0.301251	0.426833	-3967.696085	-3969.774125	-

2.5 Conclusion

In summary, we investigated mechanism of several carbene transfer reactions with theoretical calculations in this chapter. Firstly, detailed mechanistic calculations unveil the underlying reaction pathway and selectivity of C-H functionalization of carbazole, which proceeds via a reversible nucleophilic addition of the gold carbene intermediate and is driven by residual amounts of water in solvent.

Secondly, we have proposed a dual role of aniline to promote HF elimination in the Cu-catalyzed *gem*-difluoroolefination of anilines through computational study. With the same trifluoromethylated diazoalkanes, we have reported a practical protocol of palladium-catalyzed crossing-coupling reaction with vinyl bromides and trifluoromethylated diazoalkanes. It opens up a novel methodology for the synthesis of trifluoromethylated, tetrasubstituted allenes.

Finally, the nature of metal-catalyzed rearrangement reactions with triazoles as carbene precursor via free ylide intermediates has been studied by DFT calculations. In this case, we computationally identified that 1,3-migration or [2,3]-sigmatropic rearrangement is strongly dependent on the adjacent substituent of sulfur or selenium center.

3.

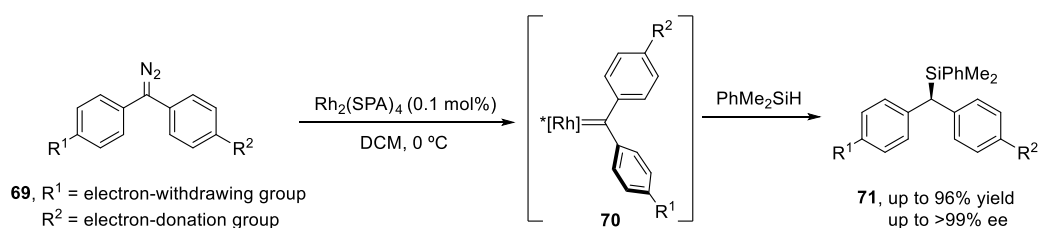
Mechanism Study of Photochemical Carbene Reactions

3.1 Mechanism Study of Multi-reactivity of Diaryl Carbene with Alkynes

3.1.1 Brief Introduction: Reactions of Donor-donor Carbenes

Beyond multifarious applications of donor-acceptor carbenes, donor-donor carbenes have been underdeveloped over decades due to its unstable and potentially explosive diazo precursors, such as diaryl diazomethanes.²⁷ Recently, low temperatures, diluted solutions and suitable substituent groups open up its development and application.^{236,237} Despite of intramolecular carbene transfer reaction with built-in diaryl diazomethane skeletons, enantioselective intermolecular cyclopropanation and X-H insertion reactions have been reported.²³⁸⁻²⁴⁰

Importantly, the Zhou group modified the dirhodium complex with chiral spiro phosphate ligands and developed novel $\text{Rh}_2(\text{SPA})_4$ catalyst, which has been applied in a high enantioselective Si-H insertion with diaryl diazomethanes **69** (Scheme 37).²³⁸ Collaborating with the Houk group, detailed theoretical study revealed that high enantioselectivity was accessed when using markedly different substituents on both aromatic rings. In the favored transition state **70**, the electron-rich aromatic ring was always nearly coplanar with the carbene plane, while the other aryl ring presented a near orthogonal orientation. Thus, electronic difference between two aryls of carbene and chiral environment of catalyst resulted in high enantioselectivity of the reaction.

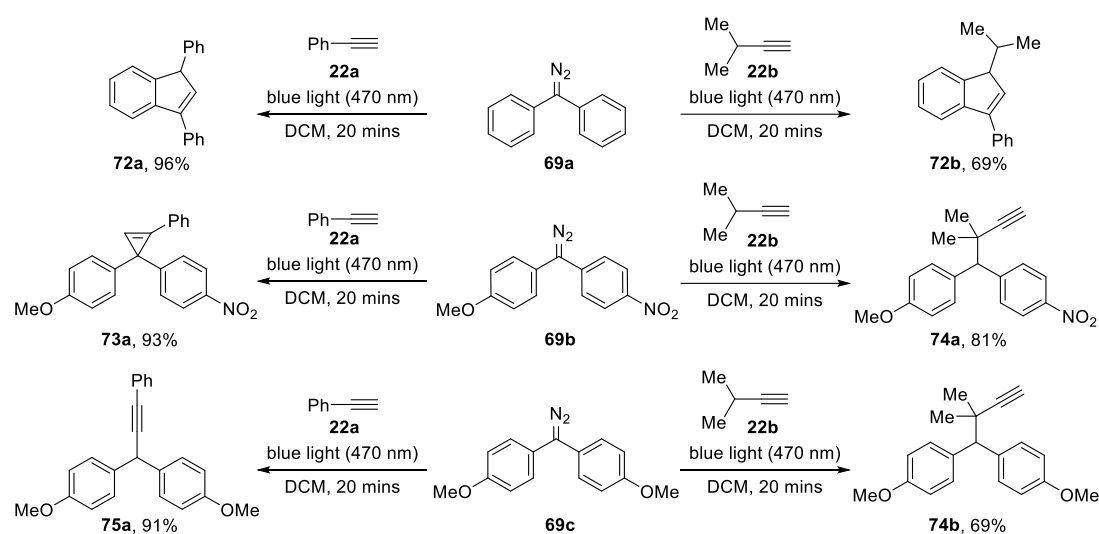


Scheme 37: Rh(II)-catalyzed enantioselective Si-H insertion reaction with diaryl diazomethanes

Based on the emerging photochemical carbene chemistry, we hypothesized that the electronic properties of carbene intermediate could also have similar impact on its reactivity and selectivity. To our delight, when testing the reaction of diaryl diazomethane **69** with alkynes, our group identified the substituent-controlled multi-reactivity of diaryl diazomethanes with alkynes under blue light irradiation (Scheme 38).²⁴¹ When phenyl acetylene **22a** and 3-methyl but-1-yne **22b** were employed in the reaction with diphenyl diazomethane **69a**, both reactions led to an unexpected indenenes **72a** and **72b** in 96% and

69% yield, respectively. In addition, introduction of one electron-withdrawing group onto phenyl ring exhibited a similar reactivity to classic donor-acceptor carbene, which underwent cyclopropanation reaction with phenyl acetylene. Instead, propargyl C(sp³)-H insertion product **74a** was obtained in 81% yield using alkyne **22b**. Similarly, C(sp³)-H insertion of **22b** could also be realized with the photolysis of electron-rich diaryl diazoalkane **69c**. Unexpectedly, treating diaryl diazoalkane **69c** with phenyl acetylene led to a high efficient C(sp)-H insertion reaction and delivered **75a** in 91% yield, which was only accessed with *N*-heterocyclic carbenes.²⁴²

**Experimental work was done by Sripati Jana.*



Scheme 38: Photochemical carbene transfer reactions of diaryl diazomethanes with alkynes

3.1.2 Computational Study

We then intended to investigate the inherent mechanisms experimentally and computationally. Firstly, my colleague has measured the UV-Vis spectra of these three types of diaryl diazomethane (**69a-c**, Figure 17).²⁴¹ In turn, we conducted the TD-DFT calculation of these diazo compounds at B3LYP-D3/def2-TZVP level of theory, and the HOMO to LUMO excitation was predicted to be the first excited state at their absorption wavelength. The computational data showed similar trend to the experimental results. Diazoalkane **69b** with electron-poor substituent absorbed visible light in the purple light region ($\lambda_{\text{max}} = 409$ nm), which extended to blue light area and similar to the phenyl diazoacetate.¹⁰⁸ Besides, the absorptions of electron-neutral or electron-rich diaryl diazomethane **69a** and **69c** were both red-shifted towards the green light region. This difference in absorption suggested a potential distinct reactivity of in situ generated diaryl carbene intermediates via photolysis process.

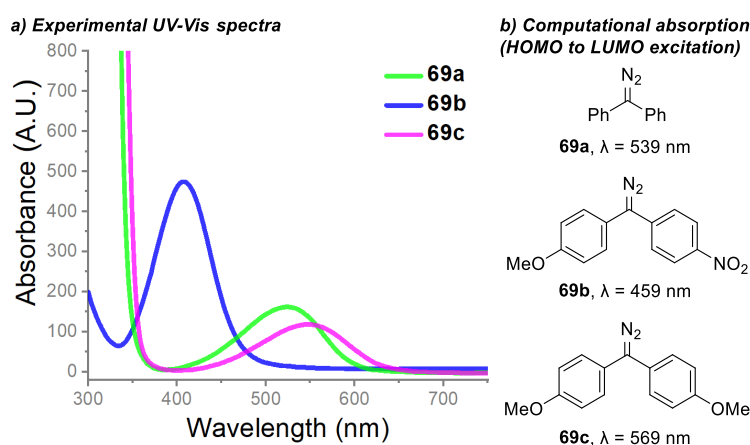
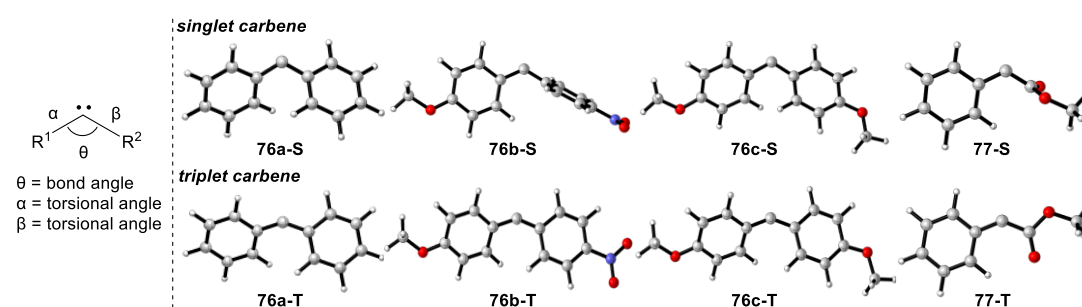


Figure 17: Carbene transfer reactions of electronically distinct diaryl diazomethanes with alkynes

To better understand the properties of diaryl carbenes, we set out our investigations by studying geometrical and electronic properties of carbenes **69a-c** at B3LYP-D3/def2-TZVP(DCM)//B3LYP-D3/def2-SVP(DCM) level of theory (Table 6). We firstly observed a significant difference in the singlet-triplet energy splitting of diaryl carbenes **76a-c**, which strongly depended on the substituents of the aromatic ring. For diphenyl carbene **76a**, this energy gap was calculated to be 4.5 kcal/mol, which was close to the previous calculation at CCSD(T) level ($\Delta E_{S/T} = 3.2$ kcal/mol) and experimental energy gap of 4.6 kcal/mol.⁴ In addition, for the diaryl carbene **76b**, a smaller energy gap of -0.3 kcal/mol was found at this computational level. In case of more electron-rich *bis*(4-methoxyphenyl)carbene **76c**, an overestimation of the splitting energy (0.4 kcal/mol) was obtained computationally compared to previous experimental and theoretical study.⁵ Although, calculations with B3LYP-D3 functional did not perfectly reflect experimentally observations, diphenyl carbene **76a** had largest splitting energy and thus supported a favored triplet carbene intermediate. Small singlet-triplet splitting of **76b** or **76c** indicated a coexistence of both spin states in solution and a facile intersystem crossing, which was proved by the Sander group experimentally and computationally.⁵

By comparing the geometric properties of **76a-c** with donor-acceptor carbene **77** (derived from phenyl diazoacetate **1a**), the geometries of all triplet carbene intermediates were remarkably close. However, the introduction of the electron-withdrawing group in singlet carbene **76b-S** led to a near orthogonal position of two phenyl rings, which was similar to the donor-acceptor singlet carbene **77-S** or aryl/aryl Rh-carbene complexes.²³⁸ This structural resemblance reflected the potential similar reactivity to donor-acceptor carbene **77-S**, which led to cyclopropenation of phenyl acetylene.¹⁰⁸ Further charge distribution analysis with NBO method indicated that singlet carbene **76c-S** was significantly more nucleophilic than others, and **76b-S** was the most electrophilic among these three carbenes.

Table 6: Geometrical and electronic properties of diaryl carbenes



Carbene ^[a]	Spin state	θ	α	β	NPA charge ^[b]	$\Delta E_{S/T}/\Delta G_{S/T}$ ^[c]
76a-S	singlet	119.1°	148.5°	-34.8°	0.035	3.0 (4.5)
76a-T	triplet	141.6°	156.5°	-25.0°	0.224	
76a-S	singlet	124.7°	177.1°	-82.4°	0.106	-0.8 (-0.3)
76a-T	triplet	141.9°	166.4°	-33.5°	0.251	
76a-S	singlet	119.2°	152.0°	-30.8°	-0.038	-1.5 (0.4)
76a-T	triplet	141.0°	156.0°	-25.6°	0.188	
77-S	singlet	120.5°	177.3°	-89.6°	0.023	-0.9 (-0.7)
77-T	triplet	135.5°	0.002°	0.005°	0.157	

^[a] Calculations were performed at B3LYP-D3/def2-TZVP(DCM)//B3LYP-D3/def2-SVP(DCM). ^[b] Natural population analysis (NPA) was performed with NBO methods, and the partial charges of the carbene carbon were listed. ^[c] Positive values indicate an energetically favored triplet state, negative values indicate an energetically favored singlet state. Energies are given in kcal/mol in DCM.

We next studied the reaction of diphenyl carbene **76a-S** and **76a-T** with phenyl acetylene **22a** in detail (Figure 18). In the singlet energy surface, we identified two possible pathways. One was cyclopropenation step via **TS1_s** to form the cyclopropene **73b**, which needed an activation free energy of 15.0 kcal/mol. Another one was the direct C(sp)-H insertion reaction through **TS2_s** with an energy barrier of 17.2 kcal/mol. In addition, similar hydrogen abstraction with triplet carbene **76a-T** had a high lying transition state **TS2_T** ($\Delta G^\ddagger = 27.5$ kcal/mol), which was not feasible to account for C(sp)-H functionalization. However, we found a facile radical-like process involving addition of triplet carbene onto the distal acetylene carbon atom, which proceeded via **TS1_T** with a low energy barrier of 11.4 kcal/mol to give diradical species **INT1_T**. Further intramolecular radical cyclization of **INT1_T** via **TS4_T** led

to triplet indene intermediate **INT2_T**, which followed by intersystem crossing to give closed shell singlet species **INT2_S**. Finally, [1,2]-hydrogen shift of isoindene **INT2_S** realized the rearomatization via **TS5_S** with an activation free energy of 9.2 kcal/mol, which gave the desired indene product **72a**. The whole process was energetically favorable and consistent with the experimental observation.

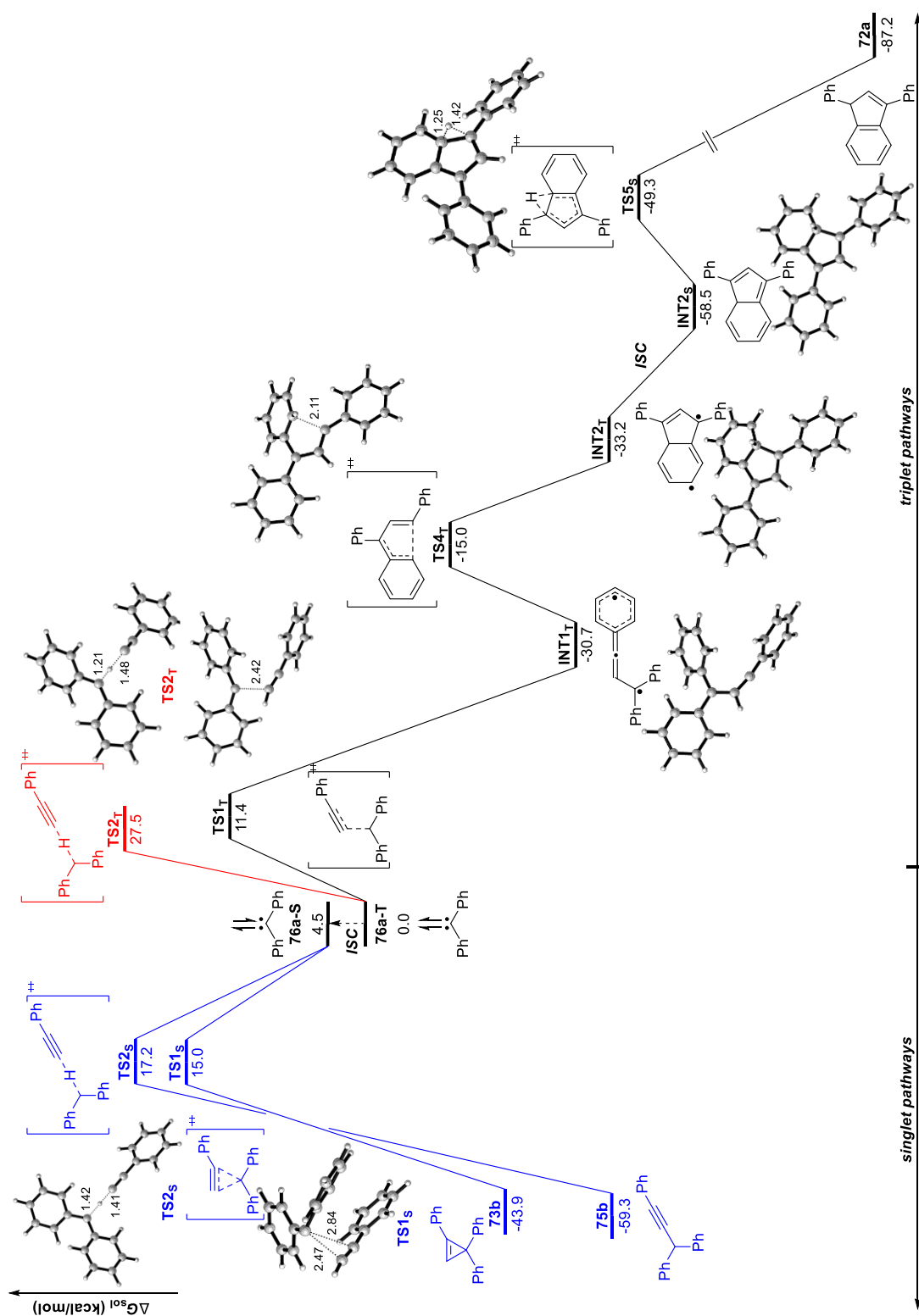


Figure 18: Potential energy surfaces of the reaction of diphenyl carbene and phenyl acetylene

In case of the reaction with 3-methyl but-1-yne **22b**, all the transition states that located in singlet energy surface were less favorable than these in the triplet energy surface (Table 7). Indeed, a propargyl hydrogen abstraction via **TS3_T** ($\Delta G^\ddagger = 12.7$ kcal/mol) was slightly favored over indene formation ($\Delta G^\ddagger = 13.6$ kcal/mol), which resulted in generating a mixture of indene and C(sp³)-H insertion product computationally. The slightly contradictory results could be attributed to spin contamination in the open shell species calculations. Furthermore, more accurate calculations using DLPNO-CCSD(T) method provided a good rationale on the chemoselectivity ($\Delta G^\ddagger = 14.0$ kcal/mol for indene formation vs. $\Delta G^\ddagger = 14.8$ kcal/mol for C(sp³)-H insertion).

Subsequently, we focused on the research of reaction with diaryl carbene **76b** and **76c** (Table 7). Previous singlet-triplet splitting calculation with the B3LYP-D3 functional suggested a slightly stabilized singlet state of **76b-S** (Table 3). Indeed, for the reaction of **76b-S** with phenyl acetylene, the calculations indicated a sharp decline of activation free energy in cyclopropanation step ($\Delta G^\ddagger = 10.6$ kcal/mol for indene **76b-S** vs. $\Delta G^\ddagger = 15.0$ kcal/mol for **76a-S**), which might result from the more electrophilicity of carbene carbon in **76b-S**. In addition, cyclopropene formation was almost identical to indene formation, while the singlet carbene was the energetically favored intermediate and the cyclopropene was thus formed as the main reaction product. Contrarily, for the reaction with 3-methyl but-1-yne **22b**, the lowest energy transition state was C(sp³)-H functionalization via **TS3_T**, which was the same as the reaction of bis(4-methoxyphenyl)carbene **76c**.

Table 7: Different reaction pathways of diaryl carbene with phenyl acetylene and 3-methyl but-1-yne

TS1 _S	TS2 _S	TS3 _S	TS1 _T	TS2 _T	TS3 _T
cyclopropanation	C(sp)-H insertion	C(sp ³)-H insertion	indene formation	C(sp)-H abstraction	C(sp ³)-H abstraction
singlet pathways			triplet pathways		

Carbene ^[a]	R	Singlet spin state			Triplet spin state		
		TS1 _S	TS2 _S	TS3 _S	TS1 _T	TS2 _T	TS3 _T
76a	Ph	15.0	17.2	-	11.4	27.5	-
76a	<i>i</i> Pr	17.9	21.0	16.7	13.6 (14.0) ^[b]	33.4	12.7 (14.8) ^[b]
76b	Ph	10.6	17.2	-	10.2	27.4	-
76b	<i>i</i> Pr	15.5	20.4	14.0	12.9	33.5	12.3
76c	Ph	12.0	9.8	-	11.3	27.5	-
76c	<i>i</i> Pr	15.7	13.0	13.8	14.1	33.1	12.7

^[a] Calculations were performed at B3LYP-D3/def2-TZVP(DCM)//B3LYP-D3/def2-SVP(DCM). Gibbs free energies are given in kcal/mol. ^[b] Gibbs free energies are improved at DLPNO-CCSD(T)/cc-pVDZ level.

In the last step, we considered the influence of two electron-donating methoxy groups on the chemoselectivity of the reaction with diaryl diazomethane **69c** (Figure 19 and Scheme 38). A significant increase of nucleophilicity of carbene atom (NBO analysis in Table 6)

facilitated the deprotonation of C(sp)–H bond in phenyl acetylene via a low-lying transition state **TS2_s** ($\Delta G^\ddagger = 9.8$ kcal/mol). This process led to a carbocation and acetylide ion pair **INT3_s**, which was stabilized by weak hydrogen-bonding and π - π stacking interaction between alkynyl anion and diaryl cation. The following barrierless nucleophilic addition furnished the formal C(sp)–H functionalization and formed the final product **75a**. In the reaction of **69c** with 3-methyl but-1-yne **22b**, the most favored hydrogen atom abstraction pathway via **TS3_T** ($\Delta G^\ddagger = 12.7$ kcal/mol) afforded two radicals **INT4_T**, which underwent further intersystem crossing (ISC) and radical-radical recombination to give the C(sp³)–H functionalization product **74b**.

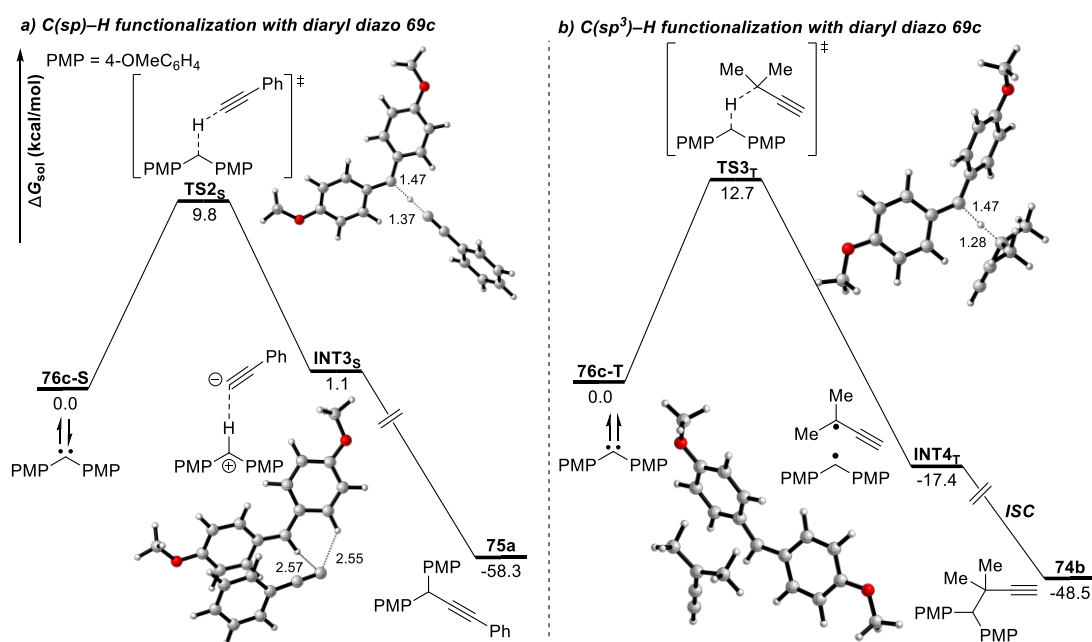


Figure 19: Potential energy surfaces of the reaction of diaryl carbene **69c** with alkynes

3.1.3 Computational Data

Computational Details at (U)B3LYP-D3/def2-TZVP Level

All the calculations were performed with the Gaussian 16 program.¹⁸³ The geometries of all stationary points were optimized using the (U)B3LYP functional^{204,205} together with Grimme's dispersion correction²⁰⁹ (denoted (U)B3LYP-D3), and the def2-SVP basis set²³⁵ was used for all atoms. Due to the local ionicity found in the transition states and intermediates of C(sp)-H insertion process, all geometry optimization were performed in the dichloromethane ($\epsilon = 8.93$) using PCM solvation model.¹⁹⁴ Harmonic vibrational frequency calculations at the same level were performed for all of the stationary points to confirm them as a local minima or transition structures. Key transition-state structures were confirmed to connect corresponding reactants and products by intrinsic reaction coordinate (IRC) calculations.^{192,193} To improve the calculation accuracy, single point calculations were performed using the (U)B3LYP-D3 level and PCM solvation model, and the def2-TZVP basis set²³⁵ was used for all atoms. The given Gibbs free energies in dichloromethane were calculated according to the formula: $G_{sol} = TCG + E_{sol}$ (kcal/mol). The CYL View software was employed to show the 3D structures of the studied species.¹⁹⁵ Natural population analysis (NPA) were performed with natural bond orbital (NBO) method at (U)B3LYP-D3/def2-TZVP level.²⁴³

Thermal correction to Gibbs free energies (**TCG**, in Hartree), thermal correction to enthalpies (**TCH**, in Hartree), sum of electronic and thermal free energies (**G**, in Hartree), single point energies in dichloromethane computed at the (U)B3LYP-D3/def2-TZVP level (**E_{sol}**, in Hartree), and total spin-squared operator of open-shell species **S²** are shown in Table 8.

Table 8: Computed Energies of all Stationary Points

Name	TCG/a.u.	TCH/a.u.	G/a.u.	E _{sol} /a.u.	S ²
22a	0.079927	0.116989	-308.106012	-308.521894	-
22b	0.083676	0.119536	-195.066837	-195.370112	-
77-S	0.109187	0.157508	-497.660794	-498.331014	
77-T	0.108976	0.157303	-497.665378	-498.329594	2.0305
76a-S	0.148530	0.195853	-500.809870	-501.498799	-
76a-T	0.146190	0.195211	-500.820536	-501.503567	2.0549
76a-TS_{22a1T}	0.243670	0.313027	-808.910746	-810.024794	2.0602
76a-INT_{22a1T}	0.248821	0.315799	-808.983264	-810.097133	2.0735
76a-TS_{22a4T}	0.251169	0.314504	-808.959349	-810.074454	2.0694
76a-INT_{22a2T}	0.253096	0.316175	-808.990624	-810.105290	2.0495
76a-INT_{22a2S}	0.257280	0.318345	-809.030370	-810.149801	-
76a-TS_{22a5S}	0.254720	0.314988	-809.017254	-810.132552	-
72a	0.257718	0.319539	-809.075935	-810.195947	-
76a-TS_{22a2T}	0.238785	0.309858	-808.885209	-809.994279	2.0526
75b	0.250078	0.318760	-809.026171	-810.143847	-

76a-TS_{22a1s}	0.248241	0.314059	-808.903226	-810.023717	-
73b	0.252815	0.317429	-809.006426	-810.122193	-
76a-TS_{22a2s}	0.239722	0.311041	-808.900283	-810.011643	-
76a-TS_{22b1T}	0.248146	0.315524	-695.868699	-696.870287	2.0633
72b	0.263561	0.322272	-696.037629	-697.045897	-
76a-TS_{22b2T}	0.246450	0.314655	-695.836048	-696.837097	2.0473
76a-TS_{22b3T}	0.245142	0.311133	-695.871057	-696.868736	2.0496
76a-TS_{22b1s}	0.252295	0.316436	-695.859611	-696.867599	-
76a-TS_{22b2s}	0.245399	0.313581	-695.854432	-696.855694	-
76a-TS_{22b3s}	0.248533	0.312276	-695.862922	-696.865708	-
76b-S	0.174834	0.23624	-819.592187	-820.683008	-
76b-T	0.174040	0.235733	-819.595051	-820.681698	2.0479
76b-TS_{22a1T}	0.271046	0.353521	-1127.687086	-1129.204433	2.0596
76b-TS_{22a2T}	0.266671	0.349929	-1127.660199	-1129.17266	2.0459
76b-TS_{22a1s}	0.276366	0.354229	-1127.685679	-1129.209482	-
73a	0.280573	0.357758	-1127.77829	-1129.296929	-
76b-TS_{22a2s}	0.268115	0.351433	-1127.675873	-1129.190814	-
76b-TS_{22b1T}	0.276348	0.3561	-1014.645132	-1016.050652	2.0562
76b-TS_{22b2T}	0.27458	0.354096	-1014.611135	-1016.015321	2.0414
76b-TS_{22b3T}	0.273207	0.351697	-1014.64582	-1016.047178	2.0458
74a	0.287415	0.361032	-1014.74357	-1016.156283	-
76b-TS_{22b1s}	0.279969	0.356727	-1014.638462	-1016.049777	-
76b-TS_{22b2s}	0.272976	0.353967	-1014.631209	-1016.035029	-
76b-TS_{22b3s}	0.27657	0.352797	-1014.642386	-1016.048809	-
76c-S	0.207198	0.266096	-729.646509	-730.658373	-
76c-T	0.204186	0.265246	-729.651140	-730.656005	2.0517
76c-TS_{22a1T}	0.301176	0.383032	-1037.741618	-1039.176928	2.0644
76c-TS_{22a2T}	0.298086	0.380115	-1037.715710	-1039.148068	2.0501
75a	0.308427	0.388647	-1037.854695	-1039.294521	-
76c-TS_{22a1s}	0.306591	0.384092	-1037.737997	-1039.180666	-
76c-TS_{22a2s}	0.297772	0.381243	-1037.742111	-1039.175200	-
76c-INT_{22a3s}	0.309839	0.387190	-1037.752690	-1039.201173	-
76c-TS_{22b1T}	0.305818	0.385458	-924.698326	-926.021500	2.0615
76c-TS_{22b2T}	0.304831	0.384745	-924.667019	-925.990328	2.0431
76c-TS_{22b3T}	0.303024	0.381126	-924.701709	-926.021056	2.0469
76c-INT_{22b4T}	0.303318	0.385520	-924.748783	-926.069234	2.0494
74b	0.317379	0.390489	-924.801355	-926.132942	-
76c-TS_{22b1s}	0.310687	0.386452	-924.693112	-926.023196	-
76c-TS_{22b2s}	0.303067	0.383791	-924.697455	-926.019917	-
76c-TS_{22b3s}	0.306418	0.382203	-924.697538	-926.021992	-

Computational Details at DLPNO-CCSD(T) Level

Before the calculations at DLPNO-CCSD(T) level on the ORCA software,²⁴⁴ we got the more accurate structures at B3LYP-D3/def2-tzvp level with Gaussian 16.²⁴⁵ The reference wave function is sensitive in our system due to high spin contamination in the triplet state. According to previous investigations, we used the TightPNO criteria and the ROHF as the reference wave function.⁴ In our case, we use a better approximation of iterative (T) called DLPNO-CCSD(T1),⁴ and the Dunning correlation consistent basis sets cc-pVDZ was used.²⁴⁶ Furthermore, to investigate the solution effect of the carbene species and some controversial transition states, we used more accurate the continuum solvation model based on the density (SMD) at M05-2x/6-31G(d) level.²⁰⁸

Thermal correction to Gibbs free energies (**TCG**, in Hartree) calculated at B3LYP-D3/def2-tzvp level, single point energies calculated at M05-2X/6-31G(d) level in gas phase (E_{gas} , in Hartree), single point energies calculated at M05-2X/6-31G(d) level in dichloromethane using SMD model (E_{sol} , in Hartree), single point energies computed at the DLPNO-CCSD(T)/cc-pVDZ level (**SPE**, in Hartree), and Gibbs free energies (G_{sol} , in Hartree) in dichloromethane were calculated according to the formula: $G_{sol} = SPE + TCG + E_{sol} - E_{gas} + 1.89$ kcal/mol.

Table 9: Computed Energies of all Stationary Points

Name	TCG/a.u.	E_{gas}/a.u.	E_{sol}/a.u.	SPE/a.u.	G_{sol}/a.u.
76b-S	0.175233	-820.222379	-820.249670	-818.134745	-817.983791
76b-T	0.173006	-820.231500	-820.253981	-818.139978	-817.986441
76a-S	0.148593	-501.233503	-501.256226	-499.861757	-499.732875
76a-T	0.145949	-501.246269	-501.265292	-499.869155	-499.739217
76c-S	0.206563	-730.254852	-730.281207	-728.336488	-728.153268
76c-T	0.203311	-730.261847	-730.283321	-728.338286	-728.153437
22b	0.083955	-195.243314	-195.250884	-194.712601	-194.633204
76a-TS_{22b1}T	0.247883	-696.489589	-696.512282	-694.578333	-694.350132
76a-TS_{22b3}T	0.244542	-696.481234	-696.504494	-694.573096	-694.348802

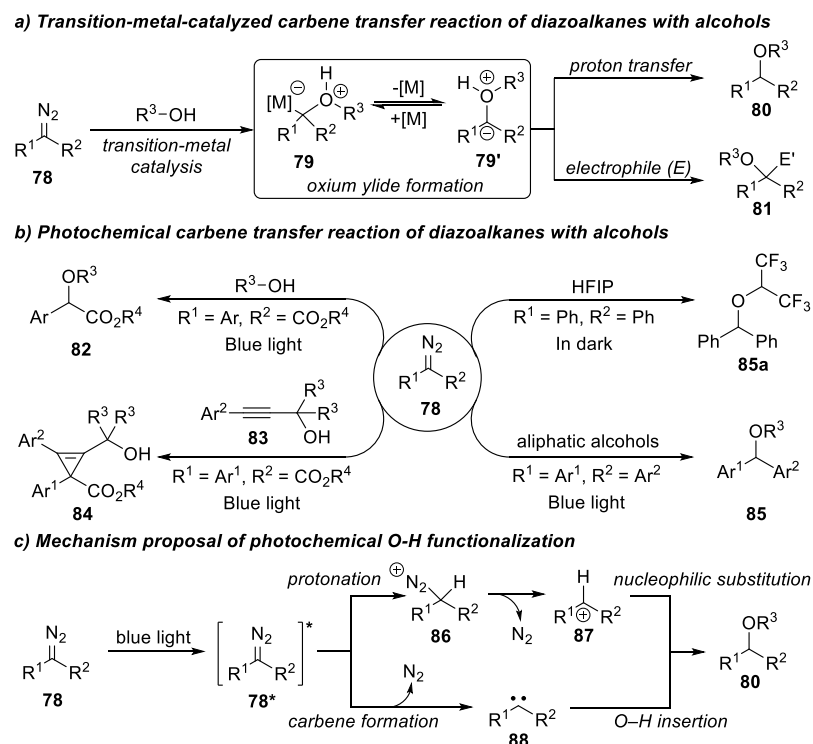
3.2 Mechanism study of Photoinduced O–H Insertion Reactions

3.2.1 Brief Introduction: Carbene-mediated O–H Insertion Reaction

Transition-metal-catalyzed carbene insertion reactions into the O–H bond of alcohols from diazo compounds represents a typical strategy for alkylation reactions and has been widely used for the construction of ethers.^{73,74} This methodology usually reacts through metal-bound or metal-free oxonium intermediate **79** and **79'**, which were proven to further undergo electrophilic addition by electrophiles (Scheme 39a).⁸⁰

Recently, the photolysis of diazoalkanes emerged as a powerful strategy for carbene transfer reactions under metal-free conditions, which avoids the use of transition metal catalysts.¹⁰⁰⁻¹⁰⁴ Moreover, the photochemical reaction of diazoalkanes with alcohols that was reported by our and other groups presented a metal-free O–H insertion reaction with alcohols.^{107,116,122,247-249} Besides the typical outcomes of the reaction with diazoacetates and alcohols, different substituents on the diazoalkanes or alcohols resulted in distinct chemoselectivity, such as cyclopropanation with propargyl alcohols (Scheme 39b).¹¹⁸ In addition, diaryl diazoalkanes can undergo O–H functionalization reactions with or without light, which is strongly dependent on the acidity of alcohols and substituents on the aryls.²⁴⁷

Accordingly, two possible pathways are proposed to account for the photochemical O–H functionalization of alcohols with diazoalkanes (Scheme 39c). One is the direct protonation of the photoexcited species **78***, followed by denitrogenation and nucleophilic substitution to afford ether **80**. An alternative pathway is the free carbene-involved O–H insertion process.



Scheme 39: Carbene transfer reaction with diazo compounds and alcohols

3.2.2 Computational Study

This unusual reactivity of photochemical O–H insertion reaction promoted us to elucidate the detailed reaction mechanism computationally. Firstly, we performed computational studies on photochemical O–H functionalization of alcohols with aryldiazoacetates at B3LYP-D3/def2-TZVP(dichloromethane)//B3LYP-D3/def2-SVP (dichloromethane) level of theory, in which methyl phenyldiazoacetate (**1a**) and hexafluoro isopropanol (HFIP) were used as model substrates.²⁵⁰ The hydrogen bond between the OH group and C=O group in methyl phenyldiazoacetate **1a** was proposed computationally and resulted in slight structural variation of **1a**, which was validated experimentally (Figure 20).¹¹⁶ Contrarily, weakly acidic alcohols like trifluoroethanol (TFE) and isopropanol (*i*PrOH) presented a weak interaction with ester group of diazoacetate.

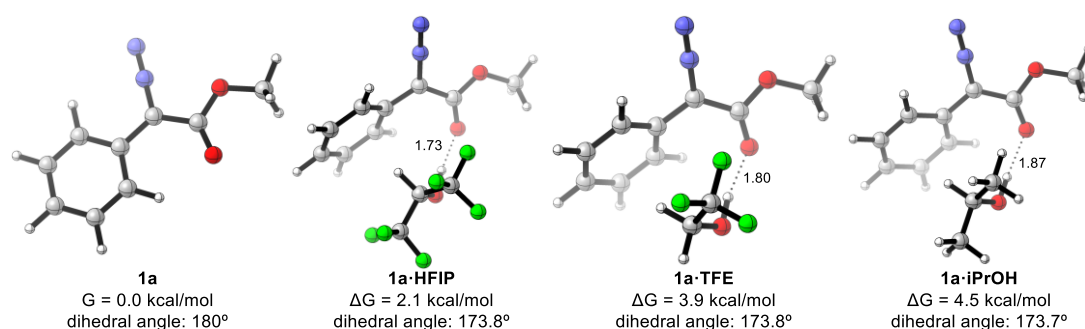


Figure 20: Analysis of the hydrogen bonding of alcohols with methyl phenyldiazoacetate **1a**

As shown in Scheme 39c, we first studied the direct protonation of the photoexcited diazoacetate **1a**^{*} with *Ab initio* molecular dynamics (AIMD), which was performed for first excited state of **1a**-HFIP (Figure 21). At the beginning of this calculation, a weak interaction of OH group with the carbon of the diazo group was found. While the whole system reached to a equilibrium at approximate 350 fs, it formed a more stable hydrogen bond between HFIP and ester group of **1a**, which ruled out the possibility of a direct protonation pathway.

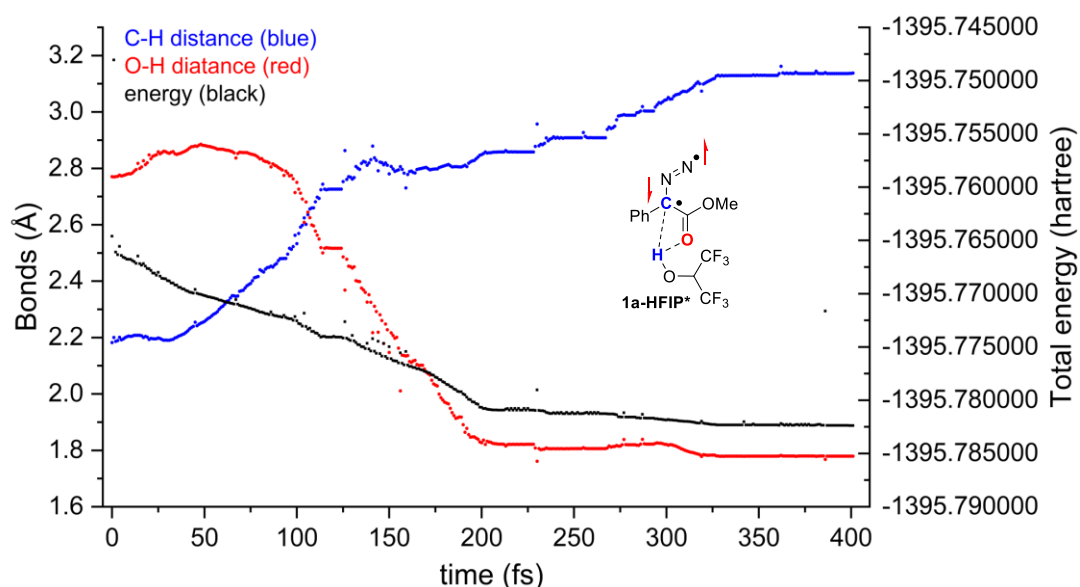


Figure 21: *Ab initio* molecular dynamics (AIMD) simulation of excited state of **1a**-HFIP

We next performed TD-DFT calculations for analysis of the photoexcitation step with methyl phenyldiazoacetate **1a** and HFIP (Figure 22). Calculations indicated that the HOMO to LUMO was predicted to be the first excited state ($\lambda = 468.2$ nm), which was consistent with previous UV-Vis absorption spectra with a shoulder from 430 to 470 nm.¹⁰⁸ Further calculations revealed that both the hydrogen-bonded complex **1a**·HFIP and free methyl phenyldiazoacetate **1a** underwent a photochemical excitation to the respective singlet excited state, which converted to the more stable triplet species **1a**-T or **1a**-T·HFIP via intersystem crossing. Further denitrogenation via low-lying transition state **TS1** or **TS1**·HFIP led to corresponding triplet carbene intermediates **77**-T or **77**-T·HFIP, respectively. Next, a facile alcohol-assisted intersystem crossing occurred via minimum energy-crossing point (**MECP**, $\Delta E = 5.0$ kcal/mol) to give a hydrogen-bonded singlet carbene intermediate **77**-S·HFIP.

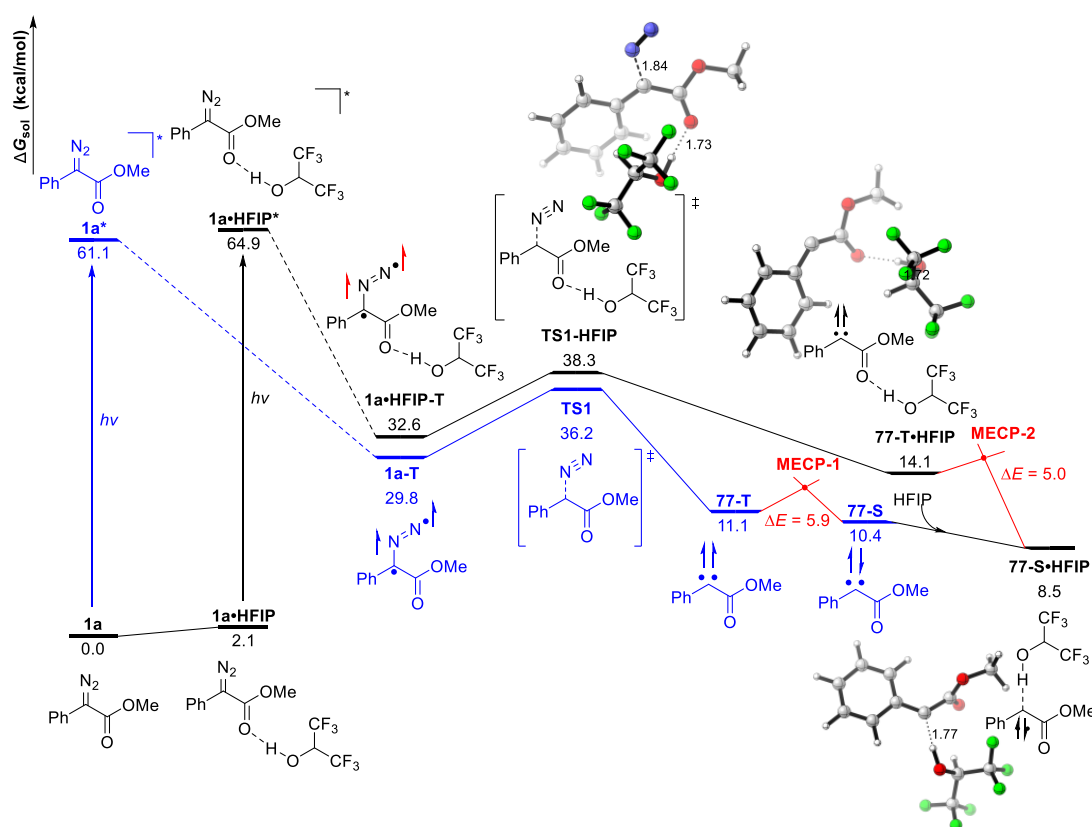


Figure 22: Potential energy surfaces of photoinduced formation of free carbene

We further examined the downstream reaction of the hydrogen-bonded carbene intermediate **77**-S·HFIP (Figure 23). In a first reaction pathway, a direct protonation of the carbene carbon was identified via **TS2** with a low activation free energy of 2.0 kcal/mol, which directly led to the formation of the insertion product **82a**. According to mechanism of the metal-catalyzed OH insertion reaction, we then attempted to locate an oxonium ylide formation, yet no transition states could be found computationally. Instead, all the attempts led to a formal protonation of the C=O group of the ester and C–O bond formation via **TS3** with an energy barrier of 12.2 kcal/mol, which resulted in the formation of an enol intermediate **89a**. In this case, the enol formation process was disfavored over the direct carbene protonation with acidic alcohol HFIP.

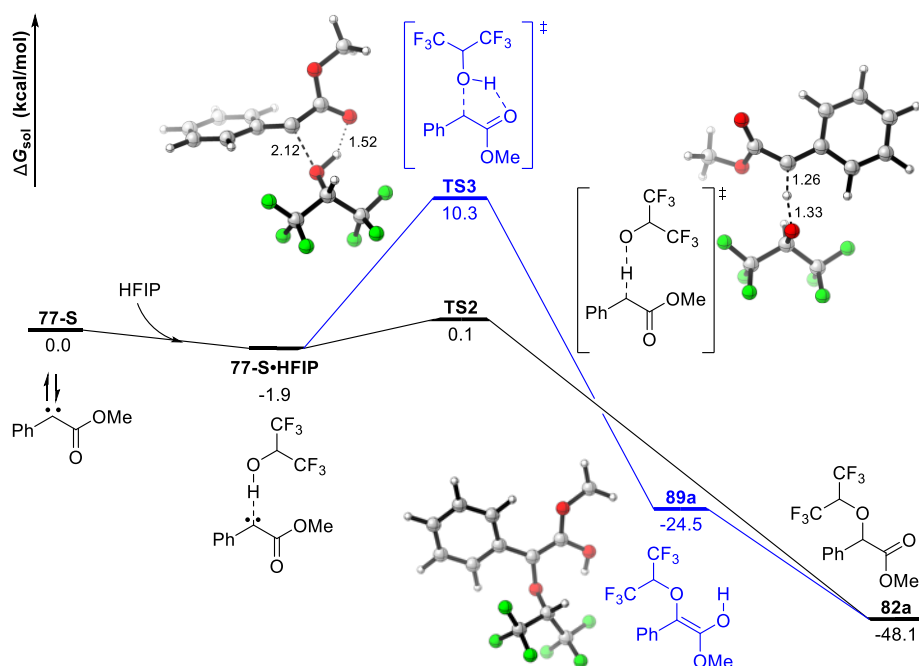


Figure 23: Potential energy surfaces of reaction pathways of singlet carbene with HFIP

We hypothesized that the acidity of alcohols could influence both protonation of carbene carbon or C=O bond of ester group. For this purpose, we next examined various alcohols with different pK_a , such as TFE, 4-cyano phenol, perfluoro-*tert*-butanol (PFTB), and simple aliphatic alcohols (Table 10). Calculations indicated that hydrogen bond interaction between alcohol and singlet carbene **77-S** was strongly dependent on the acidity of the alcohols. In the case of more acidic alcohols such as PFTB, 4-CN phenol and HFIP, this hydrogen bond interaction was energetically preferred. And yet, the interaction for aliphatic alcohols or TFE was endergonic and probably led to a distinct reaction pathway. Furthermore, evaluation

Table 10: Reaction pathways of singlet carbene with different alcohols

alcohol	pK_a	77-S·ROH ΔG (kcal/mol)	77-S'·ROH ΔG (kcal/mol)	TS2 ΔG^\ddagger (kcal/mol)	TS3 ΔG^\ddagger (kcal/mol)
PFTB	5.4	-3.5	0.8	-1.7	14.8
4-CN-phenol	7.95	-1.3	1.2	0.2	10.7
HFIP	9.42	-1.9	1.2	2.0	12.2
TFE	12.46	1.0	3.5	7.4	7.9
MeOH	15.5	2.1	4.2	12.7	5.9
<i>i</i> PrOH	16.5	3.7	5.1	12.0	6.6
<i>t</i> BuOH	16.54	3.9	5.1	14.5	8.0

of a direct protonation (via **TS2**) or enol pathway (via **TS3**) for this set of alcohols exhibited a contrary selectivity, which depended on the acidity of alcohols. In the case of strongly acidic alcohol PFTB, 4-CN phenol, and HFIP, the direct protonation via **TS2** was near barrierless, which significantly favored over the enol pathway (**TS3**). Instead, weakly acidic alcohols such as MeOH, *i*PrOH, and *t*BuOH suppress the protonation process, and preferentially reacted via enol pathway due to the increased nucleophilicity of aliphatic alcohols compared to the alcohols with electron-withdrawing group. In the case of TFE, both reaction pathways were viable to account for O–H insertion product formation.

We have also investigated the final tautomerization of enol intermediate that led to the reaction product (Figure 24). With the reaction of MeOH as the model, an alcohol-mediated proton transfer via **TS4** with an activation free energy of 17.0 kcal/mol could afford the O–H functionalization product **82e**. Moreover, chiral Brønsted acid catalysts can promote the enol tautomerization in an asymmetric mode, which will open up novel photochemically co-catalytic and enantioselective carbene transfer reactions.²⁵¹

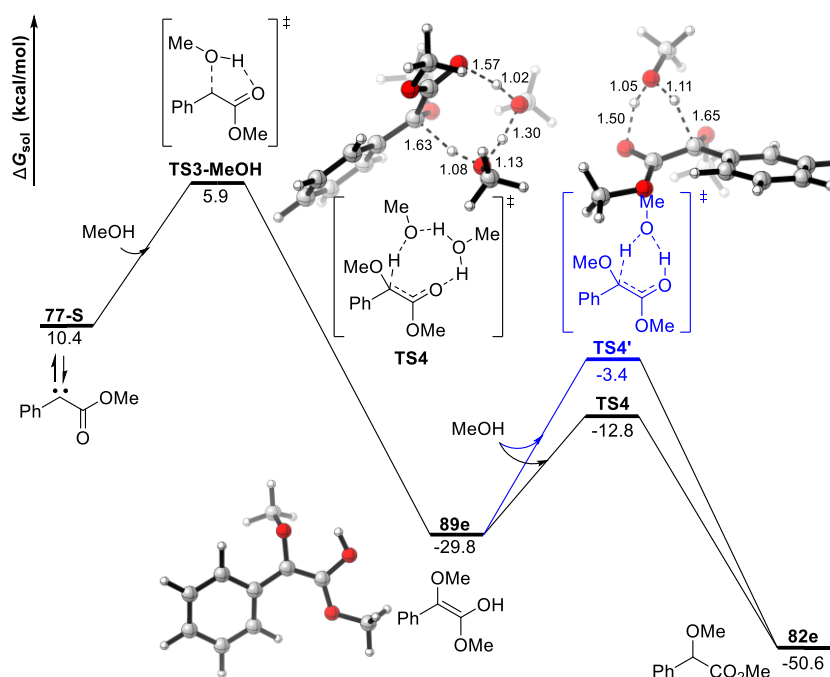
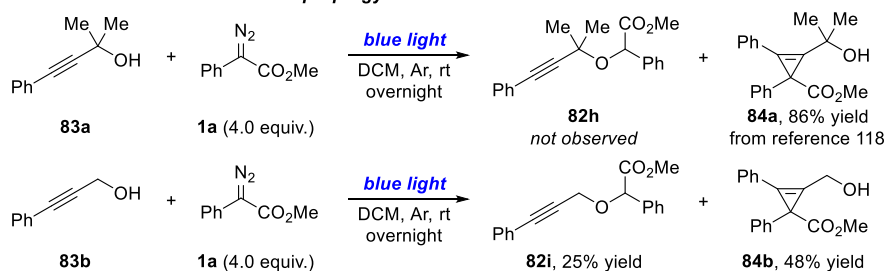


Figure 24: Potential energy surfaces of tautomerization of enol intermediate

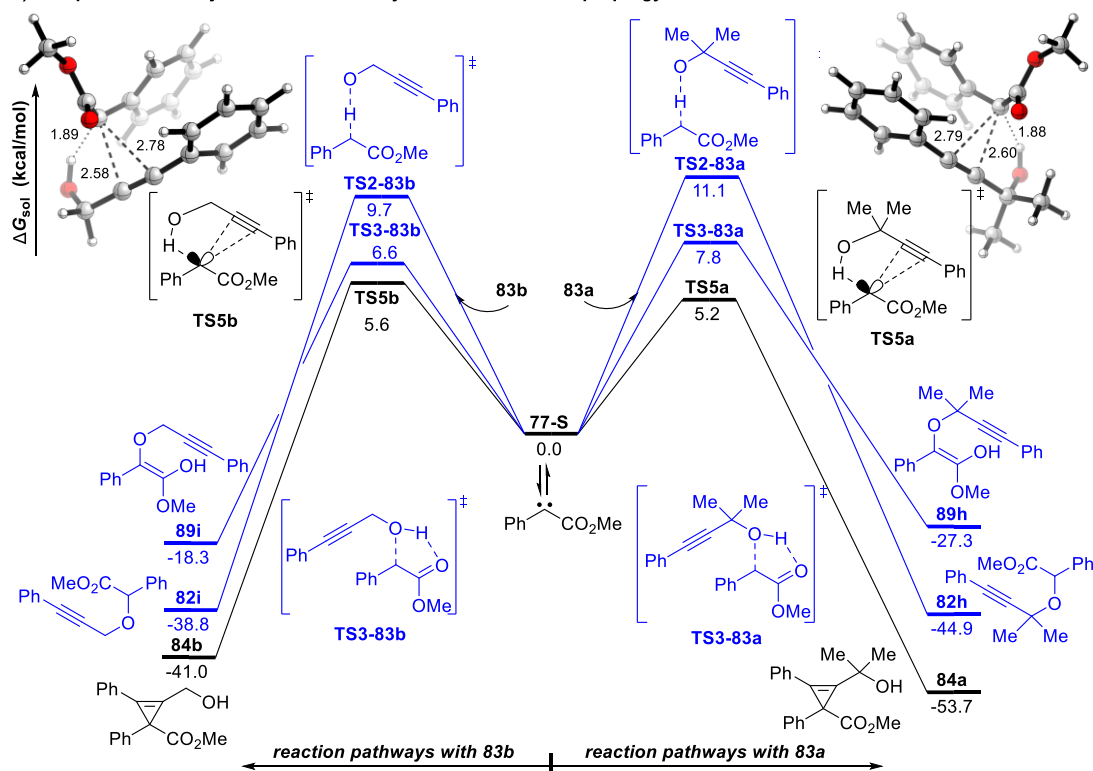
Previously, our group observed a highly selective cyclopropanation in the photochemical reaction of tertiary propargylic alcohols with aryl diazoacetate **1**.¹¹⁸ In this case, we have not observed any O–H functionalization or rearrangement products, which is already well documented in transition-metal catalysis.⁸³ In addition, a subtle energy difference was also identified for the increasing steric demand of alcohols, in which the activation free energy for the enol formation process (**TS3**) increases accordingly (Table 10). These observations and calculations prompted us to examine the photochemical reaction with a primary propargylic alcohol **83b**. To our surprise, poor chemoselectivity and a mixture of O–H insertion product **82i** and cyclopropene **84b** were observed experimentally (Scheme 40a).

Based on distinct reactivity of tertiary propargylic alcohol **83a** and primary propargylic alcohol **83b**, we then embarked on the computational studies (Scheme 40b). Calculations indicated that this amphiphilic free singlet carbene preferred a cyclopropenation process in an electrophilic fashion via **TS5a** instead of protonation in a nucleophilic fashion via **TS3-83a**. Specifically, hydrogen bonding of OH group with the filled sp^2 -like orbital of carbene enhanced the electrophilicity of the vacant orbital, which facilitated the cycloaddition with the electron-rich triple bond (via **TS5a**). The energy difference of 2.6 kcal/mol between **TS5a** and **TS3-83a** resulted in a highly chemoselective cyclopropenation reaction, which was consistent with the experimental result. On the contrary, for primary propargylic alcohol **83b**, the energy difference of **TS5b** and **TS3-83b** significantly reduced to 1.0 kcal/mol, which resulted in a mixture of **82i** and **84b** and was in accordance with control experiments. This reduced energy difference possibly resulted from increasing barrier of the enol pathway due to sterically demanding tertiary propargylic alcohols, which was reflected by the case of MeOH and *t*BuOH in Table 10.

a) Experimental results of the reaction with propargylic alcohols



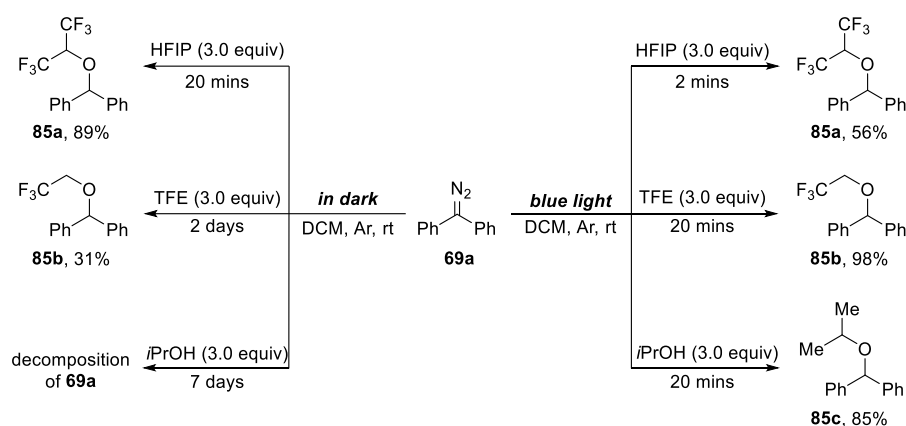
b) Computational study on chemoselectivity of the reaction with propargylic alcohols



Scheme 40: Experimental and computational studies of the reaction with propargylic alcohols

Besides donor-acceptor diazoacetates, our group found that the donor-donor diazoalkanes, such as diphenyl diazomethane **69a**, could also undergo similar O–H functionalization with alcohols.²⁴⁷ However, due to the poor acid resistance of diphenyl diazomethane **69a**, the formal O–H insertion reaction were strongly dependent on the acidity of alcohols. When we tested the acidic HFIP as the substrate, this alkylation reaction of HFIP with **69a** could be done in 20 minutes in 89% yield under dark condition (Scheme 41). This reaction was significantly promoted with blue light irradiation (470 nm) to give the same product **85a** within only two minutes reaction time. Instead, less acidic alcohols TFE and *i*PrOH showed poorly or no unreactive with diazoalkane **69a** in the dark reaction condition. However, irradiation with blue light was proved to highly accelerate the reactions with inert alcohols. Both reactions could finish in 20 minutes and corresponding O–H functionalization **85b** and **85c** were obtained in 98% and 85% yield, respectively.

**Experimental work was done by Claire Empel.*



Scheme 41: O–H functionalization reactions of diphenyl diazomethane with alcohols

The unexpected observation prompted us to investigate the underlying mechanism of this O–H functionalization reaction and to evaluate the possibility of proton or carbene transfer reaction pathway under dark and light conditions. We then performed detailed computational studies at the same calculation level of theory with **69a**, HFIP, TFE and *i*PrOH as the model substrates. Based on Mayr's nucleophilicity scale, diphenyl diazomethane should be much less nucleophilic as compared to diazomethane (*N* parameter for **69a** = 5.29 vs. 10.48 for CH₂N₂).²⁵² Taking the acidity of HFIP into account, we firstly considered the direct protonation of diphenyl diazomethane **69a** with HFIP in the dark condition (Figure 25). A weak hydrogen bond interaction between the two molecules of HFIP and diphenyl diazomethane formed, which subsequently converted to the protonation intermediate **INT1** via **TS6** with a reasonable energy barrier of 22.2 kcal/mol. This process could be regarded as a concerted, asynchronous nucleophilic addition of diazo carbon with electrophilic HFIP. After release of nitrogen, benzhydryl cation/hexafluoro isopropoxide ion pair **INT2** easily transferred to final ether product **85a** via **TS7** with a low activation free energy of 2.8 kcal/mol. In addition, we also considered the protonation step with one or three molecules of HFIP, which both present a little higher energy barrier.

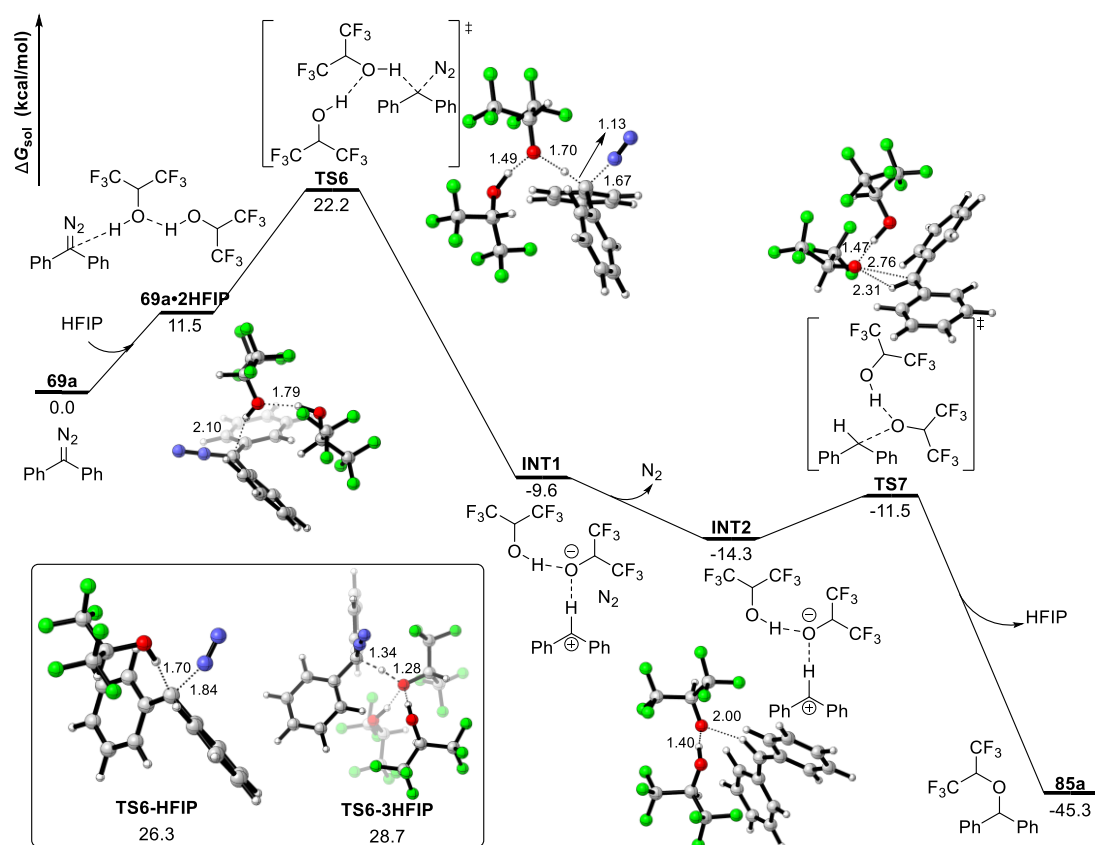
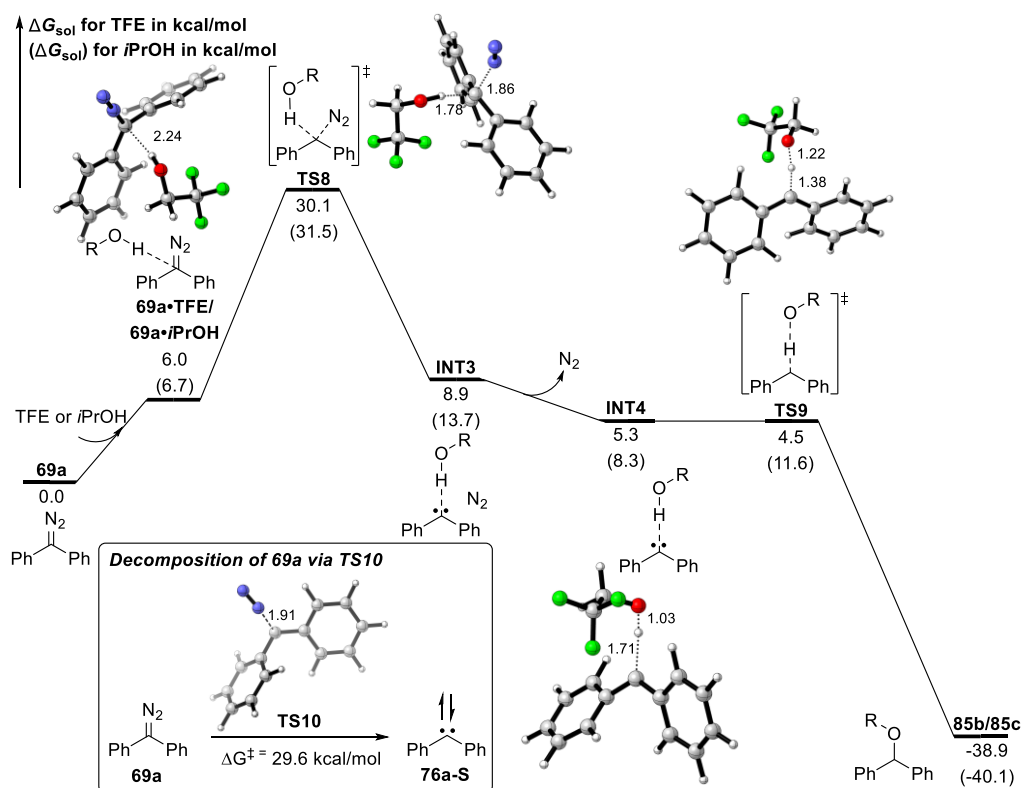


Figure 25: Potential energy surfaces of the reaction of diphenyl diazomethane with HFIP

Figure 26: Potential energy surfaces of the reaction of diphenyl diazomethane with TFE and *i*PrOH

We next investigated the protonation pathway with less acidic alcohols like TFE and *i*PrOH (Figure 26). In the case of TFE, protonation step via **TS8** involving one molecule of TFE was preferred over other transition states involving more molecules of TFE, which led to the initial formation of a hydrogen-bonded, singlet carbene intermediate **INT3** ($\Delta G^\ddagger = 30.1$ kcal/mol). Further release of nitrogen and stepwise protonation-addition reaction of **INT4** directly afforded the product **85b** via a barrierless transition state **TS9**. Notably, the activation free energy for **TS8** was close to the background decomposition process of diphenyl diazomethane **69a** (**TS10**, $\Delta G^\ddagger = 29.6$ kcal/mol), for which the formed singlet carbene thus easily underwent decomposition and rationalized the observed low yield experimentally. Furthermore, the formation of hydrogen-bonded singlet carbene with *i*PrOH was energetically unfavored with an higher energy barrier of 31.5 kcal/mol compared to the decomposition process via **TS10**.

Besides the thermal condition, we hypothesized that overcoming the carbene formation by using photochemical strategy would promote this O–H functionalization. Actually, the diphenyl diazomethane **69a** absorbs visible light from 450 to 550 nm ($\lambda_{\text{max}} = 522$ nm).²⁴¹ Further TD-DFT calculation of **69a** at B3LYP-D3/def2-TZVP level of theory revealed an absorption of 539 nm, which reasoned from HOMO to LUMO excitation. On the basis of photochemical property of **69a**, calculations indicated that initial photoexcitation led to the first excited state, in which intersystem crossing occurred to give more stable triplet species

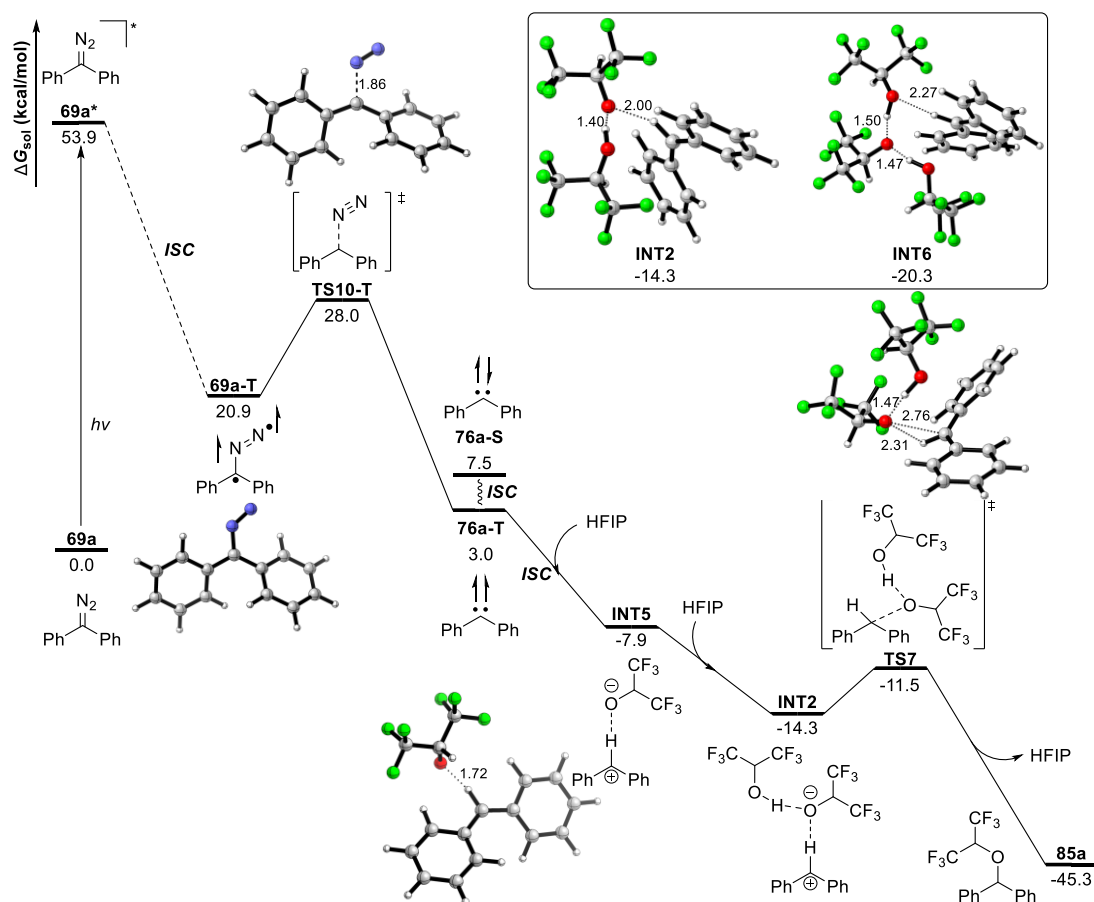


Figure 27: Potential energy surfaces of photochemical reaction with diphenyl diazomethane and HFIP

3.2.3 Computational Data

All calculations were performed using the Gaussian 16, Revision B.01 package.¹⁸³ All structures were optimized at the (U)B3LYP of theory^{204,205} in combination with D3 dispersion corrections.²⁰⁹ All atoms were described with the def2-SVP basis set,²³⁵ in which solvent effects were included implicitly through the use of the PCM model¹⁹⁴ for dichloromethane. Analytical frequency calculations were carried out at the same level of theory in order to confirm each stationary point as either an intermediate (no imaginary frequencies) or a transition state (only one imaginary frequency). Key transition-state structures were confirmed to connect corresponding reactants and products by intrinsic reaction coordinate (IRC) calculations.^{192,193} The electronic energy was then refined using def2-TZVP basis set²³⁵ at the B3LYP-D3 level on the optimized geometries in combination with PCM solvation model. The given Gibbs free energies in dichloromethane were calculated in Table S3 according to the formula: $G_{\text{sol}} = \text{TCG} + E_{\text{sol}}$ (kcal/mol). The CYL View software was employed to show the 3D structures of the studied species.¹⁹⁵ Vertical excitations energies were calculated at the TD-B3LYP-D3 level with the def2-TZVP basis set.

Ab initio molecular dynamics (AIMD) was performed for first excited state of **1a-HFIP** by using ORCA 4.2.1 code,²⁴⁴ and the dynamics trajectories were visualized by VMD software.²⁵⁶ The geometry optimized at B3LYP-D3/def2-SVP level was employed as the initial coordinate and the RIJCOSX technique²⁵⁷ was adapted in simulations to accelerate calculation of energy and force. A 400 fs trajectory was simulated at 298.15 K. In the simulations, stepsize was set to 1.0 fs and TDDFT key word was used to simulate the trajectory of HFIP with first excited state of **1a**.

The searching for minimal energy crossing points (MECPs) was conducted using a modified version of Harvey's code²⁵⁸ (sobMECP)²⁵⁹ interfaced with Gaussian 16.

Table 11: Single Point Energies (E) of MECP

name	$E/\text{a.u.}$	$\Delta E/\text{kcal}\cdot\text{mol}^{-1}$
8a-T	-497.769981	-
MECP-1	-497.764980	5.9
8a-T-HFIP	-1287.016278	-
MECP-2	-1287.008311	5.0

Thermal correction to Gibbs free energies (**TCG**, in Hartree), thermal correction to enthalpies (**TCH**, in Hartree), sum of electronic and thermal free energies (**G**, in Hartree), sum of electronic and thermal enthalpies (**H**, in Hartree), and single point energies in dichloromethane computed at the (U)B3LYP-D3/def2-TZVP level (E_{sol} , in Hartree) are shown in Table 12.

Table 12: Computed Energies of all Stationary Points

Name	TCG/a.u.	TCH/a.u.	G/a.u.	H/a.u.	E/a.u.
1a	0.118345	0.170722	-607.144969	-607.092593	-607.942807
1a-T	0.115692	0.168678	-607.097777	-607.044791	-607.892744
TS1	0.111594	0.166475	-607.083596	-607.028715	-607.878344
N₂	-0.012764	0.008981	-109.452425	-109.430680	-109.573374
77-T	0.108992	0.157297	-497.665362	-497.617057	-498.329593
77-S	0.109189	0.157508	-497.660792	-497.612473	-498.331014
HFIP	0.027248	0.072453	-789.192979	-789.147773	-790.173327
1a-HFIP	0.167420	0.245549	-1396.341381	-1396.263252	-1398.134552
1a-HFIP-T	0.163981	0.243639	-1396.293556	-1396.213898	-1398.082612
TS1-HFIP	0.159384	0.241375	-1396.280217	-1396.198226	-1398.068829
77-T-HFIP	0.155274	0.232230	-1286.861004	-1286.784048	-1288.517267
77-S-HFIP	0.155560	0.231879	-1286.864249	-1286.787929	-1288.526370
77-S'-HFIP	0.156378	0.232115	-1286.859831	-1286.784094	-1288.522350
TS2-HFIP	0.151779	0.227121	-1286.861375	-1286.786033	-1288.519432
82a	0.162861	0.234995	-1286.946984	-1286.874849	-1288.607359
TS3-HFIP	0.158757	0.230683	-1286.850517	-1286.778591	-1288.510166
89a	0.164483	0.234339	-1286.913317	-1286.843460	-1288.571384
TFE	0.027925	0.064312	-452.406604	-452.370217	-452.984507
1a-TFE	0.167760	0.237404	-1059.551242	-1059.481598	-1060.942634
77-S-TFE	0.155410	0.223847	-950.073747	-950.005310	-951.332185
77-S'-TFE	0.156440	0.224091	-950.069694	-950.002042	-951.329224
TS2-TFE	0.153335	0.218506	-950.066304	-950.001133	-951.319902
82d	0.162904	0.226590	-950.163026	-950.099340	-951.421606
TS3-TFE	0.157849	0.223080	-950.064038	-949.998807	-951.323537
89d	0.163403	0.226233	-950.129644	-950.066815	-951.385874
iPrOH	0.080078	0.113731	-194.144569	-194.110916	-194.452797
1a-iPrOH	0.217873	0.287044	-801.286839	-801.217669	-802.407940
77-S-iPrOH	0.208753	0.273860	-691.807499	-691.742392	-692.797329
77-S'-iPrOH	0.209419	0.273875	-691.805197	-691.740741	-692.795788
TS2-iPrOH	0.204825	0.268344	-691.796578	-691.733059	-692.780180
82f	0.214392	0.276127	-691.902844	-691.841109	-692.891189
TS3-iPrOH	0.208881	0.272839	-691.803002	-691.739044	-692.792864
89f	0.216010	0.275868	-691.870691	-691.810832	-692.858186

MeOH	0.028129	0.055138	-115.608793	-115.581784	-115.780704
77-S·MeOH	0.153143	0.214766	-613.269334	-613.207711	-614.124122
77-S'·MeOH	0.154878	0.215182	-613.268784	-613.208480	-614.122510
TS2-MeOH	0.153151	0.209483	-613.259529	-613.203196	-614.107310
82e	0.163698	0.217645	-613.363081	-613.309134	-614.216625
TS3-MeOH	0.155784	0.214205	-613.267464	-613.209043	-614.120681
89e	0.163426	0.217219	-613.334633	-613.280840	-614.185198
TS4	0.208915	0.269200	-728.912426	-728.852141	-729.941279
TS4'	0.255731	0.325762	-844.544297	-844.474267	-845.755510
tBuOH	0.106199	0.142530	-233.411628	-233.375297	-233.788211
77-S·tBuOH	0.235041	0.302611	-731.074953	-731.007382	-732.132590
77-S'·tBuOH	0.234375	0.302859	-731.071841	-731.003357	-732.129975
TS2-tBuOH	0.233089	0.297136	-731.060733	-730.996686	-732.113734
82g	0.244296	0.305165	-731.155813	-731.094944	-732.214473
TS3-tBuOH	0.236496	0.301568	-731.068643	-731.003571	-732.127578
89g	0.242698	0.304739	-731.133103	-731.071063	-732.189145
PFTB	0.027853	0.080068	-1125.970099	-1125.917884	-1127.350093
77-S·PFTB	0.155796	0.238026	-1623.644791	-1623.562560	-1625.705375
77-S'·PFTB	0.157169	0.239507	-1623.637697	-1623.555359	-1625.699893
TS2-PFTB	0.152734	0.234534	-1623.647164	-1623.565365	-1625.705034
82b	0.164171	0.242383	-1623.720045	-1623.641832	-1625.780033
TS3-PFTB	0.157938	0.235908	-1623.627171	-1623.549201	-1625.683988
89b	0.165418	0.241617	-1623.684141	-1623.607941	-1625.741343
4-CN-phenol	0.071924	0.111710	-399.369334	-399.329549	-399.889730
77-S·phenol	0.199583	0.271079	-897.039711	-896.968214	-898.241270
77-S'·phenol	0.201467	0.271655	-897.035922	-896.965735	-898.239063
TS2-phenol	0.195597	0.266521	-897.039405	-896.968481	-898.236894
82c	0.208044	0.274159	-897.116847	-897.050732	-898.320359
TS3-phenol	0.202480	0.270034	-897.025689	-896.958134	-898.227126
89c	0.207009	0.273589	-897.089073	-897.022493	-898.290496
83a	0.159456	0.211257	-501.063164	-501.011364	-501.778615
TS2-83a	0.289874	0.366155	-998.718144	-998.641863	-1000.113130
82h	0.297747	0.373563	-998.812736	-998.736921	-1000.210305
TS3-83a	0.289266	0.370137	-998.720736	-998.639865	-1000.117748
89h	0.296836	0.373234	-998.786705	-998.710307	-1000.181223
TS5a	0.293999	0.369950	-998.727100	-998.651148	-1000.126618
84a	0.295944	0.373258	-998.827433	-998.750119	-1000.222016
83b	0.107159	0.153296	-422.529012	-422.482875	-423.107568
TS2-83b	0.236632	0.307618	-920.185070	-920.114084	-921.443400
82i	0.245104	0.315802	-920.283287	-920.212588	-921.545657
TS3-83b	0.239071	0.312115	-920.189034	-920.115989	-921.450593

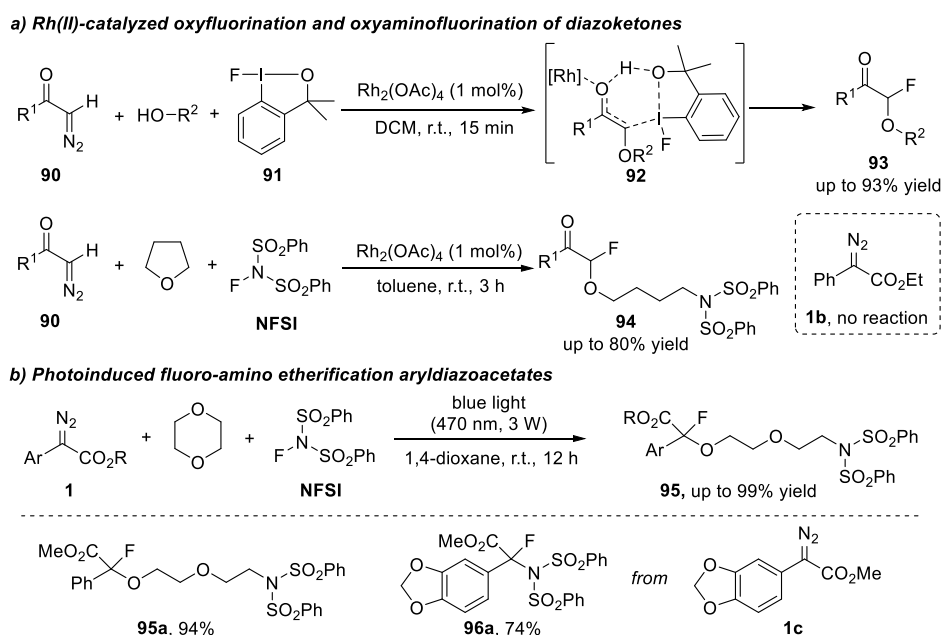
89i	0.245057	0.315263	-920.254716	-920.184509	-921.512939
TS5b	0.241219	0.311908	-920.191534	-920.120845	-921.454417
84b	0.245029	0.315372	-920.289635	-920.219292	-921.549145
69a-2HFIP	0.255219	0.358804	-2188.673585	-2188.570000	-2191.477344
TS6	0.246954	0.354530	-2188.648413	-2188.540838	-2191.452075
INT1	0.243093	0.355198	-2188.694875	-2188.582771	-2191.498879
INT2	0.245056	0.344328	-2079.247526	-2079.148255	-2081.922098
TS7	0.248299	0.343908	-2079.243869	-2079.148260	-2081.920980
INT5	0.195524	0.270380	-1290.029704	-1289.954848	-1291.715430
INT6	0.293972	0.419910	-2868.465074	-2868.339136	-2872.126789
85a	0.200275	0.273297	-1290.101029	-1290.028006	-1291.780772
TS6-HFIP	0.198077	0.279624	-1399.438439	-1399.356891	-1401.250523
TS6-3HFIP	0.301257	0.427695	-2977.853281	-2977.726843	-2981.642070
69a	0.157223	0.209102	-610.286133	-610.234254	-611.105515
TS10	0.151350	0.205523	-610.232724	-610.178551	-611.052637
76a-S	0.148530	0.195853	-500.809870	-500.762547	-501.498799
69a-T	0.154820	0.207375	-610.253086	-610.200532	-611.069864
TS10-T	0.150724	0.204829	-610.237914	-610.183810	-611.054371
76a-T	0.146190	0.195211	-500.820536	-500.771515	-501.503567
69a-TFE	0.201993	0.275454	-1062.688517	-1062.615056	-1064.097281
TS8-TFE	0.199474	0.271752	-1062.646437	-1062.574160	-1064.056335
INT3-TFE	0.190022	0.272124	-1062.676051	-1062.593949	-1064.080766
INT4-TFE	0.194745	0.261670	-953.228221	-953.161295	-954.505102
INT4-T-TFE	0.191863	0.261308	-953.224783	-953.155338	-954.497027
TS9-TFE	0.191513	0.257180	-953.228885	-953.163218	-954.503074
85b	0.203927	0.265214	-953.305927	-953.244639	-954.584595
TS11-TFE	0.197935	0.26130	-953.194482	-953.131117	-954.470875
INT7-TFE	0.200315	0.263405	-953.202288	-953.139198	-954.477426
69a-<i>i</i>PrOH	0.254252	0.325181	-804.424538	-804.353609	-805.564523
TS8-<i>i</i>PrOH	0.250358	0.321713	-804.380516	-804.309160	-805.521250
INT3-<i>i</i>PrOH	0.245698	0.322458	-804.405412	-804.328652	-805.544867
INT4-<i>i</i>PrOH	0.246708	0.311958	-694.959895	-694.894644	-695.968339
INT4-T-<i>i</i>PrOH	0.243245	0.311149	-694.962260	-694.894356	-695.965474
TS9-<i>i</i>PrOH	0.243691	0.306785	-694.955655	-694.892561	-695.960143
85c	0.255866	0.314910	-695.043245	-694.984200	-696.054679
TS11-<i>i</i>PrOH	0.250122	0.311105	-694.939784	-694.878801	-695.949611
INT7-<i>i</i>PrOH	0.253546	0.313169	-694.954521	-694.894898	-695.963127

3.3 Mechanism Study of Photoinduced Fluoro-amino Etherification Reactions

3.3.1 Brief Introduction: Electrophilic Fluorination of Oxonium Ylide

Besides the rearrangement of *in situ* generated ylide intermediate via carbene transfer reaction, the ylides can also be trapped by further nucleophilic addition or substitution reaction.²⁶⁰ In 2016, the Szabó group reported a new oxyfluorination reaction of diazoketones **90** with alcohol and fluoro-benziodoxole **91** (Scheme 42a).²⁶¹ Further detailed mechanism study supported an enol intermediate formation from onium ylide, followed by further electrophilic addition with fluorination reagent **91**.²⁶² Recently, they extended this methodology to the oxy-aminofluorination reaction of acceptor-only diazoketones **90** with *N*-fluorobenzenesulfonimide (NFSI) and tetrahydrofuran.²⁶³ Corresponding computational investigation suggested a nucleophilic addition of ylide intermediate onto electrophilic fluorination reagent NFSI.²⁶⁴ However, donor-acceptor diazoacetate **1b** was incompatible in these Rh-catalyzed reaction due to the lower reactivity of donor-acceptor carbenoids.

With the recently emerging and efficient photochemical carbene methodology, our group identified donor-acceptor free carbene adjusted reactivity of aryl diazoacetate **1** and realized its geminal oxyfluorination reactions with NFSI and 1,4-dioxane solvent (Scheme 42b).²⁶⁵ This reaction opened up a new strategy of photochemical carbene transfer that can be conducted using stoichiometric quantities of reactants, which led to fluoroamino etherification product in nearly quantitative yield. Notably, when using more electron-rich diazoacetates like methylenedioxy-substituted aryl diazoacetate **1c**, this reaction would lead to a formal N–F insertion product **96a** instead of fluoro-amino etherification.



Scheme 42: Geminal oxyfluorination of diazocarbonyl compounds

3.3.2 Computational Study

For a better understanding of this substrate-controlled photochemical carbene transfer reaction, we performed detailed DFT calculations at B3LYP/6-311+G(2d,2p)/(1,4-dioxane)//B3LYP/6-31G(d) level of theory. We started our calculations from the free singlet carbene **77-S**, which has already been proved in the visible light-induced carbene transfer reaction (Figure 29). The facile, reversible ylide formation via transition state **TS1** led to coexistence of singlet carbene and ylide intermediate **INT1** ($\Delta G^\ddagger = 9.8$ kcal/mol, $\Delta G_R = -0.9$ kcal/mol). Due to the influence of concentration, we have already considered energy correction of 1,4-dioxane in the energy surface due to its high concentration (11.72 mol/L), which resulted in the preference of the ylide formation from singlet carbene. Ylide **INT1** then underwent fluorination reaction through nucleophilic addition onto NFSI to yield oxonium ion **INT2**, which required an activation free energy of 21.0 kcal/mol via **TS2**. The final nucleophilic substitution, ring opening process of **INT2** proceeded rapidly via a low-lying transition state **TS3** with an energy barrier of 4.2 kcal/mol to give the final fluoro-amino etherification product **95a**.

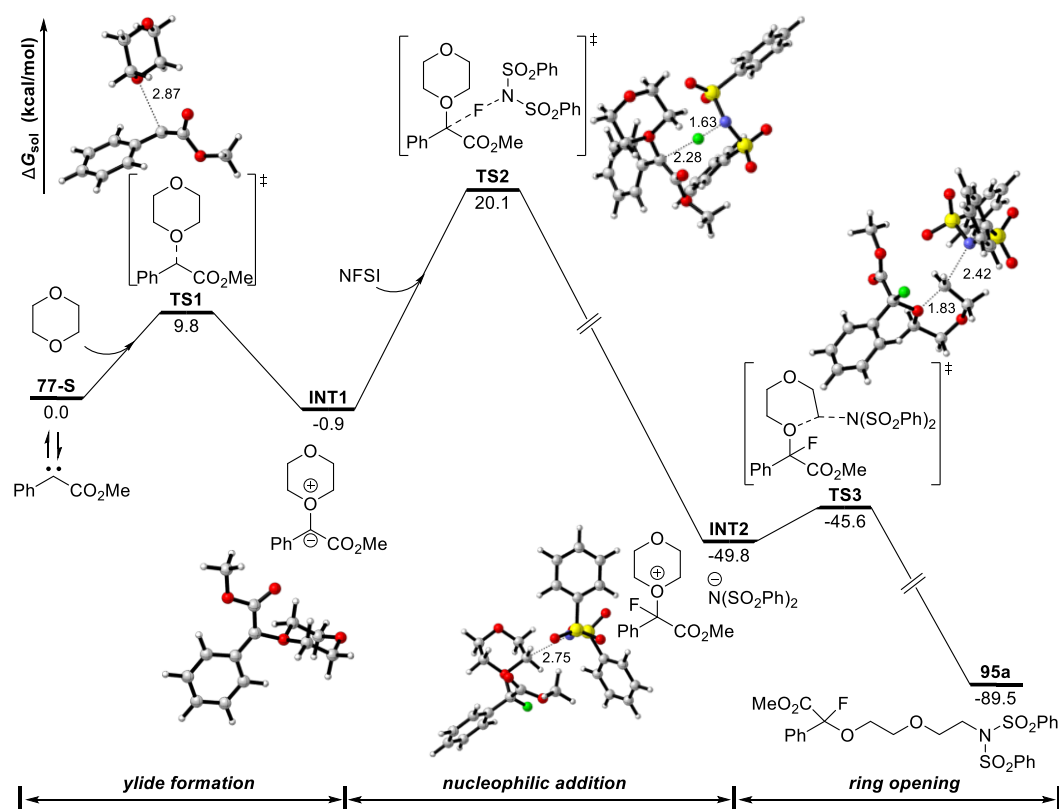


Figure 29: Potential energy surfaces of photochemical fluoro-amino etherification

Further calculations indicated that the formal N-F insertion reaction (via **TS4**) or direct ammonium ylides formation (via **TS5**) of the carbene intermediate with NFSI had higher activation free energy barriers of 22.5 or 28.1 kcal/mol, respectively (Figure 30). Both pathways were energetically unfavorable compared to fluorination of onium ylide via **TS2**. The energy difference of 2.4 kcal/mol (**TS2** vs. **TS4**) reflected a high chemoselectivity, which was consistent with experiment result.

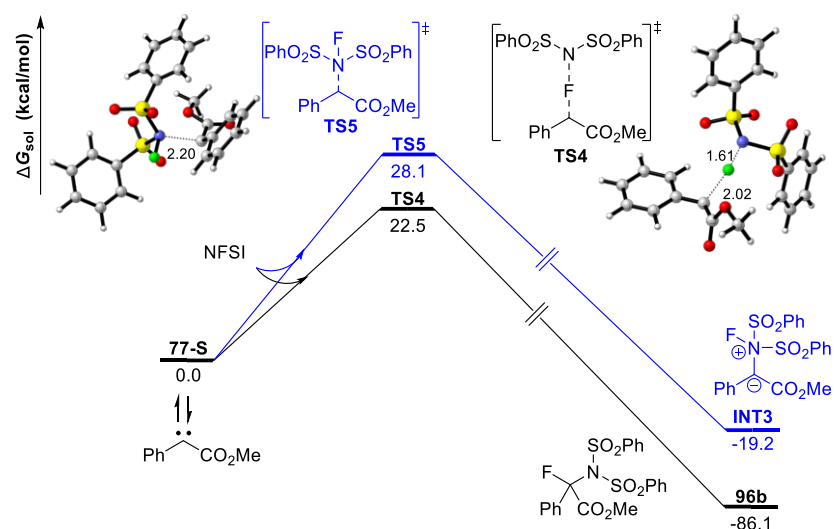


Figure 30: Potential energy surfaces of reaction of singlet carbene with NFSI

Furthermore, singlet free-carbene **97** with electron-rich substituent preferred a formal N–F insertion process to afford **96a** through an electrophilic addition of NFSI onto more nucleophilic carbene carbon (**TS9**, $\Delta G^\ddagger = 21.8$ kcal/mol). Contrarily, due to the electron-donating group, the reduced electrophilicity of **97** resulted in higher energy barriers of ylide formation and further fluorination of onium ylide **INT4** (Figure 31). This reversed energy difference of 3.7 kcal/mol (**TS7** vs. **TS9**) indicated a chemoselective formation of N–F insertion product **96a**.

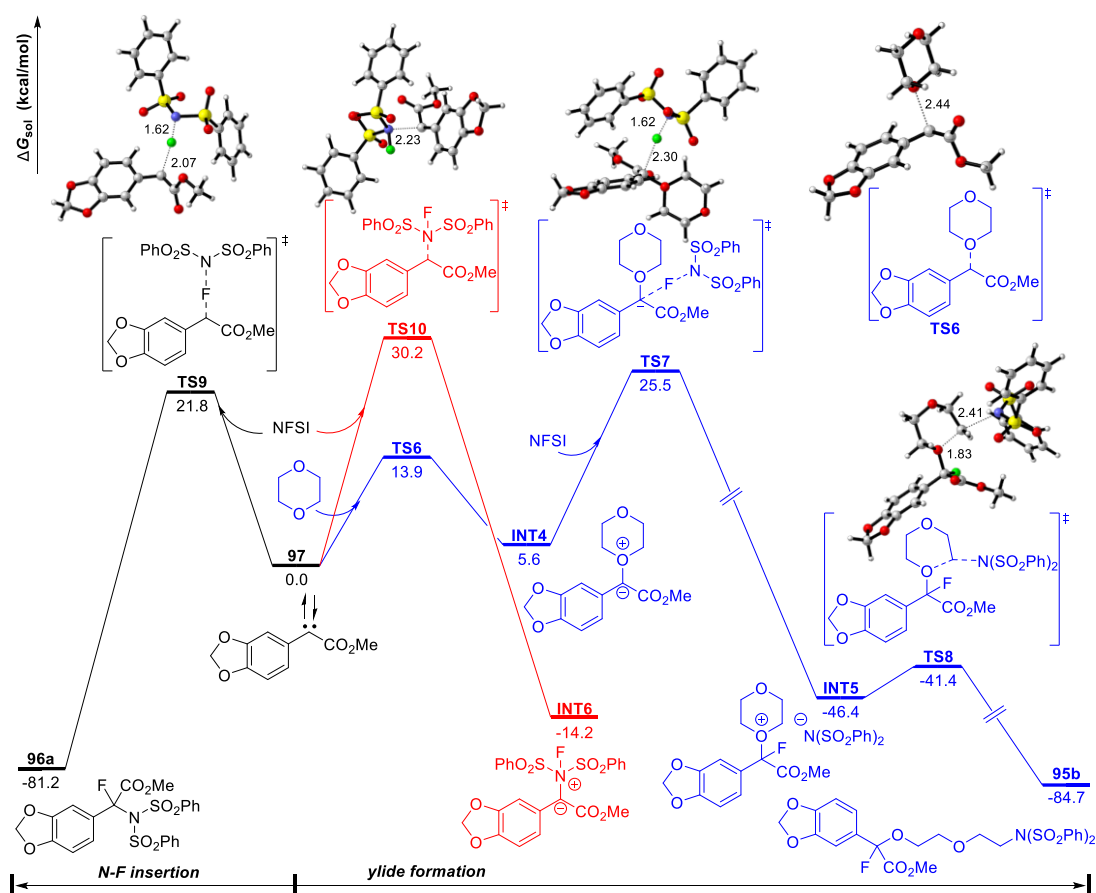


Figure 31: Potential energy surfaces of photochemical carbene transfer of 1c with NFSI

3.3.3 Computational Data

All of the calculations were performed with the Gaussian 09 program.¹⁸² The hybrid B3LYP functional^{204,205} and the 6-31G(d) basis set¹⁸⁷⁻¹⁸⁹ were applied for the optimization of all stationary points in the gas phase. Frequency calculations were performed to confirm that each stationary point is either a minimum or a transition structure. Key transition-state structures were confirmed to connect corresponding reactants and products by intrinsic reaction coordinate (IRC) calculations.^{192,193} Solvation energies in 1,4-dioxane ($\epsilon = 2.2099$) were evaluated by IEFPCM calculations with radii and non-electrostatic terms for SMD solvation model²⁰⁸ using the gas-phase optimized structures. To improve the calculation accuracy, single-point energies calculations in the chloroform were computed at the B3LYP level of theory with the 6-311+G(2d,2p) basis set^{211,266} for all the atoms. The given Gibbs free energies in 1,4-dioxane were calculated according to the formula: $G_{sol} = TCG + \Delta G_{sol} + E + 1.89$ kcal/mol, and an additional term of $RT\ln(11.72/1) = 1.46$ kcal/mol at 298 K is added for 1,4-dioxane. The CYL View software was employed to show the 3D structures of the studied species.¹⁹⁵

Thermal correction to Gibbs free energies (**TCG**, in Hartree), sum of electronic and thermal enthalpies (**H**, in Hartree), sum of electronic and thermal free energies (**G**, in Hartree), solvation Gibbs free energies in 1,4-dioxane (ΔG_{sol} , in Hartree), and single point energies computed at the B3LYP/6-311+G(2d,2p)//B3LYP/6-31G(d) (**E**, in Hartree) are shown in Table 13.

Table 13: Computed Energies of all Stationary Points

Name	TCG/a.u.	H/a.u.	G/a.u.	ΔG_{sol} /a.u.	E/a.u.
77-S	0.109730	-497.952560	-498.000926	-0.009770	-498.269390
1,4-dioxane	0.094867	-307.528929	-307.563424	-0.004939	-307.763126
NFSI	0.159487	-1714.703919	-1714.772377	-0.015180	-1715.331037
TS1	0.222245	-805.484796	-805.551031	-0.011701	-806.032200
INT1	0.230133	-805.509801	-805.570855	-0.012777	-806.056101
TS2	0.411942	-2520.211979	-2520.319549	-0.023186	-2521.377684
INT2	0.414278	-2520.313674	-2520.422179	-0.029025	-2521.485652
TS3	0.414123	-2520.312349	-2520.419364	-0.025942	-2521.481856
95a	0.415708	-2520.389464	-2520.497710	-0.020411	-2521.559006
TS4	0.289723	-2212.651829	-2212.748586	-0.020463	-2213.586625
96b	0.302320	-2212.839059	-2212.928075	-0.019039	-2213.773652
TS5	0.294355	-2212.651191	-2212.743541	-0.020331	-2213.582404
INT3	0.293240	-2212.727692	-2212.823238	-0.020443	-2213.656522
97	0.121963	-686.469304	-686.523442	-0.011948	-686.863690
TS6	0.237074	-994.000296	-994.069839	-0.012849	-994.623532
INT4	0.242759	-994.018572	-994.084969	-0.013904	-994.641452
TS7	0.423887	-2708.721947	-2708.835407	-0.024427	-2709.964136
INT5	0.425166	-2708.825339	-2708.940753	-0.030404	-2710.073959

TS8	0.425631	-2708.823593	-2708.936862	-0.027150	-2710.069649
95b	0.427393	-2708.899932	-2709.014362	-0.021638	-2710.145984
TS9	0.301644	-2401.168707	-2401.27159	-0.022971	-2402.181344
96a	0.314348	-2401.349414	-2401.444254	-0.020322	-2402.360760
TS10	0.305573	-2401.164208	-2401.263194	-0.021490	-2402.173275
INT6	0.305410	-2401.238008	-2401.339272	-0.021639	-2402.243820

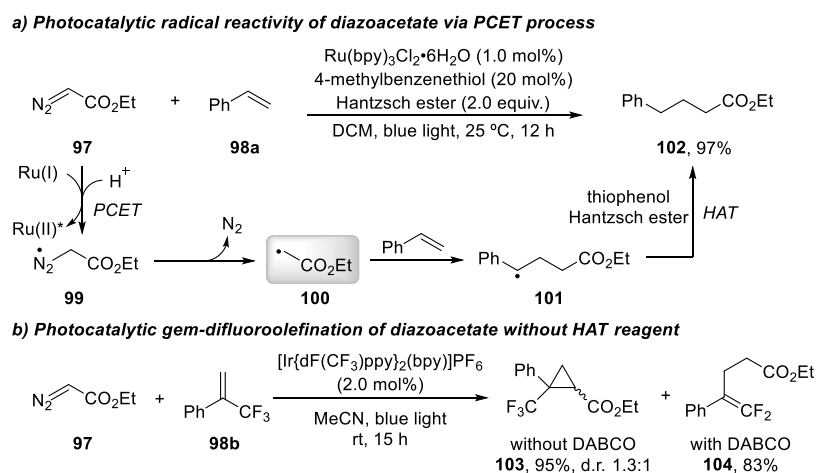
3.4 Mechanism Study of Photocatalytic Gem-Difluoroolefination Reactions

3.4.1 Brief Introduction:

For as much as the suitable absorption of aryl diazoacetates and diaryl diazomethanes in the visible spectrum, they were recently found broad application in efficient and sustainable carbene transfer reactions through photoinduced generation of free carbene. However, due to the primary absorption of ethyl diazoacetate (EDA, **97**) in the UV light region, photolysis of this acceptor-only diazo compound under ultraviolet light limits its utilization. Recently, the use of photosensitizers promotes the transformation of EDA in visible light, which undergoes fundamentally different reaction pathways via single electron (SET) or energy transfer (EnT).

Under photocatalytic conditions, a typical proton coupled electron transfer (PCET) of EDA via oxidative quenching of photocatalyst led to a key carbon-centered radical **100** for further application (Scheme 43). In this context, Doyle,²⁶⁶ Gryko²⁶⁷ and Meggers²⁶⁸ have reported initial applications of such photocatalytic radical-mediated strategies of EDA under blue light irradiation. For example, the Doyle group introduced this methodology to a hydroalkylation reaction of styrene via thiol-assisted hydrogen atom transfer (HAT).²⁶⁶ In this case, the Hantzsch ester was essential to allow for reductive process and deliver the ethyl 4-phenylbutanoate **102** (Scheme 43a).

Based on these works, our group envisioned that the method for generation of radical **100** could be competent in the synthesis of *gem*-difluoroolefins via radical-mediated defluorination reaction with α -trifluoromethyl styrene **98b** (Scheme 43b). Actually, *gem*-difluoroolefins represent important application in medicinal chemistry, and their synthesis still remains a challenge.²⁶⁹ Gratifyingly, *gem*-difluoroolefin **104** was selectively obtained in 83% yield in presence of triethylenediamine (DABCO) under the photocatalytic condition with iridium catalyst.²⁷⁰ However, without the additive of DABCO, we found an efficient cyclopropanation occurred to afford α -CF₃ cyclopropane **103**.



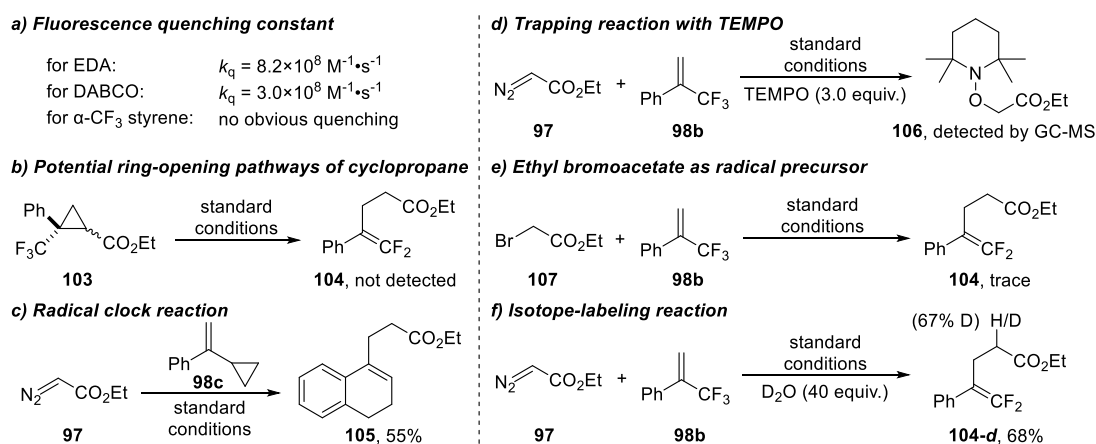
Scheme 43: Different reactivity of diazoacetates in photoredox reactions

3.4.2 Control Experiments

Considering the unexpected chemoselectivity that controlled by additive, we then tried to rationalize its detailed mechanisms experimentally and theoretically. Before the computational study, my colleague conducted a series of control experiments to reason the photochemical property of EDA and role of DABCO (Scheme 44).²⁷⁰ Firstly, Stern-Volmer experiments showcased a fluorescence quenching of the iridium photocatalyst in the presence of DABCO and EDA near the diffusion limit (Scheme 44a). They also identified that cyclopropane **103** could not convert to *gem*-difluoroolefin **104** under photocatalytic conditions, which ruled out a potential ring opening pathway (Scheme 44b). Furthermore, the reaction of EDA with α -cyclopropyl styrene **98c** resulted in ring opening of the cyclopropane ring and yielded dihydronaphthalene **105**, which indicated a benzyl radical intermediate formation (Scheme 44c). Similarly, when TEMPO was served as radical scavenger in the system, reaction was inhibited and corresponding radical adduct **106** was detected by GC-MS (Scheme 44d). Moreover, to prove the participation of radical intermediate **100** as shown in Scheme 43a, 2-bromo ethyl acetate **107** replaced the EDA as a radical precursor, which is known to form radical **100** via debromination under photoredox conditions.²⁷¹ However, only trace amount of product **104** was observed in the crude NMR analysis (Scheme 44e). Finally, to prove the participation of radical intermediate **100** as shown in Scheme 43a, 2-bromo ethyl acetate **107** replaced the EDA as a radical precursor, which is known to form radical **100** via debromination under photoredox conditions.²⁷¹ However, only trace amount of product **104** was observed in the crude NMR analysis (Scheme 44e). Additionally, to trace the proton source of the α -H of the ester group in *gem*-difluoroolefin **104**, we examined the reaction in presence of D₂O (Scheme 44f). Deuterium label was then exclusively found in the α -position to ester group in **104-d**. To be more rigorous, we also tested *gem*-difluoroolefin **104** in the presence of D₂O under standard reaction conditions, yet no deuterium label was found. Further potential proton exchange reaction was conducted with EDA, DABCO and D₂O under catalyst-free conditions, yet no deuterium was incorporated.

Importantly, to trace the proton source of the α -H of the ester group in *gem*-difluoroolefin **104**, we examined the reaction in presence of D₂O (Scheme 44f). Deuterium label was then exclusively found in the α -position to ester group in **104-d**. To be more rigorous, we also tested *gem*-difluoroolefin **104** in the presence of D₂O under standard reaction conditions, yet no deuterium label was found. Further potential proton exchange reaction was conducted with EDA, DABCO and D₂O under catalyst-free conditions, yet no deuterium was incorporated.

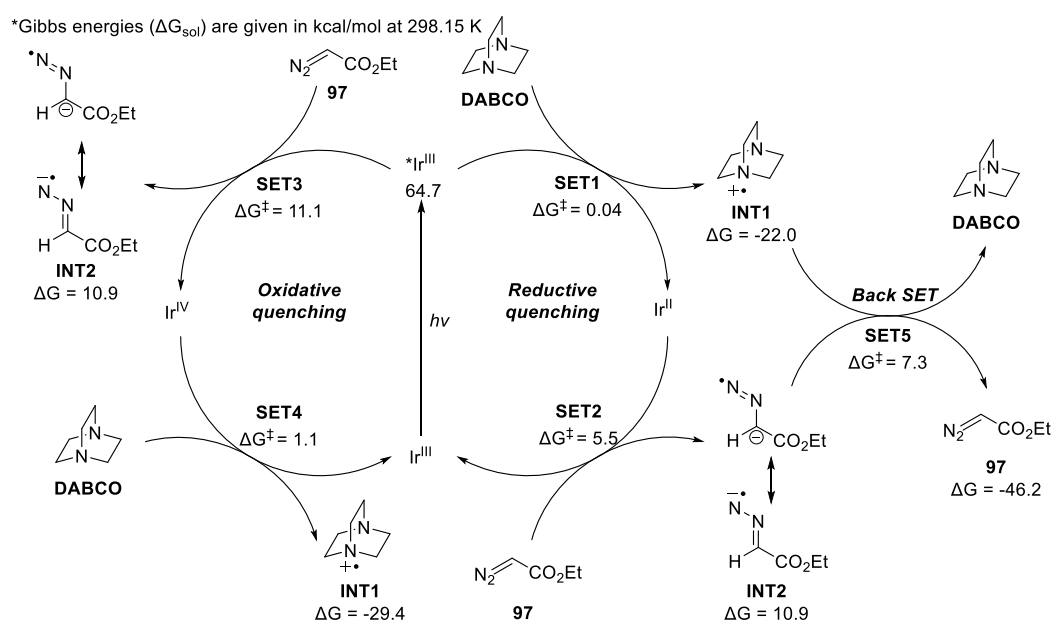
This control experiment part was performed by Fang Li.



Scheme 44: Control experiments of photocatalytic *gem*-difluoroolefination reactions

3.4.3 Computational Study

According to these key control experiments, we then performed detailed DFT calculations on this *gem*-difluoroolefination reaction at (U)M06-2X-D3/def2-TZVPP(MeCN)//(U)B3LYP-D3(BJ)/def2-SVP(MeCN) level of theory. It is well documented that the photoexcited species $^*Ir^{III}$ can behave not only as an oxidant but also as a reductant.²⁷² Correspondingly, the photocatalytic oxidative ($Ir^{III}/^*Ir^{III}/Ir^{IV}/Ir^{III}$) or reductive quenching ($Ir^{III}/^*Ir^{III}/Ir^{II}/Ir^{III}$) cycle of the $[Ir\{dF(CF_3)ppy\}_2(bpy)]PF_6$ photocatalyst was computationally evaluated in our case (Scheme 45). Irradiation of this iridium catalyst with blue light led to its excited state $^*Ir^{III}$ via metal to ligand charge transfer (MLCT), which could either be oxidized or reduced. In the reductive quenching ($Ir^{III}/^*Ir^{III}/Ir^{II}/Ir^{III}$) cycle, DABCO could easily reduce the $^*Ir^{III}$ to Ir^{II} , and the relative free energy barrier of **SET1** is 0.04 kcal/mol calculated according to Marcus-Hush theory.²⁷³ In addition, the generated Ir^{II} then reduced the EDA with a calculated energy barrier of 5.5 kcal/mol (**SET2**), which regenerated the ground state of Ir^{III} catalyst and radical anion **INT2**. However, a simple back electron transfer (**SET5**) between a putative radical anion **INT2** and DABCO⁺ radical cation **INT1** was energetically preferred, which made the whole reductive quenching pathways reversible and unproductive. Furthermore, we also considered the oxidative quenching of EDA with $^*Ir^{III}$, which was unfavorable due to its high free energy barrier of 11.1 kcal/mol (**SET3**). This unfeasible calculated oxidative quenching process was consistent with comparison of their redox potentials (EDA: $E_{red} = -1.28$ V, vs SCE; $^*Ir^{III}$: $E_{red} = -1.00$ V, vs SCE).²⁷⁰



Scheme 45: Relative free energies of oxidative quenching and reductive quenching of $^*Ir^{III}$.

Excepting the single electron transfer pathways, energy transfer of EDA with photocatalyst that generates triplet carbene species **INT3** has also been taken into account (Figure 32). The calculated singlet–triplet energy gap (ΔG_{S-T}) of EDA was 37.6 kcal/mol, which was much lower than that of Ir^{III} ($\Delta G_{S-T} = 64.7$ kcal/mol). Thus, computational results suggested that the triplet-triplet energy transfer from the photoexcited $^*Ir^{III}$ species to EDA **97**, leading to the

excited **97-T**, was applicable in this reaction. This was also in line with our previous observation of cyclopropanation via triplet carbene (Scheme 43b) and previous report of dye-sensitized reactions of ethyl diazoacetate by the Gryko group.²⁶⁷ After the formation of **97-T**, a facile denitrogenation process occurred through **TS1** with a low energy barrier of 10.2 kcal/mol, leading to triplet carbene **INT3**. Then further radical-like addition of triplet carbene to α -trifluoromethyl styrene **98b** proceeded via low-lying transition state **TS2** ($\Delta G^\ddagger = 7.6$ kcal/mol) and afforded triplet diradical species **INT4** exoergically.

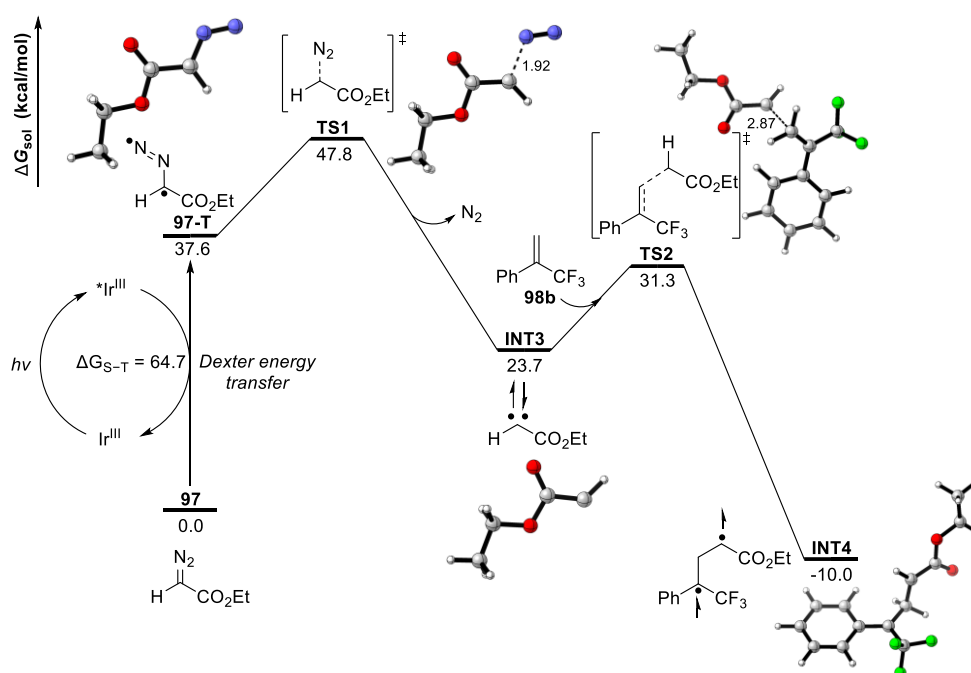


Figure 32: Potential energy surfaces of triplet carbene reactivity via energy transfer process

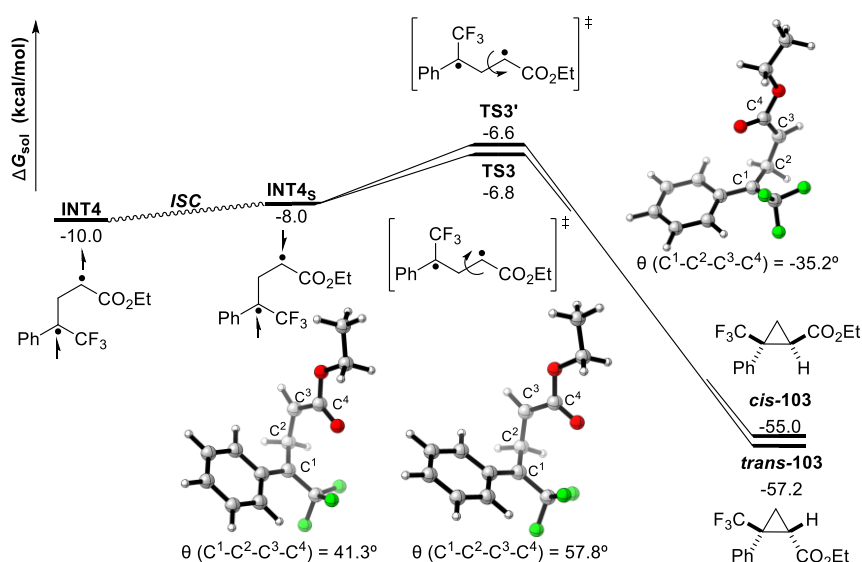
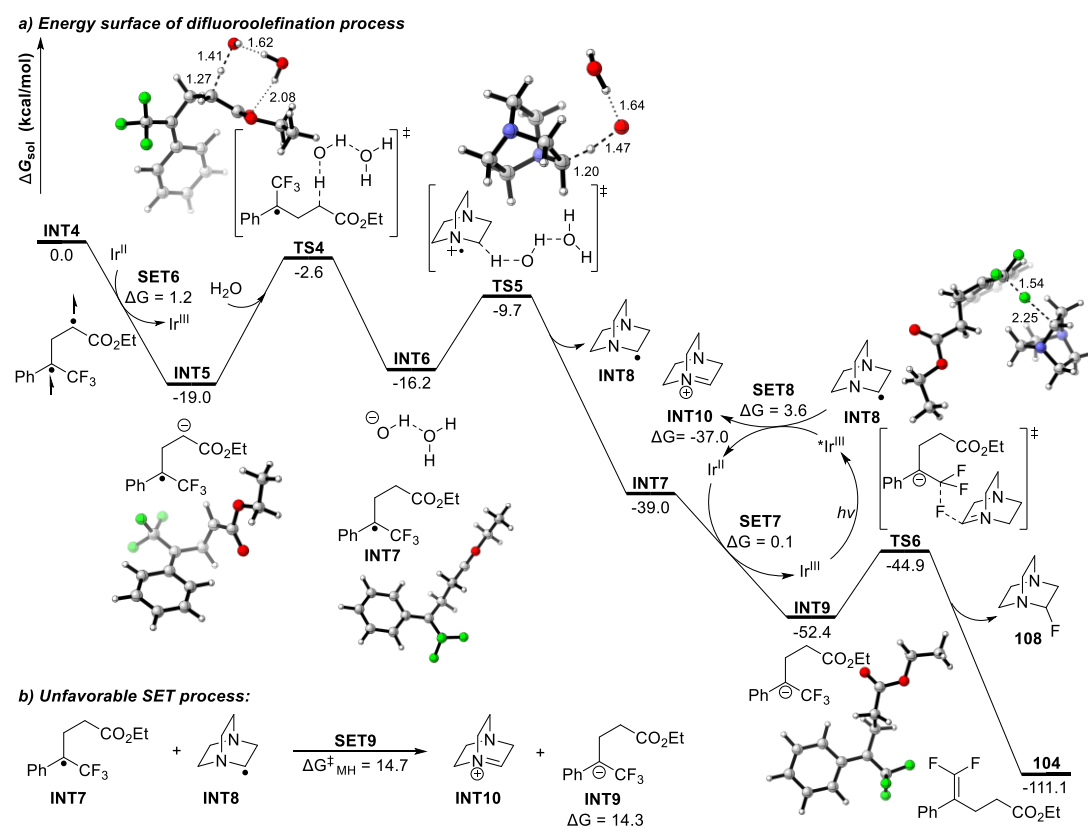


Figure 33: Potential energy surfaces of cyclopropanation process from **INT4**.

After the formation of **INT4**, we then considered further step without participation of DABCO (Scheme 43b). Open shell singlet intermediate **INT4s**, which generated from **INT4** via an intersystem crossing, proceeded to give trifluoromethylated cyclopropanes **cis-103** or **trans-**

103 via facile single bond rotational transition state **TS3** and **TS3'**, respectively (Figure 33). A minuscule energy difference of 0.2 kcal/mol between clockwise and anti-clockwise rotations indicated a poor diastereoselectivity, which was consistent with our experimental result.

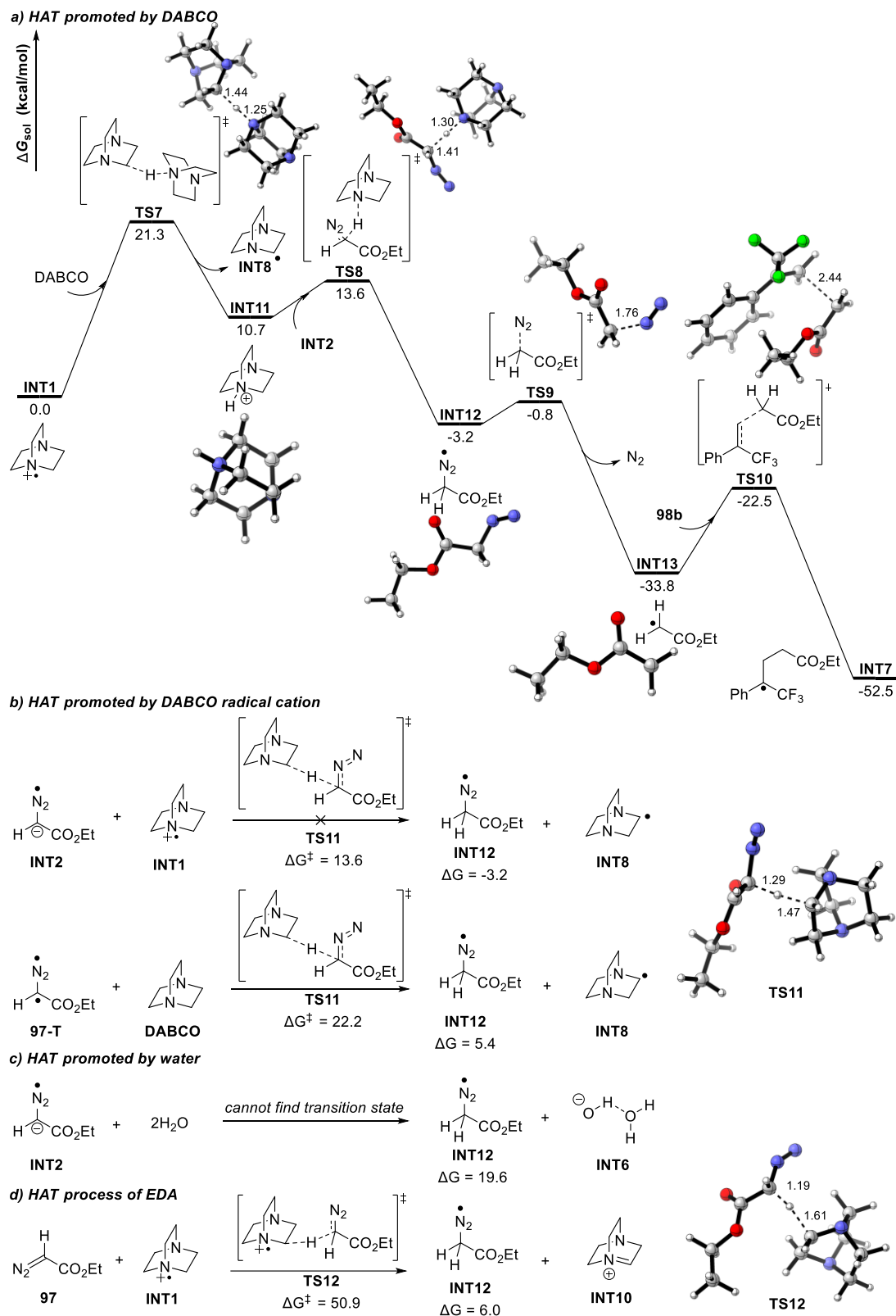
In the presence of DABCO, Ir^{II} could be readily generated through the reductive quenching as shown in Scheme 45, and subsequently reduced diradical **INT4** to radical anion species **INT5** with a small SET barrier of 1.2 kcal/mol (Scheme 46). Further protonation of this key intermediate **INT5** with trace water molecules gave **INT6** and **INT7**, which rationalized for the incorporation of deuterium in experiments. Besides that, concomitant formation of strongly basic hydroxide ion **INT6** then explained the unusual deuterium content in the Scheme 44f. Deprotonation of DABCO radical cation **INT1** led to DABCO radical **INT8** under the basic condition via **TS5**. In addition, further reduction of **INT7** to carbanion intermediate **INT9** could not be accessed by DABCO radical **INT8** (Scheme 46b). Instead, another photoredox cycle of $^*\text{Ir}^{\text{III}}$ facilitated this process and released the crucial iminiumion intermediate **INT10**, which finally promoted defluorination step via **TS6** with an energy barrier of 7.5 kcal/mol to give the *gem*-difluoroolefin product **104**.



Scheme 46: Potential energy surfaces of *gem*-difluoroolefination process via electron transfer process

Apart from the above calculated pathways, we have also considered other possible HAT processes. Firstly, HAT process between DACBO and DABCO radical cation **INT1** formed radical **INT8** and the cationic species **INT11**, which could easily protonate the radical anion **INT2**, leading to radical species **INT12** (Scheme 47a). While the whole process needed an activation free energy of 21.3 kcal/mol, it was energetically unfavored compared to previous

proposal. In addition, a potential transition state of HAT between **INT1** and **INT2** was located (Scheme 47b). In fact, intrinsic reaction coordinate (IRC) calculation indicated a HAT step between triplet state **97-T** and DABCO instead. Furthermore, water-assisted HAT of **INT2** or direct HAT of EDA with **INT1** were both computationally unfavored (Scheme 47c and d).



Scheme 47: Relative free-energy profile of several possible HAT processes

3.4.4 Computational Data

All calculations were performed using the Gaussian 16 program.¹⁸³ The (U)B3LYP functional^{204,205} together with Grimme's dispersion correction²⁰⁹ (denoted (U)B3LYP-D3BJ) and the def2-SVP basis set²³⁵ were applied for the optimization of all stationary points in the acetonitrile, in which the solvent effects ($\epsilon = 35.688$) were evaluated by SMD solvation model.²⁰⁸ Analytical frequency calculations were carried out at the same level of theory in order to confirm each stationary point as either an intermediate (no imaginary frequencies) or a transition state (only one imaginary frequency). Key transition-state structures were confirmed to connect corresponding reactants and products by intrinsic reaction coordinate (IRC) calculations.^{192,193} The electronic energy in the acetonitrile was then refined using def2-TZVPP basis set²³⁵ at the (U)M06-2X level^{184,185} on the optimized geometries in combination with D3 dispersion corrections.²⁰⁹ The given Gibbs free energies in acetonitrile were calculated according to the formula: $G_{\text{sol}} = \text{TCG} + E_{\text{sol}}$. The CYLview software was employed to show the 3D structures of the studied species.¹⁹⁵

To get more details of the singlet electron transfer (SET) process, we estimated the free energy barrier of SET process using the Marcus-Hush theory,²⁷³ which can be calculated according to the following formula:

$$\Delta G_{\text{MH}}^{\ddagger} = \frac{(\Delta G_r + \lambda)^2}{4\lambda}$$

Where ΔG_r is the Gibbs free energy change of the SET step, λ is the reorganization energy including inner sphere energy and outer sphere energy. However, the outer sphere energy is often much larger than the inner sphere contribution. Hence, the outer sphere reorganization energy (λ_{outer}) can be regarded as the total reorganization energy, which can be calculated according to the following formula:

$$\lambda = \lambda_{\text{outer}} = 332 \left(\frac{1}{2r_1} + \frac{1}{2r_2} - \frac{1}{R} \right) \left(\frac{1}{\epsilon_{\text{opt}}} - \frac{1}{\epsilon_s} \right)$$

Where r_1 and r_2 are the radii of electron donor and acceptor, R is the sum of r_1 and r_2 , ϵ_{opt} and ϵ_s is the high frequency (optical) dielectric constant and static dielectric constant of solvent respectively (for MeCN, $\epsilon_{\text{opt}} = 1.807$, $\epsilon_s = 35.688$).

Table 14: Calculated Free Energy Barriers ($\Delta G_{\text{MH}}^{\ddagger}$, kcal/mol) of Single Electron Transfer Steps

	r_1 (Å)	r_2 (Å)	R (Å)	λ (kcal.mol)	ΔG_r (kcal.mol)	$\Delta G_{\text{MH}}^{\ddagger}$ (kcal.mol)
SET1	3.60	7.67	11.27	20.12	-21.97	0.04
SET2	5.35	7.86	13.21	14.19	3.50	5.51
SET3	5.35	7.67	13.02	14.28	10.94	11.14
SET4	3.60	8.01	11.61	20.09	-29.41	1.08
SET5	3.59	5.13	8.72	21.29	-46.21	7.29
SET6	7.23	7.86	15.09	11.60	-18.99	1.18
SET7	7.24	7.86	15.10	11.59	-13.40	0.07
SET8	3.63	7.67	11.30	19.96	-36.98	3.63
SET9	7.24	3.63	10.87	20.03	14.30	14.71

Thermal correction to Gibbs free energies (**TCG**, in Hartree), thermal correction to enthalpies (**TCH**, in Hartree), sum of electronic and thermal free energies (**G**, in Hartree), single point energies in acetonitrile computed at the (U)M06-2X-D3/def2-TZVPP level (E_{sol} , in Hartree), and total spin-squared operator of open-shell species S^2 are shown in Table 15.

Table 15: Computed Energies of all Stationary Points

Name	TCG/a.u.	TCH/a.u.	G/a.u.	E_{sol} /a.u.	S^2
Ir ^{III}	0.385373	0.500543	-2626.298109	-2628.273004	-
*Ir ^{III}	0.380379	0.497729	-2626.208061	-2628.164941	2.0338
Ir ^{II}	0.379403	0.497223	-2626.407379	-2628.377625	0.7655
Ir ^{IV}	0.386682	0.501199	-2626.087722	-2628.048800	0.7701
DABCO	0.153019	0.190309	-344.970218	-345.317666	-
INT1	0.153568	0.191316	-344.802561	-345.139568	0.7574
97	0.070417	0.113982	-415.590099	-415.949080	-
INT2	0.067707	0.112117	-415.689310	-416.051377	0.7637
97-T	0.067163	0.112008	-415.535090	-415.885842	2.0350
TS1	0.061386	0.108923	-415.508969	-415.863924	2.0254
INT3	0.060324	0.099881	-306.090576	-306.358353	2.0125
N ₂	-0.012758	0.008987	-109.447723	-109.530116	-
98b	0.102473	0.149523	-646.154578	-646.720384	-
TS2	0.180419	0.250375	-952.234151	-953.084312	2.0119
INT4	0.183689	0.253159	-952.310687	-953.153326	2.0323
INT4 _s	0.187326	0.253328	-952.307806	-953.153763	1.0265
TS3	0.189277	0.252486	-952.305678	-953.153863	1.0091
TS3'	0.188152	0.252063	-952.306226	-953.152349	1.0009
cis-103	0.191125	0.255807	-952.369644	-953.232412	-
trans-103	0.192376	0.256124	-952.373259	-953.237177	-
INT5	0.186402	0.252323	-952.444957	-953.296900	0.7627
H ₂ O	0.003312	0.024765	-76.362776	-76.436930	-
TS4	0.227247	0.303548	-1105.161065	-1106.178885	0.7729
INT6	0.198008	0.266827	-952.954958	-953.812769	0.7739
INT7	0.006067	0.035138	-152.195592	-152.364635	-
TS5	0.179750	0.228393	-497.025728	-497.513863	0.7569
INT8	0.138474	0.176242	-344.318723	-344.652127	0.7549
INT9	0.197410	0.265378	-953.075355	-953.944116	-
INT10	0.142141	0.178514	-344.167987	-344.501058	-
TS6	0.359465	0.444437	-1297.244303	-1298.453098	-
104	0.198342	0.263594	-853.188749	-853.960984	-
108	0.144260	0.183416	-444.146189	-444.580781	-
TS7	0.322440	0.378948	-689.746864	-690.439206	0.7550
INT11	0.168378	0.206118	-345.431681	-345.788391	-

TS8	0.248155	0.313507	-761.127894	-761.847130	0.7571
INT12	0.078089	0.125115	-416.173697	-416.539210	0.7556
TS9	0.076811	0.122993	-416.170320	-416.534116	0.7627
INT13	0.072498	0.112072	-306.765313	-307.039564	0.7586
TS10	0.197357	0.263380	-952.909886	-953.764388	0.7636
TS11	0.235038	0.298885	-760.478799	-761.183029	2.0176
TS12	0.238665	0.301902	-760.325152	-761.022285	0.7804

3.5 Conclusion

In summary, in this chapter, we have performed detailed theoretical studies on the emerging photochemical carbene transfer reactions. Firstly, based on the discovery of multi-state reactivity of diaryl diazomethanes in photochemical reaction with alkynes, our computational results suggest that not only singlet-triplet splitting energy but also the nucleophilicity of the key diaryl carbene are controlled by the substituents on the aromatic rings.

Furthermore, we have also investigated the photochemical, transition-metal free O–H insertion reaction with diazo compounds and alcohols. The underlying reaction pathways are strongly dependent on the acidity of alcohols. In addition, the hydrogen bonding interaction between propargylic alcohols and free singlet carbene can facilitate the chemoselective cyclopropanation reactions.

We then unveil the underlying reaction mechanism of fluoro-amino etherification of aryldiazoacetate involving key ylide intermediates. Actually, the relative electrophilicity and nucleophilicity of donor-acceptor carbene with NFSI can be switched by introducing electron-donating group onto aryl rings, resulting in different reactivities.

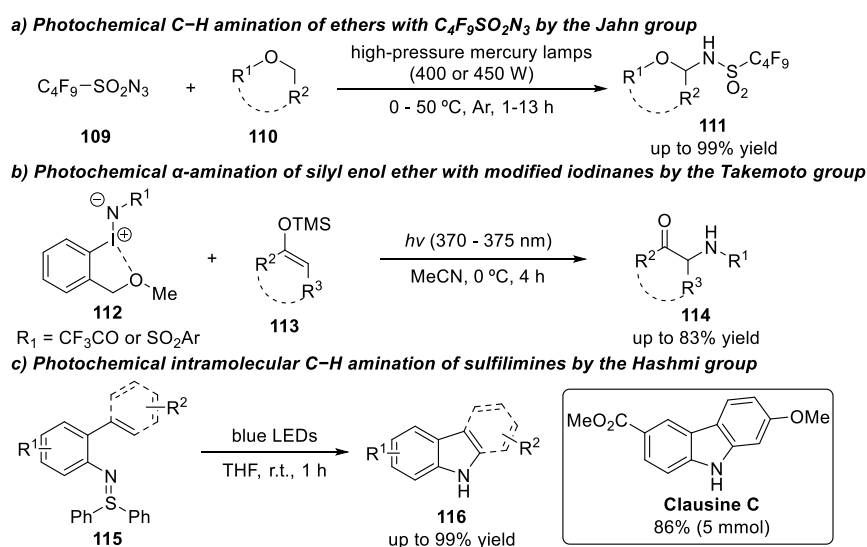
Lastly, we conduct detailed research on the recently discovered application of ethyl diazoacetate in photocatalytic reactions. Specifically, we identified a dual role of iridium photocatalyst in *gem*-difluoroolefination reactions of diazoacetates and α -trifluoromethyl styrene, involving energy and electron transfer.

4. Mechanism Study of Photoinduced Nitrene Reactions

4.1 Brief Introduction: Photochemical Nitrene Transfer Reactions

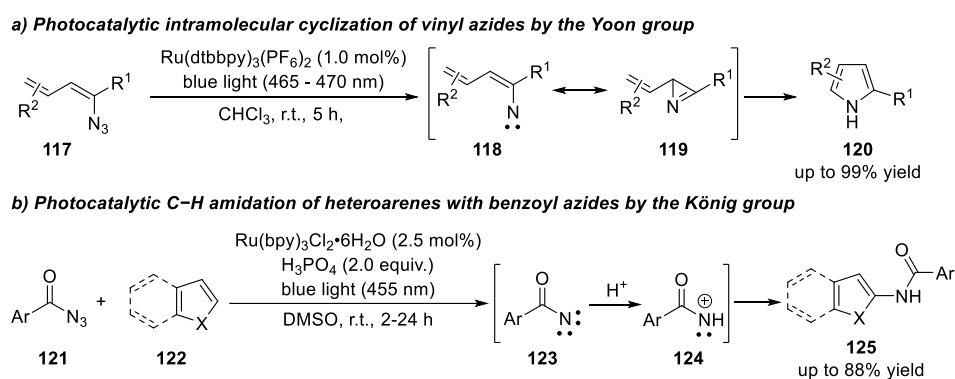
In addition to photoinduced carbene transfer reactions, recently visible-light-activated nitrene transfer reaction is receiving increased attention as well, such as in aziridination and C–H amination. To avoid the generation of free nitrene intermediate via high temperatures or strong UV-light irradiation, state-of-the-art reactive nitrene precursors that can generate nitrenes using mild and green energy sources are still sparse.

Recently, the Jahn group reported photochemical α -C–H amination of ethers using relatively reactive nonafluorobutanesulfonyl azide **109** as aminating reagent (Scheme 48a).¹⁵⁵ In this case, however, ether solvent and near ultraviolet light were required in reaction, which limited the application of this methodology. Besides azides, iminoiodinanes are a useful source of nitrene, which have been applied in transition-metal-catalyzed nitrene transfer reactions.¹³¹ By introducing an *ortho*-coordinating substituent, the Takemoto group developed a series of stable *N*-sulfonyliminoiodinanes and *N*-trifluoroacetylminoiodinane **112** (Scheme 48b).¹⁶³ Photoexcitation of these iminoiodinanes with UV light (370 - 375 nm) enabled reaction with various silyl enol ethers **113** to afford α -aminoketone derivatives in good yield. Moreover, more reactive aryl sulfilimines **115** were employed in construction of carbazoles and related heterocycles, which was reported by the Hashmi group in 2020 (Scheme 48c).¹⁵⁷ This intramolecular C–H amination reaction could be operated with milder blue light irradiation and applied in synthesis of natural products, such as Clausine C.



Scheme 48: Photochemical amination reactions with reactive nitrene precursors

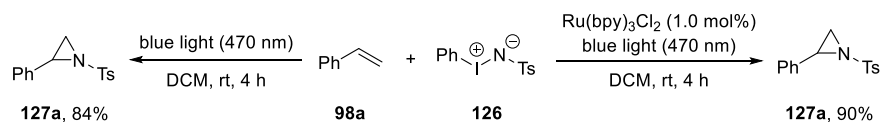
For typical nitrene precursors for metal catalysis, high-energy UV light is necessary for the formation of free nitrene, while recent transition metal photocatalysis made it more operationally accessible and tolerant of functional groups. For example, the Yoon group reported intramolecular cyclization of vinyl azides **117** with blue light in the presence of Ru(II) photocatalysts, which constructed a broad range of pyrroles and relative heterocycles (Scheme 49a).¹⁶² Triplet energy transfer process between excited state of Ru(dtbbpy)₃(PF₆)₂ and vinyl azides **117** was proposed to produce the key nitrene intermediate **118**. Further formation of azirine **119** via ring-closure underwent high-yielding rearrangement to afford pyrroles. In addition, benzoyl azides were found to allow a photocatalytic high-selective C–H amidation reaction of electron rich heteroarenes by the König group (Scheme 49a).¹⁵⁴ Mechanistically, generation of benzoyl nitrene **123** with triplet sensitizer could be protonated under the strongly acidic conditions, yielding electrophilic nitrenium ions **124** for subsequent addition with electron rich heteroarene **122**.



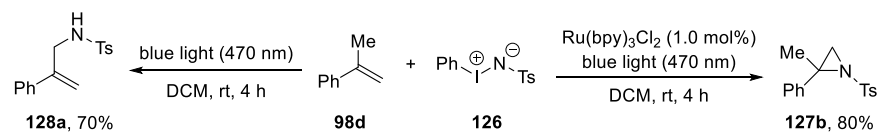
Scheme 49: Photocatalytic nitrene transfer reactions with azides

Inspired by previous reports on nitrene transfer reactions, our group uncovered a novel photoinduced nitrene transfer methodology with iminoiodinane - PhINTs. Iminoiodinane **126**, which is commonly used as the nitrene precursor in metal-catalyzed reactions, possesses unusual photochemical properties under blue light irradiation.²⁷⁴⁻²⁷⁶ For instance, our group identified that iminoiodinane **126** could undergo an aziridination reaction with styrene **98a** under blue light (470 nm) irradiation, which could also be promoted by photocatalyst Ru(bpy)₃Cl₂ (Scheme 50a).²⁷⁴ To our surprise, when testing the reaction with α -methyl styrene **98d**, we found a completely different outcome in presence of Ru(bpy)₃Cl₂ catalyst or not (Scheme 50b).²⁷⁴ Specifically, an efficient amination reaction was observed under photochemical condition without photocatalyst, leading to the selective formation of allyl C–H functionalization product **128a**. Contrarily, in presence of photocatalyst Ru(bpy)₃Cl₂, a high selective aziridine product **127b** was obtained in 80% yield. Due to the high performance of photocatalytic aziridination, we supposed to apply it in the synthesis of trifluoromethylated aziridines, which still represent an intriguing synthetic challenge. Gratefully, our group realized the highly effective aziridination of α -CF₃ styrene **98b** with PhINTs under photocatalytic condition, which was inefficient in traditional copper-catalyzed nitrene transformations (Scheme 50c).²⁷⁶

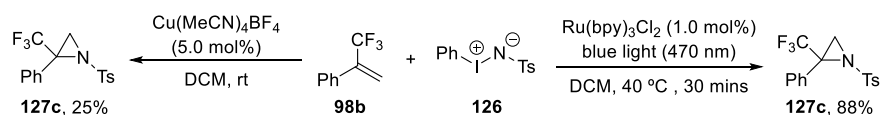
a) Photochemical and photocatalytic aziridination of styrene



b) Chemoselective aziridination or C-H functionalization α -Me styrene



c) Highly effective aziridination of α -CF₃ styrene



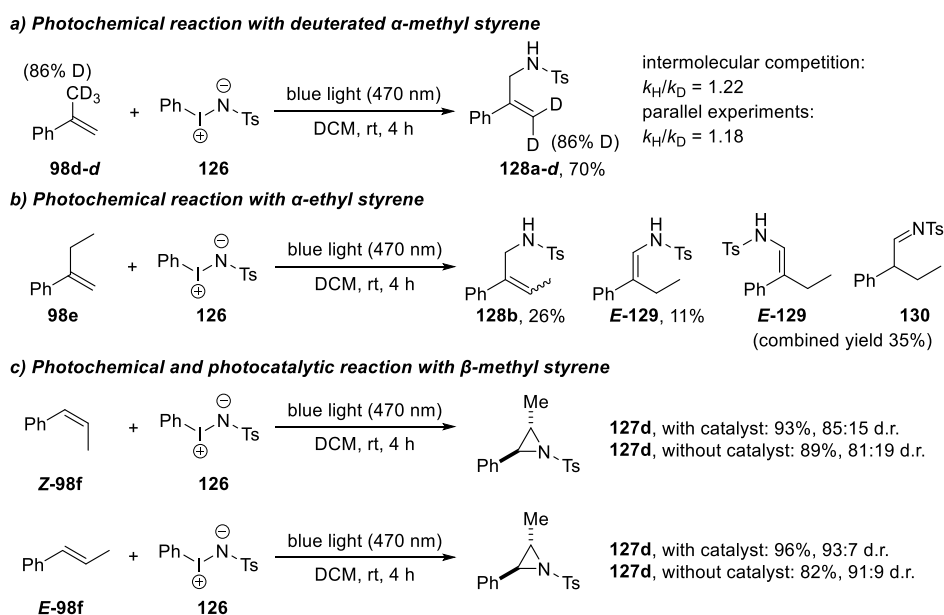
Scheme 50: Photoinduced nitrene transfer reactions of iminoiodinane with alkenes

4.2 Mechanism study of Photoinduced C–H functionalization and aziridination Reactions

4.2.1 Control Experiments

After discovery of the divergent photochemical reactions of PhINTs, we started to examine control experiments and provide an understanding of these underlying reactions. Firstly, using α -trideuteriomethyl styrene **98d-d** in the photochemical reaction, we found that deuterium content was fully preserved in the C–H functionalization product **128a-d** (Scheme 51a). Interestingly, in the case of **128a-d**, the deuterium label transferred from methyl group to the double bond position, which suggested a double-bond migration in the formal C–H insertion reaction. Further studies on the reaction kinetics of **98d** and **98d-d** showcased a small kinetic isotope effect in both intermolecular or parallel experiments, indicating that the hydrogen atom transfer was not the rate determining step. Indeed, this double-bond migration mechanism has also been supported by the photochemical reaction of α -ethyl styrene **98e** with PhINTs, in which an inner olefin **128b** and other different products (**129** and **130**) were observed (Scheme 51b). Furthermore, when testing the two isomers of β -methyl styrene (**Z-98f** and **E-98f**) in both photocatalytic and photochemical conditions, we observed major product of *trans*-aziridine **127d** with similar diastereoselectivity (Scheme 51c). This outcome represented a stepwise mechanism under both reaction conditions instead of a concerted nitrene addition of double bond. In addition, control experiments with spin trapping reagents, such as TEMPO or DMPO, a complete suppression of the reactions was found in all cases, which indicated a possible radical intermediates in the mechanism.²⁷⁴

This control experiment part was performed by Yujing Guo.



Scheme 51: Control experiments of photocatalytic and photochemical nitrene transfer reaction

4.2.2 Computational Study

Based on experimental results of photoinduced nitrene transfer reactions, we were intrigued in the corresponding mechanism and then performed detailed DFT calculation on it at SMD(DCM)-(U)M06-2X-D3/def2-TZVP//((U)M06-2X-D3/def2-SVP level of theory (Figure 34). We first utilized the iminoiodinane **126** and α -methyl styrene **98d** as the computational model. Under the photochemical condition, experiments suggested a weak absorption in the blue light and TD-DFT calculation reveal that the excitation from HOMO to LUMO was predicted to be the first excited state. Specifically, the HOMO of **126** was predominantly associated with electron density at the nitrogen and *p*-toluenesulfonyl (Ts) group, while excitation to the LUMO promoted electron transfer from the nitrogen to iodine center (Figure 34). After the photoexcitation of **126**, the singlet excited state **126*** could directly lead to a singlet nitrene **INT1_s**. Considering the detail structure of **INT1_s**, it had very short N–O bond distance of 1.68 Å, which indicated a stabilization of the low-valent nitrene with lone-pair electrons in the oxygen atom. In addition, **126*** could also undergo an intersystem crossing (ISC) and release its triplet state **126-T**, which featured a very long N–I bond of 3.45 Å. Further exergonic, barrier-free dissociation of the N–I bond led to PhI and triplet nitrene **INT1_t**, which was energetically favored intermediate than the high-lying singlet nitrene **INT1_s**. When using the photoredox catalyst, calculations supported a very facile reduction of the iodine **126** with excited state of Ru^{II} , which needed a low SET barrier of 1.4 kcal/mol calculated through Marcus-Hush theory,²⁷³ leading to a radical anion intermediate **INT2**. Similarly, this radical anion **INT2** featured a long N–I distance of 3.68 Å and a very weak interaction between nitrogen and phenyl ring with a distance of 2.20 Å, which suggested a feasible release of PhI and generation of nitrene radical anion **INT3**.

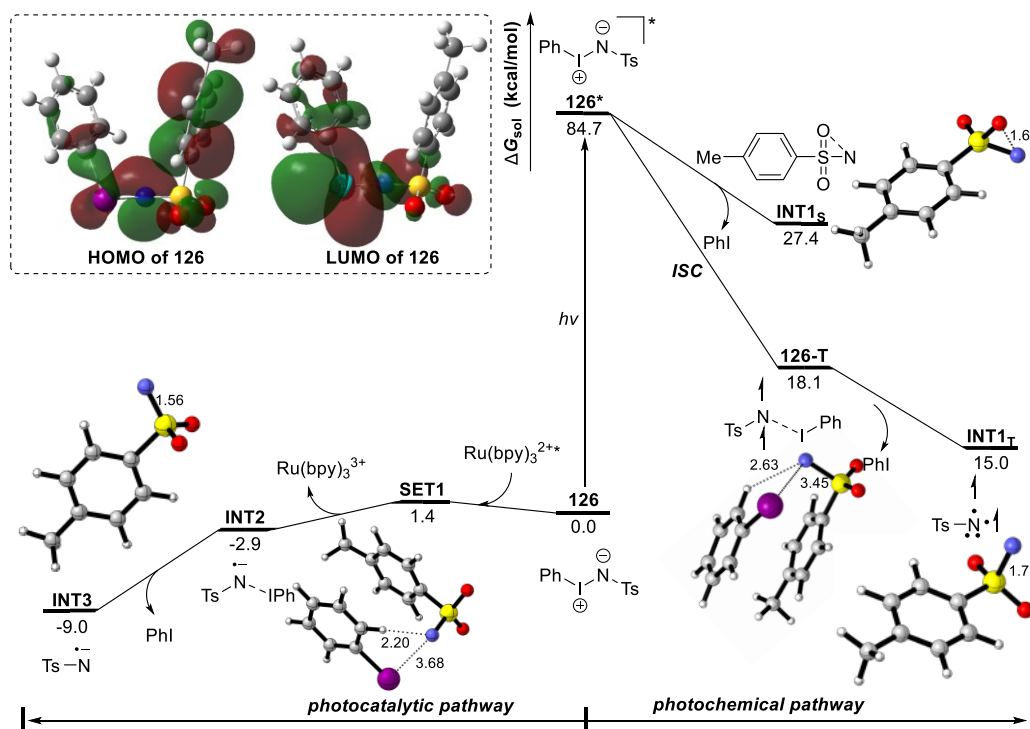


Figure 34: Potential energy surfaces of formation of nitrene intermediates

Before calculating the further reaction pathways, we first analyzed the properties of triplet nitrene **INT1_T** and nitrene radical anion **INT3** (Figure 35). The NBO charge analysis indicated that the nitrene radical anion **INT3** had a higher electron density at the nitrogen atom compared to the triplet nitrene, leading to higher nucleophilicity of the nitrene radical anion. Further spin density distribution showed that the radical is majorly located on the nitrogen atom (Figure 35a). Moreover, the SOMO orbital suggested a π bond between N and S in the **INT3**, which resembled a double bond and was reflected by a short bond length of 1.56 Å (Figure 35b). Instead, 1.71 Å bond length and 1.02 bond order represented a single S–N bond in the triplet nitrene **INT1_T**.

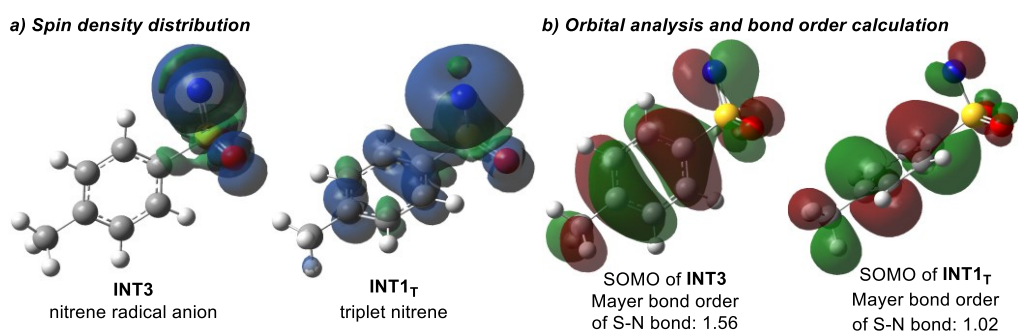


Figure 35: NBO, bond order and orbital analysis

Then we first evaluated further transformation with α -methyl styrene **98d** under photocatalytic condition (Figure 36). In this case, the radical addition of radical anion **INT3** onto the double bond occurred via **TS1** with activation free energy of 14.9 kcal/mol. Subsequent reduction of the generated radical anion species **INT4** by the oxidized state Ru^{III} catalyst led a zwitterionic intermediate **INT5**. Quick cyclization of **INT5** afforded the aziridine

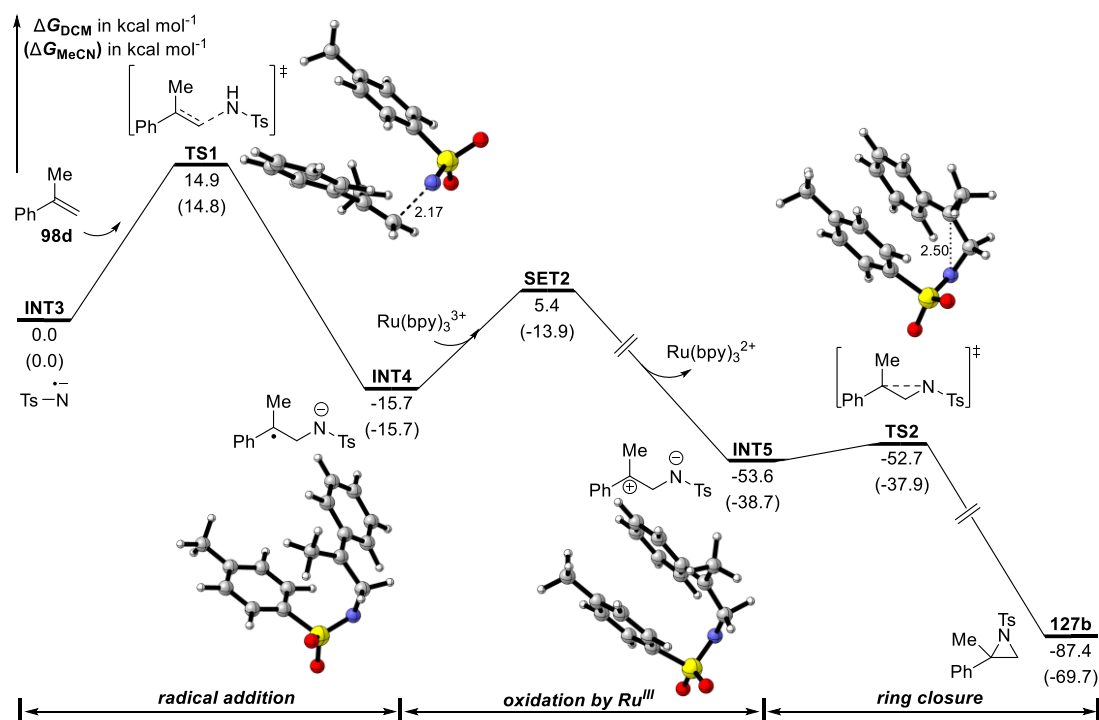


Figure 36: Potential energy surfaces of aziridination via nitrene radical anion

product with a low energy barrier of only 0.9 kcal/mol via **TS2**. However, the SET process had a slightly high energy barrier. We thought this should be a matter of reaction solvent. As the reaction was also proceeding in good yield in acetonitrile, we also calculated this reaction using acetonitrile as implicit solvent model in Figure 36. As we can see, the free energy barrier of SET process was calculated to be only 1.8 kcal/mol and thus is feasible. Further use of explicit solvent molecules or better implicit solvent models will be an important strategy to overcome these limitations in the future.

In the case of selective C–H functionalization under photochemical condition, we then performed detail calculations from triplet nitrene **INT1_T**. Firstly, we proposed a direct hydrogen abstraction of methyl group in **98d** by triplet nitrene, yet transition state **TS6** with an activation free energy of 14.7 kcal/mol was located and led to two separate radicals **INT6** (Figure 37). However, we found another triplet nitrene addition to α -methyl styrene via a **TS3** needed an activation free energy of only 6.1 kcal/mol, which was significantly favored over hydrogen transfer pathway (**TS6**). This computed selectivity was consistent with previous deuterated experiments that deuterium content was fully retained in the double bond instead of methylene group in **128a-d** (Scheme 51a). The generated triplet species **INT4_T** then underwent intersystem crossing to give an open shell singlet species **INT4_S**, while **INT4_S** could either cyclize to give the aziridine **127b**, or give the C–H functionalization product **128a** through a 1,4-hydrogen transfer. The steric hindrance of rotation in cyclization transition state **TS5** resulted in a higher activation free energy by 2.5 kcal/mol than that of hydrogen atom transfer via **TS4**. Calculated energy difference now reasoned this selective, photochemical C–H functionalization of α -methyl styrene with triplet nitrene **INT1_T**.

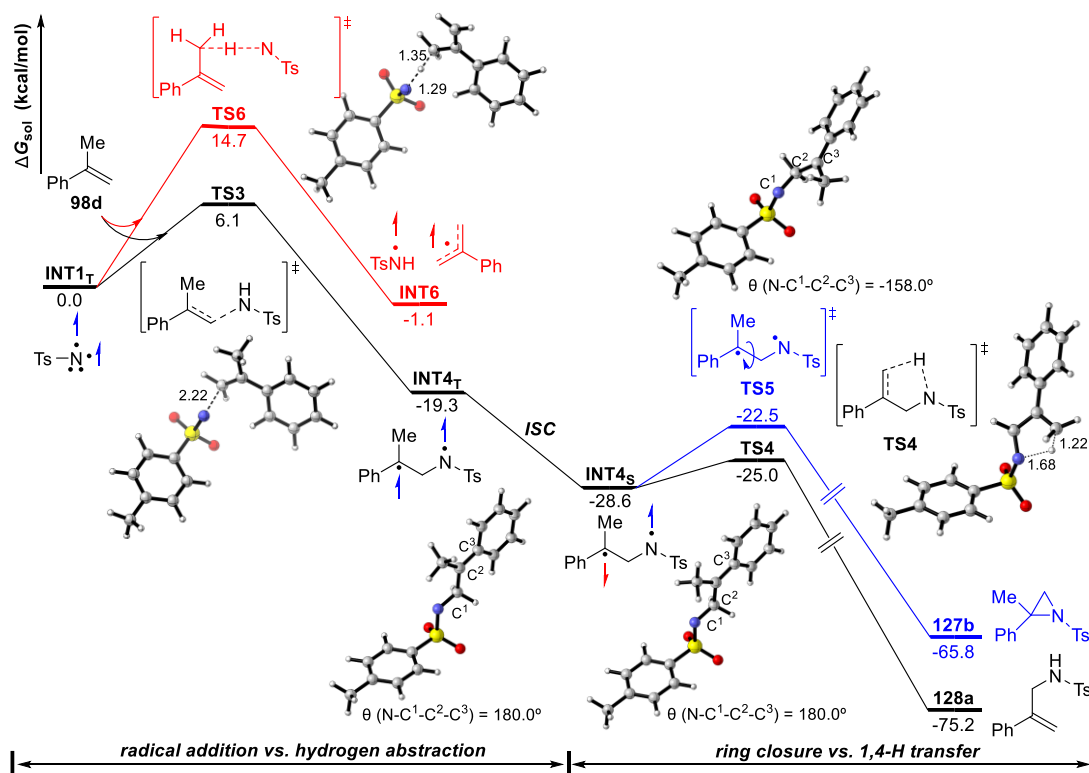


Figure 37: Potential energy surfaces of C–H functionalization via triplet nitrene

After investigating the reaction mechanism of photoinduced nitrene transfer with α -methyl styrene, the aziridination of simple styrene **98a** was also examined by DFT calculations (Figure 38). Further results suggested similar pathways as in the aziridination reaction of α -methyl styrene in both photochemical and photocatalytic conditions. Notably, the absence of the α -methyl group rendered the cyclization step to proceed via **TS8** with a very low activation free energy of only 1.4 kcal/mol, which might result from the conformational flexibility of the diradical intermediate **INT6s**.

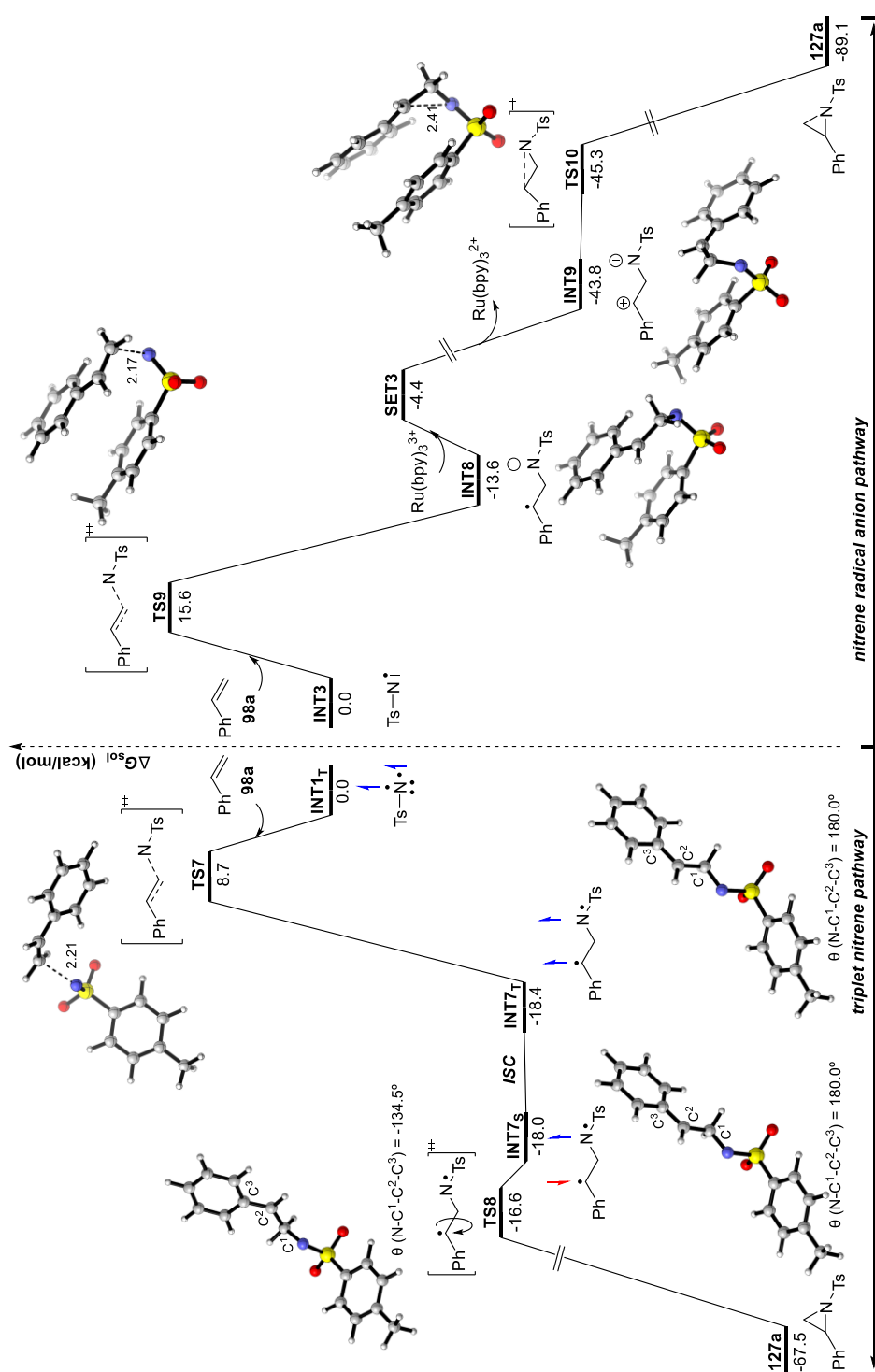


Figure 38: Potential energy surfaces of photoinduced aziridination with styrene

Furthermore, we found a similar reaction pathway of photocatalytic aziridination with α -CF₃ styrene **98b** (Figure 39). Facile radical addition and SET process revealed the key nitrene radical anion intermediate of this photocatalytic synthesis platform, which accessed fluorinated aziridines in a generalized and efficient fashion.

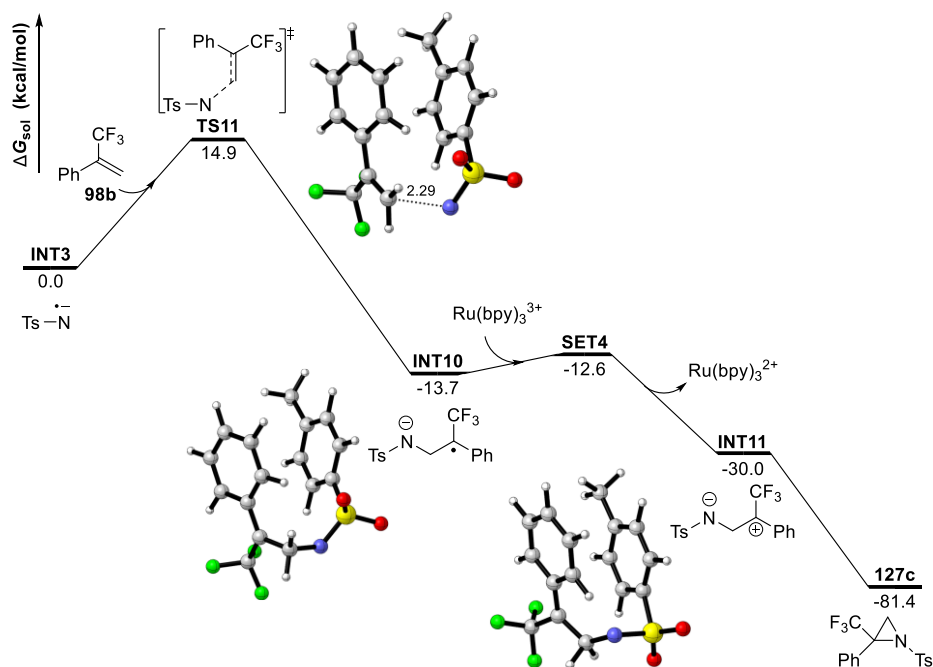


Figure 39: Potential energy surfaces of photocatalytic aziridination with α -CF₃ styrene

4.2.3 Computational Data

All calculations were performed using Gaussian 16 program.¹⁸³ All structures were optimized at (U)M06-2X level^{184,185} of theory in combination with D3 dispersion corrections,²⁰⁹ in which all atoms were described with def2-SVP basis set,²³⁵ Analytical frequency calculations were carried out at the same level of theory in order to confirm each stationary point as either an intermediate (no imaginary frequencies) or a transition state (only one imaginary frequency). Key transition-state structures were confirmed to connect corresponding reactants and products by intrinsic reaction coordinate (IRC) calculations.^{192,193} The electronic energy was then refined using def2-TZVP basis set²³⁵ at (U)M06-2X level on the optimized geometries in combination with D3 dispersion corrections. Solvation energies in DCM ($\epsilon = 8.93$) or MeCN ($\epsilon = 35.688$) were evaluated by IEFPCM calculations with radii and non-electrostatic terms for SMD solvation model²⁰⁸ based on the optimized structures. The given Gibbs free energies in dichloromethane and acetonitrile were calculated according to the formula: $G_{\text{sol}} = \text{TCG} + E_{\text{sol}} + 1.89 \text{ kcal mol}^{-1}$. Time-dependent (TD)-DFT calculations were carried out on the optimized structures of the PhINTs to obtain the absorption wavelength. The CYLview software was employed to show the 3D structures of the studied species.¹⁹⁵

To get more details of the singlet electron transfer (SET) process, we estimated the free energy barrier of SET process using the Marcus-Hush theory,²⁷³ which can be calculated according to the following formula:

$$\Delta G_{\text{MH}}^{\ddagger} = \frac{(\Delta G_{\text{r}} + \lambda)^2}{4\lambda}$$

Where ΔG_{r} is the Gibbs free energy change of the SET step, λ is the reorganization energy including inner sphere energy and outer sphere energy. However, the outer sphere energy is often much larger than the inner sphere contribution. Hence, the outer sphere reorganization energy (λ_{outer}) can be regarded as the total reorganization energy, which can be calculated according to the following formula:

$$\lambda = \lambda_{\text{outer}} = 332 \left(\frac{1}{2r_1} + \frac{1}{2r_2} - \frac{1}{R} \right) \left(\frac{1}{\epsilon_{\text{opt}}} - \frac{1}{\epsilon_{\text{s}}} \right)$$

Where r_1 and r_2 are the radii of electron donor and acceptor, R is the sum of r_1 and r_2 , ϵ_{opt} and ϵ_{s} is the high frequency (optical) dielectric constant and static dielectric constant of solvent respectively (for MeCN, $\epsilon_{\text{opt}} = 1.807$, $\epsilon_{\text{s}} = 35.688$; DCM, $\epsilon_{\text{opt}} = 2.03$, $\epsilon_{\text{s}} = 8.93$).

Table 16: Calculated Free Energy Barriers ($\Delta G_{\text{MH}}^{\ddagger}$, kcal/mol) of Single Electron Transfer Steps

	r_1 (Å)	r_2 (Å)	R (Å)	λ (kcal/mol)	ΔG_{r} (kcal/mol)	$\Delta G_{\text{MH}}^{\ddagger}$ (kcal/mol)
SET1_{DCM}	5.40	7.15	12.55	10.47	-2.88	1.38
SET2_{DCM}	6.08	7.14	13.22	9.68	-38.11	20.51
SET3_{DCM}	5.40	7.14	12.54	10.47	-30.15	9.25
SET1_{MeCN}	5.40	7.15	12.55	14.45	-17.68	0.18
SET2_{MeCN}	6.08	7.14	13.22	13.37	-23.00	1.73
SET3_{MeCN}	5.40	7.14	12.54	14.46	-14.45	0.00
SET4	5.90	7.15	13.05	9.86	-16.33	1.06

Thermal correction to Gibbs free energies (**TCG**, in Hartree), thermal correction to enthalpies (**TCH**, in Hartree), sum of electronic and thermal free energies (**G**, in Hartree), single point energies in DCM or MeCN computed at the (U)M06-2X-D3/def2-TZVP level (E_{DCM} and E_{MeCN} , in Hartree), and total spin-squared operator of open-shell species S^2 are shown in Table 17.

Table 17: Computed Energies of all Stationary Points

Name	TCG/a.u.	TCH/a.u.	G/a.u.	E_{DCM} /a.u.	E_{MeCN} /a.u.	S^2
126	0.177353	0.242490	-1402.290641	-1403.514800	-1403.517404	-
126-T	0.172441	0.241693	-1402.289544	-1403.481074	-1403.481175	2.0105
INT1_T	0.094300	0.141280	-873.358573	-874.204410	-874.204644	2.0099
INT1_S	0.094261	0.142582	-873.335132	-874.184669	-874.185024	-
Phi	0.059292	0.097728	-528.933922	-529.265727	-529.264630	-
*Ru²⁺	0.425155	0.516648	-1578.446643	-1580.731415	-1580.743282	2.0154
Ru³⁺	0.429102	0.518877	-1578.082838	-1580.590952	-1580.622206	0.7551
Ru²⁺	0.428938	0.518655	-1578.530139	-1580.807785	-1580.818006	-
INT2	0.171647	0.241317	-1402.391271	-1403.658100	-1403.664898	0.7562
INT3	0.091769	0.141810	-873.455084	-874.384549	-874.391828	0.7554
98d	0.130070	0.171714	-348.412462	-348.939666	-348.938195	-
TS1	0.245426	0.314092	-1221.861269	-1223.321025	-1223.326921	0.7833
INT4	0.247321	0.316133	-1221.912959	-1223.371752	-1223.377426	0.7705
INT5	0.250611	0.316238	-1221.802279	-1223.218386	-1223.221399	-
TS2	0.251330	0.315886	-1221.798069	-1223.217738	-1223.220851	-
127b	0.250983	0.319436	-1221.885743	-1223.272562	-1223.271219	-
TS3	0.242420	0.314998	-1221.764543	-1223.149365	-1223.148069	2.0422
INT4_T	0.241798	0.315996	-1221.806492	-1223.189179	-1223.187874	2.0267
INT4_S	0.241760	0.314988	-1221.808396	-1223.204017	-1223.205534	0.7808
TS4	0.243793	0.312832	-1221.799781	-1223.200383	-1223.200870	-
128a	0.251686	0.31984	-1221.891522	-1223.288158	-1223.288344	-
TS5	0.245307	0.314771	-1221.803881	-1223.197938	-1223.199454	0.8932
TS6	0.236607	0.309412	-1221.752338	-1223.129951	-1223.128657	2.0284
INT6_T	0.238007	0.313213	-1221.778834	-1223.156505	-1223.154975	2.0419
98a	0.102670	0.142140	-309.173011	-309.628699	-309.627427	-
TS7	0.216379	0.285421	-1182.521147	-1183.835609	-1183.834411	2.0477
INT7_T	0.216294	0.286095	-1182.563882	-1183.878730	-1183.877660	2.0305
INT7_S	0.217186	0.285917	-1182.562806	-1183.878956	-1183.875006	1.0058
TS8	0.219382	0.285469	-1182.559469	-1183.879009	-1183.877547	0.9625
127a	0.224321	0.290284	-1182.644777	-1183.965078	-1183.964015	-
TS9	0.219275	0.284222	-1182.618210	-1184.010229	-1184.016711	0.7832
INT8	0.222044	0.286180	-1182.670196	-1184.059547	-1184.065831	0.7740
INT9	0.221888	0.287355	-1182.547794	-1183.890448	-1183.892743	-
TS10	0.224321	0.290284	-1182.547262	-1183.896158	-1183.899277	-

For the calculation of PhINTs with α -CF₃ styrene, the geometries of all stationary points were optimized using the PBE functional²⁷⁷ together with Grimme's dispersion correction²⁰⁹ (denoted PBE-D3). During geometry optimization, the def2-SVP basis set²³⁵ was used for C, H, O, N and S, and the triple- ζ basis set def2-TZVP²³⁵ for Ru and I. To improve the calculation accuracy, single point calculations were performed using the M06-2X functional^{184,185} with Grimme's dispersion correction (denoted M06-2X-D3), and the def2-TZVPP basis set²³⁵ was used for all atoms. Solvation energies in dichloromethane ($\epsilon = 8.93$) were evaluated by IEFPCM calculations with radii and non-electrostatic terms for SMD solvation model²⁰⁸ based on the gas-phase optimized structures.

Thermal correction to Gibbs free energies (**TCG**, in Hartree), thermal correction to enthalpies (**TCH**, in Hartree), sum of electronic and thermal free energies (**G**, in Hartree), single point energies in dichloromethane computed at the (U)M06-2X-D3/def2-TZVPP level (**E_{sol}**, in Hartree), and total spin-squared operator of open-shell species **S²** are shown in Table 18.

Table 18: Computed Energies of all Stationary Points

Name	TCG/a.u.	TCH/a.u.	G/a.u.	E _{sol} /a.u.	S ²
126	0.167752	0.234717	-1401.756128	-1403.509142	-
*Ru²⁺	0.408016	0.499790	-1577.593127	-1580.714430	2.0076
Ru³⁺	0.412550	0.503036	-1577.213909	-1580.587895	0.7552
Ru²⁺	0.413124	0.502891	-1577.660408	-1580.802575	-
INT3	0.085480	0.136557	-872.993858	-874.379281	0.7566
98b	0.098859	0.146346	-645.415021	-646.718744	-
TS11	0.208901	0.283787	-1518.417977	-1521.098890	0.7703
INT10	0.211888	0.286062	-1518.462890	-1521.147412	0.7741
INT11	0.212313	0.285820	-1518.350729	-1520.959759	-
127c	0.213562	0.288662	-1518.417646	-1521.042892	-

4.3 Conclusion

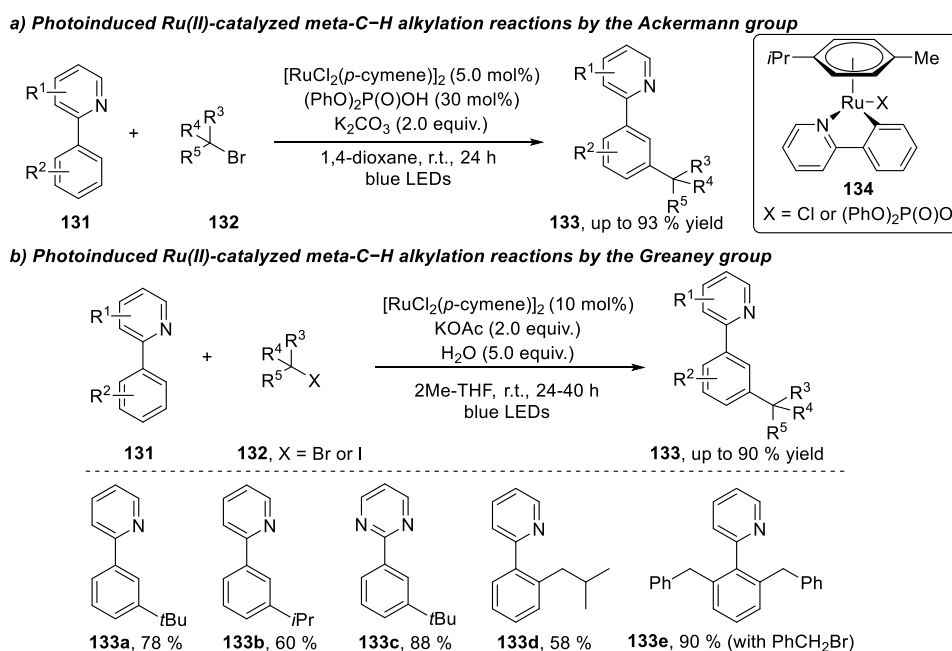
Nitrene transfer reactions represent one of the key and effective reactions to rapidly introduce nitrogen into complex skeletons and construct new C-N bonds. Our group identified the application of iminoiodinanes in amination reactions under visible light irradiation, which provides a creative photoinduced nitrene transfer methodology. In this section, we performed detailed theoretical studies on this topic, which reveal that a triplet nitrene intermediate is involved under catalyst-free condition and a nitrene radical anion intermediate under photocatalytic condition. Further computations support a favorable hydrogen atom transfer process in the case of photochemical reaction with α -methyl styrene, which leads to a formal C-H insertion product. In addition, nitrene radical anion intermediates generated in the presence of a photoredox catalyst, furnishes a highly efficient aziridination reaction with styrene and a bit inert α -CF₃ styrene. The deep understanding of this breakthrough in photoinduced nitrene transfer reaction facilitates us to utilize this novel reactivity and apply in further amination reactions.

5. Mechanism Study of Photoinduced Ruthenium and Palladium Catalysis

5.1 Brief Introduction: Visible Light-Induced Transition Metal Catalysis

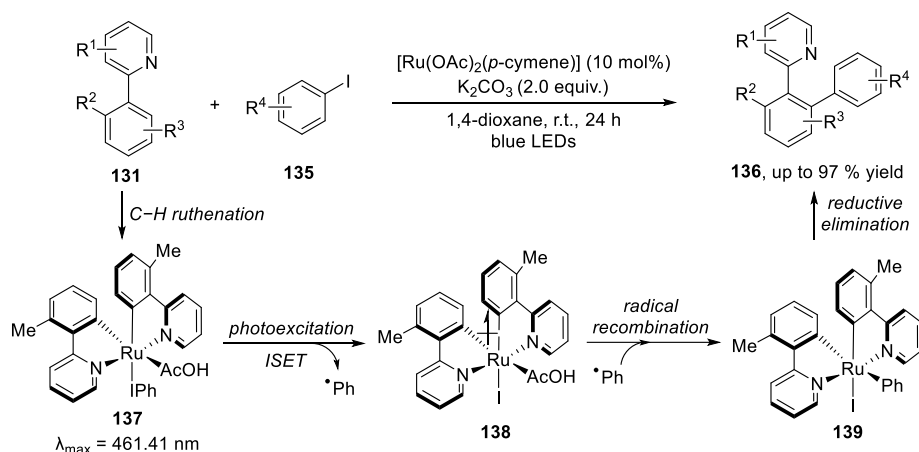
Visible light photocatalysis has found broad utility in organic synthesis. As mentioned above, reactive reagents, like diazo compounds and iminoiodinanes, can be directly employed in photochemical reactions, while photocatalysis (via energy transfer or electron transfer) can either activates slightly inert substrates or alter reaction pathways. Recently, another emerging area involving visible light-induced transition metal catalysis, receives a growing attention among chemists.²⁷⁸⁻²⁸²

The Ackermann and Greaney group independently reported seminal photoinduced Ru(II)-catalyzed *meta*-C–H alkylation reaction of arenes, which usually requires high temperature in thermal reactions (Scheme 52).^{283,284} In both reports, $[\text{RuCl}_2(p\text{-cymene})]_2$ that successfully employed as the single catalyst, however, had dual role to promote directed C–H ruthenation and photoredox catalysis for radical generation. The *in situ* generated ruthenacycle **134** had weak, yet significant absorption in visible light area, which served as photoredox catalyst to promote alkyl radical formation from alkyl halides **132**. Instead of *meta*-C–H alkylation with tertiary or secondary halides, the Greaney group found that primary alkyl iodides led to the *ortho*-selective alkylation products due to their less steric hindrance (Scheme 52b).



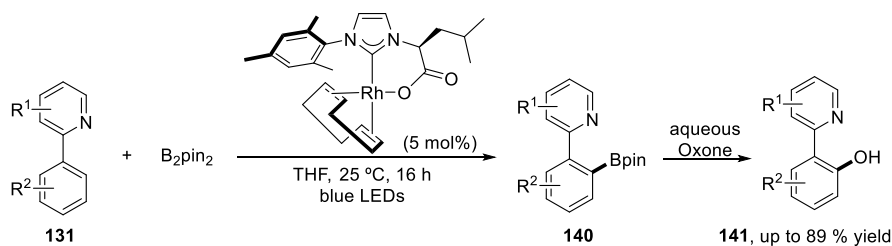
Scheme 52: Photoinduced Ru(II)-catalyzed *meta*-C–H alkylation of 2-aryl pyridines

Shortly after the initial work of photocatalytic *meta*-selective C–H alkylation, the Ackermann and Greaney group both expanded this photoinduced ruthenium catalysis towards *ortho*-C–H arylation reactions with aryl halides (Scheme 53).^{285,286} Computational studies indicated a biscyclometalated ruthenacycle **137** should be the key intermediate, which had a maximum absorption at 461.44 nm. Further calculation supported a facile inner-sphere electron transfer (ISET) of photoexcited Rh(II) complex with iodobenzene, yielding high reactive phenyl radical. Following recombination of phenyl radical led to Ru(IV) intermediate **139**, which underwent reductive elimination to deliver the *ortho*-arylated product **136**.



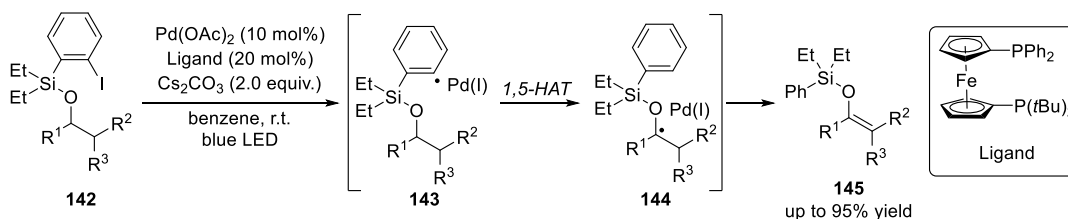
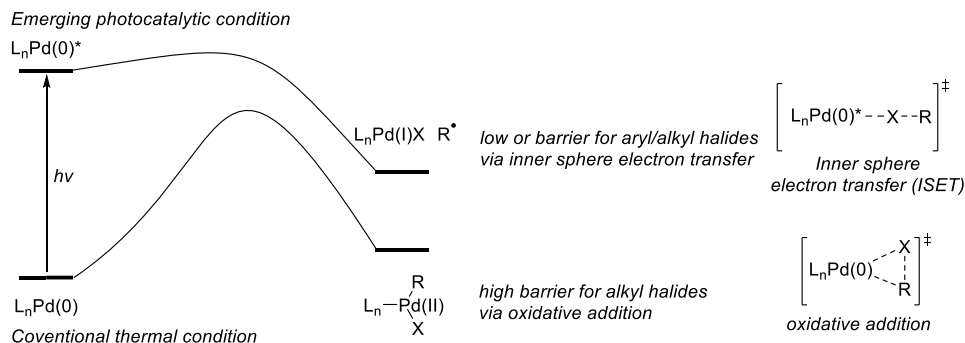
Scheme 53: Photoinduced Ru(II)-catalyzed *ortho*-C–H arylation reaction

In addition to selective C–H alkylation and arylation via ruthenium catalysis, Baslé and co-workers have realized a photoinduced Rh(I)-catalyzed *ortho*-C–H borylation reactions (Scheme 54).²⁸⁷ In this case, a new class of bidentate carboxylate NHC ligand based Rh(I) catalysts were developed, which had an expected visible-light absorption in blue light area and promoted *ortho*-C–H bond oxidation under blue light irradiation.

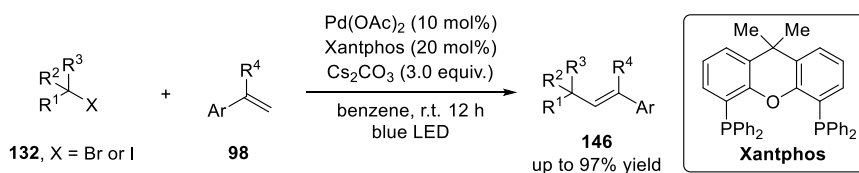


Scheme 54: Photoinduced Rh(I)-catalyzed *ortho*-C–H borylation reaction

Notably, chemists found that palladium complexes could serve as photosensitizers under visible light condition.^{278,279} The first visible light-induced palladium catalysis was reported by Gevorgyan's group in 2016 (Scheme 55a).²⁸⁸ In this case, visible light irradiation led to the formation of photoexcited Pd(0) species, which was capable of transferring a single electron to aryl iodide **142**. The generated hybrid Pd/aryl radical species **143** underwent 1,5-hydrogen atom transfer (HAT) process, and produced silyl enol ether **145** through a subsequent β -H elimination of **144**. This unique reactivity of photo-palladium catalysis opens up novel hybrid Pd/radical chemistry, which overcomes the high-barrier oxidative addition of less-active alkyl halides in the ground state (Scheme 55b).

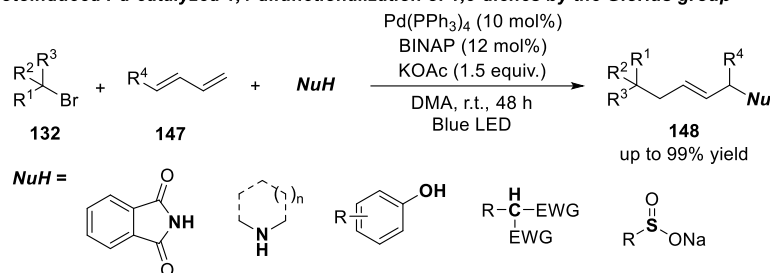
a) First photoinduced palladium catalysis in formation of aryl radical species by the Gevorgyan group

b) Palladium catalysis in ground state vs. in photoexcited state

Scheme 55: Ground-state vs. photoexcited palladium catalysis

Shortly after the seminal work, several groups independently revealed the employment of this methodology in the Heck reaction of alkyl bromides.²⁸⁹⁻²⁹¹ As an example, the Gevorgyan group reported the photocatalytic Heck reaction of vinyl arenes **98** with diverse alkyl iodides and bromides **132** (Scheme 56). Importantly, unactivated primary or secondary alkyl iodides were well competent in this transformation, thereby generating functionalized allylic systems in good yields.

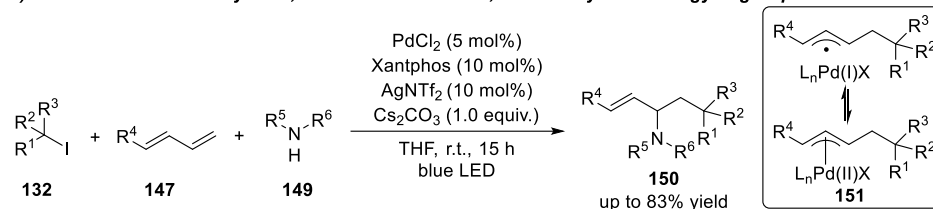

Scheme 56: Photoinduced Pd-catalyzed Heck reaction of alkyl halides

Besides vinyl arenes, the Glorius group reported a related multicomponent reaction with photoinduced palladium catalysis, in which 1,4-carbofunctionalization was realized by using alkyl bromides with conjugated 1,3-dienes **147** and nucleophiles (Scheme 57a).²⁹² In this case, a remarkably broad scope of nucleophiles were compatible in this reaction, ranging from phthalimide, aliphatic amines, phenols, carbon-based pronucleophiles, to sulfinates, identifying great functional tolerance of this protocol. In the meantime, the Gevorgyan group found a similar three component difunctionalization reactions, while distinguishable steric and electronic environments at termini led to a 1,2-carboamination of 1,3-dienes (Scheme 57b).²⁹³ Mechanistically, triflimide anion was found capable of stabilizing π -allylpalladium complex **151** and suppressing the undesired radical dimerization process.

a) Photoinduced Pd-catalyzed 1,4-difunctionalization of 1,3-dienes by the Glorius group

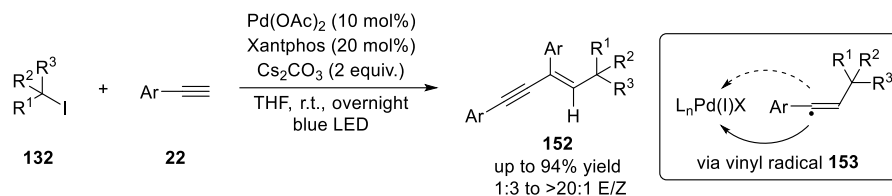


b) Photoinduced Pd-catalyzed 1,2-carboamination of 1,3-dienes by the Gevorgyan group



Scheme 57: Photoinduced Pd-catalyzed difunctionalization of 1,3-dienes

Recently, our group reported a photochemically Pd-catalyzed alkylation-alkynylation of terminal alkynes with alkyl iodides, leading to important 1,3-enynes with good yield and stereoselectivity (Scheme 58).²⁹⁴ In the proposed mechanism, reactive and linear vinyl radical **153** was regarded as the key intermediate. It underwent further coordination of Pd(I) from the less hindered side, resulting in favored *cis* geometry of aryl and alkyl group. Final Sonogashira coupling type reaction under base condition afforded the 1,3-enynes product **152**.



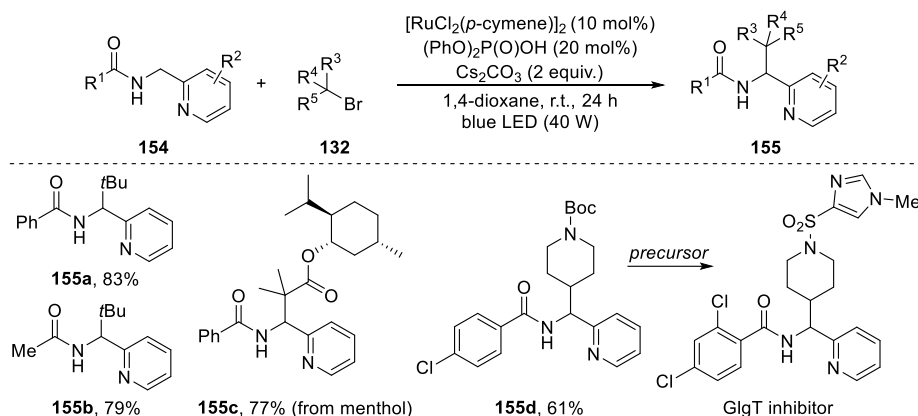
Scheme 58: Photoinduced Pd-catalyzed dicarbofunctionalization of terminal alkynes

5.2 Mechanism Study of Photoinduced Ruthenium-Catalyzed C(sp³)-H Alkylation Reactions

5.2.1 Control Experiments

Inspired by photoinduced ruthenium catalysis in site-selective C(sp²)-H alkylation, arylation and borylation reactions, our group has recently applied this strategy towards Ru(II)-catalyzed C(sp³)-H functionalization (Scheme 59).²⁹⁵ To be specific, using [Ru(cymene)Cl₂]₂ as catalyst under the blue light irradiation, methylpyridyl-substituted amides **154** and alkyl bromide **132** provided the corresponding benzylic C(sp³)-H alkylation products in high yield. Notably, diverse secondary and tertiary alkyl bromides or bromoacetates were accessible in this transformation. Furthermore, these functionalized pyridine compounds find intriguing in the medicinal chemistry and organic synthesis, such as **155d**, which is the potential precursor of GlgT inhibitor.²⁹⁶

**Experimental work was done by Sripati Jana.*

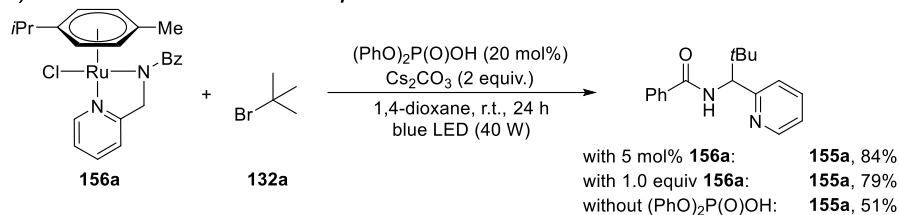


Scheme 59: Photoinduced ruthenium-catalyzed C(sp³)-H alkylation

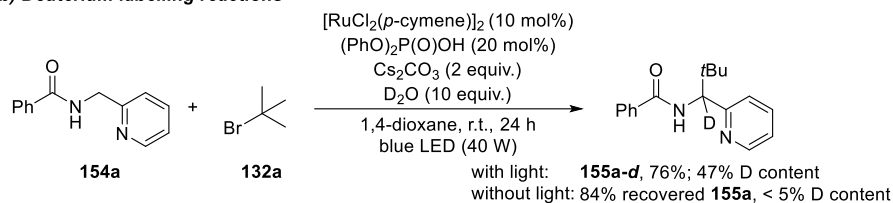
With such site-selective photochemical C(sp³)-H alkylation in hand, it was of high demand to understand the reaction mechanism experimentally and theoretically, which was beneficial for further application and expansion of this methodology. Initially, my colleague conducted a series of control experiments on this chemistry. In absence of alkyl bromide, the cyclometalated ruthenium complex **156a** was isolated from the reaction mixture, which showed high catalytic activity and regarded as a viable catalyst (Scheme 60a). Indeed, the phosphoric acid showed a significant effect on yield in this reaction, however, a moderate yield was obtained without the assistance of phosphoric acid. We reckoned that the phosphoric acid could assist protonation and product release, and also stabilize the reaction intermediates. Moreover, when introducing ten equivalents of deuterated water to the reaction system, 47% deuterium content was observed in the isotopomers of **155a-d**, in which irradiation of blue light is essential to promote this deuterium exchange (Scheme 60b). In addition, employing TEMPO and 1,1-diphenylethylene as radical trapping reagents, suppression or inhibition of this photocatalytic reaction indicated that radical intermediates are involved in this reaction (Scheme 60c).

This control experiment part was performed by Sripati Jana.

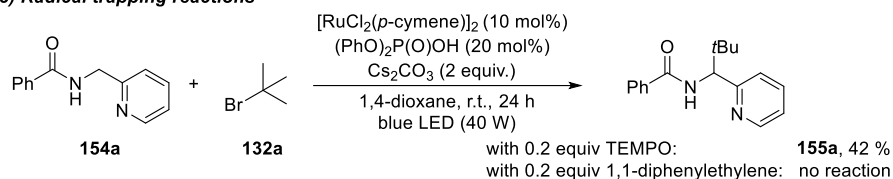
a) Reactions with an isolated Ru-complex



b) Deuterium labelling reactions



c) Radical trapping reactions



Scheme 60: Control experiments of photoinduced Ru-catalyzed C(sp³)-H functionalization

5.2.2 Computational Study

Based on the experimental results, we then performed detailed computational studies on the reaction mechanism. Firstly, we investigated the photoexcited state of cyclometalated ruthenium complex **156a** and **156b** with time-dependent TD-DFT method at SMD(1,4-dioxane)-(U)PBE0-D3/ def2-TZVP// (U)B3LYP/def2-SVP/SDD level of theory (Figure 40). The calculated UV-Vis spectra of **156a** and **156b** were similar to the experimental data of **156a**, whose HOMO to LUMO band system were predicted at 468.15 nm and 462.25 nm, respectively (Figure 40b). Importantly, the orbital analysis of both ruthenium complexes suggested a metal to ligand charge transfer (MLCT) from its HOMO orbital to LUMO orbital, which could serve as in situ generated photoredox catalysts.

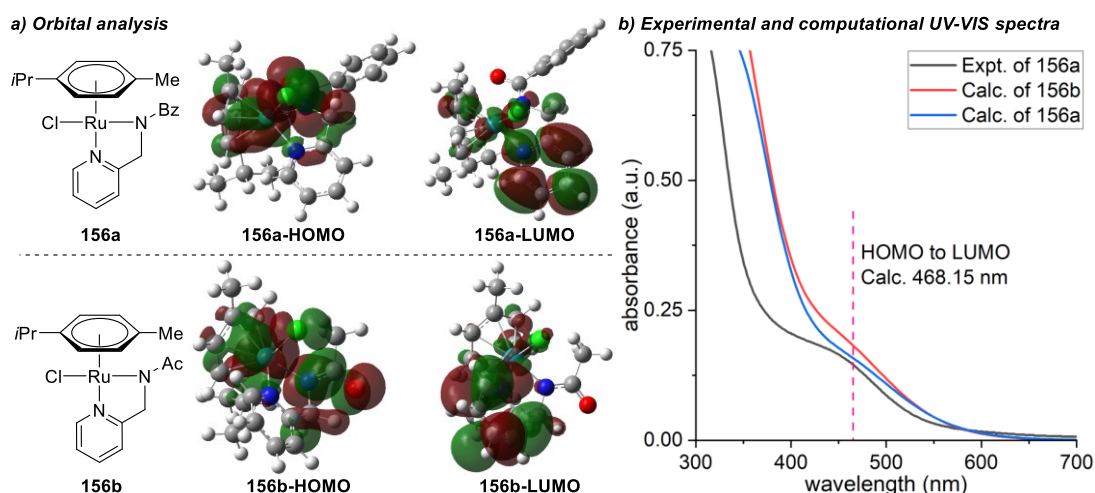


Figure 40: Experimental and computational study of photoexcited property of Ru-complexes

After identifying the suitable photoredox properties of viable catalyst **156a** or **156b**, we worked on the whole energy surface of this reaction theoretically, using **156b** and *t*BuBr **132a** as model substrates (Figure 41). Irradiation of **156b** by blue light resulted in the excited state of complex **156b***, which further led to more stable triplet state **156b-T** via intersystem crossing (ISC). In this step, coordination mode of cymene ligand with ruthenium changed from η^6 -cymene to η^2 -cymene, which might lead to an electronically unsaturated Ru(II) complex and facilitate the further deprotonation step. Subsequent coordination of Cs_2CO_3 yielded **INT1**, which was ready to undergo a deprotonation process via **TS1** with a low energy barrier of 4.1 kcal/mol. Ru complex **INT2** was exergonically generated with a η^6 -coordination of cymene ligand, which was consistent with the previous experimental result that the blue light was necessary to promote the deuterium exchange. Ligand exchange of **INT2** with *t*BuBr furnished **INT3**, serving as a reductant to convert *t*BuBr to a *tert*-butyl radical and Ru^{III}-complex **INT4**. This inner sphere electron transfer via **TS2** needed only an activation free energy of 6.8 kcal/mol. However, we have also calculated the outer sphere electron transfers by Marcus-Hush theory,²⁷³ which had high energy barriers and thus were unfavorable pathways (Scheme 61). Finally, Ru^{III}-complex **INT4** underwent a barrierless radical-radical coupling to afford the C(sp³)-H alkylation complex **INT5**, and this barrierless process could be accounted for by the coordinate scan in Figure 42. Simultaneously, protonation of **INT5**

with weak acid released the product and regenerated the ruthenium catalyst for the next catalytic cycle.

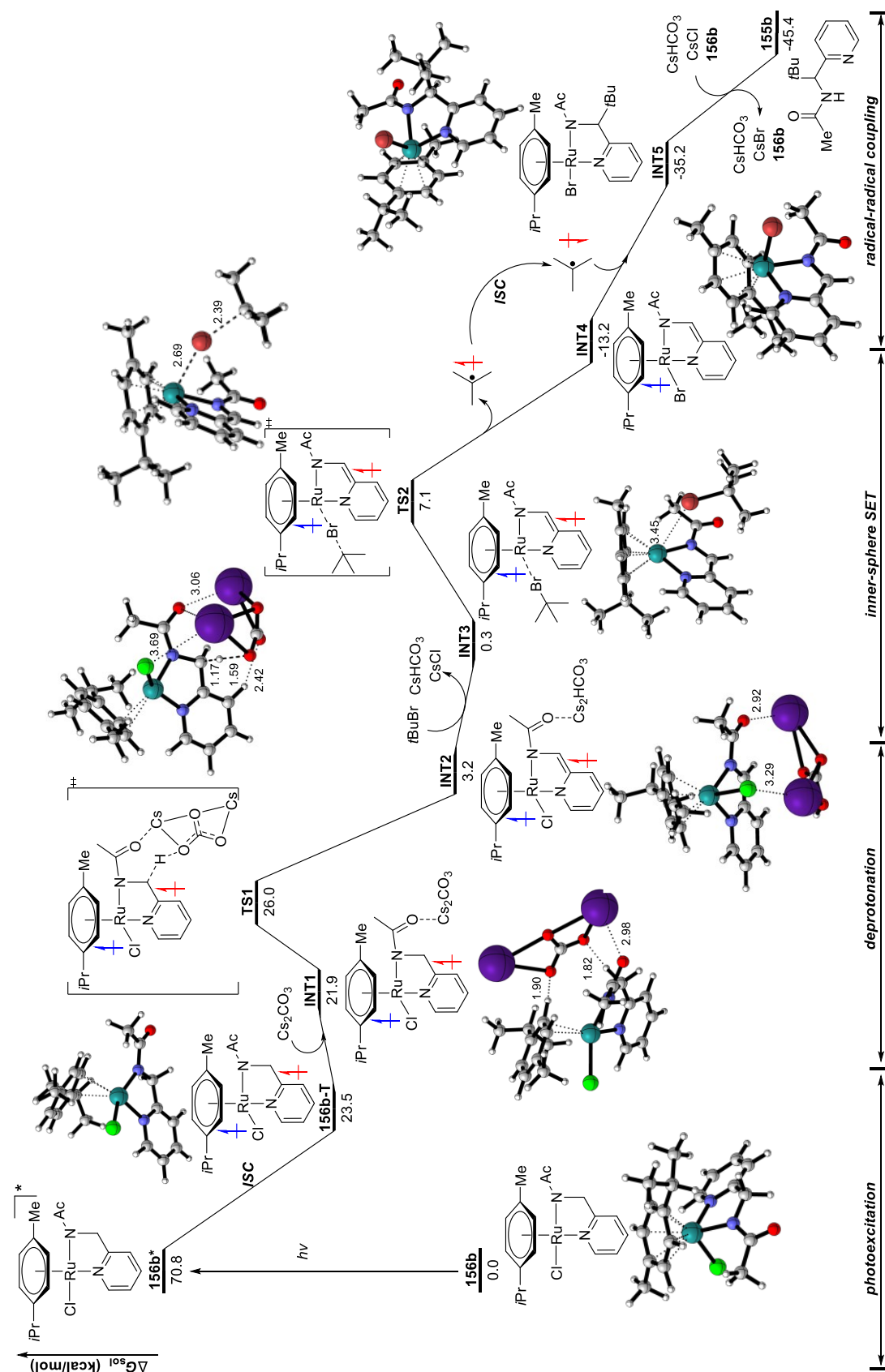
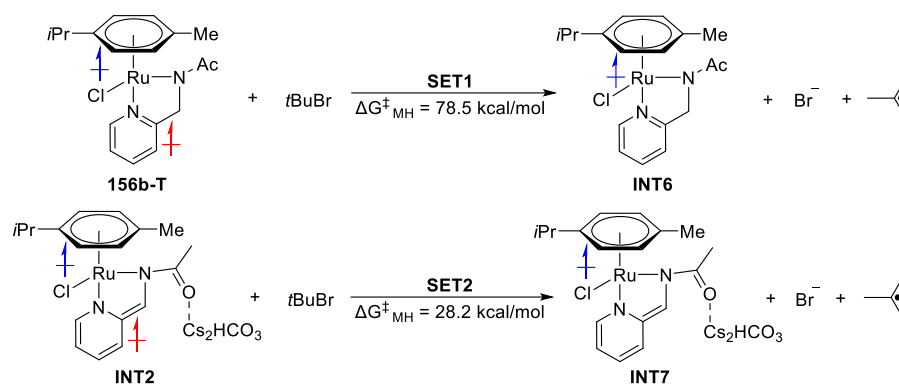
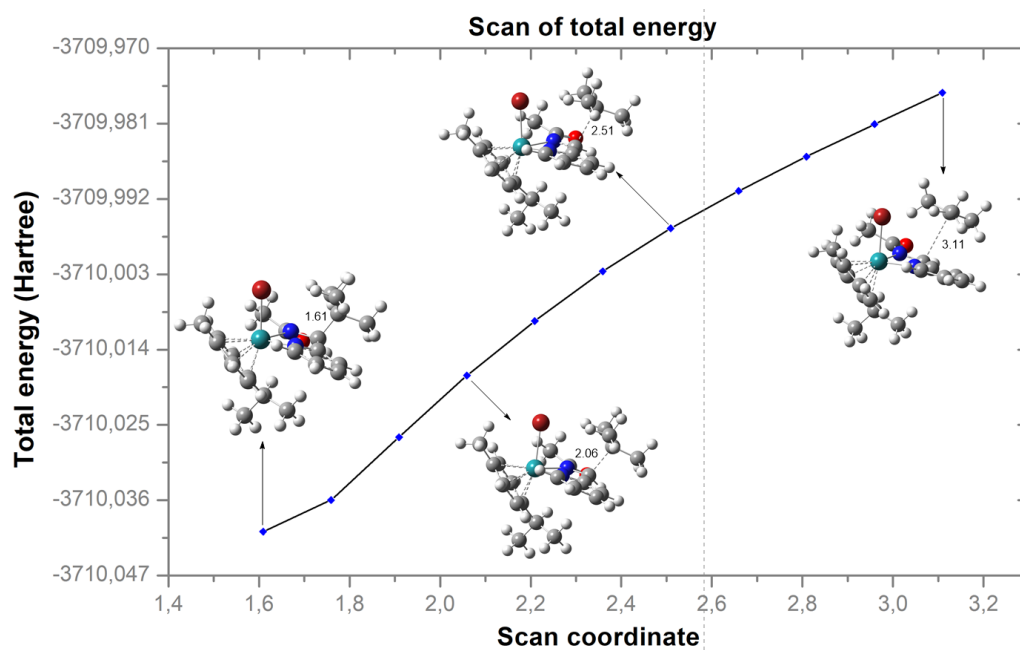


Figure 41: Potential energy surfaces of photoinduced Ru-catalyzed C(sp³)-H functionalization



Scheme 61: Activation free energy of outer sphere electron transfer steps

Figure 42: Coordinate scan of Ru(III)-complex INT4 with *tert*-butyl radical

5.2.3 Computational Data

All the calculations were performed with the Gaussian 16 program.¹⁸³ The geometries of all stationary points were optimized using the (U)B3LYP functional^{204,205} in combination with Grimme's dispersion correction with a Becke-Johnson damping scheme (D3BJ).²⁰⁹ During geometry optimization, the def2-SVP basis set²³⁵ was used for C, H, O, N, Cl and Br, and the basis set SDD^{297,298} and pseudopotential for Ru and Cs. Harmonic vibrational frequency calculations at the same level were performed for all of the stationary points to confirm them as a local minima or transition structures. Key transition-state structures were confirmed to connect corresponding reactants and products by intrinsic reaction coordinate (IRC) calculations.^{192,193} To improve the calculation accuracy, the electronic energy was then refined using def2-TZVP basis set²³⁵ at the (U)PBE0 level²⁹⁹ on the optimized geometries in combination with dispersion corrections (D3BJ). Solvation effect in 1,4-dioxane ($\epsilon = 2.2099$) were evaluated by IEFPCM calculations with radii and non-electrostatic terms for SMD solvation model²⁰⁸ based on the optimized structures. The given Gibbs free energies in 1,4-dioxane were calculated according to the formula: $G_{\text{sol}} = \text{TCG} + E_{\text{sol}} + 1.89 \text{ kcal mol}^{-1}$. Ruthenium complex **156a** and **156b** and their excited states were analyzed at (U)PBE0/def2-TZVP level of theory via time-dependent (TD)-DFT calculations (first twenty excited states). The CYLview software was employed to show the 3D structures of the studied species.¹⁹⁵

To get more details of the singlet electron transfer (SET) process, we estimated the free energy barrier of SET process using the Marcus-Hush theory,²⁷³ which can be calculated according to the following formula:

$$\Delta G_{\text{MH}}^{\ddagger} = \frac{(\Delta G_r + \lambda)^2}{4\lambda}$$

Where ΔG_r is the Gibbs free energy change of the SET step, λ is the reorganization energy including inner sphere energy and outer sphere energy. However, the outer sphere energy is often much larger than the inner sphere contribution. Hence, the outer sphere reorganization energy (λ_{outer}) can be regarded as the total reorganization energy, which can be calculated according to the following formula:

$$\lambda = \lambda_{\text{outer}} = 332 \left(\frac{1}{2r_1} + \frac{1}{2r_2} - \frac{1}{R} \right) \left(\frac{1}{\epsilon_{\text{opt}}} - \frac{1}{\epsilon_s} \right)$$

Where r_1 and r_2 are the radii of electron donor and acceptor, R is the sum of r_1 and r_2 , ϵ_{opt} and ϵ_s is the high frequency (optical) dielectric constant and static dielectric constant of solvent respectively (for 1,4-dioxane, $\epsilon_{\text{opt}} = 2.02$, $\epsilon_s = 2.21$).

Table 19: Calculated Free Energy Barriers ($\Delta G_{\text{MH}}^{\ddagger}$, kcal/mol) of Single Electron Transfer Steps

	r_1 (Å)	r_2 (Å)	R (Å)	λ (kcal/mol)	ΔG_r (kcal/mol)	$\Delta G_{\text{MH}}^{\ddagger}$ (kcal/mol)
SET1	3.45	6.55	10.00	1.71	54.8	55.0
SET2	3.45	7.84	11.29	1.70	17.2	25.0

Thermal correction to Gibbs free energies (**TCG**, in Hartree), thermal correction to enthalpies (**TCH**, in Hartree), sum of electronic and thermal free energies (**G**, in Hartree), single point energies in 1,4-dioxane computed at the (U)PBE0-D3/def2-TZVP level (**E_{sol}**, in Hartree), and total spin-squared operator of open-shell species **S²** are shown in Table 20.

Table 20: Computed Energies of all Stationary Points

Name	TCG/a.u.	TCH/a.u.	G/a.u.	E _{sol} /a.u.	S ²
156a	0.373860	0.459048	-1630.330630	-1630.528378	
156b	0.323933	0.402045	-1438.754046	-1438.940107	
156b-T	0.318480	0.401696	-1438.738990	-1438.897132	2.0154
Cs₂CO₃	-0.021549	0.023975	-304.003542	-304.093476	
INT1	0.319155	0.427404	-1742.790939	-1743.015429	2.0118
TS1	0.320059	0.424991	-1742.787810	-1743.009811	2.0159
INT2	0.316914	0.425991	-1742.831056	-1743.042939	2.0576
tBuBr	0.090625	0.128916	-2731.546902	-2731.589993	
CsHCO₃·CsCl	-0.012327	0.040026	-764.789325	-764.851478	
INT3	0.416808	0.51629	-3709.555689	-3709.783113	2.0241
TS2	0.416631	0.514217	-3709.546529	-3709.772108	2.0518
tBu·	0.086153	0.122999	-157.612139	-157.658883	0.7553
INT4	0.309981	0.389605	-3551.957839	-3552.125101	0.7662
INT5	0.431984	0.519941	-3709.607428	-3709.854903	
154b	0.133063	0.182862	-495.163462	-495.255998	
155b	0.240402	0.300632	-652.226108	-652.384350	
CsHCO₃·CsBr	-0.013777	0.039993	-2878.606237	-2878.651917	
INT6	0.323623	0.402849	-1438.526535	-1438.742207	0.7582
Br⁻	-0.016176	0.002360	-2573.942954	-2573.983251	
Br·	-0.01683	0.002360	-2573.843366	-2573.815374	0.7532
INT7	0.322567	0.429393	-1742.700837	-1742.948448	0.7680

5.3 Photoinduced Palladium-Catalyzed Cascade Cyclization with Isonitriles

5.3.1 Results and Discussion

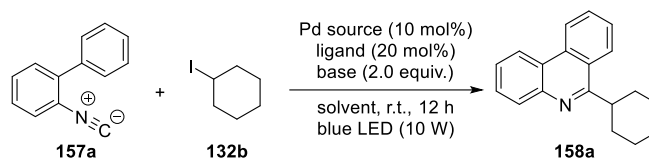
As mentioned above, the burgeoning photo-palladium catalysis mainly focuses on the functionalization of alkenes or alkynes.^{278,279} Inspired by this, we hypothesized that carbon-heteroatom unsaturated bonds can serve as radical acceptor and furnish cascade cyclization to construct complex heteropolycyclic skeletons. We then considered isonitriles as suitable substrates, which can introduce fused heterocycles into final products.

Thus, we started the investigation of the reaction of isonitriles **157a** with cyclohexyl iodide **132b** according to previous photoinduced palladium-catalyzed reaction conditions. Fortunately, the phenanthridine product **158a** was obtained in 33% yield in a first attempt when Pd(OAc)₂ was used as palladium catalyst and Xantphos as ligand under blue light irradiation (Table 21, entry 1). We next tested different palladium(II) and palladium(0) catalysts, such as Pd(TFA)₂, Pd(PPh₃)₂Cl₂, which all gave lower yields (Table 21, entry 2 and 3). Before the screening of ligand, we tested different equivalents of substrates and found 3.0 equivalents of isonitriles **157a** led to highest yield (77%, entry 6). Subsequently, phosphine ligands were found to play an important role in this transformation, and bidentate phosphine ligands like BINAP and XantPhos showed best catalytic activity (Table 21, entry 7-16). With the Xantphos as the optimal ligand, further screening of solvents and bases did not lead to a perceptible increase of the reaction yield (Table 21, 17-23). Unexpectedly, a significantly improved yield of 92% was obtained when using 5.0 equivalents of Cs₂CO₃ (Table 21, entry 20). Moreover, when conducting the reaction in the dark, catalyst-free, ligand-free or base-free conditions, complete inhibition reaction or sharply declining yields were observed (Table 21, entry 24-27). Additionally, cyclohexyl chloride and bromide proved less efficient under the current conditions and the corresponding phenanthridine product was obtained in trace amount and 30% yield, respectively (Table 21, entry 28 and 29).

After establishing the optimized conditions, we next turned to evaluate the influence of the different alkyl iodide and the groups of isonitrile moiety on this cascade cyclization reactions (Scheme 62). Firstly, different isonitriles showed excellent reactivity under standard reaction condition using cyclohexyl iodide **132b** (**158a** to **158d**). In addition, tertiary alkyl iodides like tertiary butyl iodide and adamantyl iodide led to the phenanthridine products **158e** and **158f** in 81% and 61% yield, respectively. An epiandosterone-derived iodide was investigated under the present conditions. To our delight, this corresponding phenanthridine product **158g** was obtained in moderate yield with high stereoselectivity. In this context, we also examined primary alkyl iodides such as cyclopropyl methyl iodide, which underwent a ring-opening process to give the homoallyl-substituted phenanthridine **158h** in 79% yield. This radical clock reaction thus suggested that an alkyl radical intermediate was involved.

This optimization part was performed by Zhen Yang.

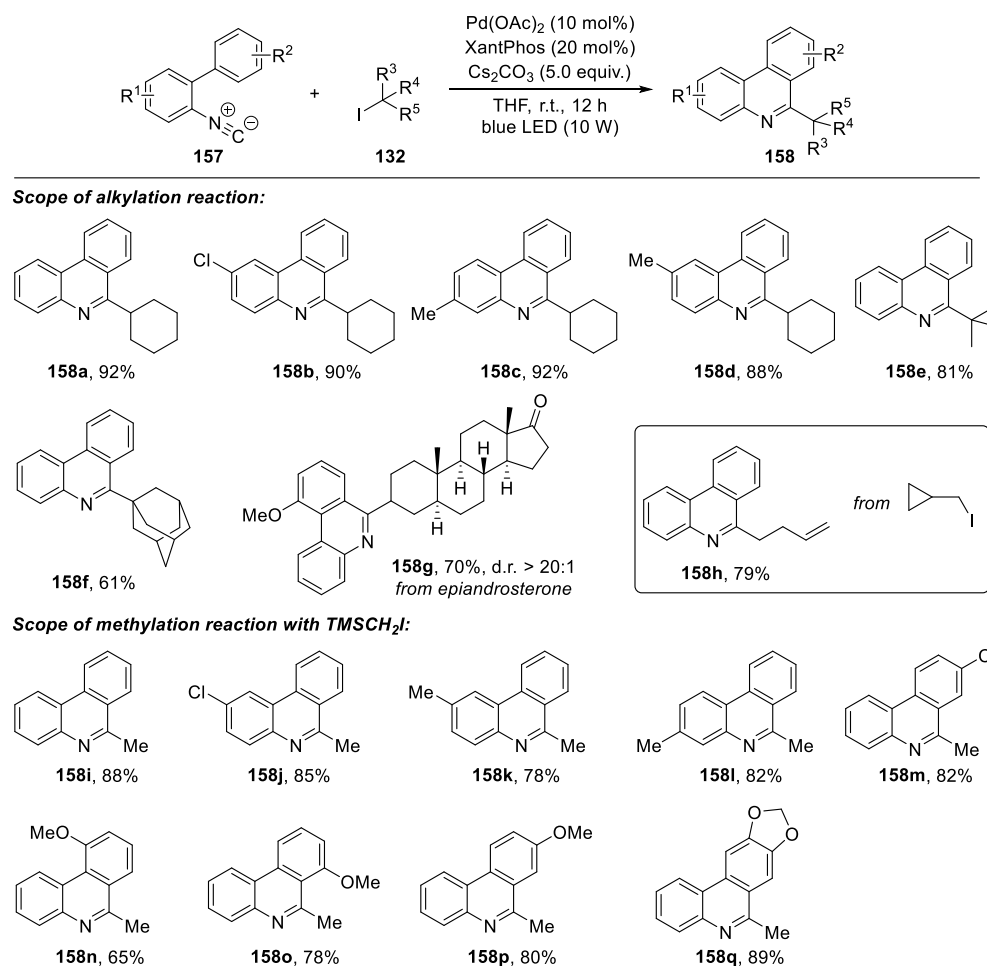
Table 21: Optimization of photoinduced Pd-catalyzed cascade cyclization reaction of isonitriles



Entry ^[a]	Catalyst	Ligand	157a : 132b	Base	Solvent	Yield (%)
1	Pd(OAc) ₂	XantPhos	1 : 2	Cs ₂ CO ₃	THF	33
2	Pd(TFA) ₂	XantPhos	1 : 2	Cs ₂ CO ₃	THF	11
3	Pd(PPh ₃) ₂ Cl ₂	XantPhos	1 : 2	Cs ₂ CO ₃	THF	8
4	Pd(OAc) ₂	XantPhos	1 : 1	Cs ₂ CO ₃	THF	31
5	Pd(OAc) ₂	XantPhos	2 : 1	Cs ₂ CO ₃	THF	56
6	Pd(OAc) ₂	XantPhos	3 : 1	Cs ₂ CO ₃	THF	77
7	Pd(OAc) ₂	SPhos	3 : 1	Cs ₂ CO ₃	THF	50
8	Pd(OAc) ₂	dppbe	3 : 1	Cs ₂ CO ₃	THF	55
9	Pd(OAc) ₂	RuPhos	3 : 1	Cs ₂ CO ₃	THF	43
10	Pd(OAc) ₂	dppm	3 : 1	Cs ₂ CO ₃	THF	38
11	Pd(OAc) ₂	DavePhos	3 : 1	Cs ₂ CO ₃	THF	44
12	Pd(OAc) ₂	PPh ₃	3 : 1	Cs ₂ CO ₃	THF	39
13	Pd(OAc) ₂	Cy-XantPhos	3 : 1	Cs ₂ CO ₃	THF	47
14	Pd(OAc) ₂	N-XantPhos	3 : 1	Cs ₂ CO ₃	THF	67
15	Pd(OAc) ₂	DPEPhos	3 : 1	Cs ₂ CO ₃	THF	34
16	Pd(OAc) ₂	rac-BINAP	3 : 1	Cs ₂ CO ₃	THF	70
17	Pd(OAc) ₂	XantPhos	3 : 1	Li ₂ CO ₃	THF	15
18	Pd(OAc) ₂	XantPhos	3 : 1	K ₂ CO ₃	THF	25
19 ^[c]	Pd(OAc) ₂	XantPhos	3 : 1	Cs ₂ CO ₃	THF	85
20 ^[d]	Pd(OAc) ₂	XantPhos	3 : 1	Cs ₂ CO ₃	THF	93 (92) ^[e]
21 ^[d]	Pd(OAc) ₂	XantPhos	3 : 1	Cs ₂ CO ₃	toluene	57
22 ^[d]	Pd(OAc) ₂	XantPhos	3 : 1	Cs ₂ CO ₃	CH ₃ CN	41
23 ^[d]	Pd(OAc) ₂	XantPhos	3 : 1	Cs ₂ CO ₃	DMA	29
24 ^{[d],[f]}	Pd(OAc) ₂	XantPhos	3 : 1	Cs ₂ CO ₃	THF	n.r.
25	Pd(OAc) ₂	XantPhos	3 : 1	-	THF	n.r.
26	Pd(OAc) ₂	-	3 : 1	Cs ₂ CO ₃	THF	10
27	-	XantPhos	3 : 1	Cs ₂ CO ₃	THF	n.r.
28 ^{[d],[g]}	Pd(OAc) ₂	XantPhos	3 : 1	Cs ₂ CO ₃	THF	trace
29 ^{[d],[h]}	Pd(OAc) ₂	XantPhos	3 : 1	Cs ₂ CO ₃	THF	30

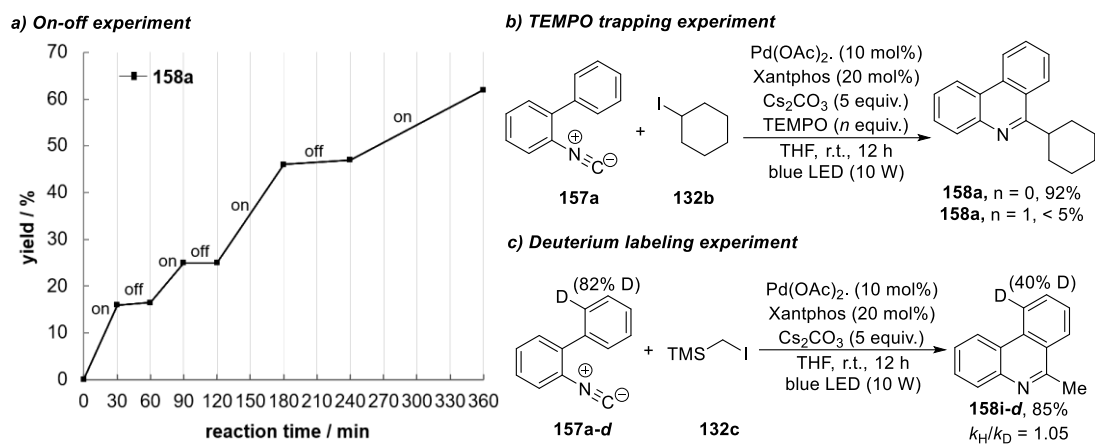
^[a] Reaction condition: cyclohexyl iodide **132b**, isonitrile **157a**, Cs₂CO₃, 10 mol% Pd(OAc)₂ and 20 mol% ligand were dissolved in 1 mL THF under argon atmosphere, irradiated with 10W blue LED (470 nm) at room temperature overnight. ^[b] The yield was determined by ¹H-NMR of the reaction crude with 1,3,5-trimethoxybenzene as the internal standard. ^[c] 0.6 mmol Cs₂CO₃ was used. ^[d] 1.0 mmol Cs₂CO₃ was used. ^[e] Isolated yield. ^[f] In the dark condition. ^[g] Cyclohexyl chloride was used instead of cyclohexyl iodide. ^[h] Cyclohexyl bromide was used instead of cyclohexyl iodide. n.r. = no reaction.

Furthermore, when testing the TMSCH₂I as the coupling partner, a desilylation process occurred and methylated phenanthridine was obtained in good yield. We therefore explored the scope of a variety of biphenyl isocyanides in the methylation reaction, which all examined to give the corresponding phenanthridines in high yield (**158i** to **158q**). In this case, we assumed that the methylated products were generated due to facile desilylation of benzylic TMS group under current reaction conditions.⁹⁸



Scheme 62: Substrate scopes of photocatalytic cascade cyclization of isocyanides with alkyl iodides

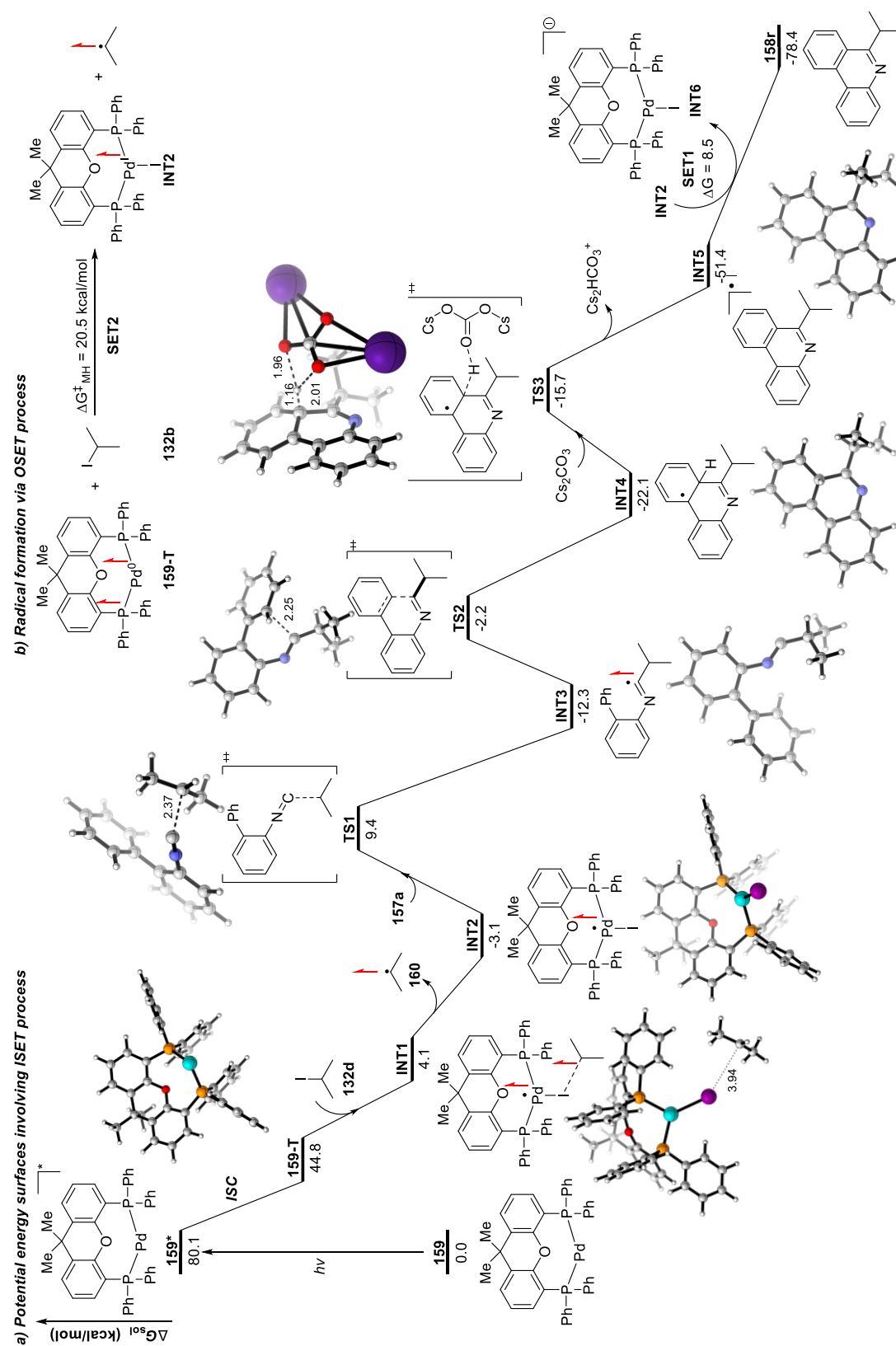
To gain insight into the reaction mechanism, a series of control experiments were then performed. Firstly, the on/off experiment of the reaction with isocyanide **157a** and cyclohexyl iodide **132b** revealed that the light is necessary in this reaction and ruled out a potential radical-chain process (Scheme 63a). Furthermore, in the presence of spin trapping reagents, such as 2,2,6,6-tetramethylpiperidinyloxy (TEMPO), the reaction was completely suppressed (Scheme 63b). This observation is consistent with the previous radical clock and supported the participation of alkyl radical intermediates. In addition, this photocatalytic reaction involves a C(sp²)-H functionalization step, which encouraged us to investigate kinetic isotope effect of this C-H bond cleavage. In the intramolecular competition reaction of **157a-d** with TMSCH₂I, we observed the half consumption of deuterium in the final product **158i-d**, which supported that the deprotonation process is not the rate determining step (Scheme 63c).



Scheme 63: Control experiments.

5.3.2 Computational Study

Based on the experimental results and previous reports,²⁹¹ we performed detailed theoretical studies on this underlying reaction mechanism. We used isonitrile **157a** and 2-



Scheme 64: Potential energy surfaces of photoinduced Pd-catalyzed cyclization of isonitrile

iodopropane **132d** as model substrates, which afforded phenanthridine **158r** in 93% yield, to simplify the calculation at M06-2X-D3/def2-TZVPP(SMD=THF)//PBE0-D3/def2-SVP/SDD(SMD=THF) level of theory (Scheme 64a). Photoexcitation of *in situ* generated Pd(0)XantPhos **159** was considered to initiate this reaction and leads to its first singlet excited state **159***. Singlet state **159*** would undergo intersystem crossing and deliver more stable triplet state of Pd(0)XantPhos **159-T** ($\Delta G = 44.8$ kcal/mol). In the next step, coordination of photoexcited Pd(0) complex **159-T** with 2-iodopropane **132d** directly led free isopropyl radical and Pd(I)XantPhos complex **INT2**. When enlarging the distance of C–I bond in the initial structure of **INT1**, we have not seen an obvious energy barrier, which suggested this inner-sphere single electron transfer (ISET) process was consecutively barrierless (Figure 43). Instead, we have also taken the outer-sphere SET between Pd(0)XantPhos **159-T** and 2-iodopropane **132d** into account (Scheme 64b). However, calculated free energy barrier was 20.5 kcal/mol via Marcus theory (SET2), which was unfavorable compared to ISET process.

Following formation of the isopropyl radical, a facile radical addition onto the isonitrile group occurred *via* **TS1** with an activation free energy of 12.5 kcal/mol, giving the imine radical **INT3**. Subsequently, imine radical **INT3** underwent an exergonically dearomative radical cyclization step *via* **TS2**, which required an activation free energy of 10.1 kcal/mol and led to intermediate **INT4**. In presence of Cs_2CO_3 , key intermediate **INT4** then underwent a deprotonation and generated the radical anion **INT5** *via* **TS3** with a free energy barrier of 6.4 kcal/mol. Indeed, this low-lying transition state ruled out the deprotonation process as a rate determining step, which was consistent with the intramolecular KIE experiment. Final SET between Pd(I)XantPhos **INT2** and **INT5** afforded phenanthridine product **158r** and released Pd(0)XantPhos **INT6** for further catalytic cycle ($\Delta G_{\text{MH}}^\ddagger = 8.5$ kcal/mol).

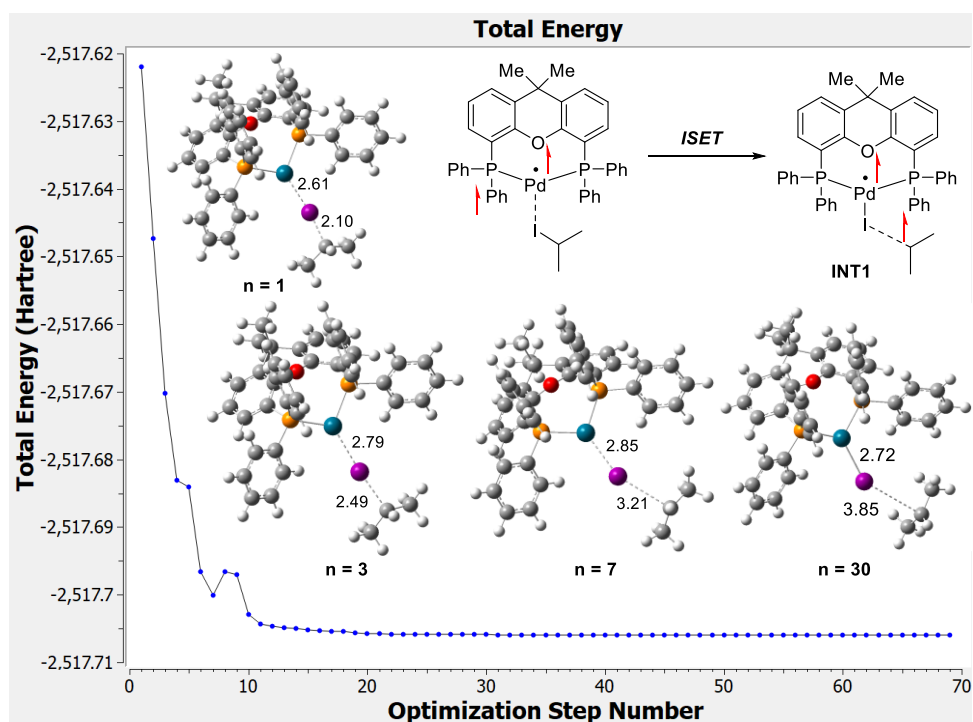


Figure 43: Optimization plots of coordination of photoexcited Pd(0) catalyst with 2-iodopropane

Besides the radical cyclization pathway, we have also considered the coordination of Pd(I) species with radical intermediates. For example, the coupling of imine radical **INT3** with Pd(I)XantPhos **INT2** formed imidoyl-Pd(II) complex **INT7**, which was exergonic by 16.7 kcal/mol. However, subsequent hypothetical C–H activation via **TS4** and reductive elimination process were proved with a high energy barrier of 25.3 kcal/mol and thus were less favored than radical cyclization pathway via **TS2** (Figure 44). In addition, an alternative η^3 coordination mode of Pd(I)XantPhos **INT2** with radical species **INT4** was also energetically favored (Figure 45). However, all attempts in locating further β -hydride elimination transition states from **INT9** led to product **158r** directly. This pathway cannot be ruled out at this level of theory, which might also serve regard as a possible mechanism.

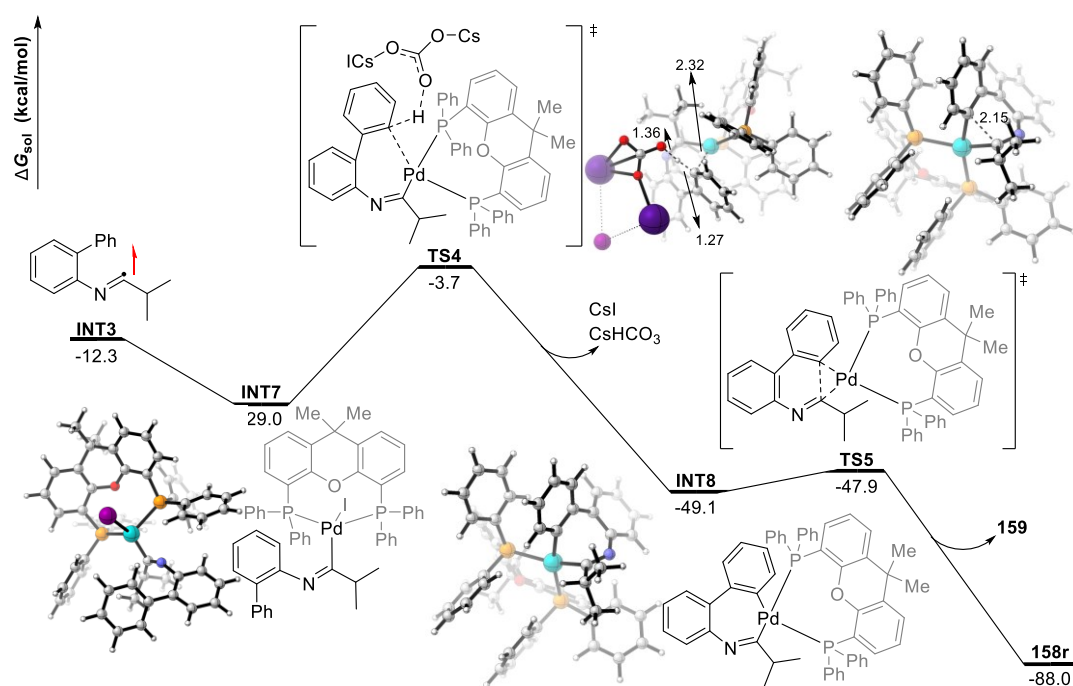


Figure 44: Potential energy surfaces of C–H activation and reductive elimination

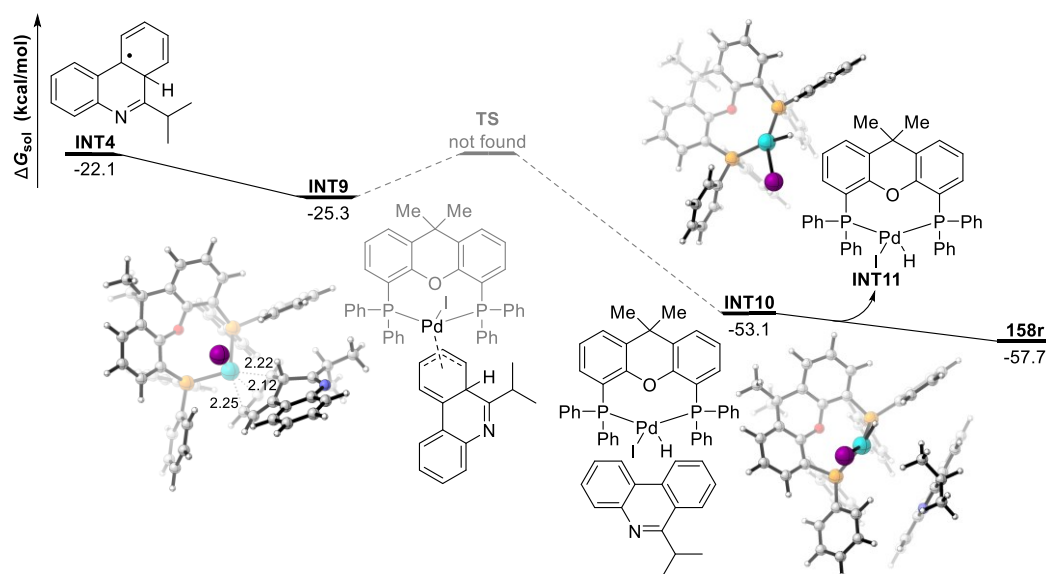


Figure 45: Potential energy surfaces of Pd-assisted β -hydride elimination process

5.3.3 Experimental Data

General procedure of photoinduced Pd-catalyzed cascade cyclization reaction

In a transparent test tube equipped with a stirring bar, Pd(OAc)₂ (10 mol%, 4.5 mg) and Xantphos (20 mol%, 23.2 mg), Cs₂CO₃ (5.0 equiv., 1.0 mmol, 326 mg) were added. The reaction tube was evacuated and filled with argon for three times. Then isonitriles (3.0 equiv., 0.6 mmol), iodide compounds (1.0 equiv., 0.2 mmol) and 1 mL fresh THF were added via a syringe under argon atmosphere, and the reaction tube was irradiated with a 10 W blue LED lamp (5 cm distance). A cooling fan is used to maintain room temperature (near 25 °C). The reaction mixture was stirred at room temperature overnight. The corresponding phenanthridines product was obtained after column chromatography using *n*-hexane / EtOAc as eluent.

6-Cyclohexylphenanthridine (158a).

Colorless oil; ¹H NMR (600 MHz, Chloroform-*d*): δ = 8.66 (d, *J* = 8.2 Hz, 1H), 8.54 (d, *J* = 8.1 Hz, 1H), 8.32 (d, *J* = 8.3 Hz, 1H), 8.13 (d, *J* = 8.1 Hz, 1H), 7.81 (t, *J* = 7.6 Hz, 1H), 7.69 (dd, *J* = 13.8, 6.9 Hz, 2H), 7.60 (t, *J* = 7.5 Hz, 1H), 3.65 – 3.56 (m, 1H), 2.08 (d, *J* = 12.1 Hz, 2H), 2.00 – 1.92 (m, 4H), 1.84 (d, *J* = 12.8 Hz, 1H), 1.62 – 1.55 (m, 2H), 1.49 – 1.39 (m, 1H) ppm. ¹³C NMR (151 MHz, Chloroform-*d*): 165.2, 143.8, 132.9, 129.9, 129.8, 128.3, 127.0, 126.0, 125.5, 124.7, 123.3, 122.5, 121.7, 41.9, 32.2, 26.8, 26.3 ppm.

2-Chloro-6-cyclohexylphenanthridine (158b).

Colorless oil; ¹H NMR (600 MHz, CDCl₃): δ = 8.54 (d, *J* = 8.2 Hz, 1H), 8.47 (d, *J* = 2.3 Hz, 1H), 8.31 (d, *J* = 8.2 Hz, 1H), 8.05 (d, *J* = 8.7 Hz, 1H), 7.81 (ddd, *J* = 8.3, 6.9, 1.3 Hz, 1H), 7.71 (ddd, *J* = 8.2, 6.9, 1.2 Hz, 1H), 7.62 (dd, *J* = 8.7, 2.3 Hz, 1H), 3.59 (tt, *J* = 11.4, 3.3 Hz, 1H), 2.06 (d, *J* = 12.8 Hz, 2H), 2.00 – 1.87 (m, 4H), 1.87 – 1.79 (m, 1H), 1.57 (qt, *J* = 12.6, 3.4 Hz, 2H), 1.43 (qt, *J* = 13.0, 3.7 Hz, 1H) ppm. ¹³C NMR (151 MHz, CDCl₃): δ = 165.7, 142.4, 132.1, 132.0, 131.5, 130.3, 128.9, 127.8, 125.8, 124.9, 124.5, 122.7, 121.6, 42.1, 32.4, 26.9, 26.4 ppm.

6-Cyclohexyl-3-methylphenanthridine (158c).

Colorless oil; ¹H NMR (600 MHz, CDCl₃): δ = 8.60 (dd, *J* = 8.4, 1.2 Hz, 1H), 8.41 (d, *J* = 8.3 Hz, 1H), 8.30 (d, *J* = 8.3 Hz, 1H), 7.96 (s, 1H), 7.78 (ddd, *J* = 8.3, 6.9, 1.2 Hz, 1H), 7.65 (ddd, *J* = 8.2, 6.9, 1.2 Hz, 1H), 7.43 (dd, *J* = 8.3, 1.8 Hz, 1H), 3.80 – 3.37 (m, 1H), 2.59 (s, 3H), 2.09 (d, *J* = 11.6 Hz, 2H), 2.03 – 1.91 (m, 4H), 1.86 (d, *J* = 12.8 Hz, 1H), 1.63 – 1.54 (m, 2H), 1.51 – 1.40 (m, 1H) ppm. ¹³C NMR (151 MHz, CDCl₃): δ = 165.4, 144.1, 138.6, 133.2, 129.9, 129.6, 127.9, 126.6, 125.7, 124.5, 122.5, 121.7, 121.1, 42.0, 32.4, 27.0, 26.4, 21.5 ppm.

6-Cyclohexyl-2-methylphenanthridine (158d).

Colorless oil; ¹H NMR (600 MHz, CDCl₃): δ = 8.63 (d, *J* = 8.2 Hz, 1H), 8.31 (s, 1H), 8.30 (d, *J* = 8.2 Hz, 1H), 8.03 (d, *J* = 8.3 Hz, 1H), 7.78 (ddd, *J* = 8.3, 7.0, 1.3 Hz, 1H), 7.66 (ddd, *J* = 8.2, 6.9, 1.2 Hz, 1H), 7.53 (dd, *J* = 8.3, 1.9 Hz, 1H), 3.60 (tt, *J* = 11.5, 3.2 Hz, 1H), 2.61 (s, 3H), 2.08 (d, *J* = 11.8 Hz, 2H), 2.02 – 1.90 (m, 4H), 1.85 (d, *J* = 13.3 Hz, 1H), 1.58 (qt, *J* = 14.1, 4.1 Hz, 2H), 1.44 (qt, *J* = 13.0, 3.6 Hz, 1H) ppm. ¹³C NMR (151 MHz, CDCl₃): δ = 164.3, 142.3, 135.9, 132.9, 130.1, 129.8, 127.0, 125.6, 124.9, 123.2, 122.6, 121.5, 42.0, 32.4, 27.0, 26.4, 22.0 ppm.

6-(*tert*-Butyl)phenanthridine (158e).

Colorless oil; ^1H NMR (400 MHz, CDCl_3): δ = 8.70 (d, J = 8.0 Hz, 1H), 8.64 (d, J = 8.5 Hz, 1H), 8.53 (d, J = 8.2 Hz, 1H), 8.14 (d, J = 8.0 Hz, 1H), 7.84 – 7.76 (m, 1H), 7.73 – 7.55 (m, 3H), 1.74 (s, 9H) ppm. ^{13}C NMR (151 MHz, CDCl_3): δ = 166.7, 143.0, 134.1, 130.4, 129.3, 128.4, 128.3, 126.5, 126.0, 124.4, 123.5, 123.1, 121.7, 40.3, 31.3 ppm.

6-((3*S*)-Adamantan-1-yl)phenanthridine (158f).

Colorless oil; ^1H NMR (400 MHz, CDCl_3): δ = 8.86 (d, J = 8.6 Hz, 1H), 8.70 (d, J = 8.3 Hz, 1H), 8.52 (d, J = 8.2 Hz, 1H), 8.12 (dd, J = 8.3, 1.6 Hz, 1H), 7.82 – 7.74 (m, 1H), 7.73 – 7.56 (m, 3H), 2.50 (s, 6H), 2.24 (s, 3H), 1.92 (q, J = 12.4 Hz, 6H) ppm. ^{13}C NMR (151 MHz, CDCl_3): δ = 167.7, 143.2, 134.2, 130.3, 129.2, 128.4, 128.1, 126.5, 125.8, 124.6, 123.4, 123.2, 121.7, 42.1, 37.3, 29.4 ppm.

(5*S*,8*R*,9*S*,10*S*,13*S*,14*S*)-3-(10-Methoxyphenanthridin-6-yl)-10,13-dimethylhexadecahydro-17*H*-cyclopenta[*a*]phenanthren-17-one (158g).

White solid; ^1H NMR (600 MHz, CDCl_3): δ = 9.45 (dd, J = 8.5, 1.4 Hz, 1H), 8.15 (dd, J = 8.0, 1.5 Hz, 1H), 7.86 (d, J = 8.2 Hz, 1H), 7.69 (ddd, J = 8.2, 6.9, 1.4 Hz, 1H), 7.64 – 7.55 (m, 2H), 7.28 (d, J = 8.0 Hz, 1H), 4.14 (s, 3H), 4.02 (t, J = 6.2 Hz, 1H), 2.41 (dd, J = 19.4, 8.8 Hz, 1H), 2.26 (d, J = 12.5 Hz, 1H), 2.11 – 1.93 (m, 4H), 1.88 (ddd, J = 14.3, 8.8, 5.9 Hz, 1H), 1.84 – 1.78 (m, 2H), 1.71 (ddt, J = 16.4, 12.8, 6.7 Hz, 3H), 1.63 – 1.59 (m, 1H), 1.46 (tt, J = 12.5, 9.0 Hz, 1H), 1.38 – 1.10 (m, 7H), 0.95 (s, 3H), 0.87 (s, 3H), 0.79 (td, J = 11.5, 4.1 Hz, 1H) ppm. ^{13}C NMR (151 MHz, CDCl_3): δ = 222.2, 164.2, 158.9, 144.0, 130.1, 127.9, 127.7, 127.1, 126.9, 126.1, 123.7, 123.1, 118.5, 110.9, 55.9, 54.7, 51.6, 48.0, 40.8, 36.2, 36.05, 36.02, 35.3, 35.2, 33.0, 31.7, 30.9, 28.7, 25.4, 21.9, 20.2, 13.9, 12.0 ppm. HRMS (ESI) m/z : $[\text{M} + \text{H}]^+$ mass found: 482.30514, mass calculated for $\text{C}_{33}\text{H}_{40}\text{O}_2\text{N}$: 482.30536. IR (KBr): 3458, 3073, 2922, 2854, 2499, 2250, 2168, 2032, 1952, 1734, 1574, 1529, 1448, 1352, 1290, 1261, 1238, 1205, 1141, 1098, 1022, 970, 909, 824, 765, 727 cm^{-1} .

6-(But-3-en-1-yl)phenanthridine (158h).

Yellow solid; ^1H NMR (600 MHz, CDCl_3): δ = 8.65 (d, J = 8.3 Hz, 1H), 8.55 (d, J = 8.1 Hz, 1H), 8.26 (d, J = 8.2 Hz, 1H), 8.13 (d, J = 8.1 Hz, 1H), 7.87 – 7.80 (m, 1H), 7.77 – 7.68 (m, 2H), 7.66 – 7.60 (m, 1H), 6.06 (ddt, J = 16.9, 10.2, 6.5 Hz, 1H), 5.17 (d, J = 17.2 Hz, 1H), 5.05 (d, J = 10.1 Hz, 1H), 3.51 – 3.45 (m, 2H), 2.77 – 2.66 (m, 2H) ppm. ^{13}C NMR (151 MHz, CDCl_3): δ = 161.4, 143.8, 138.2, 133.0, 130.4, 129.7, 128.7, 127.4, 126.5, 126.3, 125.3, 123.8, 122.6, 122.0, 115.2, 35.5, 33.2 ppm.

6-Methylphenanthridine (158i).

Yellow oil; ^1H NMR (600 MHz, CDCl_3): δ = 8.64 (d, J = 8.3 Hz, 1H), 8.55 (d, J = 8.1 Hz, 1H), 8.23 (d, J = 8.2 Hz, 1H), 8.10 (d, J = 8.1 Hz, 1H), 7.85 (t, J = 7.6 Hz, 1H), 7.71 (q, J = 7.0 Hz, 2H), 7.62 (t, J = 7.5 Hz, 1H), 3.05 (s, 3H) ppm. ^{13}C NMR (151 MHz, CDCl_3): δ = 158.8, 143.7, 132.6, 130.4, 129.4, 128.6, 127.3, 126.5, 126.3, 125.9, 123.8, 122.3, 121.9, 23.4 ppm.

6-methylphenanthridine-10-*d* (158i-d).

Yellow oil; ^1H NMR (600 MHz, CDCl_3): δ = 8.67 – 8.60 (m, 0.6H), 8.53 (dddd, J = 8.1, 3.3, 1.4, 0.6 Hz, 1H), 8.21 (dt, J = 8.1, 1.0 Hz, 1H), 8.16 – 8.07 (m, 1H), 7.89 – 7.79 (m, 1H), 7.70 (dddd, J = 12.2, 8.1, 7.0, 1.2 Hz, 2H), 7.62 (ddd, J = 8.3, 6.9, 1.4 Hz, 1H), 3.05 (s, 3H). ^{13}C NMR (151 MHz, CDCl_3): δ = 159.0, 143.8, 132.7, 130.5, 129.5, 128.7, 127.4, 126.6, 126.4, 126.0, 123.9, 122.4, 122.0, 23.5 ppm.

2-Chloro-6-methylphenanthridine (158j).

Colorless oil; ^1H NMR (600 MHz, CDCl_3): δ = 8.54 (d, J = 8.2 Hz, 1H), 8.49 (d, J = 2.3 Hz, 1H), 8.23 (d, J = 8.0 Hz, 1H), 8.02 (d, J = 8.7 Hz, 1H), 7.86 (ddd, J = 8.3, 7.0, 1.3 Hz, 1H), 7.74 (ddd, J = 8.2, 7.0, 1.2 Hz, 1H), 7.65 (dd, J = 8.7, 2.3 Hz, 1H), 3.03 (s, 3H) ppm. ^{13}C NMR (151 MHz, CDCl_3): δ = 159.4, 142.3, 132.3, 131.7, 131.0, 130.9, 129.2, 128.1, 126.7, 126.2, 125.0, 122.5, 121.8, 23.5 ppm.

2,6-Dimethylphenanthridine (158k).

Colorless oil; ^1H NMR (600 MHz, CDCl_3): δ = 8.62 (d, J = 8.5 Hz, 1H), 8.32 (s, 1H), 8.21 (d, J = 8.3 Hz, 1H), 7.99 (d, J = 8.2 Hz, 1H), 7.83 (ddd, J = 8.2, 7.0, 1.3 Hz, 1H), 7.68 (ddd, J = 8.2, 7.0, 1.2 Hz, 1H), 7.54 (dd, J = 8.3, 1.9 Hz, 1H), 3.03 (s, 3H), 2.62 (s, 3H) ppm. ^{13}C NMR (151 MHz, CDCl_3): δ = 157.9, 142.1, 136.2, 132.5, 130.5, 130.4, 129.2, 127.2, 126.6, 126.1, 123.7, 122.4, 121.7, 23.4, 22.0 ppm.

3,6-Dimethylphenanthridine (158l).

Colorless oil; ^1H NMR (600 MHz, CDCl_3): δ = 8.59 (d, J = 8.5 Hz, 1H), 8.43 (d, J = 8.3 Hz, 1H), 8.21 (d, J = 8.1 Hz, 1H), 7.90 (s, 1H), 7.82 (ddd, J = 8.3, 7.0, 1.3 Hz, 1H), 7.67 (ddd, J = 8.2, 7.0, 1.2 Hz, 1H), 7.45 (dd, J = 8.2, 1.8 Hz, 1H), 3.04 (s, 3H), 2.58 (s, 3H) ppm. ^{13}C NMR (151 MHz, CDCl_3): δ = 159.0, 143.9, 138.9, 132.8, 130.5, 129.1, 128.1, 126.9, 126.7, 125.8, 122.3, 121.8, 121.5, 23.5, 21.7 ppm.

8-Chloro-6-methylphenanthridine (158m).

Colorless oil; ^1H NMR (600 MHz, CDCl_3): δ = 8.49 (d, J = 8.8 Hz, 1H), 8.43 (dd, J = 8.1, 1.4 Hz, 1H), 8.13 (d, J = 2.1 Hz, 1H), 8.08 (d, J = 8.1 Hz, 1H), 7.74 (dd, J = 8.8, 2.2 Hz, 1H), 7.71 (ddd, J = 8.2, 7.0, 1.4 Hz, 1H), 7.61 (ddd, J = 8.2, 7.0, 1.3 Hz, 1H), 2.98 (s, 3H) ppm. ^{13}C NMR (151 MHz, CDCl_3): δ = 157.8, 143.7, 133.2, 131.1, 131.0, 129.6, 129.0, 126.9, 126.8, 125.9, 124.2, 123.2, 121.9, 23.4 ppm.

10-Methoxy-6-methylphenanthridine (158n).

Colorless oil; ^1H NMR (600 MHz, CDCl_3): δ = 9.46 (dd, J = 8.6, 1.4 Hz, 1H), 8.11 (dd, J = 8.1, 1.6 Hz, 1H), 7.87 (dd, J = 8.2, 1.1 Hz, 1H), 7.70 (ddd, J = 8.2, 7.0, 1.4 Hz, 1H), 7.66 (t, J = 8.0 Hz, 1H), 7.60 (ddd, J = 8.5, 6.9, 1.5 Hz, 1H), 7.34 (d, J = 8.0 Hz, 1H), 4.16 (s, 3H), 3.04 (s, 3H) ppm. ^{13}C NMR (151 MHz, CDCl_3): δ = 158.4, 129.0, 128.9, 128.0, 127.97, 127.91, 127.4, 126.1, 123.6, 123.1, 118.8, 115.6, 111.6, 55.8, 24.1 ppm. HRMS (ESI) m/z : $[\text{M} + \text{H}]^+$ mass found: 224.10703, mass calculated for $\text{C}_{15}\text{H}_{14}\text{ON}$: 224.10699. IR (KBr): 3463, 3372, 3067, 2924, 2850, 2505, 2327, 1931, 1827, 1729, 1576, 1527, 1450, 1369, 1313, 1246, 1181, 1115, 1047, 1002, 956, 847, 810, 761, 719, 658 cm^{-1} .

7-Methoxy-6-methylphenanthridine (158o).

Colorless oil; ^1H NMR (600 MHz, CDCl_3): δ = 8.47 (dd, J = 8.3, 1.4 Hz, 1H), 8.20 (d, J = 8.2 Hz, 1H), 8.04 (dd, J = 8.2, 1.3 Hz, 1H), 7.71 (t, J = 8.1 Hz, 1H), 7.68 (ddd, J = 8.2, 7.0, 1.3 Hz, 1H), 7.57 (ddd, J = 8.3, 6.9, 1.3 Hz, 1H), 7.07 (d, J = 8.0 Hz, 1H), 4.01 (s, 3H), 3.17 (s, 3H) ppm. ^{13}C NMR (151 MHz, CDCl_3): δ = 159.0, 158.6, 143.8, 135.5, 131.0, 129.1, 128.8, 126.1, 123.2, 122.5, 117.8, 114.5, 108.2, 55.7, 30.2 ppm. HRMS (ESI) m/z : $[\text{M} + \text{H}]^+$ mass found: 224.10706, mass calculated for $\text{C}_{15}\text{H}_{14}\text{ON}$: 224.10699. IR (KBr): 3369, 3063, 2937, 2839, 2514, 2327, 2190, 2110, 1992, 1814, 1709, 1607, 1579, 1527, 1497, 1458, 1363, 1317, 1255, 1174, 1130, 1091, 1048, 1015, 946, 853, 746, 695 cm^{-1} .

8-Methoxy-6-methylphenanthridine (158p).

Colorless oil; ^1H NMR (400 MHz, CDCl_3): δ = 8.52 (d, J = 9.0 Hz, 1H), 8.44 (d, J = 8.1 Hz, 1H), 8.07 (dd, J = 8.1, 1.5 Hz, 1H), 7.65 (ddd, J = 8.1, 6.9, 1.5 Hz, 1H), 7.59 (ddd, J = 8.3, 7.0, 1.5 Hz, 1H), 7.49 (d, J = 2.6

Hz, 1H), 7.45 (dd, $J = 8.9, 2.6$ Hz, 1H), 3.99 (s, 3H), 3.00 (s, 3H) ppm. ^{13}C NMR (101 MHz, CDCl_3): $\delta = 158.7, 158.0, 142.9, 129.4, 127.7, 127.3, 126.9, 126.4, 124.1, 123.9, 121.5, 120.8, 106.9, 55.6, 23.6$ ppm.

6-Methyl-[1,3]dioxolo[4,5-*j*]phenanthridine (158q).

Yellow oil; ^1H NMR (600 MHz, CDCl_3): $\delta = 8.30$ (d, $J = 8.2$ Hz, 1H), 8.05 (d, $J = 8.1$ Hz, 1H), 7.88 (s, 1H), 7.64 (t, $J = 7.5$ Hz, 1H), 7.55 (t, $J = 7.5$ Hz, 1H), 7.47 (s, 1H), 6.13 (s, 2H), 2.94 (s, 3H) ppm. ^{13}C NMR (151 MHz, CDCl_3): $\delta = 157.2, 150.7, 148.0, 143.4, 130.1, 129.3, 127.9, 125.9, 123.8, 122.3, 121.7, 103.8, 101.8, 100.2, 23.7$ ppm. HRMS (ESI) m/z : $[\text{M} + \text{H}]^+$ mass found: 238.08541, mass calculated for $\text{C}_{15}\text{H}_{12}\text{O}_2\text{N}_1$: 238.08626. IR (KBr): 3360, 3062, 2905, 2777, 2323, 2075, 1669, 1620, 1576, 1453, 1387, 1309, 1241, 1108, 1031, 927, 862, 819, 757, 730 cm^{-1} .

5.3.4 Computational Data

All the calculations were performed with the Gaussian 16 program.¹⁸³ The geometries of all stationary points were optimized at the (U)PBE0 level of theory²⁹⁹ in combination with Grimme's dispersion correction with a Becke-Johnson damping scheme (D3BJ),²⁰⁹ in which solvent effects were included implicitly through the use of the SMD model for tetrahydrofuran.²⁰⁸ During geometry optimization, the def2-SVP basis set²³⁵ was used for C, C, H, O, N and P, and the basis set SDD^{297,298} and pseudopotential for Pd, I and Cs. Harmonic vibrational frequency calculations at the same level were performed for all of the stationary points to confirm them as a local minima or transition structures. Key transition-state structures were confirmed to connect corresponding reactants and products by intrinsic reaction coordinate (IRC) calculations.^{192,193} The electronic energy in tetrahydrofuran was then refined using def2-TZVPP basis set²³⁵ for all atoms at the (U)M06-2X level^{184,185} with D3 dispersion corrections on the optimized geometries. The given Gibbs free energies in dichloromethane were calculated according to the formula: $G_{\text{sol}} = \text{TCG} + E_{\text{sol}}$ (kcal/mol). The CYL View software was employed to show the 3D structures of the studied species.¹⁹⁵ Vertical excitations energies were calculated at the TD-M06-2X-D3 level with the def2-TZVPP basis set.

To get more details of the singlet electron transfer (SET) process, we estimated the free energy barrier of SET process using the Marcus-Hush theory,²⁷³ which can be calculated according to the following formula:

$$\Delta G_{\text{MH}}^{\ddagger} = \frac{(\Delta G_r + \lambda)^2}{4\lambda}$$

Where ΔG_r is the Gibbs free energy change of the SET step, λ is the reorganization energy including inner sphere energy and outer sphere energy. However, the outer sphere energy is often much larger than the inner sphere contribution. Hence, the outer sphere reorganization energy (λ_{outer}) can be regarded as the total reorganization energy, which can be calculated according to the following formula:

$$\lambda = \lambda_{\text{outer}} = 332 \left(\frac{1}{2r_1} + \frac{1}{2r_2} - \frac{1}{R} \right) \left(\frac{1}{\epsilon_{\text{opt}}} - \frac{1}{\epsilon_s} \right)$$

Where r_1 and r_2 are the radii of electron donor and acceptor, R is the sum of r_1 and r_2 , ϵ_{opt} and ϵ_s is the high frequency (optical) dielectric constant and static dielectric constant of solvent respectively (for 1,4-dioxane, $\epsilon_{\text{opt}} = 1.97$, $\epsilon_s = 7.43$).

Table 22: Calculated Free Energy Barriers ($\Delta G_{\text{MH}}^{\ddagger}$, kcal/mol) of Single Electron Transfer Steps

	r_1 (Å)	r_2 (Å)	R (Å)	λ (kcal/mol)	ΔG_r (kcal/mol)	$\Delta G_{\text{MH}}^{\ddagger}$ (kcal/mol)
SET1	8.24	5.85	14.09	9.30	-27.07	8.48
SET2	7.93	3.67	11.60	13.99	-47.85	20.48

Thermal correction to Gibbs free energies (**TCG**, in Hartree), thermal correction to enthalpies (**TCH**, in Hartree), sum of electronic and thermal free energies (**G**, in Hartree), sum of electronic and thermal enthalpies (**H**, in Hartree), and single point energies in tetrahydrofuran computed at the (U)M06-2X-D3/def2-TZVPP level (E_{sol} , in Hartree) are shown in Table 23.

Table 23: Computed Energies of all Stationary Points

Name	TCG/a.u.	TCH/a.u.	G/a.u.	H/a.u.	E_{sol} /a.u.
159	0.529154	0.638715	-2387.440518	-2387.330957	-2391.201275
159-T	0.528821	0.638309	-2387.370232	-2387.260744	-2391.129603
132d	0.063443	0.100002	-129.666830	-129.630271	-416.154515
INT1	0.597607	0.737946	-2517.108365	-2516.968026	-2807.354238
INT2	0.522101	0.642332	-2398.935531	-2398.815299	-2688.899524
160	0.060695	0.093865	-118.183921	-118.150751	-118.451385
157a	0.144232	0.192816	-554.340002	-554.291417	-555.502821
TS1	0.225736	0.288251	-672.507592	-672.445077	-673.955052
INT3	0.230890	0.292332	-672.550786	-672.489344	-673.994912
TS2	0.232634	0.290347	-672.539022	-672.481309	-673.980484
INT4	0.236058	0.291971	-672.575841	-672.519929	-674.015560
Cs₂CO₃	-0.023198	0.024513	-303.777404	-303.729692	-304.179898
TS3	0.234964	0.315966	-976.366752	-976.285749	-978.207372
Cs₂HCO₃⁻	-0.011559	0.037295	-304.306713	-304.257859	-304.682242
INT5	0.222998	0.279422	-672.126797	-672.070373	-673.558491
INT6	0.526459	0.641221	-2399.051682	-2398.936919	-2689.018930
158r	0.229529	0.283556	-672.054744	-672.000717	-673.493106
INT7	0.785098	0.937446	-3071.530122	-3071.377775	-3362.953124
TS4	0.782935	0.958485	-3375.313890	-3375.138340	-3667.113633
CsI·CsHCO₃	-0.019837	0.040117	-315.930909	-315.870954	-602.509509
INT8	0.781642	0.921866	-3059.446451	-3059.306226	-3064.655388
TS5	0.782950	0.920634	-3059.450228	-3059.312545	-3064.654827
INT9	0.792075	0.938323	-3071.534305	-3071.388057	-3362.954251
INT10	0.788019	0.936055	-3071.571815	-3071.423779	-3362.994455
INT11	0.533478	0.650617	-2685.807145	-2685.690007	-2689.483701

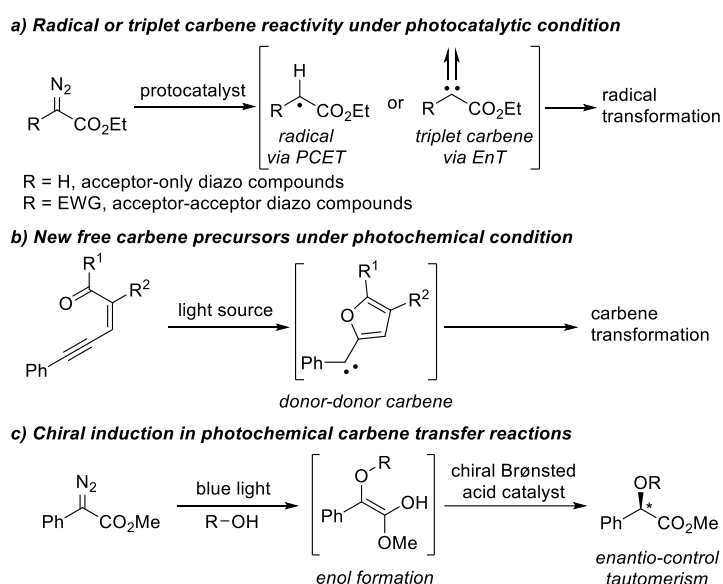
5.4 Conclusion

In summary, in this chapter we performed detailed computational study on a visible-light-induced ruthenium-catalyzed C(sp³)-H alkylation reaction. Theoretical calculations revealed a key ruthenacycle intermediate, which can serve as photosensitizer for further radical formation and C-C bond forming event. In addition, palladium catalyst can also be utilized as photocatalyst and facilitate a feasible C(sp³)-I cleavage under blue light irradiation. We introduced this methodology into the cascade cyclization of isonitriles, which provides a one-step strategy to access phenanthridines derivatives. In addition, experiments and calculations were conducted to reveal the underlying reaction pathways. The mechanism learning in this novel radical and classical Pd-type catalysis promotes us to develop more novel useful transformations.

6. Outlook

As discussed above, recent photochemical carbene transfer reactions mainly focus on colored aryl diazoacetate or diaryl diazomethane, which have achieved great progress. Instead, weakly colored acceptor-only diazoacetate or acceptor-acceptor diazo compounds that absorb light primarily in the UV light region, are attracting less attention in photochemistry (Scheme 65a). However, photolysis of these inert diazo compounds in the presence of photosensitizer under visible light irradiation opens up their triplet carbene reactivity via energy transfer (EnT) or radical reactivity via proton-coupled electron transfer (PCET). In addition, non-diazo carbene precursors that applied in transition metal-catalysis successfully, could be employed in photochemical or photocatalytic carbene transfer reactions with suitable light source, such as conjugated enynones (Scheme 65b). These carbene precursors will introduce diverse functional group into product formation, while different substituents that tethered with carbene center can also adjust the potential singlet or triplet reactivity.

Combining experimental observation with theoretical study reveals some potential intermediates or different reaction pathways. For example, we computationally identified an enol intermediate in photochemical O–H insertion reaction with phenyl diazoacetate, which could convert to final ether product with the assistance of chiral Brønsted acid (Scheme 65c). In this case, we probably realize asymmetric O–H insertion reaction via chiral induction in tautomerism step.

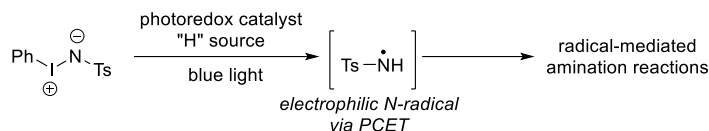


Scheme 65: Potential photochemical carbene transformations

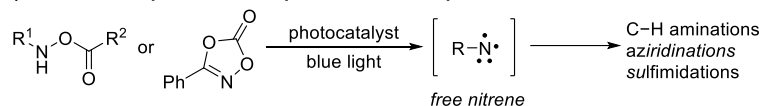
Regarding the photoinduced nitrene transfer reactions, can we utilize suitable proton sources or HAT agents to promote the formation of electrophilic N-radical via PCET process (Scheme 66a)? Such N-radical intermediate can furnish a series of amination reactions

through radical reactivity, which construct important building blocks for the synthesis of biologically active compounds. Furthermore, other nitrene precursors like dioxazoles and amide *N*-ethers/esters are worth trying in photoredox catalysis, which introduce important functional groups into amination products (Scheme 66b).

a) *N*-radical reactivity from nitrene precursor through PCET process



b) Novel nitrene precursors for photochemical or photoredox nitrene transformations



Scheme 66: Potential photochemical nitrene transformations

Finally, I am convinced that proper computational simulation offers reasonable dataset, which can provide effective prediction on the reaction mechanism. Thus, it can guide us to design new reactions, trap potential intermediates and develop novel ligands or catalysts. Combination of experimental and theoretical study plays a crucial role in organic chemistry, even in the whole chemistry.

7.

General Information

NMR spectroscopy

^1H -, ^{13}C - and ^{19}F -NMR spectra were recorded on either Varian AV600/AV400 or an Agilent DD2 400 NMR spectrometer using CDCl_3 as solvents. Spectra are referenced to the corresponding solvents. Data are reported in the following order: chemical shift (δ) in ppm; multiplicities are indicated b (broadened singlet), s (singlet), d (doublet), t (triplet), q (quartet), m (multiplet)); coupling constants (J) are in Hertz (Hz).

IR spectra

IR spectra were recorded on a Jasco FT/IR-420 and a Perkin Elmer Spectrum 100 spectrometer and are reported in terms of frequency of absorption (cm^{-1}).

HRMS spectra

HRMS data were recorded on a ThermoFisher Scientific LTQ Orbitrap XL using ESI ionization or on a Finnigan MAT 95 using EI ionization at 70 eV.

Thin layer chromatography

Analytical thin-layer chromatography (TLC) was performed on Merck silica gel aluminium plates with F-254 indicator, visualized by irradiation with UV light.

Solvents

Solvents used in reactions were p.A. grade and dried only if indicated. Solvents for chromatography were technical grade and distilled before use.

Blue LEDs

Blue LEDs used in this manuscript were Kessil PR160L, 467 nm, 10 – 40 W. Reactions were irradiated from 5 cm, temperature was set to ambient and cooling was realized with a fan.

Reagents

Unless otherwise noted, all commercially available compounds were used as provided without further purification.

8.

Abbreviations

Ac	acetyl
Ad	adamantly
AIMD	<i>Ab initio</i> molecular dynamics
Ar	aryl
BINAP	2,2'-bis(diphenylphosphino)-1,1'-binaphthyl
Bn	benzyl
BOX	bis(oxazoline) ligand
Bu	butyl
CAM	carbene/alkyne metathesis
CPA	chiral phosphoric acid
Cy	cyclohexyl
DavePhos	2-dicyclohexylphosphino-2'-(<i>N,N</i> -dimethylamino)biphenyl
DCE	1,2-dichloroethane
DCM	dichloromethane
DFT	density functional theory
dppb	1,4-bis(diphenylphosphino)butane
dppbe	1,2-bis(diphenylphosphino)benzene
dppe	1,2-bis(diphenylphosphino)ethane
dppf	1,1'-diphenylphosphino ferrocene
dpph	1,6-bis(diphenylphosphino)hexane
d.r	diastereoselective ratio
EDG	electron-donating group
ee	enantioselective excess
EnT	energy transfer
equiv.	equivalent
Et	ethyl
EtOAc	ethyl acetate
EWG	electron-withdrawing group
Fe(dmhdCl) ₃	iron(III) 4-chloro-2,6-dimethyl-3,5-heptanedionate
GC	gas chromatography
HAT	hydrogen atom transfer
HFIP	1,1,1,3,3,3-hexafluoro-2-propanol
HOMO	highest occupied molecular orbital
iPr	isopropyl
ISC	intersystem crossing
ISCT	inner-sphere electron transfer
IRC	intrinsic reaction coordinate
KIE	kinetic isotope effect
LED	light emitting diode
LUMO	lowest unoccupied molecular orbital
Me	methyl
MeCN	acetonitrile
MECP	minimum energy-crossing point
MLCT	metal to ligand charge transfer
MS	mass spectrometry

NaBAR _F	sodium tetrakis[3,5-bis(trifluoromethyl)phenyl]borate
NBO	Natural Bond Orbital
n.d	not detected
NFSI	<i>N</i> -fluorobenzenesulfonimide
NHC	<i>N</i> -heterocyclic carbene
n.r	no reaction
NMR	nuclear Magnetic Resonance
Nu	nucleophile
OSET	outer-sphere electron transfer
OTf	trifluoromethanesulfonate
PCET	proton-coupled electron transfer
Pd(OAc) ₂	palladium (II) acetate
Pd(TFA) ₂	palladium (II) triflate
Ph	phenyl
Piv	pivaloyl
PFTB	perfluoro- <i>tert</i> -butanol
rac	racemic
Rh ₂ esp ₂	bis[rhodium(α,α,α',α'-tetramethyl-1,3-benzenedipropionic acid)
Rh ₂ (OAc) ₄	rhodium(II) acetate
Rh ₂ (Oct) ₄	dirhodium(II) tetraoctanoate
Rh ₂ (<i>R</i> -DOSP) ₄	tetrakis[(<i>R</i>)-(+)- <i>N</i> -(<i>p</i> -dodecylphenylsulfonyl)prolinato]dirhodium(II)
Rh ₂ (5 <i>S</i> -MEPY) ₄	dirhodium(II) tetrakis[methyl 2-pyrrolidone-5(<i>S</i>)-carboxylate]
Rh ₂ (<i>S</i> -PTTL) ₄	dirhodium(II) tetrakis[<i>N</i> -phthaloyl-(<i>S</i>)- <i>tert</i> -leucinate]
Rh ₂ (TPA) ₄	tetrakis-(triphenylacetato)-dirhodium(II)
RuPhos	dicyclohexyl-[2-[2,6-di(propan-2-yloxy)phenyl]phenyl]phosphane
[RuCl ₂ (<i>p</i> -cymene)] ₂	dichloro(<i>p</i> -cymene)ruthenium(II) dimer
r.t.	room temperature
SET	single electron transfer
Sphos	2-dicyclohexylphosphino-2',6'-dimethoxybiphenyl
SPS	Solvent Purification System
TBAC	tetrabutylammonium chloride
TBME	methyl <i>tert</i> -butyl ether
<i>t</i> Bu	tertiary butyl
TD-DFT	Time-dependent density functional theory
TEMPO	2,2,6,6-tetramethyl-piperidine- <i>N</i> -oxide
TFE	trifluoroethanol
THF	tetrahydrofuran
TMS	trimethylsilyl group
TPCP	triphenylcyclopropane carboxylate
Ts	<i>p</i> -toluenesulfonyl
UV	ultraviolet
Vis	visible
Xantphos	4,5-bis(diphenylphosphino)-9,9-dimethylxanthene
Xphos	2-(dicyclohexylphosphino)-2',4',6'-tri- <i>i</i> -propyl-1,1'-biphenyl

9.

References

1. Shainyan, B. A.; Kuzmin, A. V.; Moskalik, M. Y. *Comput. Theor. Chem.* **2013**, 1006, 52.
2. Nemirowski, A.; Schreiner, P. R. *J. Org. Chem.* **2007**, 72, 9533.
3. Gronert, S.; Keeffe, J. R.; O'Ferrall, R. A. M. *J. Am. Chem. Soc.* **2011**, 133, 3381.
4. Ghafarian Shirazi, R.; Neese, F.; Pantazis, D. A., *J. Chem. Theory Comput.* **2018**, 14, 4733.
5. Costa, P.; Lohmiller, T.; Trosien, I.; Savitsky, A.; Lubitz, W.; Fernandez-Oliva, M.; Sanchez-Garcia, E.; Sander, W. *J. Am. Chem. Soc.* **2016**, 138, 1622.
6. Doyle, M. P. *Chem. Rev.* **1986**, 86, 919.
7. de Frémont, P.; Marion, N.; Nolan, S. P. *Coord. Chem. Rev.* **2009**, 253, 862.
8. W. von E. Doering, K. Hoffmann. *J. Am. Chem. Soc.* **1954**, 76, 6162.
9. Nelson, D. J.; Nolan, S. P. *Chem. Soc. Rev.* **2013**, 42, 6723.
10. Hopkinson, M. N.; Richter, C.; Schedler, M.; Glorius, F. *Nature* **2014**, 510, 485.
11. Cardin, D. J.; Cetinkaya, B.; Lappert, M. F. *Chem. Rev.* **1972**, 72, 545.
12. Tschugajeff, L.; Skanawy-Grigorjewa, M.; Posnjak, A. Z. *Anorg. Allg. Chem.* **1925**, 148, 37.
13. Burke, A.; Balch, A. L.; Enemark, J. H. *J. Am. Chem. Soc.* **1970**, 92, 2555.
14. Butler, W. M.; Enemark, J. H.; Parks, J.; Balch, A. L. *Inorg. Chem.* **1973**, 12, 451.
15. Rouschias, G.; Shaw, B. L. *J. Chem. Soc. A* **1971**, 2097.
16. Fischer, E. O.; Maasböl, A. *Angew. Chem., Int. Ed.* **1964**, 3, 580.
17. Schrock, R. R. *J. Am. Chem. Soc.* **1974**, 96, 6796.
18. Taylor, T. E.; Hall, M. B. *J. Am. Chem. Soc.* **1984**, 106, 1576.
19. Vyboishchikov, S. F.; Frenking, G. *Chem. - Eur. J.* **1998**, 4, 1428.
20. Schrock, R. R. *Chem. Rev.* **2002**, 102, 145.
21. Grubbs, R. H. *Tetrahedron* **2004**, 60, 7117.
22. Grubbs, R. H.; Chang, S. *Tetrahedron* **1998**, 54, 4413.
23. Fürstner, A. *Angew. Chem., Int. Ed.* **2000**, 39, 3012.
24. Kornecki, K. P.; Briones, J. F.; Boyarskikh, V.; Fullilove, F.; Autschbach, J.; Schrote, K. E.; Lancaster, K. M.; Davies, H. M.; Berry, J. F. *Science* **2013**, 342, 351.
25. Davies, H. M.; Morton, D. *Chem. Soc. Rev.* **2011**, 40, 1857.
26. Ye, T.; McKervey, M. A. *Chem. Rev.* **1994**, 94, 1091.
27. Maas, G. *Angew. Chem., Int. Ed.* **2009**, 48, 8186.
28. Ford, A.; Miel, H.; Ring, A.; Slattery, C. N.; Maguire, A. R.; McKervey, M. A. *Chem. Rev.* **2015**, 115, 9981.
29. Fulton, J. R.; Aggarwal, V. K.; de Vicente, J. *Eur. J. Org. Chem.* **2005**, 1479.
30. Xia, Y.; Wang, J. *Chem. Soc. Rev.* **2017**, 46, 2306.
31. Shao, Z.; Zhang, H. *Chem. Soc. Rev.* **2012**, 41, 560.
32. Barluenga, J.; Valdés, C. *Angew. Chem., Int. Ed.* **2011**, 50, 7486.
33. Jiang, Y.; Sun, R.; Tang, X. Y.; Shi, M. *Chem. - Eur. J.* **2016**, 22, 17910.
34. Davies, H. M.; Alford, J. S. *Chem. Soc. Rev.* **2014**, 43, 5151.
35. Muller, P., *Acc. Chem. Res.* **2004**, 37, 243.
36. Burtoloso, A. C. B.; Dias, R. M. P.; Leonarczyk, I. A. *Eur. J. Org. Chem.* **2013**, 5005.
37. Rubin, M.; Rubina, M.; Gevorgyan, V. *Chem. Rev.* **2007**, 107, 3117.
38. Solorio-Alvarado, C. R.; Wang, Y.; Echavarren, A. M., *J. Am. Chem. Soc.* **2011**, 133, 11952.
39. Zhang, L. *Acc. Chem. Res.* **2014**, 47, 877.
40. Asiri, A. M.; Hashmi, A. S. *Chem. Soc. Rev.* **2016**, 45, 4471.
41. Soheli, S. M. A.; Liu, R. S., *Chem. Soc. Rev.* **2009**, 38, 2269.
42. Deng, Y.; Qiu, H.; D. Srinivas, H.; P. Doyle, M. *Curr. Org. Chem.* **2016**, 20, 61.
43. Doyle, M. P. *J. Org. Chem.* **2006**, 71, 9253.

44. Kennedy, M.; McKerverey, M. A.; Maguire, A. R.; Roos, G. H. P. *J. Chem. Soc., Chem. Commun.* **1990**, 361.
45. Briones, J. F.; Hansen, J.; Hardcastle, K. I.; Autschbach, J.; Davies, H. M. *J. Am. Chem. Soc.* **2010**, *132*, 17211.
46. Qin, C.; Boyarskikh, V.; Hansen, J. H.; Hardcastle, K. I.; Musaev, D. G.; Davies, H. M. *J. Am. Chem. Soc.* **2011**, *133*, 19198.
47. Kitagaki, S.; Anada, M.; Kataoka, O.; Matsuno, K.; Umeda, C.; Watanabe, N.; Hashimoto, S.-i. *J. Am. Chem. Soc.* **1999**, *121*, 1417.
48. DeAngelis, A.; Dmitrenko, O.; Yap, G. P.; Fox, J. M. *J. Am. Chem. Soc.* **2009**, *131*, 7230.
49. Doyle, M. P.; Winchester, W. R.; Hoorn, J. A. A.; Lynch, V.; Simonsen, S. H.; Ghosh, R. *J. Am. Chem. Soc.* **2002**, *115*, 9968.
50. Pellissier, H. *Tetrahedron* **2008**, *64*, 7041.
51. Lebel, H.; Marcoux, J. F.; Molinaro, C.; Charette, A. B. *Chem. Rev.* **2003**, *103*, 977.
52. Chen, Y.; Ruppel, J. V.; Zhang, X. P. *J. Am. Chem. Soc.* **2007**, *129*, 12074.
53. Xue, Y.-S.; Cai, Y.-P.; Chen, Z.-X. *RSC Adv.* **2015**, *5*, 57781.
54. Lu, H.; Dzik, W. I.; Xu, X.; Wojtas, L.; de Bruin, B.; Zhang, X. P. *J. Am. Chem. Soc.* **2011**, *133*, 8518.
55. Chirila, A.; Brands, M. B.; de Bruin, B. *J. Catal.* **2018**, *361*, 347.
56. Batista, V. F.; G. A. Pinto, D. C.; Silva, A. M. S. *ACS Catal.* **2020**, *10*, 10096.
57. Morandi, B.; Carreira, E. M. *Science* **2012**, *335*, 1471.
58. Wei, Y.; Tinoco, A.; Steck, V.; Fasan, R.; Zhang, Y. *J. Am. Chem. Soc.* **2018**, *140*, 1649.
59. Groves, J. T. *Proc. Natl. Acad. Sci. U.S.A.* **2003**, *100*, 3569.
60. Davies, H. M.; Manning, J. R. *Nature* **2008**, *451*, 417.
61. Davies, H. M. L.; Liao, K. *Nat. Rev. Chem.* **2019**, *3*, 347.
62. Wang, B.; Qiu, D.; Zhang, Y.; Wang, J. *Beilstein J. Org. Chem.* **2016**, *12*, 796.
63. Qin, C.; Davies, H. M. *J. Am. Chem. Soc.* **2014**, *136*, 9792.
64. Yoshikai, N.; Nakamura, E. *Adv. Synth. Catal.* **2003**, *345*, 1159.
65. Bess, E. N.; Guptill, D. M.; Davies, H. M. L.; Sigman, M. S. *Chem. Sci.* **2015**, *6*, 3057.
66. Nakamura, E.; Yoshikai, N.; Yamanaka, M. *J. Am. Chem. Soc.* **2002**, *124*, 7181.
67. Hansen, J.; Autschbach, J.; Davies, H. M. *J. Org. Chem.* **2009**, *74*, 6555.
68. Clark, J. S.; Wong, Y.-S.; Townsend, R. J. *Tetrahedron Lett.* **2001**, *42*, 6187.
69. Padwa, A. *J. Organomet. Chem.* **2001**, *617*, 3.
70. Torres, Ò.; Pla-Quintana, A. *Tetrahedron Lett.* **2016**, *57*, 3881.
71. Pei, C.; Zhang, C.; Qian, Y.; Xu, X. *Org. Biomol. Chem.* **2018**, *16*, 8677.
72. Dong, K.; Pei, C.; Zeng, Q.; Wei, H.; Doyle, M. P.; Xu, X. *ACS Catal.* **2018**, *8*, 9543.
73. Zhu, S. F.; Zhou, Q. L. *Acc. Chem. Res.* **2012**, *45*, 1365.
74. Ren, Y. Y.; Zhu, S. F.; Zhou, Q. L. *Org. Biomol. Chem.* **2018**, *16*, 3087.
75. Bulughapitiya, P.; Landais, Y.; Parra-Rapado, L.; Planchenault, D.; Weber, V. *J. Org. Chem.* **1997**, *62*, 1630.
76. Zhu, S. F.; Chen, C.; Cai, Y.; Zhou, Q. L. *Angew. Chem., Int. Ed.* **2008**, *47*, 932.
77. Maier, T. C.; Fu, G. C. *J. Am. Chem. Soc.* **2006**, *128*, 4594.
78. Liang, Y.; Zhou, H.; Yu, Z. X. *J. Am. Chem. Soc.* **2009**, *131*, 17783.
79. Li, Y.; Zhao, Y. T.; Zhou, T.; Chen, M. Q.; Li, Y. P.; Huang, M. Y.; Xu, Z. C.; Zhu, S. F.; Zhou, Q. L. *J. Am. Chem. Soc.* **2020**, *142*, 10557.
80. Guo, X.; Hu, W. *Acc. Chem. Res.* **2013**, *46*, 2427.
81. Xu, B.; Li, M. L.; Zuo, X. D.; Zhu, S. F.; Zhou, Q. L. *J. Am. Chem. Soc.* **2015**, *137*, 8700.
82. Li, Z.; Parr, B. T.; Davies, H. M. *J. Am. Chem. Soc.* **2012**, *134*, 10942.
83. Li, Z.; Boyarskikh, V.; Hansen, J. H.; Autschbach, J.; Musaev, D. G.; Davies, H. M. *J. Am. Chem. Soc.* **2012**, *134*, 15497.
84. Li, Z.; Davies, H. M. *J. Am. Chem. Soc.* **2010**, *132*, 396.
85. Koenigs, R. M.; Empel, C.; Jana, S. *Synthesis* **2021**, *53*, 4567.
86. West, T. H.; Spoehrle, S. S. M.; Kasten, K.; Taylor, J. E.; Smith, A. D. *ACS Catal.* **2015**, *5*, 7446.
87. Jana, S.; Guo, Y.; Koenigs, R. M. *Chem. Eur. J.* **2021**, *27*, 1270.

88. Zhang, Y.; Wang, J. *Coord. Chem. Rev.* **2010**, *254*, 941.
89. Zhang, Z.; Sheng, Z.; Yu, W.; Wu, G.; Zhang, R.; Chu, W. D.; Zhang, Y.; Wang, J. *Nat. Chem.* **2017**, *9*, 970.
90. Liu, Z.; Jin, X.; Dang, Y. *ACS Catal.* **2020**, *11*, 691.
91. Laconsay, C. J.; Tantillo, D. J. *ACS Catal.* **2021**, *11*, 829.
92. Xia, Y.; Qiu, D.; Wang, J. *Chem. Rev.* **2017**, *117*, 13810.
93. Xia, Y.; Zhang, Y.; Wang, J. *ACS Catal.* **2013**, *3*, 2586.
94. Hyster, T. K.; Ruhl, K. E.; Rovis, T. *J. Am. Chem. Soc.* **2013**, *135*, 5364.
95. Barluenga, J.; Moriel, P.; Valdés, C.; Aznar, F. *Angew. Chem., Int. Ed.* **2007**, *46*, 5587.
96. Patel, P. K.; Dalvadi, J. P.; Chikhaliya, K. H. *RSC Adv.* **2014**, *4*, 55354.
97. Xia, Y.; Hu, F.; Liu, Z.; Qu, P.; Ge, R.; Ma, C.; Zhang, Y.; Wang, J. *Org. Lett.* **2013**, *15*, 1784.
98. Xu, S.; Chen, R.; Fu, Z.; Zhou, Q.; Zhang, Y.; Wang, J. *ACS Catal.* **2017**, *7*, 1993.
99. Chu, W. D.; Zhang, L.; Zhang, Z.; Zhou, Q.; Mo, F.; Zhang, Y.; Wang, J. *J. Am. Chem. Soc.* **2016**, *138*, 14558.
100. Candeias, N.; Afonso, C. *Curr. Org. Chem.* **2009**, *13*, 763.
101. Empel, C.; Koenigs, R. M. *Synlett* **2019**, *30*, 1929.
102. Ciszewski, L. W.; Rybicka-Jasinska, K.; Gryko, D. *Org. Biomol. Chem.* **2019**, *17*, 432.
103. Empel, C.; Pei, C.; Koenigs, R. M. *Chem. Commun.* **2022**, *58*, 2788.
104. Yang, Z.; Stivanin, M. L.; Jurberg, I. D.; Koenigs, R. M. *Chem. Soc. Rev.* **2020**, *49*, 6833.
105. Meier, H.; Zeller, K.-P. *Angew. Chem., Int. Ed. Engl.* **1975**, *14*, 32.
106. Kirmse, W. *Eur. J. Org. Chem.* **2002**, 2193.
107. Jurberg, I. D.; Davies, H. M. L. *Chem. Sci.* **2018**, *9*, 5112.
108. Hommelsheim, R.; Guo, Y.; Yang, Z.; Empel, C.; Koenigs, R. M. *Angew. Chem., Int. Ed.* **2019**, *58*, 1203.
109. Xiao, T.; Mei, M.; He, Y.; Zhou, L. *Chem. Commun.* **2018**, *54*, 8865.
110. Yang, Z.; Guo, Y.; Koenigs, R. M. *Chem. Eur. J.* **2019**, *25*, 6703.
111. Orłowska, K.; Rybicka-Jasinska, K.; Krajewski, P.; Gryko, D. *Org. Lett.* **2020**, *22*, 1018.
112. Yang, J.; Wang, J.; Huang, H.; Qin, G.; Jiang, Y.; Xiao, T. *Org. Lett.* **2019**, *21*, 2654.
113. Empel, C.; Patureau, F. W.; Koenigs, R. M. *J. Org. Chem.* **2019**, *84*, 11316.
114. Maiti, D.; Das, R.; Sen, S. *J. Org. Chem.* **2021**, *86*, 2522.
115. Jana, S.; Li, F.; Empel, C.; Verspeek, D.; Aseeva, P.; Koenigs, R. M. *Chem. Eur. J.* **2020**, *26*, 2586.
116. Jana, S.; Yang, Z.; Li, F.; Empel, C.; Ho, J.; Koenigs, R. M. *Angew. Chem., Int. Ed.* **2020**, *59*, 5562.
117. Stivanin, M. L.; Fernandes, A. A. G.; Silva, A. F.; Okada, C. Y.; Jurberg, I. D. *Adv. Synth. Catal.* **2020**, *362*, 1106.
118. He, F.; Koenigs, R. M. *Chem. Commun.* **2019**, *55*, 4881.
119. Guo, Y.; Nguyen, T. V.; Koenigs, R. M. *Org. Lett.* **2019**, *21*, 8814.
120. Chauhan, J.; Ravva, M. K.; Gremaud, L.; Sen, S. *Org. Lett.* **2020**, *22*, 4537.
121. Song, M.-P.; Niu, J.-L.; Zhang, X.; Du, C.; Zhang, H.; Li, X.-C.; Wang, Y.-L. *Synthesis* **2019**, *51*, 889.
122. Zhang, Z.; Yadagiri, D.; Gevorgyan, V. *Chem. Sci.* **2019**, *10*, 8399.
123. Moulay, S., *Chem. Educ.: Res. Pract.* **2002**, *3*, 33.
124. Wang, Y.-C.; Lai, X.-J.; Huang, K.; Yadav, S.; Qiu, G.; Zhang, L.; Zhou, H. *Org. Chem. Front.* **2021**, *8*, 1677.
125. Shimbayashi, T.; Sasakura, K.; Eguchi, A.; Okamoto, K.; Ohe, K. *Chem. Eur. J.* **2019**, *25*, 3156.
126. Ochiai, M.; Miyamoto, K.; Kaneaki, T.; Hayashi, S.; Nakanishi, W. *Science* **2011**, *332*, 448.
127. Kennedy, S. H.; Dherange, B. D.; Berger, K. J.; Levin, M. D. *Nature* **2021**, *593*, 223.
128. Qin, H.; Cai, W.; Wang, S.; Guo, T.; Li, G.; Lu, H. *Angew. Chem., Int. Ed.* **2021**, *60*, 20678.
129. Shin, K.; Kim, H.; Chang, S. *Acc. Chem. Res.* **2015**, *48*, 1040.
130. Intrieri, D.; Zardi, P.; Caselli, A.; Gallo, E. *Chem. Commun.* **2014**, *50*, 11440.
131. Ochiai, M.; Miyamoto, K.; Hayashi, S.; Nakanishi, W. *Chem. Commun.* **2010**, *46*, 511.
132. van Vliet, K. M.; de Bruin, B. *ACS Catal.* **2020**, *10*, 4751.
133. Lee, S.; Lei, H.; Rovis, T. *J. Am. Chem. Soc.* **2019**, *141*, 12536.
134. Lebel, H.; Huard, K.; Lectard, S. *J. Am. Chem. Soc.* **2005**, *127*, 14198.
135. Ma, Z.; Zhou, Z.; Kurti, L. *Angew. Chem., Int. Ed.* **2017**, *56*, 9886.

136. Jat, J. L.; Paudyal, M. P.; Gao, H.; Xu, Q. L.; Yousufuddin, M.; Devarajan, D.; Ess, D. H.; Kurti, L.; Falck, J. R. *Science* **2014**, *343*, 61.
137. Campbell, M. M.; Johnson, G. *Chem. Rev.* **1978**, *78*, 65.
138. Roizen, J. L.; Harvey, M. E.; Du Bois, J. *Acc. Chem. Res.* **2012**, *45*, 911.
139. Davies, H. M.; Long, M. S. *Angew. Chem., Int. Ed.* **2005**, *44*, 3518.
140. Gephart, R. T.; Warren, T. H. *Organometallics* **2012**, *31*, 7728.
141. Pellissier, H. *Adv. Synth. Catal.* **2014**, *356*, 1899-1935.
142. Bizet, V.; Hendriks, C. M.; Bolm, C. *Chem. Soc. Rev.* **2015**, *44*, 3378.
143. Fan, L.; Hao, J.; Yu, J.; Ma, X.; Liu, J.; Luan, X. *J. Am. Chem. Soc.* **2020**, *142*, 6698.
144. Llaveria, J.; Beltran, A.; Sameera, W. M.; Locati, A.; Diaz-Requejo, M. M.; Matheu, M. I.; Castillon, S.; Maseras, F.; Perez, P. J. *J. Am. Chem. Soc.* **2014**, *136*, 5342.
145. Wu, Q.; Hu, J.; Ren, X.; Zhou, J. *Chem. Eur. J.* **2011**, *17*, 11553.
146. Shen, M.; Leslie, B. E.; Driver, T. G. *Angew. Chem., Int. Ed.* **2008**, *47*, 5056.
147. Stokes, B. J.; Jovanovic, B.; Dong, H.; Richert, K. J.; Riell, R. D.; Driver, T. G., *J. Org. Chem.* **2009**, *74*, 3225.
148. Ju, M.; Zerull, E. E.; Roberts, J. M.; Huang, M.; Guzei, I. A.; Schomaker, J. M. *J. Am. Chem. Soc.* **2020**, *142*, 12930.
149. Wang, J.; Frings, M.; Bolm, C. *Angew. Chem., Int. Ed.* **2013**, *52*, 8661.
150. Thornton, A. R.; Martin, V. I.; Blakey, S. B. *J. Am. Chem. Soc.* **2009**, *131*, 2434.
151. Mace, N.; Thornton, A. R.; Blakey, S. B. *Angew. Chem., Int. Ed.* **2013**, *52*, 5836.
152. Thornton, A. R.; Blakey, S. B. *J. Am. Chem. Soc.* **2008**, *130*, 5020.
153. Hong, K.; Su, H.; Pei, C.; Lv, X.; Hu, W.; Qiu, L.; Xu, X. *Org. Lett.* **2019**, *21*, 3328.
154. Brachet, E.; Ghosh, T.; Ghosh, I.; Konig, B. *Chem. Sci.* **2015**, *6*, 987.
155. Hernandez-Guerra, D.; Hlavackova, A.; Pramthaisong, C.; Vespoli, I.; Pohl, R.; Slanina, T.; Jahn, U. *Angew. Chem., Int. Ed.* **2019**, *58*, 12440.
156. Tang, J. J.; Yu, X.; Wang, Y.; Yamamoto, Y.; Bao, M. *Angew. Chem., Int. Ed.* **2021**, *60*, 16426.
157. Tian, X.; Song, L.; Hashmi, A. S. K. *Angew. Chem., Int. Ed.* **2020**, *59*, 12342.
158. Du, Y. D.; Zhou, C. Y.; To, W. P.; Wang, H. X.; Che, C. M. *Chem. Sci.* **2020**, *11*, 4680.
159. Scholz, S. O.; Farney, E. P.; Kim, S.; Bates, D. M.; Yoon, T. P. *Angew. Chem., Int. Ed.* **2016**, *55*, 2239.
160. Bizet, V.; Buglioni, L.; Bolm, C. *Angew. Chem., Int. Ed.* **2014**, *53*, 5639.
161. Lebel, H.; Piras, H.; Borduy, M. *ACS Catal.* **2016**, *6*, 1109.
162. Farney, E. P.; Yoon, T. P. *Angew. Chem., Int. Ed.* **2014**, *53*, 793.
163. Kobayashi, Y.; Masakado, S.; Takemoto, Y. *Angew. Chem., Int. Ed.* **2018**, *57*, 693.
164. Shilov, A. E.; Shul'pin, G. B., *Chem. Rev.* **1997**, *97*, 2879.
165. Arndtsen, B. A.; Bergman, R. G.; Mobley, T. A.; Peterson, T. H. *Acc. Chem. Res.* **1995**, *28*, 154.
166. Bergman, R. G. *Nature* **2007**, *446*, 391.
167. Fu, J.; Ren, Z.; Bacsa, J.; Musaev, D. G.; Davies, H. M. L. *Nature* **2018**, *564*, 395.
168. Liao, K.; Pickel, T. C.; Boyarskikh, V.; Bacsa, J.; Musaev, D. G.; Davies, H. M. L. *Nature* **2017**, *551*, 609.
169. Liu, W.; Ren, Z.; Bosse, A. T.; Liao, K.; Goldstein, E. L.; Bacsa, J.; Musaev, D. G.; Stoltz, B. M.; Davies, H. M. L. *J. Am. Chem. Soc.* **2018**, *140*, 12247.
170. Liao, K.; Liu, W.; Niemeyer, Z. L.; Ren, Z.; Bacsa, J.; Musaev, D. G.; Sigman, M. S.; Davies, H. M. L. *ACS Catal.* **2017**, *8*, 678.
171. Ye, L. W.; Zhu, X. Q.; Sahani, R. L.; Xu, Y.; Qian, P. C.; Liu, R. S. *Chem. Rev.* **2021**, *121*, 9039.
172. Liu, L.; Zhang, J. *Chem. Soc. Rev.* **2016**, *45*, 506.
173. Yu, Z.; Ma, B.; Chen, M.; Wu, H. H.; Liu, L.; Zhang, J. *J. Am. Chem. Soc.* **2014**, *136*, 6904.
174. Ma, B.; Chu, Z.; Huang, B.; Liu, Z.; Liu, L.; Zhang, J. *Angew. Chem., Int. Ed.* **2017**, *56*, 2749.
175. Xi, Y.; Su, Y.; Yu, Z.; Dong, B.; McClain, E. J.; Lan, Y.; Shi, X. *Angew. Chem., Int. Ed.* **2014**, *53*, 9817.
176. Jana, S.; Empel, C.; Pei, C.; Vinh Nguyen, T.; Koenigs, R. M. *Adv. Synth. Catal.* **2020**, *362*, 5721.
177. Jana, S.; Empel, C.; Pei, C.; Aseeva, P.; Nguyen, T. V.; Koenigs, R. M. *ACS Catal.* **2020**, *10*, 9925.
178. Jana, S.; Empel, C.; Nguyen, T. V.; Koenigs, R. M. *Chem. Eur. J.* **2021**, *27*, 2628.
179. Shen, H. Q.; Wu, B.; Xie, H. P.; Zhou, Y. G. *Org. Lett.* **2019**, *21*, 2712.
180. Shen, H.-Q.; Xie, H.-P.; Sun, L.; Zhou, Y.-G. *Organometallics* **2019**, *38*, 3902.

181. Arredondo, V.; Hiew, S. C.; Gutman, E. S.; Premachandra, I. D.; Van Vranken, D. L. *Angew. Chem., Int. Ed.* **2017**, *56*, 4156.
182. M. J. Frisch, et al., Gaussian 09, Revision D.01, Gaussian, Inc., Wallingford CT, **2013**.
183. M. J. Frisch, et al., Gaussian 16, Revision C.01, Gaussian, Inc., Wallingford CT, **2019**.
184. Zhao, Y.; Truhlar, D. G. *Acc. Chem. Res.* **2008**, *41*, 157.
185. Zhao, Y.; Truhlar, D. G. *Theor. Chem. Acc.* **2007**, *120*, 215.
186. Hay, P. J.; Wadt, W. R. *J. Chem. Phys.* **1985**, *82*, 270.
187. Hariharan, P. C.; Pople, J. A. *Theor. Chem. Acc.* **1973**, *28*, 213.
188. Hehre, W. J.; Ditchfield, R.; Pople, J. A. *J. Chem. Phys.* **1972**, *56*, 2257.
189. Ditchfield, R.; Hehre, W. J.; Pople, J. A. *J. Chem. Phys.* **1971**, *54*, 724.
190. Liu, Y.; Yu, Z.; Zhang, J. Z.; Liu, L.; Xia, F.; Zhang, J. *Chem. Sci.* **2016**, *7*, 1988.
191. Liu, Y.; Yu, Z.; Luo, Z.; Zhang, J. Z.; Liu, L.; Xia, F. *J. Phys. Chem. A* **2016**, *120*, 1925.
192. Fukui, K. *Acc. Chem. Res.* **1981**, *14*, 363.
193. Fukui, K. *J. Chem. Phys.* **1970**, *74*, 4161.
194. Scalmani, G.; Frisch, M. J. *J. Chem. Phys.* **2010**, *132*, 114110.
195. Legault, C. Y. CYLview20, Université de Sherbrooke, **2020** (<http://www.cylview.org>).
196. Pan, Y.; Qiu, J.; Silverman, R. B. *J. Med. Chem.* **2003**, *46*, 5292.
197. Messaoudi, S.; Treguier, B.; Hamze, A.; Provot, O.; Peyrat, J. F.; De Losada, J. R.; Liu, J. M.; Bignon, J.; Wdzieczak-Bakala, J.; Thoret, S.; Dubois, J.; Brion, J. D.; Alami, M. *J. Med. Chem.* **2009**, *52*, 4538.
198. Meanwell, N. A. *J. Med. Chem.* **2011**, *54*, 2529.
199. Zhang, X.; Cao, S. *Tetrahedron Lett.* **2017**, *58*, 375.
200. Hu, J.; Ni, C. *Synthesis* **2014**, *46*, 842.
201. Dilman, A. D.; Levin, V. V. *Acc. Chem. Res.* **2018**, *51*, 1272.
202. Yang, Z.; Moller, M.; Koenigs, R. M. *Angew. Chem., Int. Ed.* **2020**, *59*, 5572.
203. Yang, Z.; Pei, C.; Koenigs, R. M. *Org. Lett.* **2020**, *22*, 7234.
204. Lee, C.; Yang, W.; Parr, R. G. *Phys. Rev. B* **1988**, *37*, 785.
205. Becke, A. D. *J. Chem. Phys.* **1993**, *98*, 5648.
206. Igel-Mann, G.; Stoll, H.; Preuss, H. *Mol. Phys.* **1988**, *65*, 1321.
207. Dolg, M.; Wedig, U.; Stoll, H.; Preuss, H. *J. Chem. Phys.* **1987**, *86*, 866.
208. Marenich, A. V.; Cramer, C. J.; Truhlar, D. G. *J. Phys. Chem. B* **2009**, *113*, 6378.
209. Grimme, S.; Antony, J.; Ehrlich, S.; Krieg, H. *J. Chem. Phys.* **2010**, *132*, 154104.
210. McLean, A. D.; Chandler, G. S. *J. Chem. Phys.* **1980**, *72*, 5639.
211. Krishnan, R.; Binkley, J. S.; Seeger, R.; Pople, J. A. *J. Chem. Phys.* **1980**, *72*, 650.
212. Uehara, M.; Suematsu, H.; Yasutomi, Y.; Katsuki, T. *J. Am. Chem. Soc.* **2011**, *133*, 170.
213. Tran, U. P. N.; Hommelsheim, R.; Yang, Z.; Empel, C.; Hock, K. J.; Nguyen, T. V.; Koenigs, R. M. *Chem. Eur. J.* **2020**, *26*, 1254.
214. Mertens, L.; Hock, K. J.; Koenigs, R. M. *Chem. Eur. J.* **2016**, *22*, 9542.
215. Hock, K. J.; Mertens, L.; Metze, F. K.; Schmittmann, C.; Koenigs, R. M. *Green Chem.* **2017**, *19*, 905.
216. Hyde, S.; Veliks, J.; Liegault, B.; Grassi, D.; Taillefer, M.; Gouverneur, V. *Angew. Chem., Int. Ed.* **2016**, *55*, 3785.
217. Carreras, V.; Besnard, C.; Gandon, V.; Ollevier, T. *Org. Lett.* **2019**, *21*, 9094.
218. Zhang, Z.; Zhou, Q.; Yu, W.; Li, T.; Wu, G.; Zhang, Y.; Wang, J. *Org. Lett.* **2015**, *17*, 2474.
219. Wang, X.; Xu, Y.; Deng, Y.; Zhou, Y.; Feng, J.; Ji, G.; Zhang, Y.; Wang, J. *Chem. Eur. J.* **2014**, *20*, 961.
220. Jiménez-Aquino, A.; Vega, J. A.; Trabanco, A. A.; Valdés, C. *Adv. Synth. Catal.* **2014**, *356*, 1079.
221. Pei, C.; Yang, Z.; Koenigs, R. M. *Org. Lett.* **2020**, *22*, 7300.
222. Noel, F.; Vukovic, V. D.; Yi, J.; Richmond, E.; Kravljanić, P.; Moran, J. *J. Org. Chem.* **2019**, *84*, 15926.
223. Zhang, Q.; Muhammad, M. T.; Chiou, M. F.; Jiao, Y.; Bao, H.; Li, Y. *Org. Lett.* **2020**, *22*, 5261.
224. Ambler, B. R.; Peddi, S.; Altman, R. A. *Org. Lett.* **2015**, *17*, 2506.
225. Zhang, G.; Song, Y. K.; Zhang, F.; Xue, Z. J.; Li, M. Y.; Zhang, G. S.; Zhu, B. B.; Wei, J.; Li, C.; Feng, C. G.; Lin, G. Q. *Nat. Commun.* **2021**, *12*, 728.
226. Jana, S.; Yang, Z.; Pei, C.; Xu, X.; Koenigs, R. M. *Chem. Sci.* **2019**, *10*, 10129.

227. Yadagiri, D.; Anbarasan, P. *Chem. Eur. J.* **2013**, *19*, 15115.
228. Miura, T.; Fujimoto, Y.; Funakoshi, Y.; Murakami, M. *Angew. Chem., Int. Ed.* **2015**, *54*, 9967.
229. Li, F.; Pei, C.; Koenigs, R. M. *Org. Lett.* **2020**, *22*, 6816.
230. Mugesh, G.; du Mont, W. W.; Sies, H. *Chem. Rev.* **2001**, *101*, 2125.
231. Santoro, S.; Azeredo, J. B.; Nascimento, V.; Sancineto, L.; Braga, A. L.; Santi, C. *RSC Adv.* **2014**, *4*, 31521.
232. Wirth, T. *Angew. Chem., Int. Ed.* **2000**, *39*, 3740.
233. Li, F.; Pei, C.; Koenigs, R. M. *Chem. Sci.* **2021**, *12*, 6362.
234. Li, F.; Pei, C.; Quaranta, C.; Koenigs, R. M. *Adv. Synth. Catal.* **2021**, *363*, 4365.
235. Weigend, F.; Ahlrichs, R. *Phys. Chem. Chem. Phys.* **2005**, *7*, 3297.
236. Zhu, D.; Chen, L.; Fan, H.; Yao, Q.; Zhu, S. *Chem. Soc. Rev.* **2020**, *49*, 908.
237. Bergstrom, B. D.; Nickerson, L. A.; Shaw, J. T.; Souza, L. W. *Angew. Chem., Int. Ed.* **2021**, *60*, 6864.
238. Yang, L. L.; Evans, D.; Xu, B.; Li, W. T.; Li, M. L.; Zhu, S. F.; Houk, K. N.; Zhou, Q. L. *J. Am. Chem. Soc.* **2020**, *142*, 12394.
239. Jagannathan, J. R.; Fetting, J. C.; Shaw, J. T.; Franz, A. K. *J. Am. Chem. Soc.* **2020**, *142*, 11674.
240. Lee, M.; Ren, Z.; Musaev, D. G.; Davies, H. M. L. *ACS Catal.* **2020**, *10*, 6240.
241. Jana, S.; Pei, C.; Empel, C.; Koenigs, R. M. *Angew. Chem., Int. Ed.* **2021**, *60*, 13271.
242. Arduengo Iii, A. J.; Calabrese, J. C.; Davidson, F.; Rasika Dias, H. V.; Goerlich, J. R.; Krafczyk, R.; Marshall, W. J.; Tamm, M.; Schmutzler, R. *Helv. Chim. Acta* **1999**, *82*, 2348.
243. Weinhold, F.; Landis, C. R. *Chem. Educ. Res. Pract.* **2001**, *2*, 91.
244. Neese, F. *Wiley Interdiscip. Rev. Comput. Mol. Sci.* **2018**, *8*, e1327.
245. Xu, J.; Mieres-Perez, J.; Sanchez-Garcia, E.; Lee, J. K. *J. Org. Chem.* **2019**, *84*, 7685.
246. Dunning, T. H. *J. Chem. Phys.* **1989**, *90*, 1007.
247. Empel, C.; Pei, C.; He, F.; Jana, S.; Koenigs, R. M. *Chem. Eur. J.* **2022**, *28*, e202104397.
248. Li, Q.; Cai, B. G.; Li, L.; Xuan, J. *Org. Lett.* **2021**, *23*, 6951.
249. Empel, C.; Jana, S.; Pei, C.; Nguyen, T. V.; Koenigs, R. M. *Org. Lett.* **2020**, *22*, 7225.
250. Pei, C.; Koenigs, R. M. *J. Org. Chem.* **2022**, *87*, 6832.
251. Ajitha, M. J.; Huang, K. W. *Org. Biomol. Chem.* **2015**, *13*, 10981.
252. Bug, T.; Hartnagel, M.; Schlierf, C.; Mayr, H. *Chem. Eur. J.* **2003**, *9*, 4068.
253. Knorr, J.; Sokkar, P.; Schott, S.; Costa, P.; Thiel, W.; Sander, W.; Sanchez-Garcia, E.; Nuernberger, P. *Nat. Commun.* **2016**, *7*, 12968.
254. Costa, P.; Sander, W. *Angew. Chem., Int. Ed.* **2014**, *53*, 5122.
255. Standard, J. M. *J. Phys. Chem. A* **2017**, *121*, 381.
256. Humphrey, W.; Dalke, A.; Schulten, K. *J. Mol. Graph.* **1996**, *14*, 33.
257. Kossmann, S.; Neese, F., *Chem. Phys. Lett.* **2009**, *481*, 240.
258. Harvey, J. N.; Aschi, M.; Schwarz, H.; Koch, W. *Theor. Chem. Acc.* **1998**, *99*, 95.
259. Lu, T. sobMECP program; <http://sobereva.com/286>.
260. Szabó, K. J.; Lübcke, M. *Synlett* **2020**, *32*, 1060.
261. Yuan, W.; Eriksson, L.; Szabo, K. J. *Angew. Chem., Int. Ed.* **2016**, *55*, 8410.
262. Mai, B. K.; Szabó, K. J.; Himo, F. *ACS Catal.* **2018**, *8*, 4483.
263. Yuan, W.; Szabó, K. J. *ACS Catal.* **2016**, *6*, 6687.
264. Mai, B. K.; Szabo, K. J.; Himo, F. *Org. Lett.* **2018**, *20*, 6646.
265. He, F.; Pei, C.; Koenigs, R. M. *Chem. Commun.* **2020**, *56*, 599.
266. Su, Y. L.; Liu, G. X.; Liu, J. W.; Tram, L.; Qiu, H.; Doyle, M. P. *J. Am. Chem. Soc.* **2020**, *142*, 13846.
267. Rybicka-Jasinska, K.; Shan, W.; Zawada, K.; Kadish, K. M.; Gryko, D. *J. Am. Chem. Soc.* **2016**, *138*, 15451.
268. Huang, X.; Webster, R. D.; Harms, K.; Meggers, E. *J. Am. Chem. Soc.* **2016**, *138*, 12636.
269. Zhang, X.-J.; Cheng, Y.-M.; Zhao, X.-W.; Cao, Z.-Y.; Xiao, X.; Xu, Y. *Org. Chem. Front.* **2021**, *8*, 2315.
270. Li, F.; Pei, C.; Koenigs, R. M. *Angew. Chem., Int. Ed.* **2022**, *61*, e202111892.
271. Narayanam, J. M.; Stephenson, C. R. *Chem. Soc. Rev.* **2011**, *40*, 102.
272. Twilton, J.; Le, C.; Zhang, P.; Shaw, M. H.; Evans, R. W.; MacMillan, D. W. C. *Nat. Rev. Chem.* **2017**, *1*, 0052.

273. Marcus, R. A. *J. Chem. Phys.* **1956**, *24*, 966.
274. Guo, Y.; Pei, C.; Koenigs, R. M. *Nat. Commun.* **2022**, *13*, 86.
275. Guo, Y.; Pei, C.; Empel, C.; Jana, S.; Koenigs, R. M. *ChemPhotoChem* **2022**, *6*, e20210029.
276. Guo, Y.; Pei, C.; Jana, S.; Koenigs, R. M. *ACS Catal.* **2020**, *11*, 337.
277. Perdew, J. P.; Burke, K.; Ernzerhof, M. *Phys. Rev. Lett.* **1996**, *77*, 3865.
278. Kancherla, R.; Muralirajan, K.; Sagadevan, A.; Rueping, M. *Trends in Chemistry* **2019**, *1*, 510.
279. Chuentragool, P.; Kurandina, D.; Gevorgyan, V. *Angew. Chem., Int. Ed.* **2019**, *58*, 11586.
280. Cheng, W.-M.; Shang, R. *ACS Catal.* **2020**, *10*, 9170.
281. Cheung, K. P. S.; Sarkar, S.; Gevorgyan, V. *Chem. Rev.* **2022**, *122*, 1543.
282. Pei, C.; Empel, C.; Koenigs, R. M. *Angew. Chem., Int. Ed.* **2022**, e202201743.
283. Sagadevan, A.; Greaney, M. F. *Angew. Chem., Int. Ed.* **2019**, *58*, 9826.
284. Gandeepan, P.; Koeller, J.; Korvorapun, K.; Mohr, J.; Ackermann, L. *Angew. Chem., Int. Ed.* **2019**, *58*, 9820.
285. Sagadevan, A.; Charitou, A.; Wang, F.; Ivanova, M.; Vuagnat, M.; Greaney, M. F. *Chem. Sci.* **2020**, *11*, 4439.
286. Korvorapun, K.; Struwe, J.; Kuniyil, R.; Zangarelli, A.; Casnati, A.; Waeterschoot, M.; Ackermann, L. *Angew. Chem., Int. Ed.* **2020**, *59*, 18103.
287. Thongpaen, J.; Manguin, R.; Dorcet, V.; Vives, T.; Duhayon, C.; Mauduit, M.; Basle, O. *Angew. Chem., Int. Ed.* **2019**, *58*, 15244.
288. Parasram, M.; Chuentragool, P.; Sarkar, D.; Gevorgyan, V. *J. Am. Chem. Soc.* **2016**, *138*, 6340.
289. Wang, G. Z.; Shang, R.; Cheng, W. M.; Fu, Y. *J. Am. Chem. Soc.* **2017**, *139*, 18307.
290. Kurandina, D.; Parasram, M.; Gevorgyan, V. *Angew. Chem., Int. Ed.* **2017**, *56*, 14212.
291. Kancherla, R.; Muralirajan, K.; Maity, B.; Zhu, C.; Krach, P. E.; Cavallo, L.; Rueping, M. *Angew. Chem., Int. Ed.* **2019**, *58*, 3412.
292. Huang, H. M.; Bellotti, P.; Pfluger, P. M.; Schwarz, J. L.; Heidrich, B.; Glorius, F. *J. Am. Chem. Soc.* **2020**, *142*, 10173.
293. Cheung, K. P. S.; Kurandina, D.; Yata, T.; Gevorgyan, V. *J. Am. Chem. Soc.* **2020**, *142*, 9932.
294. Yang, Z.; Koenigs, R. M. *Chem. Eur. J.* **2021**, *27*, 3694-3699.
295. Jana, S.; Pei, C.; Bahukhandi, S. B.; Koenigs, R. M. *Chem Catal.* **2021**, *1*, 467.
296. Sheffler, D. J.; Nedelcovych, M. T.; Williams, R.; Turner, S. C.; Duerk, B. B.; Robbins, M. R.; Jadhav, S. B.; Niswender, C. M.; Jones, C. K.; Conn, P. J.; Daniels, R. N.; Lindsley, C. W. *Bioorg. Med. Chem. Lett.* **2014**, *24*, 1062.
297. Fuentealba, P.; Stoll, H.; von Szentpály, L.; Schwerdtfeger, P.; Preuss, H. *J. Phys. B* **1983**, *16*, L323.
298. Andrae, D.; Huermann, U.; Dolg, M.; Stoll, H.; Preu, H. *Theor. Chim. Acta* **1990**, *77*, 123.
299. Adamo, C.; Barone, V. *J. Chem. Phys.* **1999**, *110*, 6158.